REDIRECTION OF CURRENT IN A DENSE PLASMA FOCUS

By

Rocky Yasuaki Gonzalez

Bachelor of Science – Electrical and Computer Engineering
University of Nevada, Las Vegas
2019

A thesis submitted in partial fulfillment
of the requirements for the

Master of Science in Engineering – Electrical Engineering

Department of Electrical and Computer Engineering
Howard R. Hughes College of Engineering
The Graduate College

University of Nevada, Las Vegas
May 2024

UNLV | GRADUATE COLLEGE

Thesis Approval

The Graduate College
The University of Nevada, Las Vegas

April 3, 2024

This thesis prepared by

Rocky Gonzalez

entitled

Redirection of Current in a Dense Plasma Focus

is approved in partial fulfillment of the requirements for the degree of

Master of Science in Engineering – Electrical Engineering
Department of Electrical and Computer Engineering

Robert Schill, Ph.D.
Examination Committee Chair

Biswajit Das, Ph.D.
Examination Committee Member

Yahia Baghzouz, Ph.D.
Examination Committee Member

Jichun Li, Ph.D.
Graduate College Faculty Representative

Alyssa Crittenden, Ph.D.
Vice Provost for Graduate Education &
Dean of the Graduate College

Abstract

The Mission Support & Test Services (MSTS) reports that significant amounts of energy needed for generating high energy neutrons is lost within a Dense Plasma Focus between its pinch-end of the anode stalk and at its base near the insulating sleeve. It is their mission and the goal of this research effort to both experimentally and theoretically study current redirection in a DPF during and after pinch dynamics. It is hypothesized that current redirection, due to restrike, behind the dynamic sheath of a dense plasma focus will result in a measurable change in the magnetic field along the longitudinal axis of a DPF. It is further hypothesized that a linear monopole antenna will be able to measure the loss current and determine the location of redirection. Theory and software will be utilized to demonstrate the expected current distribution within a dense plasma focus and then be compared to experimental data measured by the linear monopole antenna.

Table of Contents

List of Tables

List of Figures

List of Acronyms

CT:	Compact Toroid
DPF:	Dense Plasma Focus
GPM:	Gyrating Particle Model
HV:	High Voltage
LTspice	Linear Technology Simulation Program with Integrated Circuit Emphasis
MATLAB	Matrix Laboratory
MSTS:	Mission Support & Test Services
PCS:	Plasma Current Sheath
PF:	Plasma Focus
TEM:	Transverse Electromagnetic
TL:	Transmission Line
VF:	Velocity Factor

Chapter 1: Introduction

1.1 Introduction to the Dense Plasma Focus

The Plasma Focus (PF) device has been studied in plasma sciences beginning as early as the 1960s with an interest in further understanding controlled thermonuclear fusion processes [1]-[3]. The process of nuclear fusion involves the fusing of two or more nuclei by overcoming electrostatic Coulomb repulsion and then coming close enough and long enough such that their strong nuclear forces pull one another to form into heavier nuclei [4]-[6]. Nuclei lighter than iron-56 are more likely to fuse and have an exothermic reaction where the final mass of fused nuclei is slightly less than the total initial mass of the separate nuclei [4]-[6]. This mass difference (Δm) then appears as a form of kinetic energy (E) by Einstein's law $E = (\Delta m)c^2$ where c is the speed of light [5]-[6].

One method of overcoming Coulomb barriers in a controlled fusion system involves increasing the temperature and the density of the system [7]. In neutron production, hydrogen isotopes deuterium $({}^2H)$ and tritium $({}^3H)$ are generally favored energetic reactants for controlled fusion processes [4]. Fusion reactions involving nuclei with higher atomic number generally require more energy to overcome Coulomb barriers [5]. Deuterium and tritium can be fused to form a helium nucleus and a neutron particle $({}^1n)$ as a result of the interactions shown in Equations (1.1a-c) [5]-[6].

$$ {}^2H + {}^2H \rightarrow {}^3He + {}^1n + 3.27MeV \tag{1.1a}$$

$$ {}^2H + {}^2H \rightarrow {}^3H + {}^1H + 4.03MeV \tag{1.1b}$$

$$ {}^2H + {}^3H \rightarrow {}^4He + {}^1n + 17.58MeV \tag{1.1c}$$

Successfully containing nuclear fusion reactions in a controlled environment then requires the confinement of hot dense plasma [4]-[6]. An example of naturally occurring thermonuclear fusion reactions occur in the sun or stars where plasma is confined by their gravitational forces [4]-[5]. The PF device is designed to magnetically confine its electrically conductive plasma into a cylindrical column by means of Z-pinch dynamics as demonstrated in Fig. 1.1 [4], [6], [8]-[9]. During discharge in a Z-pinch device, the current density (J_z) flows in a partially ionized gas medium inducing an azimuthal magnetic field (B_θ) [7], [9]. By Lorentz force action $(\boldsymbol{F} = \boldsymbol{J} \times \boldsymbol{B})$ acting on the plasma, the gas medium becomes compressed radially inward [7], [9].

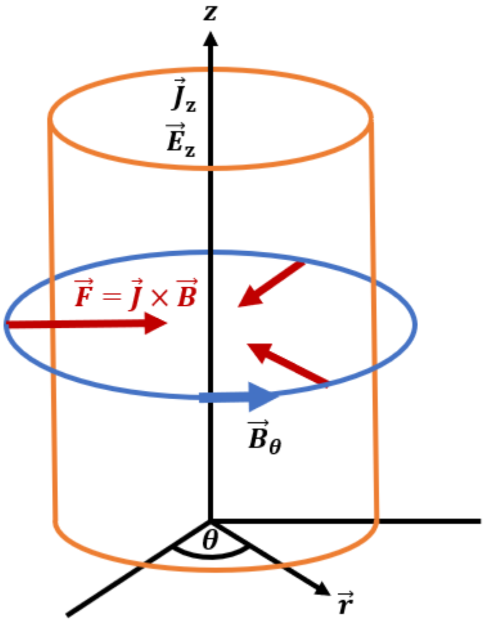

Fig. 1.1 During discharge in a Z-pinch device, the current density (J_z) flows in a partially ionized gas medium inducing an azimuthal magnetic flux field (B_θ). This results in a radially inward Lorentz force density action $(\boldsymbol{f} = d\boldsymbol{F}/dV = \boldsymbol{J} \times \boldsymbol{B})$ compressing the ionized gas and neutral gas trapped in the plasma sheath within the pinch region [7], [9].

What initially began as an investigation to understand controlled thermonuclear fusion in PF devices, it would later be elucidated that the production of neutrons in a plasma focus is a result of not only thermonuclear mechanisms, but dominantly beam-target mechanisms [3], [10]. A combination of both thermonuclear and beam-target models has shown to better demonstrate neutron yield output of a PF device [3], [7]-[8]. Various models for characterizing the neutron yield of a plasma focus will be further discussed in Section 1.2.

Beam-target processes differ from thermonuclear processes in that energy-output from nuclear reactions are produced by a beam of energetic particles, accelerated by strong electric fields caused by instabilities during pinch, strike a plasma target [8], [11]. Whereas thermonuclear processes differ in which high levels of temperature in a confined space is required for fusion to take place resulting in an isotropic emission of neutrons from pinch discharge [10]. However, experimentally during pinch discharge in a PF device, emission is dominantly observed in the axial direction than the radial direction suggesting the anisotropy being attributed to non-thermal processes such as that of ion beam-target processes [10].

Neutron output from a PF device, as described by a beam-target model, is based on interactions occurring due to instabilities from a very dense cylindrical Z-pinch transforming itself into a string of plasma-focuses [8]. Refer to Fig. 1.2. Each plasma focus formed then presents the opportunity for generating a beam of deuterium ions before being lost out of the system [8]. Beam-target interaction for plasma in a cylindrical column, such as in the case of Z-pinch formation, is shown in Fig. 1.3. Generally, in beam-target interactions, the beam is referred to as the non-thermal highly energetic ion beam and the target as the hot dense plasma in the pinch column [11].

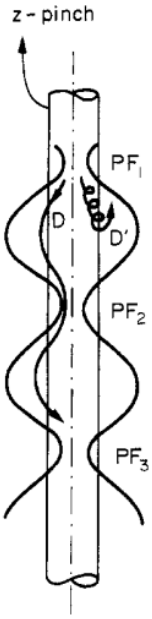

Fig. 1.2 During Z-pinch formation, strings of “plasma focuses” due to plasma instabilities (sausage instability and/or Rayleigh-Taylor instabilities) result in large field gradients causing energetic collisions among ions allowing for the fusion of nuclei to occur [8]. This photo is taken from [8].

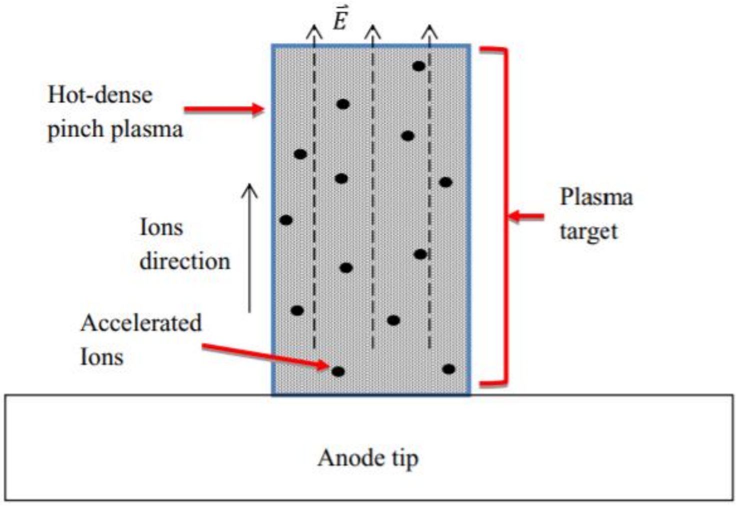

Fig. 1.3 The mechanism for beam-target interactions in a plasma column after Z-pinch formation is demonstrated. Photo is taken from [11].

For high energy density plasma formed by a dense plasma focus (DPF) device has made it a source of multiple radiation streams that may include ions, electrons, neutrons, and x-ray radiation [13]-[15]. This can be extended to application in fields of lithography, radiography, imaging, radioisotopes production, and plasma nanoscience [13]. The DPF has been optimized for its total neutron yield [16]. The typical structure of a PF is comprised of coaxial electrodes inside a chamber typically filled with a low-pressure gas mixture. The gas of choice for neutron generation is typically deuterium or deuterium-tritium [17]. The center anode electrode of the coax structure is covered by an insulator near the base side of anode allowing for plasma current sheath formation [17]. The outer electrode is generally comprised of a cage of cathode bars [17].

The physics of current pulse discharge in a DPF can be divided into four different phases. In the first phase, a capacitor bank releases a high-voltage pulse at the insulator end of the anode stalk. Gas ionization, insulator flashover, plasma sheath formation, and lift-off processes take place in this stage [16], [18]. In the second phase, or run-down phase, the current-carrying plasma sheath is accelerated towards the end of the anode due to $\boldsymbol{J} \times \boldsymbol{B}$ forces [16], [18]. The plasma sheath is then accelerated radially inward compressing trapped charges and neutral particles to form a filamentary plasma in the third phase, or the run-in phase [16], [18]. Finally, during the pinch phase, the plasma density and temperature begin to increase enabling fusion reactions [16], [18]. It is during the pinch phase, or implosion phase, that instabilities occur driving energetic beam formation [12]. The generation of neutrons in a DPF is then a consequence of MHD instabilities, such as sausage instabilities and Rayleigh-Taylor instabilities, during pinch dynamics [7]-[9], [11]. These different phases are summarized in Fig. 1.4 for reference.

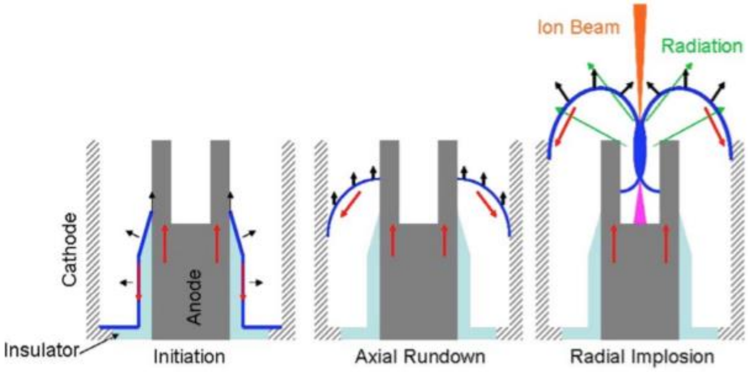

Fig. 1.4 Current pulse discharge into the DPF is demonstrated beginning with the initiation stage where plasma sheath formation takes place. The current-carrying plasma sheath is accelerated towards the end of the anode due to $\boldsymbol{J} \times \boldsymbol{B}$ forces during axial run-down. During radial implosion, the plasma sheath is accelerated radially inward compressing trapped charges and neutral particles to form a filamentary plasma leading to the pinch phase. This photo is taken from [12].

Now that the physics involved in a DPF has been covered, the rest of this chapter will build up the motivation involved in this research effort. In neutron production, numerous studies have been made to investigate the optimization of neutron yield output modeling for a DPF device. Section 1.2 will highlight scaling laws used to model neutron yield based on previous research involved with DPFs. An important aspect of section 1.2 will discuss the differences between I_{peak} and I_{pinch} currents and how they may help understand the idea of current redirection in a DPF. Section 1.3 will outline previous research involved with DPF devices. After obtaining an overview of previous DPF research, then Section 1.4 will open the discussion of identifying possible current redirection in a DPF system using antenna-based sensors and why it may be of interest to the DPF research community.

1.2 Scaling Laws for a DPF and Current Redirection

Recall in Section 1.1, research in PF devices began with an interest in understanding controlled thermonuclear fusion processes [3]. However, characterization of neutron yield from a PF device has expanded beyond investigating thermonuclear processes. Thermonuclear modeling failed to demonstrate high levels of neutron output suggesting alternate mechanisms to explain the measured yield Y_n [19]. Some of these mechanisms included beam-target, moving boiler, gyrating particles, and quasi-Maxwellian hot plasmoids for modeling [19]. Because the PF device is an inexpensive device for generating large neutron yield, interest to further investigate the underlying processes would continue to be pursued [16]. Of the research, the PF device's geometry, material properties, pressure environment, and energy supplied to the system has been investigated [3], [12], [16]. Most relevant physics and scaling laws for neutron yield in PF devices would become better established during the 1970s and 1980s [3], [12].

An example model used for characterizing neutron yield in PF devices is that of the Lee model code which has been implemented in numerous research efforts to assist in PF device design and interpretation [20]. The initial model was first developed in 1985 as a 2-phase code during the UNU Training Programme in Plasma and Laser Technology to describe and optimize the design of the PF [20]. The initial code took into consideration coupling of electrical circuit equations with PF dynamics, thermodynamics, and radiation physics [19], [12], [20]-[21]. The Lee model code would then transition to an improved 5-phase code incorporating finite small disturbance speed, radiation and radiation-coupled dynamics, and plasma self-absorption [20].

The total neutron yield due to thermonuclear processes and beam-target processes in a PF device is characterized by $Y_n = Y_{th} + Y_{b-t}$ where Y_{th} is the thermonuclear component and Y_{b-t}

is the beam-target component [10]. From [19]-[20], the beam-target neutron yield Y_{b-t} in a DPF is shown to be characterized by

$$Y_{b-t} = C_n n_i I_{pinch}^2 z_p^2 \ln\left(b/r_p\right) \frac{\sigma}{U^{0.5}} \tag{1.2}$$

The parameters characterizing the beam-target neutron yield are summarized in Table 1.1.

Table 1.1 A description of values is provided for characterizing the amount of neutron yield in a beam-target mechanism for a DPF using the Lee model code.

Value	**Description:**
C_n	Experimental calibration constant
n_i	ion density
z_p	Length of plasma pinch
b	Inner radius of Outer Electrode (Cathode)
r_p	Radius of plasma pinch
σ	Fusion Reaction Cross-section
U	Beam energy

While many parameters are involved for characterizing a PF and optimizing neutron yield Y_n, scaling laws provide a mean to understand the relationship between energy supplied to a PF and its neutron output. Previous PF device efforts have shown that Y_n scaling changes from $Y_n \sim E^2$ for low kilojoules and sub-kilojoules PF devices to $Y_n \sim E^{0.8}$ for high kilojoules and megajoules PF devices, where E is the storage energy in the PF system [3], [22]. Because energy supplied to a PF device and neutron yield is a complex relationship, other scaling laws have been examined when relating neutron yield to I_{total}, I_{peak}, and I_{pinch}. The total discharge current into a PF device is denoted by I_{total}, the peak value of the discharge current is denoted by I_{peak}, and the current flowing through the pinch at the start of the slow compression phase (end of radial phase) is denoted by I_{pinch} [20], [22].

An example current profile is shown in Fig. 1.5 for energy discharged into the PF1000 device as taken from [21]. In this figure, it is shown that during pulse discharge, the current distributed into the plasma column pinch is less than the peak current value as demonstrated by the dip in current. Using the 5-phase Lee model code, a curve is computed to fit onto the experimental data using model parameters based on the PF1000 system [21]. The model parameters include: the axial mass swept-up factor f_m, axial current factor f_c, radial mass swept-up factor f_{mr}, and the radial current factor f_{cr} [19], [20]-[21]. The pinch current can be found by multiplying the total peak current at the time of pinch to the axial current factor f_c [19], [20]-[21].

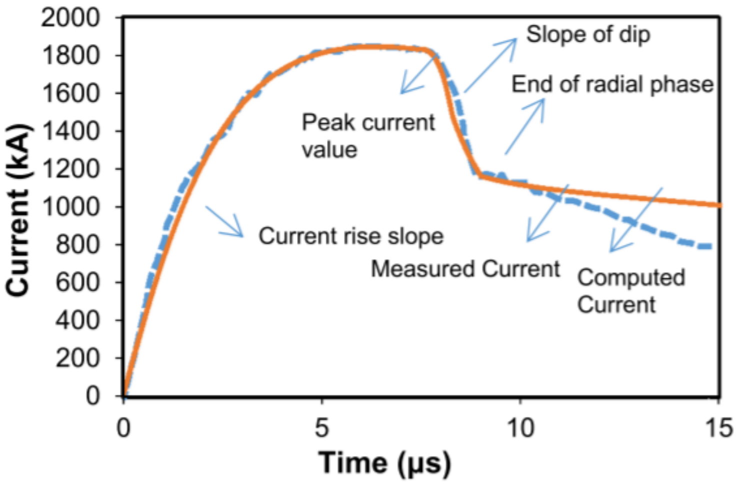

Fig. 1.5 The current profile for energy discharged into the PF1000 is shown as taken from [21]. The blue dashed line represents measured current from the PF1000 and the orange line represents a computed curve using the 5-phase Lee model code. In this current profile, it is shown that the total discharge current peaks at a value before dropping to a value at the end of the PF device's radial phase.

In [21], numerical experiments were conducted to compute additional curves using the 5-Phase Lee model code on the PF1000. In Fig. 1.6, these curves are shown demonstrating that an increase in pressure to the PF1000 system results in a lower pinch current and slightly increased peak current [21].

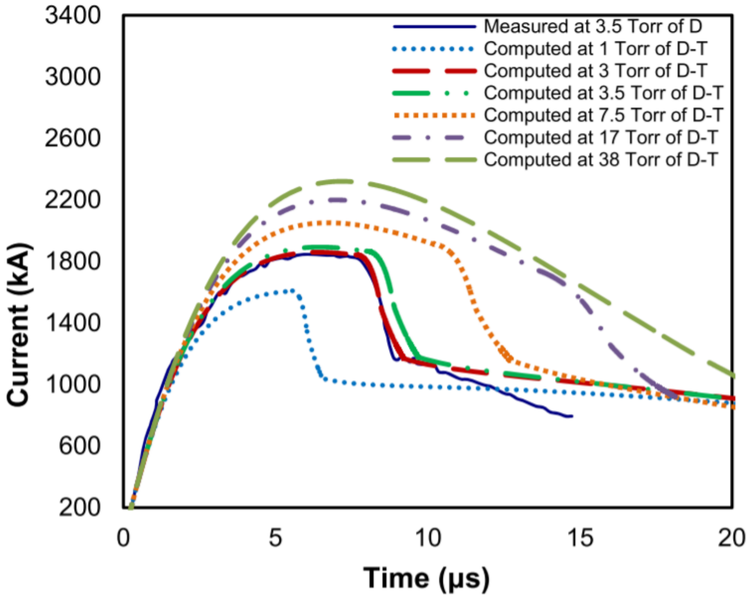

Fig. 1.6 Additional computed current waveforms for the PF1000 device are shown when adjusting the pressure of the gas of the PF system as taken from [21].

In [23], a similar numerical experiment is performed to compute additional curves to the PF1000 device when modifying static inductance in the system. For a fixed capacitance, the numerical experiments demonstrate that while there is an optimum inductance in which peak current increases, the pinch current I_{pinch} and neutron yield Y_n does not increase but instead decreases as a result of pinch current limitation effects in the PF [23]. This can be shown in the current waveforms provided in Fig. 1.7.

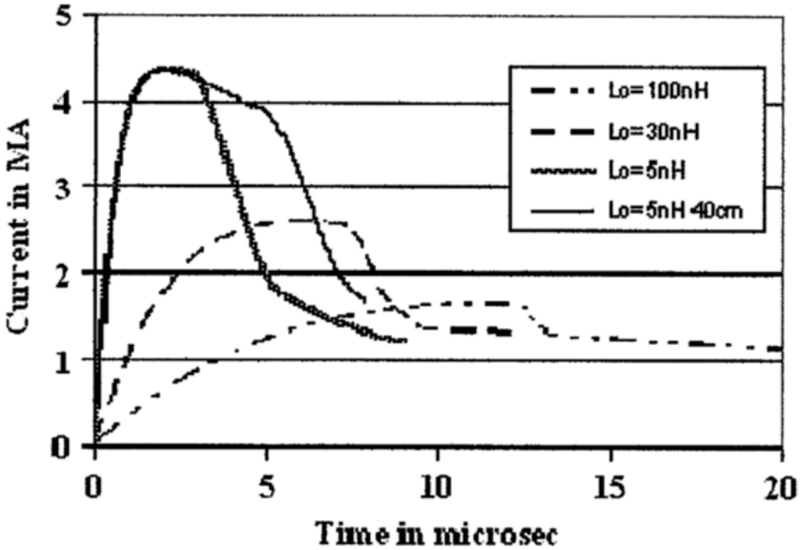

Fig. 1.7 Computed current waveforms in the PF1000 at 35kV, 3.5 Torr $D_2$for a range of L_0 for adjusted static inductance is shown as taken from [23].

Generally, the amount of current flowing inside the plasma column pinch I_{pinch} is less than the total amount of current supplied to the DPF I_{peak} [3]. This then suggests that the total amount of current supplied to the DPF is not being completely distributed into the plasma column. However, by following energy conservation laws, then this energy provided by current must be distributed elsewhere in the DPF system. Furthermore, pressure in a DPF is constrained by breakdown physics where most DPFs operate in pressures of 1-30 torr [12]. Lower pressures would create volume breakdown (glow discharge) preventing a coherent sheet from driving a shock [12]. Hence, this loss of current from the total amount of current supplied to the DPF will be referred to as current redirection (sometimes described as glow discharge or lightning strikes in a DPF).

1.3 Previous Research on DPF Current Redirection

While interest in studying the PF as a possible device for controlled thermonuclear fusion took place in the early 1960s, earlier forms of controlled thermonuclear fusion research existed in Z-pinches where MHD and Rayleigh-Taylor instabilities lead to highly unstable pinches [24], [3]. However, the PF would be able to demonstrate enhanced stability properties in plasmas with densities up to 10^{25} m^{-3} and 1keV temperatures within a narrow filament of 1mm radius [3]. In neutron production, the PF was determined to produce neutrons involving thermonuclear mechanisms and beam target mechanisms [24].

The PF was initially developed in the early 1960s independently by Mather in the U.S. and Filappov, Filippova, and Vinogradov in the U.S.S.R. [1]-[2], [12]. The two PF were similar in design but differed in their electrode aspect ratio [3]. In the Mather configuration, the PF originated from a plasma accelerator, designed with an electrode height larger than the inner electrode diameter [3], [24]-[25]. In the Filappov configuration, the PF is designed with an inner electrode diameter larger than the electrode height [3], [24]-[25]. The two geometric arrangements of the PF configurations are provided in Fig. 1.8 for reference.

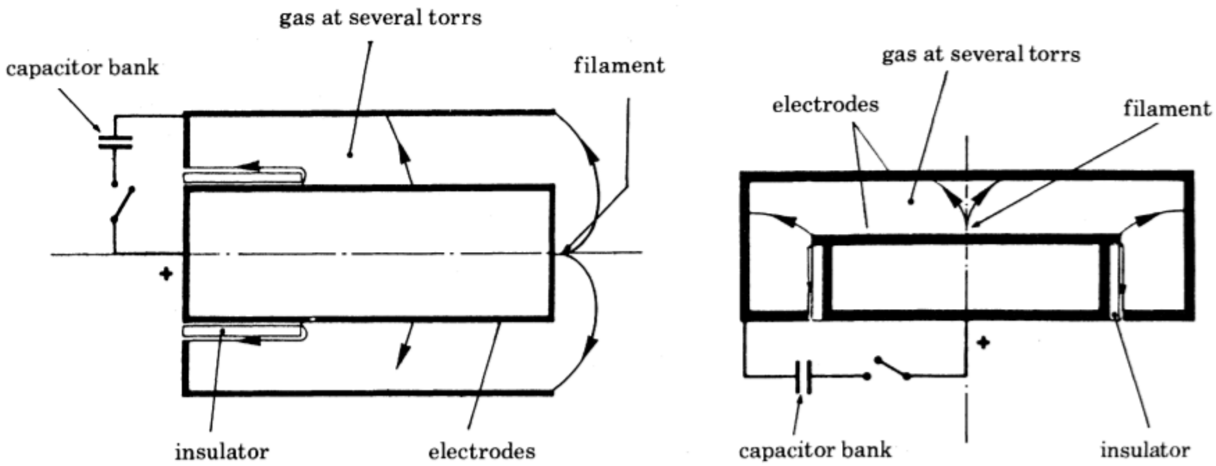

Fig. 1.8 Two geometric arrangements of the PF are provided demonstrating differences in electrode aspect ratio (electrode height divided by inner electrode diameter). On the left, a PF due to Mather configuration has an aspect ratio > 1. On the right, a PF due to Filippov configuration has an aspect ratio < 1. This photo is taken from M. G. Haines as cited from Gentilini et al. 1979 [24].

According to G. Decker and R. Wienecke [25], all PF devices rely on the same principle and are influenced by their parameters: dimensions of the PF; dense plasma lifetime; plasma density; produced electric and magnetic fields; electron temperature, turbulence, electron beams, and X-ray emission; ion temperature, ion distribution functions, and neutron emission.

Different mechanisms have been suggested for possible redirection of current in a Dense Plasma Focus system. According to [26], current shunting and loss of pinch drive pressure in the DPF may occur due to restrike across the insulation. This restrike is caused by the combination of ultraviolet photons from the plasma current sheath and large inductive voltages during the subsequent run-down and implosion phases. According to [17], a lower static inductance in a DPF system will result in a higher pinch and peak current. It is also worth mentioning according to [27], that current discharged in a DPF can be subdivided into the following: current flowing along the front of a shockwave, skin-layer current at the back side of a plasma-current sheath (PCS), residual current behind the PCS not captured, and remnant current on the base insulator surface. The rest of this chapter will highlight aspects from the articles provided from [17], [26]-[27].

According to MSTS, it has been suggested that formation of the plasma sheath in the DPF may cause changes in pressure before and after the sheath. The pressure near the insulator base is thought to be low due to deuterium gas forming near the base. The insulation above the sheath is thought to be higher due to near vacuum pressure. As the sheath moves along the axis of the DPF, the pressure near the insulator base may cause a new current path to be redirected resulting into loss pinch current I_{pinch} due to the total peak current I_{peak}.

1.3.1 Article by G. F. Kiuttu et al.

According to G. F. Kiuttu et al. [26], plasma focus discharges have historically output neutrons and x-rays following a current power law typically within 3rd and 4th powers with up to one megampere current and one megajoule stored capacitor energy. However, during high-energy operation, an issue of restrike occurs due to a combination of ultraviolet photons from the plasma current sheathe and large inductive voltages during run-down and implosion phases [26]. The resultant is then current shunting and loss of pinch drive pressure [26]. G. F. Kiuttu et al [26] were able to observe no loss of current after performing an experiment using a compact toroid (CT) magnetized plasma flow switch to initiate focus implosion from a shieled insulator.

1.3.2 Article by R. Verma

According to R. Verma et al. [17], peak current and pinch current in a PF system mainly depend on the value of static inductance. Furthermore, the ratio of (pinch current)/(peak current) can be improved by minimizing the static inductance in a PF system [17]. The case study demonstrates that pinch current serves as a more reliable scaling parameter for neutron yield as compared to peak current alone [17].

1.3.3 Article by V. A. Gribkov et al.

According to Gribkov et al. [27], an experiment was performed to study the electron and ion beam dynamics for a Mather type DPF, the PF-1000, at its upper energy limit. The PF-1000 is operated with deuterium gas at an energy up to 1MJ [27]. The neutron yield, based on scaling laws, is expected to reach approximately 10^{13} neutrons per shot. But, it resulted in 2×10^{11} neutrons for typical shots and 6×10^{11} neutrons at best [27]. It is concluded through the experiments that three groups of temporal parameters rule the neutron yield in tune with a gyrating particle model (GPM), that is: the time of energy release from the plasma inductive storage system after the moment of current abruption; the confinement time of fast deuterons produced above current abruption and gyrated in the magnetic field within the pinch; and the confinement time of the pinch plasma, density, and volume [27].

1.4 Organization of Thesis

Now that a foundation has been set for the processes and physics underlying a DPF and possible current redirection mechanisms, the rest of this thesis will discuss how to model a DPF using a sensor to determine possible locations of current redirection. Mission Support & Test Services (MSTS) reports that significant amounts of energy needed for generating high energy neutrons is lost somewhere between the pinch-end of the anode stalk and the base of the DPF near the insulating sleeve [28]. It is their mission and the goal of this research effort to both experimentally and theoretically study current redirection in the DPF just before or after the pinch occurs at the anode end [28].

This research effort will explore the use of a linear monopole antenna to detect changes in the magnetic and electric fields relative to the orientation and position of the mock DPF. Further, discussion of the use of the linear monopole antenna will be provided in Chapter 4.

The rest of this thesis will follow a certain format. Chapter 2 will detail the theory for modeling a DPF as a two-segment transmission line (TL) system provided a known current flowing through its geometry. Laplace transformation techniques are utilized in this analysis to then build a program to simulate the redirection of current in a DPF system. Chapter 3 will cover the experimental setup for a mock DPF for two different configurations. One configuration utilizes an RC circuit input and another configuration utilizes a pulse generator input. Chapter 4 will demonstrate results from a current redirected mock DPF system and compare to those expected from theoretical analysis and results from software. Chapter 5 concludes the study.

Chapter 2: Theory and Modeling

2.1 General Construction for a DPF

The general construction of a dense plasma focus (DPF) comprises a central anode, cathode cage, and an insulating sleeve. For the sake of this research effort, a mock DPF is constructed to demonstrate current redirection mechanisms. The mock DPF is similar to Mission Support and Test Services's (MSTS) DPF. Fig. 2.1 provides an angled, 3-dimensional view of the different parts used to construct the mock DPF.

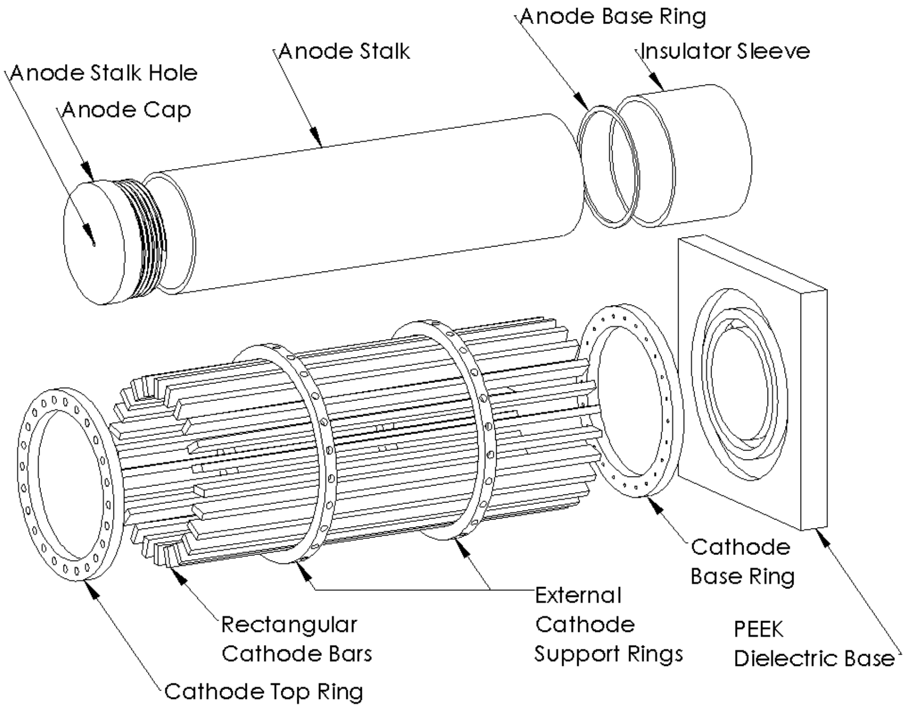

Fig. 2.1 An angled view of the mock DPF's components is provided. The cathode of the DPF is assembled by 24 rectangular radially equidistant bars connected by base and top rings and external support rings. The anode sits inside along the axis of the cathode cage.

A number of assumptions are made to simplify the complexity of the theory. These assumptions include characterizing the mock DPF as a coaxial structure that extends from $-\infty$ to $+\infty$ in the z-direction. However, it is apparent from Fig. 2.1 that the mock DPF is finite in length and has extra geometries that differ from the typical coaxial structure. Nevertheless, the solutions provide approximations that will be compared to simulations. Consistency in results is sought. A quasi-static theory is employed. Theory and experiment will be compared. Although the cathode cage in the mock DPF is comprised of rectangular bars, another geometrical cross-section may be used. Refer to Fig. 2.2. Furthermore, Fig. 2.3 demonstrates how the coaxial structures may differ using different shaped cathode bars. Benefits from a knife-edge rod, as shown in Fig. 2.2(b), is thought to produce a more uniform liftoff sheet leaving behind a better vacuum to prevent restrike of the insulator of a DPF [12]. In addition, it can enhance breakdown, improve neutron output and reliability [12].

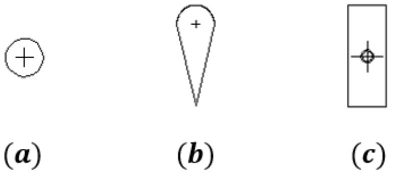

Fig. 2.2 (a, b, c) A top view of different cathode bars are presented from left to right that can be used for a DPF. The magnetic fields due to a (a) cylindrical rod, (b) knife-edge rod, and (c) rectangular bar can be approximated as a displaced wire filament.

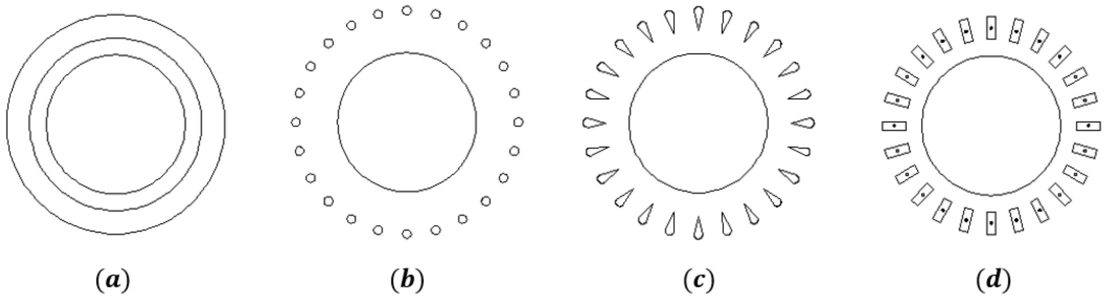

Fig 2.3 (a, b, c, d) A top view of different coaxial arrangements are presented from left to right. In general, the coaxial structures are shown with a center anode conductor and outer cathode conductors. In a DPF, the outer conductor is generally comprised of an external cage of bars. Where the outer conductor can be (a) a solid cage, or a cathode cage composed of (b) cylindrical rods, (c) knife-edge rods, or (d) rectangular bars.

For simplicity in analysis, the external cathode cage is composed of rectangular bars. It is possible to extend the analysis by taking into consideration the geometry of the different cathode bars, but since all bars can be approximated as wire filaments, then assuming a cylindrical shape simplifies the analysis.

2.2 Introduction to Propagation of a Pulsed Signal Along a DPF

Consider an initial analysis to determine the voltage and current of a DPF modeled as a transmission line measured spatially along $-l_{DPF} \leq z \leq 0$ and for all time $0 \leq t \leq \infty$. To simplify the analysis in this section, Laplace transformation techniques are utilized. While it is possible to perform the same analysis strictly within the time-domain, complications arise as time t approaches infinity. In Appendix A, notes from [29] are implemented as scripts in MATLAB to simulate voltage and current for a DPF using a time-domain based-model without Laplace transformation techniques.

For this section, consider a time-domain model of the circuit shown in Fig. 2.4, let C represent a capacitor bank discharging into the DPF system. Assume charge is initially stored in the capacitor bank for some time since time $t = 0$ and no voltage or current flow exists anywhere along the DPF transmission line (TL). Furthermore, there is no excitation in the DPF until the switch connecting the capacitor bank and the DPF is closed at time $t = 0$. At $t = 0^-$, voltage and current along the line is

$$V(z, t = 0^-) = 0$$

$$I(z, t = 0^-) = 0$$

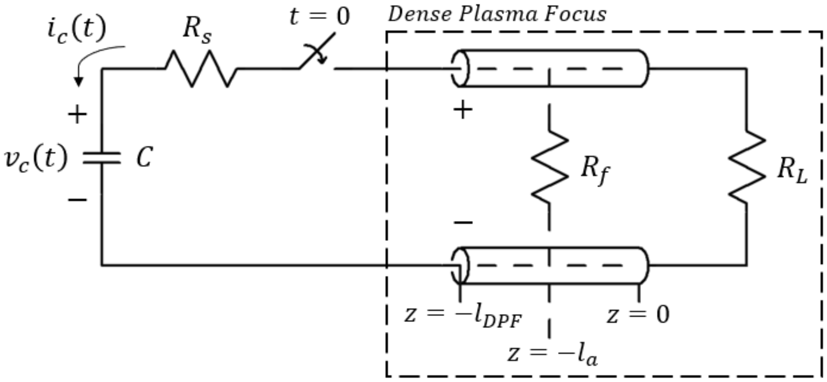

Fig. 2.4 A general RC circuit model of discharging energy from a capacitor bank into a DPF TL is presented.

To aid in the mathematics, the base of the DPF structure near the insulation sleeve is defined to be at the point $z = -l_{DPF}$ and the pinch-end of the DPF is defined to be at point $z = 0$. It is noted that significant amounts of energy, needed to generate high-energy neutrons from the DPF, is lost along the line suggesting an alternate path for current to flow through. This alternate path is defined to be a resistive path occurring at the point $z = -l_a$ connecting the cathode and anode by resistive impedance R_f. The path connecting the pinch-end of the DPF is defined by the path connected by a resistive load impedance R_L.

Because of this alternate path occurring somewhere along the DPF TL, a two-segment TL model is used to better represent the circuit as portrayed in Fig. 2.5. It is assumed that the DPF characteristic impedance and propagation coefficient do not change throughout $-l_{DPF} \leq z \leq 0$. Since the schematic to be analyzed in Fig. 2.5 is a discharge circuit model, then before time $t = 0$, energy is stored in the capacitor bank. Energy from the capacitor bank is then discharged throughout the circuit moments after the switch is closed at time $t = 0$.

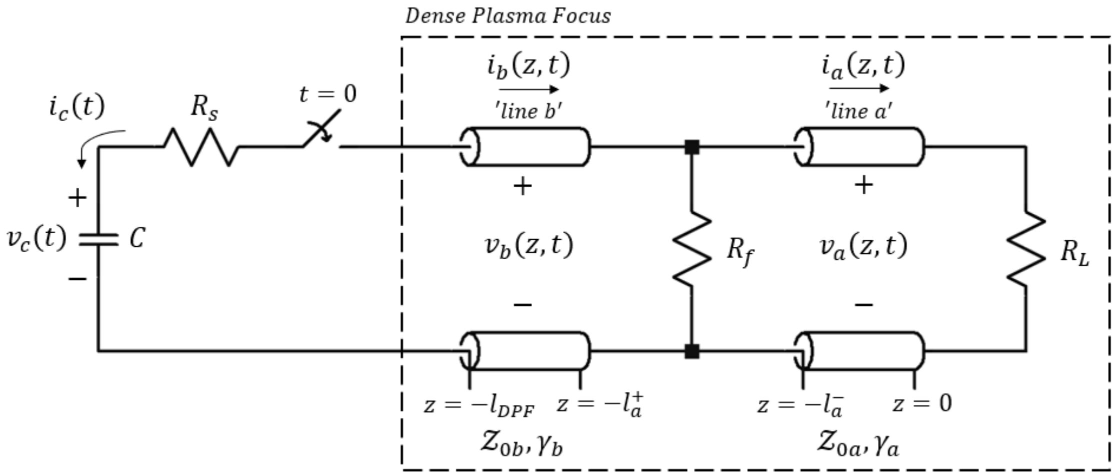

Fig. 2.5 The DPF TL circuit can be modeled as a two-segment transmission line circuit with a resistive path between the two lines defined R_f. The schematic models a capacitor bank discharging stored energy at time $t = 0$ into the DPF system.

2.3 Propagation of a Pulsed Signal Along a DPF

A general transmission line can be characterized by the Telegrapher's equations in the transient domain using equations (2.1a) and (2.1b) [30].

$$\frac{\partial v(z,t)}{\partial z} = -\bar{L}\frac{\partial i(z,t)}{\partial t} - \bar{R}i(z,t) \tag{2.1a}$$

$$\frac{\partial i(z,t)}{\partial z} = -\bar{C}\frac{\partial v(z,t)}{\partial t} - \bar{G}v(z,t) \tag{2.1b}$$

These equations can be transformed from the time domain to the Laplacian domain using Laplace transformation techniques. The definition of the forward Laplace Transform is given by equation (2.2) for reference. Note that $f(t)$ represents a function in the transient domain as where $F(s)$ represents a function in the Laplacian domain.

$$F(s) = \mathcal{L}\{f(t)\} = \int_{t=0^-}^{t=\infty} f(t)e^{-st}dt \tag{2.2a}$$

Taking the forward Laplace transform of equations (2.1a) and (2.1b), the Telegrapher's equations become

$$\frac{dV(z,s)}{dz} = -[s\bar{L} + \bar{R}]I(z,s) + \bar{L}i(z,t=0) \tag{2.3a}$$

$$\frac{dI(z,s)}{dz} = -[s\bar{C} + \bar{G}]V(z,s) + \bar{C}v(z,t=0) \tag{2.3b}$$

Utilizing techniques in [30], $V(z,t)$ and $I(z,t)$ can become decoupled from equations (2.3a) and (2.3b) by defining a constant K such that

$$\frac{d[KI(z,s)]}{dz} = -K[s\bar{C} + \bar{G}]V(z,s) + K\bar{C}v(z,t=0) \tag{2.4}$$

Adding equation (2.4) to equation (2.3a) gives rise to the derivative of a sum

$$\frac{d[V(z,s)+KI(z,s)]}{dz}=\frac{dV(z,s)}{dz}+\frac{d[KI(z,s)]}{dz}$$

$$=-[s\bar{L}+\bar{R}]I(z,s)+\bar{L}i(z,t=0)-K[s\bar{C}+\bar{G}]V(z,s)+K\bar{C}v(z,t=0)$$

$$=-K[s\bar{C}+\bar{G}]\left[V(z,s)+\frac{s\bar{L}+\bar{R}}{s\bar{C}+\bar{G}}\frac{1}{K}I(z,s)\right]+\bar{C}K\left[v(z,t=0^-)+\frac{\bar{L}}{\bar{C}K}i(z,t=0^-)\right]$$

Then let

$$K=\left[\frac{s\bar{L}+\bar{R}}{s\bar{C}+\bar{G}}\right]\frac{1}{K} \tag{2.5a}$$

$$K=\pm\left[\frac{s\bar{L}+\bar{R}}{s\bar{C}+\bar{G}}\right]^{1/2} \tag{2.5b}$$

By substituting the values of K from equations (2.5a) and (2.5b) into the previous expression, the following manipulations can be made

$$\frac{d[V(z,s)+KI(z,s)]}{dz}=$$

$$=-\left(\pm\left[\frac{s\bar{L}+\bar{R}}{s\bar{C}+\bar{G}}\right]^{1/2}\right)[s\bar{C}+\bar{G}]\left[V(z,s)+\frac{s\bar{L}+\bar{R}}{s\bar{C}+\bar{G}}\left(\left[\frac{s\bar{C}+\bar{G}}{s\bar{L}+\bar{R}}\right]K\right)I(z,s)\right]$$
$$+\bar{C}\left(\pm\left[\frac{s\bar{L}+\bar{R}}{s\bar{C}+\bar{G}}\right]^{1/2}\right)v(z,t=0^-)+\bar{L}i(z,t=0^-)$$

$$=\mp[(s\bar{C}+\bar{G})(s\bar{L}+\bar{R})]^{\frac{1}{2}}[V(z,s)+KI(z,s)]\pm\bar{C}\left[\frac{s\bar{L}+\bar{R}}{s\bar{C}+\bar{G}}\right]^{1/2}v(z,t=0^-)+\bar{L}i(z,t=0^-)$$

Then

$$\frac{d[V(z,s)+KI(z,s)]}{dz}=\mp[(s\bar{C}+\bar{G})(s\bar{L}+\bar{R})]^{1/2}[V(z,s)+KI(z,s)]$$
$$\pm\bar{C}\left[\frac{s\bar{L}+\bar{R}}{s\bar{C}+\bar{G}}\right]^{1/2}\cdot v(z,t=0^-)+\bar{L}i(z,t=0^-) \tag{2.6}$$

Let the propagation coefficient $\gamma(s)$ and characteristic impedance $\mathcal{Z}_0(s)$ be defined by

$$\gamma(s) = [(s\bar{C} + \bar{G})(s\bar{L} + \bar{R})]^{1/2} \tag{2.7}$$

$$\mathcal{Z}_0(s) = \left[\frac{s\bar{L} + \bar{R}}{s\bar{C} + \bar{G}}\right]^{1/2} \tag{2.8}$$

Define the combined coupled relation and initial conditions by

$$Q^{\pm}(z,s) = V(z,s) \pm \mathcal{Z}_0(s)I(z,s) \tag{2.9a}$$

$$q^{\pm}(z,t=0,s) = v(z,t=0) \pm \frac{\bar{L}}{\bar{C}\mathcal{Z}_0(s)}i(z,t=0) \tag{2.9b}$$

Finally, equation (2.6) may be summarized into a more friendly format as listed in equation (2.10) [30].

$$\frac{dQ^{\pm}(z,s)}{dz} = \mp\gamma(s)Q^{\pm}(z,s) \pm \bar{C}\mathcal{Z}_0(s)q^{\pm}(z,t=0,s)$$

or

$$\frac{dQ^{\pm}(z,s)}{dz} \pm \gamma(s)Q^{\pm}(z,s) \mp \bar{C}\mathcal{Z}_0(s)q^{\pm}(z,t=0,s) = 0 \tag{2.10}$$

This first-order ODE can then be solved using Abel's formula. Multiplying equation (2.10) by $e^{\pm\gamma(s)z}dz$ and integrating over z yields

$$\left(\frac{dQ^{\pm}(z,s)}{dz}\right)e^{\pm\gamma(s)z} + \big(\pm\gamma(s)Q^{\pm}(z,s)\big)e^{\pm\gamma(s)z} = \big(\pm\bar{C}\mathcal{Z}_0(s)q^{\pm}(z,0,s)\big)e^{\pm\gamma(s)z}$$

$$\left(\frac{dQ^{\pm}(z,s)}{dz}\right)e^{\pm\gamma(s)z} + \left(\frac{d}{dz}e^{\pm\gamma(s)z}\right)Q^{\pm}(z,s) = \pm\bar{C}\mathcal{Z}_0(s)q^{\pm}(z,0,s)e^{\pm\gamma(s)z}$$

$$\frac{d}{dz}\big[Q^{\pm}(z,s)e^{\pm\gamma(s)z}\big] = \pm\bar{C}\mathcal{Z}_0(s)q^{\pm}(z,0,s)e^{\pm\gamma(s)z}$$

$$\int_{\{Q^{\pm}(z,s)e^{\pm\gamma(s)z}\}_{z=z_0}}^{\{Q^{\pm}(z,s)e^{\pm\gamma(s)z}\}_{z=z}} d\left[Q^{\pm}(z,s)e^{\pm\gamma(s)z}\right] = \pm\bar{C}\mathcal{Z}_0\int_{z=z_0}^{z=z} q^{\pm}(z,0,s)\,e^{\pm\gamma(s)z}dz$$

$$Q^{\pm}(z,s) = \left\{Q_0^{\pm}(z_0,s)e^{\pm\gamma(s)z_0} \pm \bar{C}\mathcal{Z}_0\int_{z=z_0}^{z=z} q^{\pm}(z,t=0,s)\,e^{\pm\gamma(s)z}dz\right\}e^{\mp\gamma(s)z} \tag{2.11}$$

where z_0 is the reference position.

Equation (2.11) will be used as a basis for the DPF TL analysis in the Laplace domain for the rest of section 2.2.1. Now that the general solution to a TL and the associated equations have been outlined, these equations can be applied to the two-segment TL model to solve for voltage and current anywhere along the DPF.

In Fig. 2.5, subscripts a and b used for voltage and current along the DPF TL denote the segment of the TL that is being analyzed. After the switch, connecting the capacitor bank and the DPF, is closed at time $t = 0$, initial stored energy from the capacitor bank is discharged to the rest of the circuit defined from time $0 \leq t < \infty$. Furthermore, the resistive impedance defined by R_f represents the path of current redirection. Though not implemented into this thesis, a second-state analysis is possible for implementing R_f as a changing value between two different states. By sticking to a single-state analysis approach, R_f will either be defined as a high resistance value for an open circuit or a low resistance value for a short circuit throughout all time.

For 'line a' of the DPF TL, it is assumed the spatial range is from $-l_a^- \leq z \leq 0$. For 'line b', the spatial range is from $-l_{DPF} \leq z \leq -l_a^+$. It should be noted that the length of 'line a' is l_a and the length of 'line b' is l_b where l_a and l_b are greater than zero. The combined total length of the DPF is then $l_{DPF} = (l_a + l_b)$.

Since it is assumed that the DPF TL is unenergized and there is no excitation until the capacitor bank is connected to the rest of the system at time $t = 0$, then the voltage and current along the line will be 0 and will not change instantaneously following Einstein's laws. A set of initial conditions can then be identified such that the left- and right-handed limits for the voltage and current at time $t = 0$ approach the same values.

$$v_a(z, t = 0^-) = v_a(z, t = 0^+) = 0$$

$$i_a(z, t = 0^-) = i_a(z, t = 0^+) = 0$$

$$q_a^{\pm}(z, t = 0^+, s) = 0$$

$$v_b(z, t = 0^-) = v_b(z, t = 0^+) = 0$$

$$i_b(z, t = 0^-) = i_b(z, t = 0^+) = 0$$

$$q_b^{\pm}(z, t = 0^+, s) = 0$$

The initial conditions provided for 'line a' and 'line b' can be substituted directly into equation (2.11) and equated to equation (2.9a) to yield

$$Q_a^{\pm}(z, s) = Q_{0a}^{\pm}(z_0 = 0, s)e^{\mp\gamma_a(s)z} = V_a(z, s) \pm \mathcal{Z}_{0a}(s)I_a(z, s) \tag{2.12a}$$

$$for: -l_a^- < z < 0$$

$$Q_b^{\pm}(z, s) = Q_{0b}^{\pm}(z_0 = -l_a, s)e^{\mp\gamma_b(s)(z+l_a)} = V_b(z, s) \pm \mathcal{Z}_{0b}(s)I_b(z, s) \tag{2.12b}$$

$$for: -l_{DPF} < z < -l_a^+$$

where, separately, z_0 is the reference position on 'line a' and 'line b'. To reduce notation, let

$$Q_{0a}^{\pm}(z_0 = 0, s) \Leftrightarrow Q_{0a}^{\pm}(\mathrm{s})$$

$$Q_{0b}^{\pm}(z_0 = -l_a, s) \Leftrightarrow Q_{0b}^{\pm}(s)$$

$$\mathcal{Z}_0(s) = \mathcal{Z}_{0a}(s) = \mathcal{Z}_{0b}(s) \Leftrightarrow \mathcal{Z}_0 = \mathcal{Z}_{0a} = \mathcal{Z}_{0b}$$

$$\gamma(s) = \gamma_a(s) = \gamma_b(s) \Leftrightarrow \gamma = \gamma_a = \gamma_b$$

Separately, equations (2.12a) and (2.12b) can be expressed in terms of two unique relations valid on ‘line a’ and ‘line b’ respectively. Adding and subtracting equations (2.12a) ± counterparts yield the voltage and current anywhere on ‘line a’ as given by

$$V_a(z,s) = \frac{Q_{0a}^{+}e^{-\gamma_a z} + Q_{0a}^{-}e^{+\gamma_a z}}{2} \tag{2.13a}$$

$$I_a(z,s) = \frac{Q_{0a}^{+}e^{-\gamma_a z} - Q_{0a}^{-}e^{+\gamma_a z}}{2\mathcal{Z}_{0a}} \tag{2.13b}$$

The wave impedance anywhere on ‘line a’ is

$$Z_a(z,s) = \frac{V_a(z,s)}{I_a(z,s)} = \mathcal{Z}_{0a}\left[\frac{Q_{0a}^{+}e^{-\gamma z} + Q_{0a}^{-}e^{+\gamma z}}{Q_{0a}^{+}e^{-\gamma z} - Q_{0a}^{-}e^{+\gamma z}}\right] \tag{2.13c}$$

Following the same procedure using equation (2.12b), the voltage, current, and wave impedance for ‘line b’ are

$$V_b(z,s) = \frac{Q_{0b}^{+}e^{-\gamma_b(z+l_a)} + Q_{0b}^{-}e^{+\gamma_b(z+l_a)}}{2} \tag{2.13d}$$

$$I_b(z,s) = \frac{Q_{0b}^{+}e^{-\gamma_b(z+l_a)} - Q_{0b}^{-}e^{+\gamma_b(z+l_a)}}{2\mathcal{Z}_{0b}} \tag{2.13e}$$

and

$$Z_b(z,s) = \frac{V_b(z,s)}{I_b(z,s)} = \mathcal{Z}_{0b}\left[\frac{Q_{0b}^{+}e^{-\gamma_b(z+l_a)} + Q_{0b}^{-}e^{+\gamma_b(z+l_a)}}{Q_{0b}^{+}e^{-\gamma_b(z+l_a)} - Q_{0b}^{-}e^{+\gamma_b(z+l_a)}}\right] \tag{2.13f}$$

Now consider analyzing the DPF TL circuit on 'line a' at point $z = 0$ as shown in Fig. 2.6. The voltage and current on 'line a' is related to the load impedance R_L by

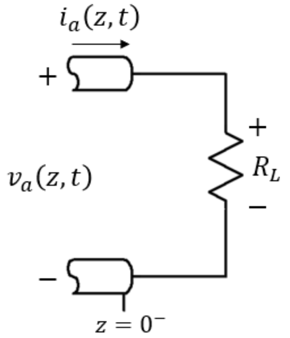

Fig. 2.6 A circuit analysis can be made when observing the voltage and current at the pinch end of the DPF or 'line a' of the DPF transmission line circuit at $z = 0$.

$$v_a(z = 0^-, t) = i_a(z = 0^-, t)R_L$$

$$\mathcal{L}\{v_a(z = 0^-, t)\} = \mathcal{L}\{i_a(z = 0^-, t)R_L\}$$

$$V_a(z = 0^-, s) = I_a(z = 0^-, s)R_L$$

Notice that $V_a(z = 0, s)$ and $I_a(z = 0, s)$ can be substituted for equations (2.13a) and (2.13b) with the condition that $z = 0$ [30]. Then

$$\left\{\frac{Q_{0a}^{+}e^{-\gamma_a z} + Q_{0a}^{-}e^{+\gamma_a z}}{2}\right\}_{z=0} = \left\{\frac{Q_{0a}^{+}e^{-\gamma_a z} - Q_{0a}^{-}e^{+\gamma_a z}}{2\mathcal{Z}_{0a}}\right\}_{z=0} \cdot R_L$$

$$\left[\frac{Q_{0a}^{+} + Q_{0a}^{-}}{2}\right] = \left[\frac{Q_{0a}^{+} - Q_{0a}^{-}}{2\mathcal{Z}_{0a}}\right] R_L$$

$$Q_{0a}^{-}\left[\frac{R_L}{\mathcal{Z}_{0a}} + 1\right] = Q_{0a}^{+}\left[\frac{R_L}{\mathcal{Z}_{0a}} - 1\right]$$

$$Q_{0a}^{-} = Q_{0a}^{+}\left[\frac{R_L - \mathcal{Z}_{0a}}{\mathcal{Z}_{0a}}\right]\left[\frac{\mathcal{Z}_{0a}}{R_L + \mathcal{Z}_{0a}}\right]$$

$$Q_{0a}^{-}(z = 0, s) = Q_{0a}^{+}\left[\frac{R_L - \mathcal{Z}_{0a}(s)}{R_L + \mathcal{Z}_{0a}(s)}\right] \tag{2.14}$$

Based on equation (2.13c) for $z = -l_a$, the input wave impedance of ‘line a’ as pictured in Fig. 2.7 is $\mathcal{Z}_{ina}(s)$.

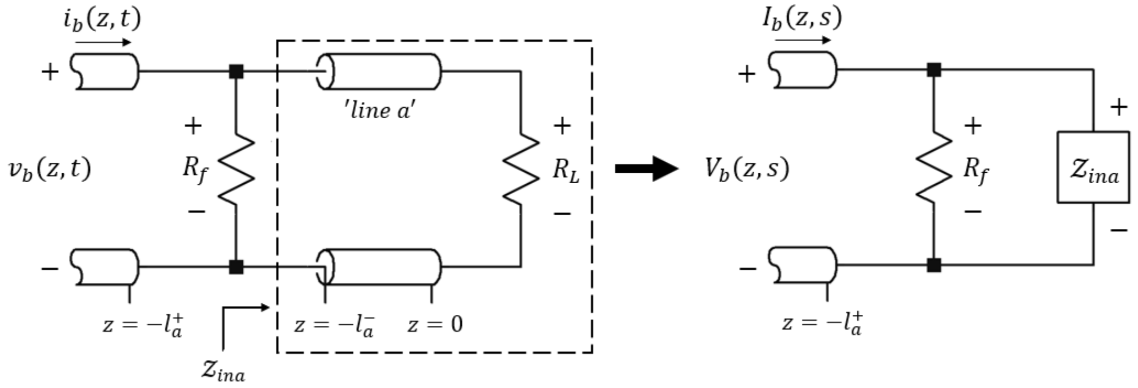

Fig. 2.7 A schematic portrayal of ‘line a’ can be characterized as an input impedance $\mathcal{Z}_{ina}$ when observing from the position of the DPF transmission line circuit at $z = -l_a$.

$$\mathcal{Z}_{ina}(s) = \{Z_a(z,s)\}_{z=-l_a^-=-l_a} \Leftrightarrow \mathcal{Z}_{ina}$$

$$\mathcal{Z}_{ina} = \left\{\mathcal{Z}_{0a}\left[\frac{Q_{0a}^{+}e^{-\gamma_a z} + Q_{0a}^{-}e^{+\gamma_a z}}{Q_{0a}^{+}e^{-\gamma_a z} - Q_{0a}^{-}e^{+\gamma_a z}}\right]\right\}_{z=l_a^-=-l_a}$$

$$\mathcal{Z}_{ina} = \mathcal{Z}_{0a}\left[\frac{Q_{0a}^{+}e^{+\gamma_a l_a} + Q_{0a}^{-}e^{-\gamma_a l_a}}{Q_{0a}^{+}e^{+\gamma_a l_a} - Q_{0a}^{-}e^{-\gamma_a l_a}}\right] \tag{2.15a}$$

Using equation (2.14), the input wave impedance can be written as

$$\mathcal{Z}_{ina} = \mathcal{Z}_{0a}\left[\frac{Q_{0a}^{+}e^{+\gamma_a l_a} + \left\{Q_{0a}^{+}\left[\frac{R_L - \mathcal{Z}_{0a}}{R_L + \mathcal{Z}_{0a}}\right]\right\}e^{-\gamma_a l_a}}{Q_{0a}^{+}e^{+\gamma_a l_a} - \left\{Q_{0a}^{+}\left[\frac{R_L - \mathcal{Z}_{0a}}{R_L + \mathcal{Z}_{0a}}\right]\right\}e^{-\gamma_a l_a}}\right]$$

$$= \mathcal{Z}_{0a}\frac{Q_{0a}^{+}}{Q_{0a}^{+}}\left[\frac{(R_L + \mathcal{Z}_{0a})e^{+\gamma_a l_a} + (R_L - \mathcal{Z}_{0a})e^{-\gamma_a l_a}}{(R_L + \mathcal{Z}_{0a})e^{+\gamma_a l_a} - (R_L - \mathcal{Z}_{0a})e^{-\gamma_a l_a}}\right]$$

$$\mathcal{Z}_{ina}(s) = \mathcal{Z}_{0a}(s)\left[\frac{\big(R_L + \mathcal{Z}_{0a}(s)\big)e^{+\gamma_a(s)l_a} + \big(R_L - \mathcal{Z}_{0a}(s)\big)e^{-\gamma_a(s)l_a}}{\big(R_L + \mathcal{Z}_{0a}(s)\big)e^{+\gamma_a(s)l_a} - \big(R_L - \mathcal{Z}_{0a}(s)\big)e^{-\gamma_a(s)l_a}}\right] \tag{2.15b}$$

The exponential terms can be suitably replaced by hyperbolic sine and hyperbolic cosine functions to obtain

$$\mathcal{Z}_{ina}(s) = \mathcal{Z}_{0a}(s)\left[\frac{R_L\cosh(\gamma_a(s)l_a) + \mathcal{Z}_{0a}(s)\sinh(\gamma_a(s)l_a)}{R_L\sinh(\gamma_a(s)l_a) + \mathcal{Z}_{0a}(s)\cosh(\gamma_a(s)l_a)}\right] \tag{2.15c}$$

Now consider the load on 'line b', $\mathcal{Z}_{Lb}$, which is the parallel configuration between R_f and $\mathcal{Z}_{ina}$ as shown in Fig. 2.8.

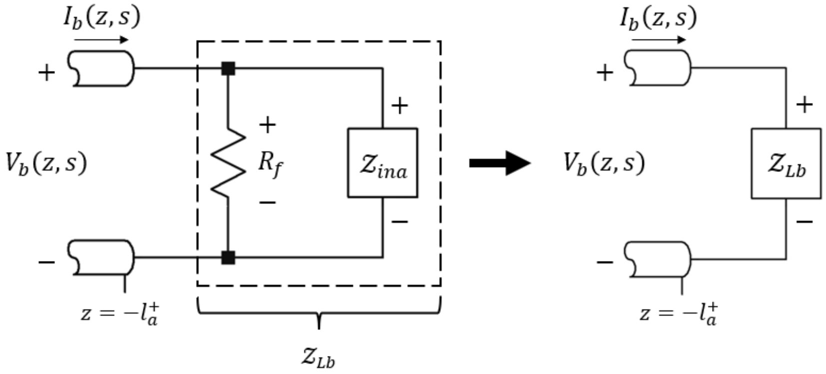

Fig. 2.8 The parallel combination of the input impedance and the path in which current redirection occurs characterized by R_f can be lumped into a parallel impedance $\mathcal{Z}_{Lb}$.

$$\mathcal{Z}_{Lb}(s) = R_f||\mathcal{Z}_{ina}(s) \Leftrightarrow \mathcal{Z}_{Lb}$$

$$\mathcal{Z}_{Lb} = \frac{R_f\mathcal{Z}_{ina}}{R_f + \mathcal{Z}_{ina}}$$

Substituting in equation (2.15a) will give rise to

$$\mathcal{Z}_{Lb} = \frac{R_f\left\{\mathcal{Z}_{0a}\left[\frac{Q_{0a}^{+}e^{+\gamma_a l_a} + Q_{0a}^{-}e^{-\gamma_a l_a}}{Q_{0a}^{+}e^{+\gamma_a l_a} - Q_{0a}^{-}e^{-\gamma_a l_a}}\right]\right\}}{R_f + \left\{\mathcal{Z}_{0a}\left[\frac{Q_{0a}^{+}e^{+\gamma_a l_a} + Q_{0a}^{-}e^{-\gamma_a l_a}}{Q_{0a}^{+}e^{+\gamma_a l_a} - Q_{0a}^{-}e^{-\gamma_a l_a}}\right]\right\}}$$

$$\mathcal{Z}_{Lb} = \frac{R_f\mathcal{Z}_{0a}[Q_{0a}^{+}e^{+\gamma_a l_a} + Q_{0a}^{-}e^{-\gamma_a l_a}]}{R_f[Q_{0a}^{+}e^{+\gamma_a l_a} - Q_{0a}^{-}e^{-\gamma_a l_a}] + \mathcal{Z}_{0a}[Q_{0a}^{+}e^{+\gamma_a l_a} + Q_{0a}^{-}e^{-\gamma_a l_a}]}$$

$$= \frac{R_f\mathcal{Z}_{0a}[Q_{0a}^{+}e^{+\gamma_a l_a} + Q_{0a}^{-}e^{-\gamma_a l_a}]}{Q_{0a}^{+}e^{+\gamma_a l_a}(R_f + \mathcal{Z}_{0a}) - Q_{0a}^{-}e^{-\gamma_a l_a}(R_f - \mathcal{Z}_{0a})}$$

Substituting in equation (2.14) then gives

$$\mathcal{Z}_{Lb} = \frac{R_f\mathcal{Z}_{0a}\left[Q_{0a}^{+}e^{+\gamma_a l_a} + \left\{Q_{0a}^{+}\left[\frac{R_L - \mathcal{Z}_{0a}}{R_L + \mathcal{Z}_{0a}}\right]\right\}e^{-\gamma_a l_a}\right]}{Q_{0a}^{+}e^{+\gamma_a l_a}(R_f + \mathcal{Z}_{0a}) - \left\{Q_{0a}^{+}\left[\frac{R_L - \mathcal{Z}_{0a}}{R_L + \mathcal{Z}_{0a}}\right]\right\}e^{-\gamma_a l_a}(R_f - \mathcal{Z}_{0a})}$$

$$= \frac{Q_{0a}^{+}}{Q_{0a}^{+}}\frac{R_f\mathcal{Z}_{0a}[(R_L + \mathcal{Z}_{0a})e^{+\gamma_a l_a} + (R_L - \mathcal{Z}_{0a})e^{-\gamma_a l_a}]}{(R_L + \mathcal{Z}_{0a})(R_f + \mathcal{Z}_{0a})e^{+\gamma_a l_a} - (R_L - \mathcal{Z}_{0a})(R_f - \mathcal{Z}_{0a})e^{-\gamma_a l_a}}$$

$$\mathcal{Z}_{Lb} = \frac{R_f\mathcal{Z}_{0a}[(R_L + \mathcal{Z}_{0a})e^{+\gamma_a l_a} + (R_L - \mathcal{Z}_{0a})e^{-\gamma_a l_a}]}{(R_L + \mathcal{Z}_{0a})(R_f + \mathcal{Z}_{0a})e^{+\gamma_a l_a} - (R_L - \mathcal{Z}_{0a})(R_f - \mathcal{Z}_{0a})e^{-\gamma_a l_a}} \tag{2.16a}$$

$$= \frac{R_f\mathcal{Z}_{0a}[(R_L + \mathcal{Z}_{0a})e^{+\gamma_a l_a} + (R_L - \mathcal{Z}_{0a})e^{-\gamma_a l_a}]}{(R_fR_L + R_f\mathcal{Z}_{0a} + R_L\mathcal{Z}_{0a} + \mathcal{Z}_{0a}^2)e^{+\gamma_a l_a} - (R_fR_L - R_f\mathcal{Z}_{0a} - R_L\mathcal{Z}_{0a} + \mathcal{Z}_{0a}^2)e^{-\gamma_a l_a}}$$

$$= \frac{R_f\mathcal{Z}_{0a}[R_L\cosh(\gamma_a l_a) + \mathcal{Z}_{0a}\sinh(\gamma_a l_a)]}{R_fR_L\sinh(\gamma_a l_a) + R_f\mathcal{Z}_{0a}\cosh(\gamma_a l_a) + R_L\mathcal{Z}_{0a}\cosh(\gamma_a l_a) + \mathcal{Z}_{0a}^2\sinh(\gamma_a l_a)}$$

$$\mathcal{Z}_{Lb}(s) = \frac{R_f\mathcal{Z}_{0a}(s)[R_L\cosh(\gamma_a(s)l_a) + \mathcal{Z}_{0a}\sinh(\gamma_a(s)l_a)]}{\left(R_f + R_L\right)\mathcal{Z}_{0a}(s)\cosh(\gamma_a(s)l_a) + \left(R_fR_L + \mathcal{Z}_{0a}^2(s)\right)\sinh(\gamma_a(s)l_a)} \tag{2.16b}$$

Furthermore, the voltage and current on ‘line b’ at $z = -l_a^+$ is related to the load $\mathcal{Z}_{Lb}$ by

$$v_b(z = -l_a^+, t) = i_b(z = -l_a^+, t)\mathcal{Z}_{Lb}$$

$$\mathcal{L}\{v_b(z = -l_a^+, t)\} = \mathcal{L}\{i_b(z = -l_a^+, t)\mathcal{Z}_{Lb}\}$$

$$V_b(z = -l_a^+, s) = I_b(z = -l_a^+, s)\mathcal{Z}_{Lb}$$

Notice that $V_b(z = -l_a^+, s)$ and $I_b(z = -l_a^+, s)$ can be substituted for equations (2.13d) and (2.13e) with the condition that $z = -l_a^-$. Then

$$\left\{\frac{Q_{0b}^+ e^{-\gamma_b(z+l_a)} + Q_{0b}^- e^{+\gamma_b(z+l_a)}}{2}\right\}_{\substack{z=-l_a^+ \\ =-l_a}} = \left\{\frac{Q_{0b}^+ e^{-\gamma_b(z+l_a)} - Q_{0b}^- e^{+\gamma_b(z+l_a)}}{2\mathcal{Z}_{0b}}\right\}_{\substack{z=-l_a^+ \\ =-l_a}} \cdot \mathcal{Z}_{Lb}$$

$$\left[\frac{Q_{0b}^+ + Q_{0b}^-}{2}\right] = \left[\frac{Q_{0b}^+ - Q_{0b}^-}{2\mathcal{Z}_{0b}}\right] \cdot \mathcal{Z}_{Lb}$$

$$Q_{0b}^-\left[\frac{\mathcal{Z}_{Lb}}{\mathcal{Z}_{0b}} + 1\right] = Q_{0b}^+\left[\frac{\mathcal{Z}_{Lb}}{\mathcal{Z}_{0b}} - 1\right]$$

$$Q_{0b}^-\left[\frac{\mathcal{Z}_{Lb} + \mathcal{Z}_{0b}}{\mathcal{Z}_{0b}}\right] = Q_{0b}^+\left[\frac{\mathcal{Z}_{Lb} - \mathcal{Z}_{0b}}{\mathcal{Z}_{0b}}\right]$$

$$Q_{0b}^-(z = -l_a, s) = Q_{0b}^+\left[\frac{\mathcal{Z}_{Lb}(s) - \mathcal{Z}_{0b}(s)}{\mathcal{Z}_{Lb}(s) + \mathcal{Z}_{0b}(s)}\right] \tag{2.17}$$

Finally, consider analyzing the TL at $z = -l_{DPF}$ looking on ‘line b’ from the input at $z = -l_{DPF}$ as shown in Fig. 2.9. Based on equation (2.13f), the input wave impedance of ‘line b’ is expressed as $\mathcal{Z}_{inb}(s)$.

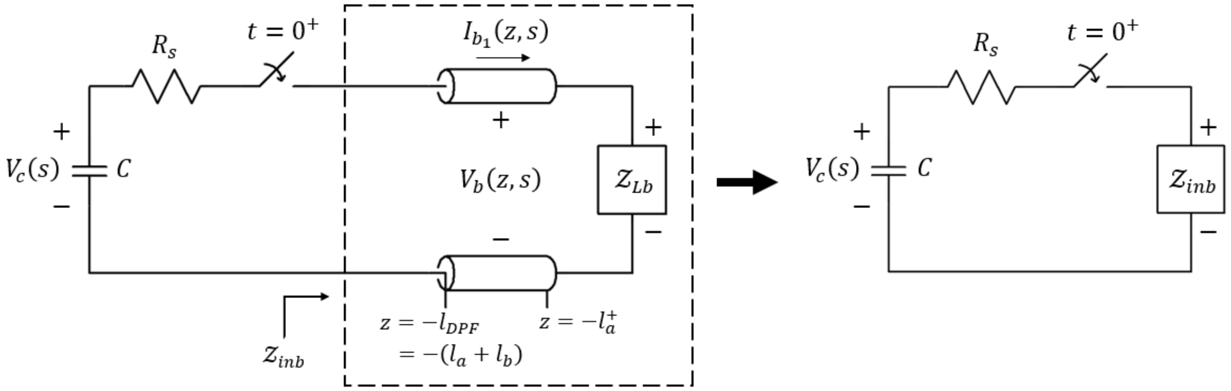

Fig. 2.9 Looking towards the DPF transmission line circuit at $z = -l_{DPF}$, 'line b' and $\mathcal{Z}_{Lb}$ can be lumped into an input impedance characterized by $\mathcal{Z}_{inb}$.

This input impedance is related to the wave impedance equation of equation (2.13f) with the condition that $z = -l_{DPF}$. Then

$$\mathcal{Z}_{inb}(s) = Z_b(z = -l_{DPF}, s) \Leftrightarrow \mathcal{Z}_{inb}$$

$$\mathcal{Z}_{inb} = \mathcal{Z}_{0b} \left\{ \frac{Q_{0b}^{+} e^{-\gamma_b(z+l_a)} + Q_{0b}^{-} e^{+\gamma_b(z+l_a)}}{Q_{0b}^{+} e^{-\gamma_b(z+l_a)} - Q_{0b}^{-} e^{+\gamma_b(z+l_a)}} \right\}_{z=-l_{DPF}=-(l_a+l_b)}$$

$$\mathcal{Z}_{inb} = \mathcal{Z}_{0b} \left[\frac{Q_{0b}^{+} e^{+\gamma_b l_b} + Q_{0b}^{-} e^{-\gamma_b l_b}}{Q_{0b}^{+} e^{+\gamma_b l_b} - Q_{0b}^{-} e^{-\gamma_b l_b}} \right] \tag{2.18a}$$

Note, the reference location is $z_0 = -l_a$. Similar to $\mathcal{Z}_{ina}$, the input impedance $\mathcal{Z}_{inb}$ can then be simplified to remove the $Q_{0b_1}^{+}$ and $Q_{0b_1}^{-}$ terms by substituting in equation (2.17) to yield

$$\mathcal{Z}_{inb} = \mathcal{Z}_{0b} \left[\frac{Q_{0b}^{+} e^{+\gamma_b l_b} + \left\{ Q_{0b}^{+} \left[\frac{\mathcal{Z}_{Lb} - \mathcal{Z}_{0b}}{\mathcal{Z}_{Lb} + \mathcal{Z}_{0b}} \right] \right\} e^{-\gamma_b l_b}}{Q_{0b}^{+} e^{+\gamma_b l_b} - \left\{ Q_{0b}^{+} \left[\frac{\mathcal{Z}_{Lb} - \mathcal{Z}_{0b}}{\mathcal{Z}_{Lb} + \mathcal{Z}_{0b}} \right] \right\} e^{-\gamma_b l_b}} \right]$$

$$= \mathcal{Z}_{0b} \frac{Q_{0b}^{+}}{Q_{0b}^{+}} \left[\frac{(\mathcal{Z}_{Lb} + \mathcal{Z}_{0b}) e^{+\gamma_b l_b} + (\mathcal{Z}_{Lb} - \mathcal{Z}_{0b}) e^{-\gamma_b l_b}}{(\mathcal{Z}_{Lb} + \mathcal{Z}_{0b}) e^{+\gamma_b l_b} - (\mathcal{Z}_{Lb} - \mathcal{Z}_{0b}) e^{-\gamma_b l_b}} \right]$$

$$\mathcal{Z}_{inb}(s) = \mathcal{Z}_{0b}(s)\left[\frac{(\mathcal{Z}_{Lb} + \mathcal{Z}_{0b})e^{+\gamma_b l_b} + (\mathcal{Z}_{Lb} - \mathcal{Z}_{0b})e^{-\gamma_b l_b}}{(\mathcal{Z}_{Lb} + \mathcal{Z}_{0b})e^{+\gamma_b l_b} - (\mathcal{Z}_{Lb} - \mathcal{Z}_{0b})e^{-\gamma_b l_b}}\right] \tag{2.18b}$$

or

$$\mathcal{Z}_{inb}(s) = \mathcal{Z}_{0b}(s)\left[\frac{\mathcal{Z}_{Lb}(s)\cosh(\gamma_b(s)l_b) + \mathcal{Z}_{0b}(s)\sinh(\gamma_b(s)l_b)}{\mathcal{Z}_{Lb}(s)\sinh(\gamma_b(s)l_b) + \mathcal{Z}_{0b}(s)\cosh(\gamma_b(s)l_b)}\right] \tag{2.18c}$$

Now consider solving the circuit equation where the load is $\mathcal{Z}_{inb}(s)$ as shown in Fig. 2.9. At $t = 0$, the capacitor C drives the effective input wave impedance load of ‘line b’. Refer to Fig. 2.10. A capacitor is characterized by

$$v_c(t) = \frac{1}{C}\int_{t=0}^{t} i_c(t)dt + V_{01} \tag{2.19}$$

where V_{01} is the initial voltage stored in the capacitor. Then using KVL, $v_c(t)$ is related to the sums of the voltage drops in the circuit.

$$\left\{\frac{1}{C}\int_{t=0}^{t} i_c(t)dt + V_{01}\right\} = \{i_b(z = -l_{DPF}, t)\}R_s + v_b(z = -l_{DPF}, t)$$

$$-\frac{1}{C}\int_{t=0}^{t} i_b(z = -l_{DPF}, t)dt + V_{01} = i_b(z = -l_{DPF}, t)R_s + v_b(z = -l_{DPF}, t)$$

$$\mathcal{L}\left\{-\frac{1}{C}\int_{t=0}^{t} i_b(z = -l_{DPF}, t)dt + V_{01}\right\} = \mathcal{L}\{i_b(z = -l_{DPF}, t)R_s + v_b(z = -l_{DPF}, t)\}$$

$$-\frac{1}{C}\left\{\frac{1}{s}I_b(z = -l_{DPF}, s)\right\} + \left\{\frac{V_{01}}{s}\right\} = \{I_b(z = -l_{DPF}, s)\}R_s + V_b(z = -l_{DPF}, s)$$

Based on Ohm’s Law

$$V_b(z = -l_{DPF}, s) = I_b(z = -l_{DPF}, s)Z_b(z = -l_{DPF}, s)$$

$$= I_b(z = -l_{DPF}, s)\mathcal{Z}_{inb}(s)$$

Then

$$\frac{V_{01}}{s} = \frac{1}{sC} I_b(z = -l_{DPF}, s) + I_b(z = -l_{DPF}, s) R_s + \{I_b(z = -l_{DPF}, s) \mathcal{Z}_{inb}(s)\}$$

$$= I_b(z = -l_{DPF}, s) \left[\frac{1}{sC} + R_s + \mathcal{Z}_{inb}(s)\right]$$

$$= I_b(z = -l_{DPF}, s) \left[\frac{1 + s\big(R_s + \mathcal{Z}_{inb}(s)\big)C}{sC}\right]$$

$$I_b(z = -l_{DPF}, s) = \left[\frac{sC}{1 + s\big(R_s + \mathcal{Z}_{inb}(s)\big)C}\right] \frac{V_{01}}{s}$$

$$I_b(z = -l_{DPF}, s) = V_{01} \left[\frac{C}{1 + s\big(R_s + \mathcal{Z}_{inb}(s)\big)C}\right] \tag{2.20a}$$

Ohm's Law at $z = -l_{DPF}$ can be used to switch between voltage and current such that

$$V_b(z = -l_{DPF}, s) = V_{01} \left[\frac{C}{1 + s\big(R_s + \mathcal{Z}_{inb}(s)\big)C}\right] \mathcal{Z}_{inb}(s) \tag{2.20b}$$

Looking at boundary condition for $z = -l_{DPF}$, then $I_b(z = -l_{DPF}, s)$ is also related to equation (2.13e). Hence

$$I_b(z = -l_{DPF}, s) = \left\{\frac{Q_{0b}^{+} e^{-\gamma_b(z+l_a)} - Q_{0b}^{-} e^{+\gamma_b(z+l_a)}}{2\mathcal{Z}_{0b}}\right\}_{z=-l_{DPF}=-(l_a+l_b)}$$

$$= \frac{Q_{0b}^{+} e^{+\gamma_b l_b} - Q_{0b}^{-} e^{-\gamma_b l_b}}{2\mathcal{Z}_{0b}}$$

$$= \frac{Q_{0b}^{+} e^{+\gamma_b l_b} - \left\{Q_{0b}^{+} \left[\frac{\mathcal{Z}_{Lb} - \mathcal{Z}_{0b}}{\mathcal{Z}_{Lb} + \mathcal{Z}_{0b}}\right]\right\} e^{-\gamma_b l_b}}{2\mathcal{Z}_{0b}}$$

$$= Q_{0b}^{+} \left[\frac{(\mathcal{Z}_{Lb} + \mathcal{Z}_{0b}) e^{+\gamma_b l_b} - (\mathcal{Z}_{Lb} - \mathcal{Z}_{0b}) e^{-\gamma_b l_b}}{2(\mathcal{Z}_{Lb} + \mathcal{Z}_{0b})\mathcal{Z}_{0b}}\right]$$

Equating this solution to equation (2.20a) then yields

$$\left\{V_{01}\left[\frac{C}{1+s\big(R_s+\mathcal{Z}_{inb}(s)\big)C}\right]\right\} = Q_{0b}^{+}\left[\frac{(\mathcal{Z}_{Lb}+\mathcal{Z}_{0b})e^{+\gamma_b l_b}-(\mathcal{Z}_{Lb}-\mathcal{Z}_{0b})e^{-\gamma_b l_b}}{2(\mathcal{Z}_{Lb}+\mathcal{Z}_{0b})\mathcal{Z}_{0b}}\right]$$

$$Q_{0b}^{+} = V_{01}\left[\frac{C}{1+s\big(R_s+\mathcal{Z}_{inb}(s)\big)C}\right]\left[\frac{2(\mathcal{Z}_{Lb}+\mathcal{Z}_{0b})\mathcal{Z}_{0b}}{(\mathcal{Z}_{Lb}+\mathcal{Z}_{0b})e^{+\gamma_b l_b}-(\mathcal{Z}_{Lb}-\mathcal{Z}_{0b})e^{-\gamma_b l_b}}\right]$$

$$Q_{0b}^{+} = \frac{2V_{01}(\mathcal{Z}_{Lb}+\mathcal{Z}_{0b})\mathcal{Z}_{0b}C}{\big[1+s\big(R_s+\mathcal{Z}_{inb}(s)\big)C\big]\big[(\mathcal{Z}_{Lb}+\mathcal{Z}_{0b})e^{+\gamma_b l_b}-(\mathcal{Z}_{Lb}-\mathcal{Z}_{0b})e^{-\gamma_b l_b}\big]} \tag{2.21a}$$

or

$$Q_{0b}^{+} = \frac{V_{01}(\mathcal{Z}_{Lb}+\mathcal{Z}_{0b})\mathcal{Z}_{0b}C}{\big[1+s\big(R_s+\mathcal{Z}_{inb}(s)\big)C\big]\big[\mathcal{Z}_{Lb}\sinh(\gamma_b l_b)+\mathcal{Z}_{0b}\cosh(\gamma_b l_b)\big]} \tag{2.21b}$$

Since a solution has been obtained for Q_{0b}^{+} using only properties of the DPF TL and the DPF circuit, then Q_{0b}^{-} has been solved for by substituting equation (2.21b) into equation (2.17). Similarly, equation Q_{0a}^{-} has been solved for in terms of Q_{0a}^{+}. To obtain a solution to Q_{0a}^{+}, the boundary condition for both ‘line a’ and ‘line b’ at $z = -l_a$ is analyzed as shown in Fig. 2.10.

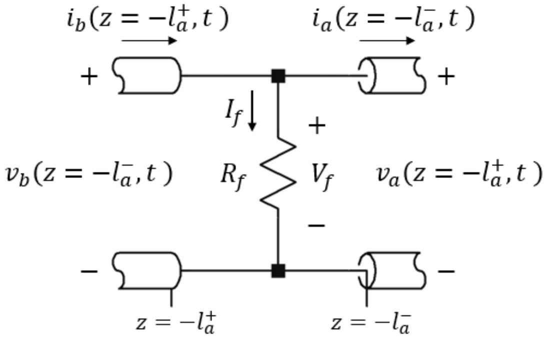

Fig. 2.10 An analysis can be made by observing voltage and current relations at the point of the fault or current redirection path between ‘line a’ and ‘line b’ of the DPF transmission line.

Note that the following KVL relation can be used

$$v_b(z = -l_a^+, s) = v_a(z = -l_a^-, s) = V_f$$

$$\mathcal{L}\{v_b(z = -l_a^+, s)\} = \mathcal{L}\{v_a(z = -l_a^-, s)\}$$

$$V_b(z = -l_a^+, s) = V_a(z = -l_a^-, s)$$

Substituting in equations (2.13d) and (2.13a) for $V_{b_1}(z = -l_a^+, s)$ and $V_{a_1}(z = -l_a^-, s)$ respectively, provided that $z = -l_a^+ \approx -l_a^- \approx -l_a$, then

$$\left\{\frac{Q_{0b}^+ e^{-\gamma_b(z+l_a)} + Q_{0b}^- e^{+\gamma_b(z+l_a)}}{2}\right\}_{z=-l_a^+=-l_a} = \left\{\frac{Q_{0a}^+ e^{-\gamma_a z} + Q_{0a}^- e^{+\gamma_a z}}{2}\right\}_{z=-l_a^-=-l_a}$$

Substituting equation (2.17) then yields

$$\frac{Q_{0b}^+ + Q_{0b}^-}{2} = \frac{Q_{0a}^+ e^{+\gamma_a l_a} + Q_{0a}^- e^{-\gamma_a l_a}}{2}$$

$$Q_{0b}^+ + \left\{Q_{0b}^+ \left[\frac{\mathcal{Z}_{Lb} - \mathcal{Z}_{0b}}{\mathcal{Z}_{Lb} + \mathcal{Z}_{0b}}\right]\right\} = Q_{0a}^+ e^{+\gamma_a l_a} + \left\{Q_{0a}^+ \left[\frac{R_L - \mathcal{Z}_{0a}}{R_L + \mathcal{Z}_{0a}}\right]\right\} e^{-\gamma_a l_a}$$

$$Q_{0b}^+ \left[\frac{(\mathcal{Z}_{Lb} + \mathcal{Z}_{0b}) + (\mathcal{Z}_{Lb} - \mathcal{Z}_{0b})}{(\mathcal{Z}_{Lb} + \mathcal{Z}_{0b})}\right] = Q_{0a}^+ \left[\frac{(R_L + \mathcal{Z}_{0a}) e^{+\gamma_a l_a} + (R_L - \mathcal{Z}_{0a}) e^{-\gamma_a l_a}}{(R_L + \mathcal{Z}_{0a})}\right]$$

$$Q_{0a}^+ = Q_{0b}^+ \left[\frac{2\mathcal{Z}_{Lb}}{(\mathcal{Z}_{Lb} + \mathcal{Z}_{0b})}\right] \left[\frac{(R_L + \mathcal{Z}_{0a})}{(R_L + \mathcal{Z}_{0a}) e^{+\gamma_a l_a} + (R_L - \mathcal{Z}_{0a}) e^{-\gamma_a l_a}}\right] \tag{2.22a}$$

or

$$Q_{0a}^+ = Q_{0b}^+ \left[\frac{\mathcal{Z}_{Lb}}{\mathcal{Z}_{Lb} + \mathcal{Z}_{0b}}\right] \left[\frac{R_L + \mathcal{Z}_{0a}}{R_L \cosh(\gamma_a l_a) + \mathcal{Z}_{0a} \sinh(\gamma_a l_a)}\right] \tag{2.22b}$$

The solution for Q_{0a}^+ is then complete. A step further can be made by substituting Q_{0b}^+ into equation (2.22b) to result in

$$Q_{0a}^{+} = \left\{\frac{V_{01}(\mathcal{Z}_{0b} + \mathcal{Z}_{Lb})\mathcal{Z}_{0b}C}{\left[1 + s\big(R_s + \mathcal{Z}_{inb}(s)\big)C\right]\left[\mathcal{Z}_{0b}\sinh(\gamma_b l_b) + \mathcal{Z}_{Lb}\cosh(\gamma_b l_b)\right]}\right\} times \ldots$$

$$\left[\frac{\mathcal{Z}_{Lb}}{\mathcal{Z}_{Lb} + \mathcal{Z}_{0b}}\right]\left[\frac{R_L + \mathcal{Z}_{0a}}{R_L\cosh(\gamma_a l_a) + \mathcal{Z}_{0a}\sinh(\gamma_a l_a)}\right]$$

$$Q_{0a}^{+} = \frac{V_{01}\mathcal{Z}_{0b}\mathcal{Z}_{Lb}(R_L + \mathcal{Z}_{0a})C}{\left[1 + s\big(R_s + \mathcal{Z}_{inb}(s)\big)C\right]} times \ldots \tag{2.22c}$$

$$\left\{\frac{1}{\left[\mathcal{Z}_{Lb}\sinh(\gamma_b l_b) + \mathcal{Z}_{0b}\sinh(\gamma_b l_b)\right]\left[R_L\cosh(\gamma_a l_a) + \mathcal{Z}_{0a}\sinh(\gamma_a l_a)\right]}\right\}$$

Now that all variables have been solved for in the DPF transmission line equations in the Laplace domain, the last step is to take the inverse Laplace transformation for equations (2.13a), (2.13b), (2.13d), and (2.13e).

$$v_a(z,t) = \mathcal{L}^{-1}\{V_a(z,s)\} \tag{2.23a}$$

$$i_a(z,t) = \mathcal{L}^{-1}\{I_a(z,s)\} \tag{2.23b}$$

$$v_b(z,t) = \mathcal{L}^{-1}\{V_b(z,s)\} \tag{2.23c}$$

$$v_b(z,t) = \mathcal{L}^{-1}\{I_b(z,s)\} \tag{2.23d}$$

Now that the voltage and current have been solved for in the time domain for the two-transmission line DPF model, a numerical computational MATLAB program can be developed, as provided in Appendix B, to determine the voltage and current anywhere along the DPF for time $t \geq 0$. The simulations from the MATLAB program can then be used to provide comparisons to experimental data that will be later demonstrated in Chapter 4.

Chapter 3: Experimental Setup

3.1 Mock MSTS-DPF used for Current Redirection Studies

To study redirection of current flow in an MSTS DPF, a newly identical DPF was built using inexpensive materials immersed in an ambient pressure and temperature environment. This DPF is denoted as a mocked DPF. Fig. 3.1 presents a cross-sectional view of an assembled mock DPF design. Details regarding the dimensions of the different structural components in the mock DPF can be found in Appendix C.

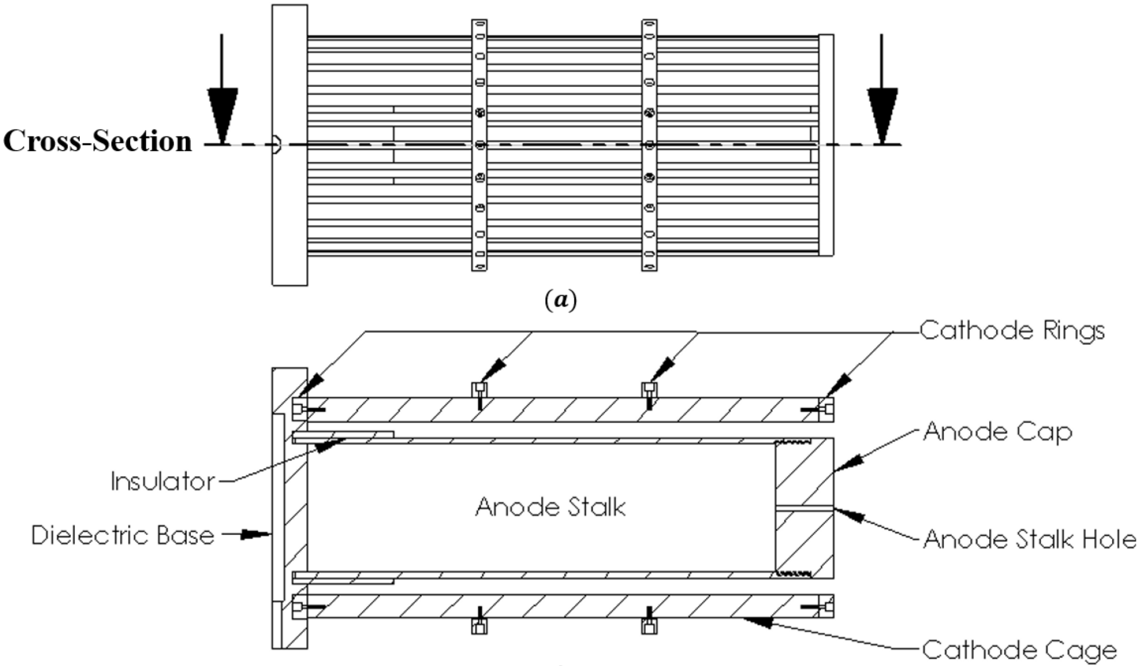

Fig. 3.1 (a, b) A composite drawing of the mock DPF is shown in (a), where a cross-sectional slice is taken along the dashed line indicated by the arrows. In (b), the cross-sectional view is shown depicting the different components used to assemble the mock DPF.

Relaxing constraints placed on the mock DPF design, non-magnetic Aluminum 6061-T6 conductors are used for the anode and cathode. The mock DPF anode is constructed of a hollow cylindrical stalk with internal threading on the pinch end of the tube-like structure. A solid cylindrical cap externally threaded on one end of the cap is intended to fit into the internally threaded stalk providing an even outer surface when both components are fitted together. A small stalk hole is drilled along the central axis of the cylindrical cap. Cathode rectangular bars are uniformly distributed in angle around the DPF anode connected by conductive rings at the base and top of the bars. An air dielectric medium fills the gap between the anode and cathode of the mock DPF. A cylindrical plexiglass insulator sleeve slides on the anode and is positioned near the base of the structure (opposite to the pinch end of the anode). Two cathode support rings are screwed externally to the cathode bars at two different positions along the DPF coaxial structure. MSTS utilizes cathode support rings external to their cathode cage to prevent the expansion of the DPF during discharge. However, they serve no purpose other than to recreate a DPF similar to the MSTS DPF. A natural unfilled PEEK dielectric base is used to sit beneath the mock DPF to prevent contact of the conductors with any other metal. An unassembled and assembled version of the experimental mock DPF structure is provided in Fig. 3.2.

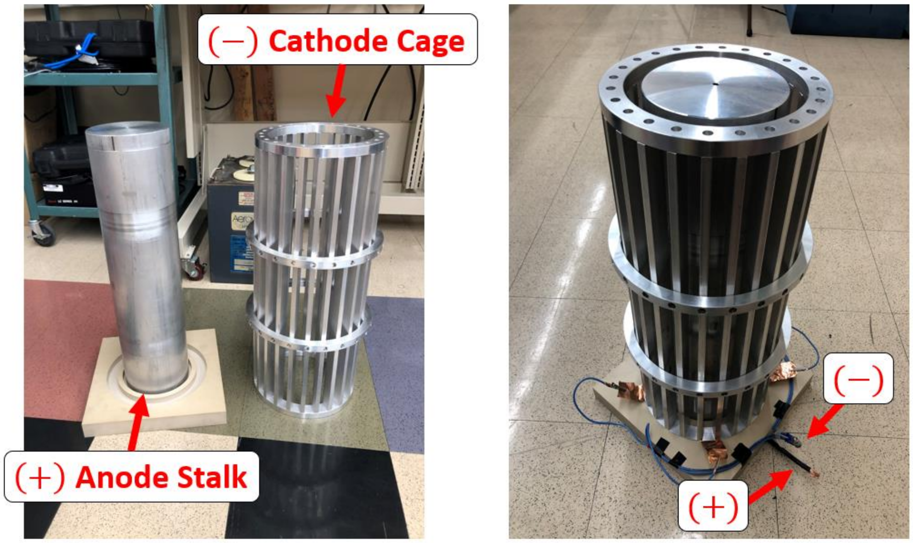

(*a*) (*b*)

Fig. 3.2 (a, b) Pictures of the mock DPF (a) unassembled and (b) assembled are shown. In (b), two-wire electrical contacts near the base of the mock DPF provide connection to the anode and cathode.

3.2 Introduction to Characteristics of the Mock DPF as a Transmission Line

In the following sections, two different analyses are used to determine the characteristic impedance and time delay of the mock DPF. In section 3.2.1, the DPF is modeled as a lossless coaxial transmission line. The characteristic impedance is calculated using the distributed parameters of a coaxial geometry. Given the distributed parameters of the line, the velocity of propagation and the transit time is approximated. In section 3.2.2 and section 3.2.3, an alternative analysis is explored using a cable tester as a time domain reflectometer (TDR) with combination of theory, simulation, and experiments. This is used to determine the characteristic impedance and velocity of propagation of the mock DPF.

3.2.1 Characteristics of a DPF TL Based on a Coax Geometry

A transmission line is characterized by its distributed parameters namely the resistance per unit length ($\bar{R}$), the conductance per unit length ($\bar{G}$), the capacitance per unit length ($\bar{C}$), and the inductance per unit length ($\bar{L}$). Consider the transmission lines to be lossless. For a two-conductor coaxial geometry such as the one provided in Fig. 3.3, the distributed parameters can be characterized by equations (3.1a-d) as derived by [30].

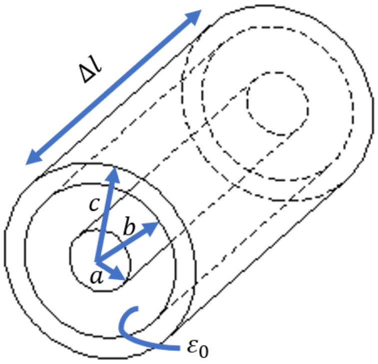

Fig. 3.3 The capacitance and inductance for a standard coaxial geometry can be characterized by defining features: the inner conductor's outer radius a, the outer conductor's inner radius b, and the permittivity $\varepsilon = \varepsilon_0\varepsilon_r$ and permeability $\mu = \mu_0\mu_r$ in the region between the conductors.

$$\bar{R} = \frac{1}{2\pi\delta\sigma_c}\left[\frac{1}{a} + \frac{1}{b}\right], \tag{3.1a}$$

$$\delta = \frac{1}{\sqrt{f\sigma_d\mu_c\pi}}$$

$$\bar{G} = \frac{2\pi\sigma_d}{\ln\left(\frac{b}{a}\right)} \tag{3.1b}$$

where δ is the skin depth, σ_c is the conductivity of the conductors, and σ_d is the conductivity of the lossy dielectric. From [30], the skin depth δ is inversely proportional to the resistance per unit length $\bar{R}$.

$$\bar{C} = \frac{2\pi\varepsilon}{\ln\left(\frac{b}{a}\right)} \tag{3.1c}$$

$$\bar{L} = \frac{\mu}{2\pi}\ln\left(\frac{b}{a}\right) \tag{3.1d}$$

Recall from Chapter 2 that the characteristic impedance and velocity of propagation of a transmission line is related to its distributed parameters by equations (3.1e) and (3.1f).

$$\mathcal{Z}_0(s) = \left[\frac{s\bar{L} + \bar{R}}{s\bar{C} + \bar{G}}\right]^{1/2} \tag{3.1e}$$

$$v = \frac{1}{\sqrt{\bar{L}\bar{C}}} = \frac{1}{\sqrt{\varepsilon\mu}} \tag{3.1f}$$

For now, consider modeling the mock DPF as a lossless coaxial cable. Using equations (3.1a-f), the characteristic impedance and the velocity of propagation of the mock DPF can be approximated. For this research effort, the region between the anode and the cathode of the DPF is that of free space ($\varepsilon = \varepsilon_0$, $\mu = \mu_0$). Moreover, let a represent the outer radius of the DPF anode structure, b represent the inner radius of the DPF cathode cage, and l_{DPF} represent the length of the DPF structure. From these values, the mock DPF can be modeled as a coaxial cable geometry as shown in Fig. 3.4. Table 3.1 summarizes the values for approximating the mock DPF as a coax cable geometry.

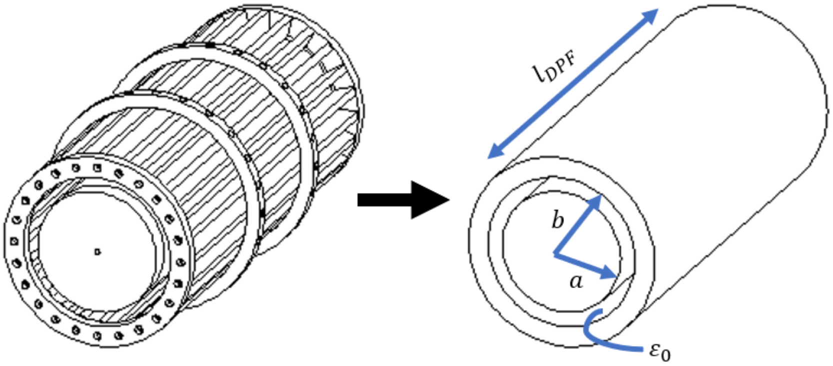

Fig. 3.4 A dimetric view of the mock DPF using SolidWorks is simplified into a coax geometry where the inner radius of the cathode cage is taken to be the value b, the outer radius of the anode rod to be the value a, the length of the DPF to be l_{DPF}, and assuming air, ε_0, to fill the gap between the anode and cathode.

Table 3.1 A summary of experimentally measured values for characterizing the mock DPF as a standard coax geometry with an accuracy up to two significant digits.

	Symbol	**Measured Value**	**Unit**
Outer Radius of Anode	a	0.15	m
Inner Radius of Cathode	b	0.19	m
Length of DPF	l_{DPF}	0.59	m
Permittivity Between the Anode and Cathode	ε_0	8.85×10^{-12}	F/m
Permeability Between the Anode and Cathode	μ_0	$4\pi \times 10^{-7}$	H/m

Since the geometry of the DPF has already been defined and built, then the distributed capacitance and distributed inductance can be determined. Hence

$$\bar{C} = \frac{2\pi\varepsilon}{\ln\left(\frac{\mathrm{b}}{\mathrm{a}}\right)} \approx \frac{2\pi\left(8.85\cdot 10^{-12}\,\frac{F}{m}\right)}{\ln\left(\frac{0.19m}{0.15m}\right)} \approx 240\,\frac{pF}{m}$$

$$\bar{L} = \frac{\mu}{2\pi}\ln\left(\frac{b}{a}\right) \approx \frac{\left(4\pi\cdot 10^{-7}\,\frac{H}{m}\right)}{2\pi}\ln\left(\frac{0.19m}{0.15m}\right) \approx 47\,\frac{nH}{m}$$

Then under lossless conditions ($\bar{R} = \bar{G} = 0$), the characteristic impedance of the mock DPF based on the ideal coax model is

$$\mathcal{Z}_0 = \left[\frac{\bar{L}}{\bar{C}}\right]^{1/2} = \left[\frac{\left(47\,\frac{nH}{m}\right)}{\left(240\,\frac{pF}{m}\right)}\right]^{1/2} \approx 14\Omega$$

Using the properties of the mock DPF, the velocity of propagation is the speed of light ($v_p = c$). Knowing the length of the DPF, one can determine the transit time by

$$\tau = \frac{l_{DPF}}{v_p} = \frac{(0.59m)}{\left(2.99\cdot 10^{8}\,\frac{m}{s}\right)} \approx 2.0ns$$

In the next section, an alternate approach to determining the characteristic impedance and velocity of propagation of the DPF is considered. The experimental analysis will involve the use of a cable tester as a time domain reflectometer (TDR). The loading effects of the cable tester is modeled by its Thevenin equivalent.

3.2.2 Characteristics of a DPF TL based on a Time Domain Reflectometer Technique (Part 1)

In Section 3.2.2 and Section 3.2.3, an experiment is performed to measure the characteristic impedance and transit times of the mock DPF using a cable tester as a time domain reflectometer (TDR). Before determining the characteristic impedance of the mock DPF, the characteristics of the TDR (or cable tester to be used) must first be determined. Fig. 3.5 depicts a typical example of a cable testing system. A Thevenin equivalent cable tester is connected to a single transmission line terminated with load R_{LL}. The electronics inside of the cable tester are unknown. A rectangular pulse is generated with an amplitude of V_0. The Thevenin resistance R_g represents the loading effect of the cable tester electronics.

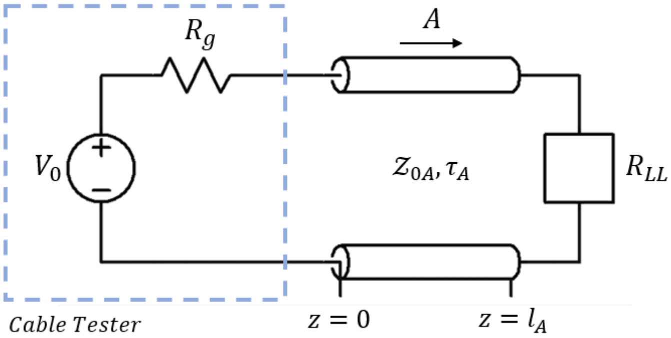

Fig. 3.5 A Thevenin equivalent of a cable tester circuit is connected to a single transmission line terminated with a load R_{LL}. Variables R_g, V_0, $\mathcal{Z}_{0A}$, and τ_A are considered to be unknown in this setup.

In application, the cable tester generates a rectangular pulse at the push of a button. This initial excitation into the transmission line system is characterized by

$$V_{A_1}^{+} = \frac{\mathcal{Z}_{0A}}{R_g + \mathcal{Z}_{0A}} V_0 \tag{3.2}$$

This result is the voltage divider equation seen at the front end of the transmission line which will always be the case for the initial excitation. The variables V_0, R_g, and $\mathcal{Z}_{0A}$ are unknown where $\mathcal{Z}_{0A}$ is the characteristic impedance of the transmission line.

Since the Thevenin model of the cable tester is unknown, consider loading down the cable tester with an open circuit. Consequently

$$V_{LL} = \frac{R_{LL}}{R_g + R_{LL}} V_0 \approx V_0 \tag{3.3}$$

Experimentally, the cable tester output is connected to a $1.5m$ BNC cable connected to Channel 1 of an oscilloscope set in high impedance mode to measure V_0. In high impedance mode, the input impedance of the cable tester $R_g \ll R_{oscope}$ where R_{oscope} is the internal resistance of the oscilloscope. Fig. 3.6 is a snapshot taken from an oscilloscope connected to the cable tester setup in this example after a pulse being generated. Notice that the oscilloscope is set up in high impedance mode by the $1M\Omega$ setting circled in red. Furthermore, at a horizontal scale of $5\mu s/div$, the rectangular pulse from the cable tester can be seen to have a pulse width of about $25\mu s$. Recall that it takes light approximately $1ns$ to travel along $0.3m$ $(1ft)$ distance. Then for very short distances between the cable tester and the oscilloscope, it can be observed that V_0 overshoots and peaks briefly at the start of the pulse but settles at a constant value V_0. This overshoot is a consequence of potential mismatch between the cable tester and the BNC cable. In agreement with Equation (3.3), $V_0 \approx 540mV$.

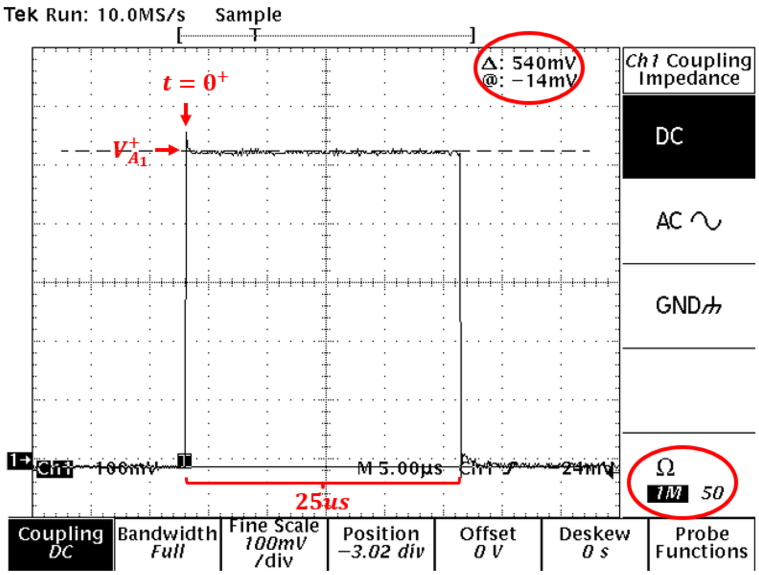

Tek Run: 10.0MS/s Sample

Δ: 540mV
@: −14mV

Ch1 Coupling Impedance

Ch1 100mV M 5.00µs Ch1 24mV

Ω 1M 50

Coupling DC

Bandwidth Full

Fine Scale 100mV /div

Position −3.02 div

Offset 0 V

Deskew 0 s

Fig. 3.6 An oscilloscope is set up with a horizontal scale of $5\mu s/div$, a vertical scale of $100mV/div$, and in high impedance mode where $R_{oscope} = 1M\Omega$. Channel 1 of the oscilloscope is connected to a $1.5m$ BNC cable to the output of a cable tester. From the snapshot of the oscilloscope, it is demonstrated that the cable tester generates and launches a rectangular $25\mu s$ pulse. The initial voltage $V_{A_1}^+$, measured by the oscilloscope at $t = 0^+$ in the open load case, stays constant throughout most of the duration of the pulse. This result is an indication of measuring V_0, the amplitude of the rectangular pulse from the cable tester device, provided an open load and possible mismatch between the BNC cable and the cable tester.

Replace the open circuit with a known load R_{LL} at the output terminals of the cable tester.

Then the initial pulse amplitude is

$$V_{A_1}^+ = \frac{R_{LL}}{R_g + R_{LL}} V_0$$

However, V_0 is now known from the open circuit experiment. With some rearrangement

$$V_{A_1}^+ (R_{LL} + R_g) = R_{LL} V_0$$

$$R_g = \frac{R_{LL}(V_0 - V_{A_1}^+)}{V_{A_1}^+} \tag{3.4}$$

By letting the scope settings be the same from the previous experiment except changing the scope impedance from $1M\Omega$ to 50Ω, then $R_{oscope} = R_{LL} = 50\Omega$. Fig. 3.7 is a snapshot of the oscilloscope with the new load now set to 50Ω. It is demonstrated that $V_{A_1}^+$ is approximately $274mV$. Then

$$R_g = \frac{(50\Omega)(540mV - 274mV)}{(274mV)} \approx 49\Omega$$

Thus, from both experiments, the cable tester can be characterized by a Thevenin source voltage $V_0 \approx 540mV$ in series with an input impedance $R_g \approx 49\Omega$.

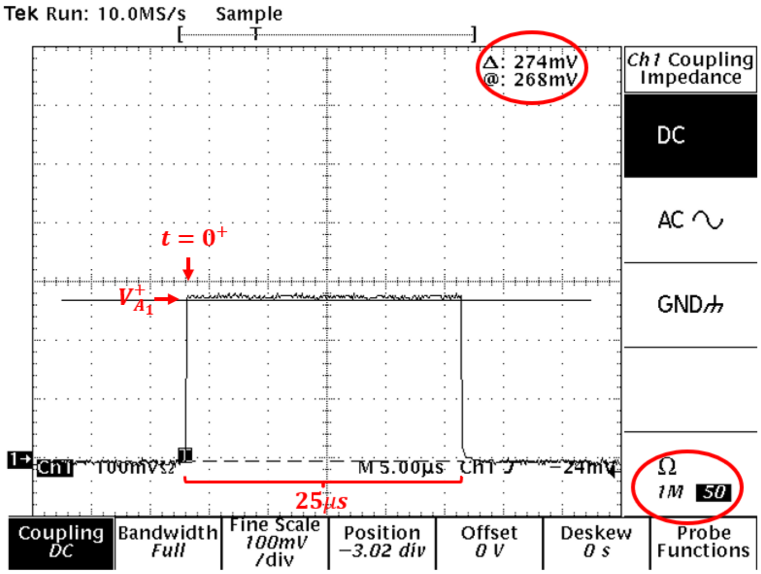

Fig. 3.7 An oscilloscope is set up with a horizontal scale of $5\mu s/div$, a vertical scale of $100mV/div$, and an oscilloscope impedance of $R_{oscope} = 50\Omega$. Channel 1 of the oscilloscope is connected to a $1.5m$ BNC cable to the output of a cable tester. From the snapshot of the oscilloscope, it is demonstrated that the cable tester generates and launches a rectangular pulse of pulse width of about $25\mu s$. The initial voltage $V_{A_1}^+$, measured by the oscilloscope at $t = 0^+$ in the matched load impedance case, stays constant throughout the duration of the pulse.

Consider the original transmission line/cable tester circuit setup as displayed in Fig. 3.5. Recall that the characteristic impedance of the connected transmission line ($1.5m$ BNC cable) $\mathcal{Z}_{0A}$ is still considered to be unknown. Further, the initial pulse $V_{A_1}^+$ only represents a fraction of the energy propagating along the transmission line over time. A voltage bounce diagram, presented in Fig. 3.8, demonstrates how changes in voltage along the transmission line occur over time in the cable tester circuit. The horizontal axis represents the voltage at a specific point in time along the transmission line from $0 \leq z \leq l_A$ where l_A represents the length of the line. Let the measured voltage of the cable tester at the front end of the line be characterized by $V_A(t)$ and the voltage at the load end of the line by $V_{LL}(t)$. The vertical axis represents the observed voltage at a particular point on the line for $0 < t < \infty$.

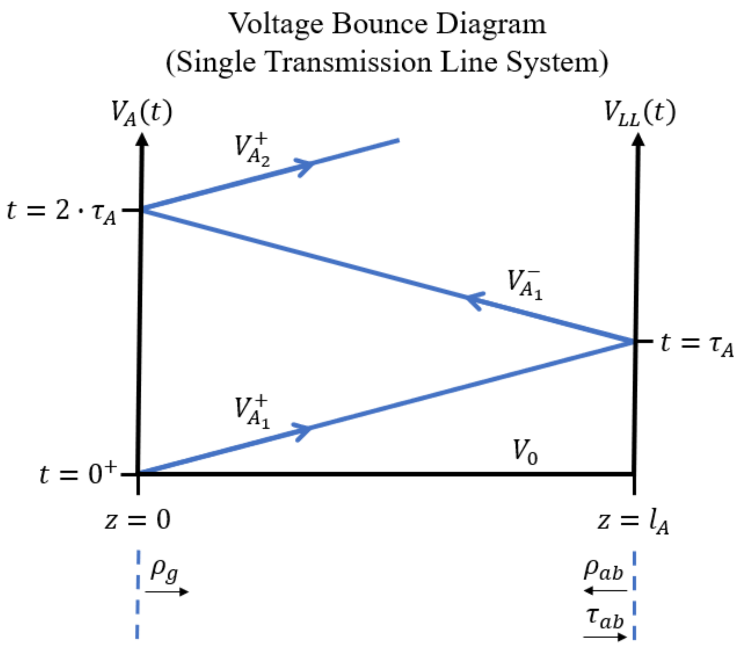

Fig. 3.8 A voltage bounce diagram is constructed demonstrating changes in voltage along a single transmission line system such as a cable tester connected to a line terminated by a load R_{LL}. The voltage wavelets are appropriately added to yield the resultant voltage at a point in time and/or space. Let cable A be associated with the BNC cable and cable B (not shown) be represented by the mock DPF. The term τ_{ab} represents the transmission coefficient of an instant voltage wave propagating from "line A" (BNC cable) to "line B" (mock DPF). The reflection coefficient ρ_{ab} is the amount of the instant voltage wave amplitude of "line A" reflected off of transmission "line B" back into "line A" at an interface.

The only spatial point of interest in the voltage bounce diagram is at the ends of the TL specifically $z = 0$. This is the only measured point from the cable tester device. However, the rest of the diagram gives an idea of when to expect reflections to occur at different points in time for the cable tester setup. For example, if there are any reflections in the cable tester circuit, the cable tester will not see the first reflection until time $t = 2 \cdot \tau_{AB}$ where τ_{AB} is the transit time of the connecting $1.5m$ BNC cable. That is, the time it takes for a signal to propagate along the length of the transmission line. However, notice that from the voltage bounce diagram, at time

$t = 0^+$, the initial voltage $V_{A_1}^+$ can still be used to determine the characteristic impedance of the transmission line without having to go into further detail beyond time $t = 0^+$. Then, rearranging equation (3.2) to solve for $\mathcal{Z}_{0A}$

$$V_{A_1}^+ = \frac{\mathcal{Z}_{0A}}{R_g + \mathcal{Z}_{0A}} V_0$$

$$V_{A_1}^+ \left(R_g + \mathcal{Z}_{0A}\right) = \mathcal{Z}_{0A} V_0$$

$$\mathcal{Z}_{0A}\left(V_0 - V_{A_1}^+\right) = R_g V_{A_1}^+$$

$$\mathcal{Z}_{0A} = \frac{R_g V_{A_1}^+}{\left(V_0 - V_{A_1}^+\right)} \tag{3.5}$$

To measure $\mathcal{Z}_{0A}$, consider the experimental setup in Fig. 3.5 where the TDR connects to an RG58 standard BNC cable of length $l_A = 1.5m$ to a resistive load R_{LL}. Then for any given load of R_{LL}, the cable tester should expect to see the same initial value of $V_{A_1}^+$ on the cable tester/TDR display. For verification, by keeping the vertical scaling of the cable tester the same for different resistive loads of R_{LL}, Fig. 3.9 – Fig. 3.11 demonstrate that the initial value $V_{A_1}^+$ is consistent. Fig. 3.9 represents the scenario for R_{LL} as an open load, Fig. 3.10 with $R_{LL} \approx 50\Omega$, and Fig. 3.11 with R_{LL} as a short circuit. In all scenarios for R_{LL}, $V_{A_1}^+$ is approximately half of V_0 before the next transit time at $t = 2 \cdot \tau_A$.

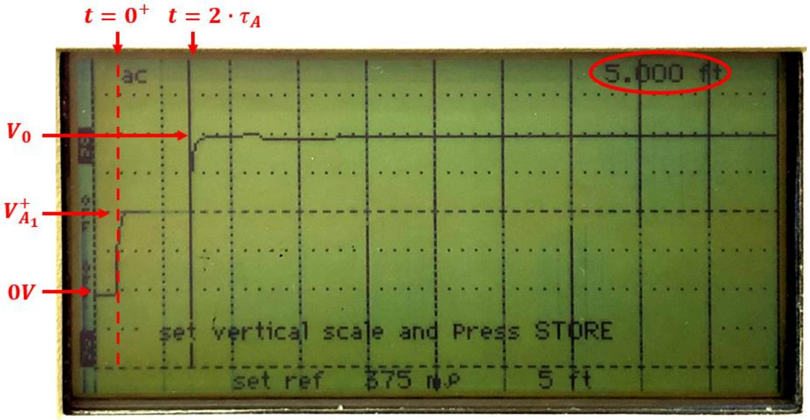

Fig. 3.9 The result of a cable tester measuring voltage at the front end of a $1.5m$ length standard BNC cable terminated by an open circuit is displayed. Notice that there are two drastic changes in voltage, one at $t = 0^+$ and $t = 2 * \tau_A$.

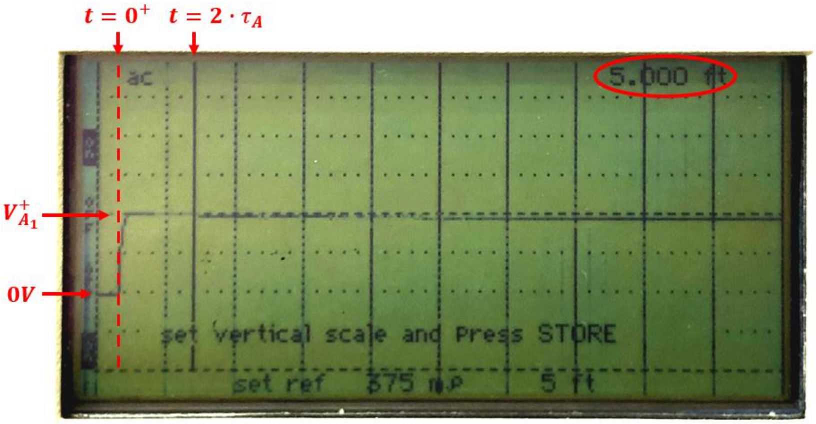

Fig. 3.10 The result of a cable tester measuring voltage at the front end of a $1.5m$ length standard BNC cable terminated by a 50Ω load is displayed. Notice that only one noticeable change in voltage occurs, that is at $t = 0^+$.

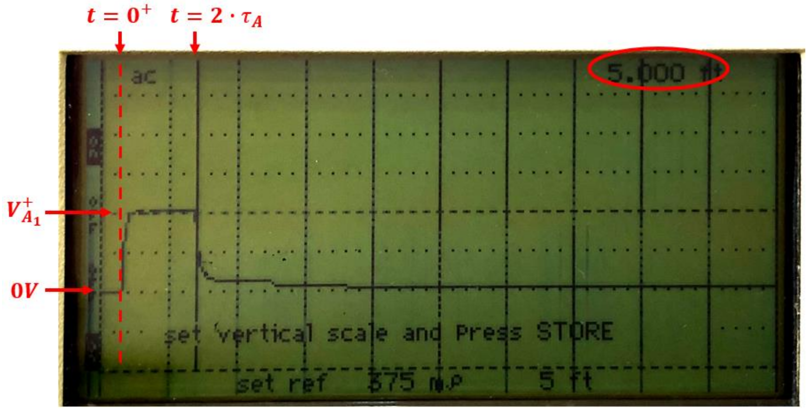

Fig. 3.11 The result of a cable tester measuring voltage at the front end of a $1.5m$ length standard BNC cable terminated by a short circuit is displayed. Notice that there are two drastic changes in voltage, one at $t = 0^+$ and $t = 2 * \tau_A$.

Since $V_{A_1}^+$ has consistently demonstrated the same value from a shorted to open load scenario, and appears to be half of V_0 from the open load experiment, then

$$\mathcal{Z}_{0A} = \frac{R_g V_{A_1}^+}{\left(V_0 - V_{A_1}^+\right)} \approx \frac{R_g(0.5 * V_0)}{V_0 - (0.5 * V_0)} \approx 50\Omega$$

Aside from determining the characteristic impedance of a line from measured voltages on the cable tester, the cable tester explicitly provides a value of length measured from a cursor. This cursor agrees with the measured length of the line only when then cable tester is set to the appropriate velocity factor setting of the line. The velocity factor, VF, is related to the phase velocity of the line by $v_{ph} = c \cdot VF$. If VF of a line is already known, then the cable tester can be set to the appropriate VF by a knob. For example, the physical properties of a typical standard RG58 BNC cable may have a velocity factor of $VF = 0.66$ [32]. When the cable tester is set to $VF = 0.66$ by a controlled knob, then the cable tester is able to measure correct lengths for a connected line with the same velocity factor. If the velocity factor is unknown as in the case of the mock DPF, then by measuring the physical length of the mock DPF, one must work backwards on the cable tester to demonstrate agreement of the length to obtain the unknown velocity factor. This will be demonstrated in the next section.

The first observed change in voltage after firing the pulse (expected at $t = 2 \cdot \tau_A$), Fig. 3.9 and Fig. 3.11 have demonstrated a measured length of $l_A = 1.5m$ at this occurrence when the VF is set to 0.66. To conclude, the cursor on the cable tester is able to measure length explicitly for a transmission line provided VF is known. If VF is not known, but the length of the line is known, then one can work backwards to obtain VF. Furthermore, the cable tester is able to indirectly measure transit times in the line provided VF is known and the measured length of the line is known. For example,

$$\tau_A = \frac{l_A}{v_{ph}} = \frac{l_A}{c \cdot VF} \approx \frac{(1.5m)}{\left(2.99 \cdot 10^8 \frac{m}{s}\right)(0.66)} \approx 7.7ns$$

Now that the properties of a cable tester and standard BNC cable have been studied, the example for determining the characteristics of the mock DPF can now be considered. A summary of values from this past section is recorded in Table 3.2 for reference.

Table 3.2 A summary of values for characterizing a cable tester and BNC cable is provided.

	Symbol	**Value**	**Unit**
Amplitude of Cable Tester	V_0	540×10^{-3}	V
Internal Input Impedance of Cable Tester	R_g	49	Ω
Length of BNC Cable	l_A	1.5	m
Characteristic Impedance of BNC Cable	$\mathcal{Z}_{0A}$	50	Ω
Transit Time of BNC Cable ($\boldsymbol{l_A \approx 5ft}$)	τ_A	7.7×10^{-9}	s
Velocity Factor of RG58 BNC Cable ($\boldsymbol{v_{phA} = VF_A * c}$)	VF_A	66% of c (speed of light)	$(Unitless)$

3.2.3 Characteristics of a DPF TL based on a Time Domain Reflectometer Technique (Part 2)

In section 3.2.1, the mock DPF was treated as a coaxial geometry to approximate the characteristics of the mock DPF. But the outer conductor of the mock DPF is not pipe-like in geometry as in the coaxial cable case. Instead, the geometry is squirrel cage-like in nature as shown on the left-hand side of Fig. 3.4. A time domain reflectometer (TDR), such as the cable tester in the previous section, can be used to characterize the mock DPF more accurately in this case.

Since reflection and transmission coefficients are related to the characteristic impedance of a transmission line, then a TDR can be used to determine the characteristic impedance of the mock DPF. The TDR will be able to send a voltage step response at the input of the transmission line system and measure the voltage change at the input over time as reflections occur along the system. Experimentally, the TDR signal output is fed into a standard 1.5m BNC cable wire connected to the base of the mock DPF terminated by a load R_L. Schematically, consider a time domain analysis for two-transmission line system connecting the TDR input to a BNC cable to the mock DPF terminated by some load R_L. Fig. 3.12 is representative of the described two-transmission line circuit. Note that the characteristic impedance of the $1.5m$ BNC cable is represented by $\mathcal{Z}_{0A}$ and the mock DPF represented by $\mathcal{Z}_{0B}$ in this circuit.

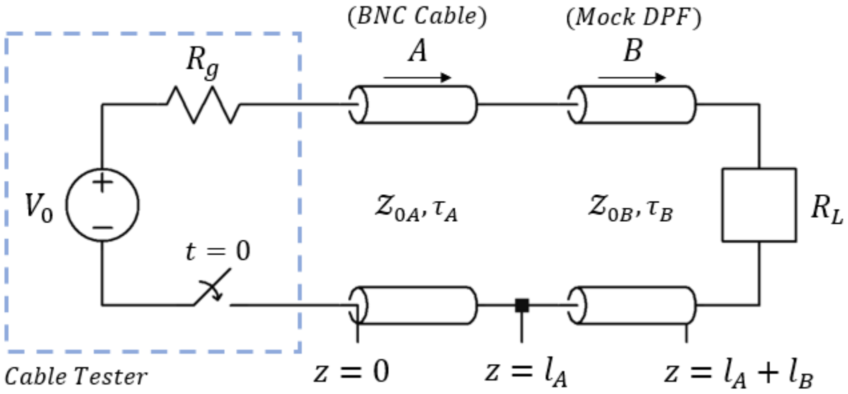

Fig. 3.12 A general schematic of two transmission lines in series is presented. This schematic is representative of a TDR feeding into a BNC cable connecting to the mock DPF terminated by a load R_L. This circuit analysis is equivalent to the two-segmented transmission analysis from Chapter 2 where the BNC cable is replacing a segment of the mock DPF.

Assume for the TDR experiment that the BNC cable and the DPF transmission line are lossless, then for $0 \leq z \leq (l_A + l_B)$, characteristic impedance mismatches can only exist at points $z = 0$, $z = l_A$, and $z = (l_A + l_B)$. These points represent where possible voltage and current changes are expected to occur in a two-transmission line circuit due to mismatch. However, from the previous section, the cable tester can only record data at $z = 0$. Hence, let

$$V_A \Leftrightarrow V_A(t) = v(z = 0, t)$$

From the previous section, the cable tester source has an amplitude of $V_0 \approx 540mV$ and an input impedance defined by $R_g \approx 49\Omega$ as documented in Table 3.2. Further, using the same BNC cable from the previous section, the characteristics of the BNC cable is also defined by Table 3.2. The length of the BNC cable and the mock DPF are considered to both be known and physically measured in this experiment. Then, allow the length of the BNC cable to be characterized by l_A and the length of the mock DPF to be characterized by l_B. The physical lengths measured in the experiment are then

$$l_A \approx 1.5m$$

$$l_B = 0.59m$$

Recall, the velocity factor for the standard RG58 BNC cable, VF_A, is known [32].

$$VF_A \approx 0.66$$

The cable tester has the capability of determining the velocity factors for unknown transmission lines provided the measured lengths of the line are known. For determining the characteristic impedance of the mock DPF in the meantime, allow the cable tester to be preset to the velocity factor defined by the BNC cable $VF_A = 0.66$. Then the velocity of propagation for the BNC cable, $v_{p,A}$, is

$$v_{p,A} = c \cdot VF \approx \left(2.99 \cdot 10^8 \frac{m}{s}\right)(0.66) \approx 1.98 \cdot 10^8 \frac{m}{s}$$

Because the cable tester is set to a velocity factor of $VF = 0.66$, then the velocity of propagation for the mock DPF in this setup, $v_{p,B}$, will be based on the velocity factor of the cable tester, or

$$v_{p,B} = c \cdot VF \approx \left(2.99 \cdot 10^8 \frac{m}{s}\right)(0.66) = 1.98 \cdot 10^8 \frac{m}{s} = v_{p,A}$$

It will be later demonstrated that $v_{p,B} \neq v_{p,A}$. However, the displayed transit times of the lines, τ_A and τ_B, are constrained to the preset velocity factor VF of the cable tester setup for now. The transit time of line b, τ_B, is an unknown. That transit time of τ_A is

$$\tau_A = \frac{l_A}{v_{p,A}} \approx 7.3ns$$

In this experiment, the transit time τ_B is smaller than the transit time τ_A. It is also worth noting that the rise time of the TDR step response is much smaller than the shortest transit time of the two-transmission line system. That is

$$t_{rise} \ll \tau_B, \tau_A$$

Lastly, assume both transmission lines are unenergized until a signal is emitted by the cable tester at time $t = 0$. This is represented schematically by the switch in Fig. 3.12.

The line voltages of the series two-transmission line system are sought. Once the voltages have been determined for this two-segment transmission line circuit, a voltage bounce diagram can be constructed to examine these changes in voltage along the two-transmission line system. This circuit model is similar to the analysis examined in [29] and can be used as a verification for this experiment. First consider the initial voltage seen at the beginning of the BNC cable $(z = 0)$ as shown in Fig. 3.13.

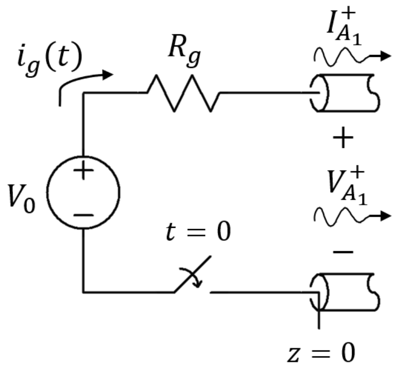

Fig. 3.13 At time $t = 0^+$, an analysis can be performed at the input of a two-transmission line system. When an initial pulse is fired from a TDR, a voltage divider equation can be applied to determine $V_{A_1}^+$.

Recall that the voltage seen at the input of the first transmission line can be defined as $V_A(t)$. Then the initial voltage seen when the pulse is fired at this input is $V_A(t = 0^+) = V_{A_1}^+$. This initial voltage comprises of the voltage divider between the input impedance of the cable tester and the characteristic impedance seen at the front end of the BNC cable. Hence

$$V_A(t = 0^+) = V_{A_1}^+ = V_0 \frac{\mathcal{Z}_{0A}}{R_g + \mathcal{Z}_{0A}} \tag{3.6}$$

This voltage, $V_{A_1}^+$, is then interpreted as the initial voltage propagating along the BNC cable. The voltage at the input $V_A(t)$ is not expected to change again until two transit times of the BNC cable, or $t = 2 \cdot \tau_A$. This change in voltage is caused by any possible reflection occurring at the mismatch point between the BNC cable and the mock DPF as demonstrated in Fig. 3.14.

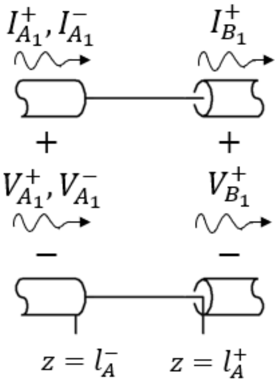

Fig. 3.14 At time $t = \tau_A$, voltage reflection and transmission due to mismatch between a BNC cable and mock DPF in a two-transmission line system is demonstrated schematically. This circuit analysis is equivalent to the two-segmented transmission analysis from Chapter 2 where the BNC cable is replacing a segment of the mock DPF.

The voltage contribution caused by this mismatch between the BNC cable and the mock DPF is partially reflected back into the BNC cable as $V_{A_1}^-$ and partially transmitted into the mock DPF as $V_{B_1}^+$. Thus, by KVL relation, equation (3.7a) is obtained.

$$V_{B_1}^+ = V_{A_1}^+ + V_{A_1}^- \tag{3.7a}$$

Similarly, for the current contribution at this mismatch point, the KCL relation can be derived by equation (3.7b).

$$I_{B_1}^+ = I_{A_1}^+ + I_{A_1}^- \tag{3.7b}$$

$$\left(\frac{V_{B_1}^+}{\mathcal{Z}_{0B}}\right) = \left(\frac{V_{A_1}^+}{\mathcal{Z}_{0A}}\right) + \left(-\frac{V_{A_1}^-}{\mathcal{Z}_{0A}}\right)$$

$$V_{B_1}^+ = \frac{\mathcal{Z}_{0B}}{\mathcal{Z}_{0A}}\left(V_{A_1}^+ - V_{A_1}^-\right)$$

Substituting equation (3.7a) results in

$$\left(V_{A_1}^+ + V_{A_1}^-\right) = \frac{\mathcal{Z}_{0B}}{\mathcal{Z}_{0A}}\left(V_{A_1}^+ - V_{A_1}^-\right)$$

$$V_{A_1}^-\left(\frac{\mathcal{Z}_{0B}}{\mathcal{Z}_{0A}} + 1\right) = V_{A_1}^+\left(\frac{\mathcal{Z}_{0B}}{\mathcal{Z}_{0A}} - 1\right)$$

$$\frac{V_{A_1}^-}{V_{A_1}^+}\left(\frac{\mathcal{Z}_{0B} + \mathcal{Z}_{0A}}{\mathcal{Z}_{0A}}\right) = \left(\frac{\mathcal{Z}_{0B} - \mathcal{Z}_{0A}}{\mathcal{Z}_{0A}}\right)$$

$$\rho_{ab} = \frac{V_{A_1}^-}{V_{A_1}^+} = \left(\frac{\mathcal{Z}_{0B} - \mathcal{Z}_{0A}}{\mathcal{Z}_{0B} + \mathcal{Z}_{0A}}\right) \tag{3.8}$$

From equation (3.7a), one can demonstrate relations with reflection and transmission coefficients.

$$\frac{V_{B_1}^+}{V_{A_1}^+} = 1 + \frac{V_{A_1}^-}{V_{A_1}^+}$$

$$\tau_{ab} = 1 + \rho_{ab}$$

The term τ_{ab} represents the transmission coefficient of a voltage wave propagating from line ‘a’ (BNC cable) to “line ‘b’ (mock DPF). The reflection coefficient ρ_{ab} is the amount of (fraction of) the incident voltage wave amplitude of line ‘a’ reflected off of transmission line ‘b’ back into line ‘a’ at an interface. $V_{B_1}^+$ and $V_{A_1}^-$ are now solvable in terms of the characteristic impedances of the BNC cable and the mock DPF. However, the reflection coefficient seen from the cable tester is also needed to fully determine the characteristic impedance of the mock DPF. Then, one can backtrack to the input of the BNC cable at $V_A(t = 2 \cdot \tau_A)$, as shown in Fig. 3.15.

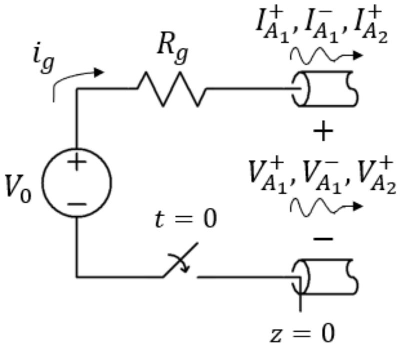

Fig. 3.15 At time $t = 2 \cdot \tau_A$, the voltage contribution at the input of a BNC cable in a two-transmission line system is demonstrated schematically.

A KVL relation can be obtained for the voltage contribution caused by the mismatch point between the BNC cable and the cable tester at time $t = 2 \cdot \tau_A$, as shown in equation (3.9a).

$$V_0 = i_g R_g + V^+_{A_1} + V^-_{A_1} + V^+_{A_2} \tag{3.9a}$$

$$i_g = \frac{V_0 - V^+_{A_1} - V^-_{A_1} - V^+_{A_2}}{R_g}$$

Similarly, a KCL relation can be obtained for the current contribution caused by this mismatch point at time $t = 2 \cdot \tau_A$, as shown in equation (3.9b).

$$i_g = I^+_{A_1} + I^-_{A_1} + I^+_{A_2} \tag{3.9b}$$

$$\left(\frac{V_0 - V^+_{A_1} - V^-_{A_1} - V^+_{A_2}}{R_g}\right) = \left(\frac{V^+_{A_1}}{\mathcal{Z}_{0A}}\right) + \left(-\frac{V^-_{A_1}}{\mathcal{Z}_{0A}}\right) + \left(\frac{V^+_{A_2}}{\mathcal{Z}_{0A}}\right)$$

$$V_0 - V^+_{A_1} - V^-_{A_1} - V^+_{A_2} = \frac{R_g}{\mathcal{Z}_{0A}}\left(V^+_{A_1} - V^-_{A_1} + V^+_{A_2}\right)$$

$$V_0 = V^+_{A_1}\left(1 + \frac{R_g}{\mathcal{Z}_{0A}}\right) + V^-_{A_1}\left(1 - \frac{R_g}{\mathcal{Z}_{0A}}\right) + V^+_{A_2}\left(1 + \frac{R_g}{\mathcal{Z}_{0A}}\right)$$

$$V_0 = V^+_{A_1}\left(\frac{\mathcal{Z}_{0A} + R_g}{\mathcal{Z}_{0A}}\right) + V^-_{A_1}\left(\frac{\mathcal{Z}_{0A} - R_g}{\mathcal{Z}_{0A}}\right) + V^+_{A_2}\left(\frac{\mathcal{Z}_{0A} + R_g}{\mathcal{Z}_{0A}}\right)$$

Recall that $V_{A_1}^{+}$ had already been defined by equation (3.6), then by substitution

$$V_0 = \left(V_0 \frac{\mathcal{Z}_{0A}}{R_g + \mathcal{Z}_{0A}}\right)\left(\frac{\mathcal{Z}_{0A} + R_g}{\mathcal{Z}_{0A}}\right) + V_{A_1}^{-}\left(\frac{\mathcal{Z}_{0A} - R_g}{\mathcal{Z}_{0A}}\right) + V_{A_2}^{+}\left(\frac{\mathcal{Z}_{0A} + R_g}{\mathcal{Z}_{0A}}\right)$$

$$V_0 = V_0 + V_{A_1}^{-}\left(\frac{\mathcal{Z}_{0A} - R_g}{\mathcal{Z}_{0A}}\right) + V_{A_2}^{+}\left(\frac{\mathcal{Z}_{0A} + R_g}{\mathcal{Z}_{0A}}\right)$$

$$V_{A_2}^{+}\left(\frac{\mathcal{Z}_{0A} + R_g}{\mathcal{Z}_{0A}}\right) = -V_{A_1}^{-}\left(\frac{\mathcal{Z}_{0A} - R_g}{\mathcal{Z}_{0A}}\right)$$

$$\rho_g = \frac{V_{A_2}^{+}}{V_{A_1}^{-}} = \frac{R_g - \mathcal{Z}_{0A}}{R_g + \mathcal{Z}_{0A}} \tag{3.10}$$

Notice that the term ρ_g represents the reflection coefficient seen by the cable tester defined by the ratio between $V_{A_2}^{+}$ and $V_{A_1}^{-}$. By following these voltage changes throughout these time instances, a partial voltage bounce diagram can be constructed as portrayed in Fig. 3.16.

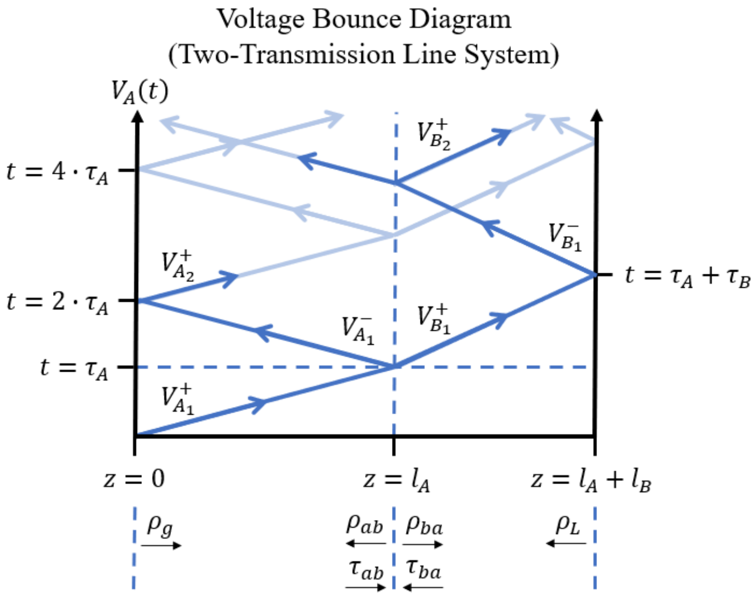

Fig. 3.16 A voltage bounce diagram is constructed demonstrating changes in voltage along a two-transmission line system such as a cable tester connected to a BNC cable to a mock DPF terminated by a load R_L. The horizontal axis indicates the position of the transmission line that the voltage is being observed from. The vertical axis indicates the time at which voltage at a particular point along the line is being observed.

Since the TDR can only measure values at the front end of the transmission line system ($z = 0$), then consider how V_A changes throughout time t. The voltage measured on the TDR at time $t = 2 \cdot \tau_A$ should be the total voltage contribution as shown in equation (3.11).

$$V_A(t = 2 \cdot \tau_A) = V_{A_1}^+ + V_{A_1}^- + V_{A_2}^+ \tag{3.11}$$

Using the relations in equations (3.8) and (3.10), $V_{A_1}^-$ and $V_{A_2}^+$ can be redefined by their reflection coefficients. Then

$$V_A(t = 2 \cdot \tau_A) = V_{A_1}^+ [1 + \rho_{ab} + \rho_g \rho_{ab}]$$

$$V_A(t = 2 \cdot \tau_A) = V_{A_1}^+ \left[1 + \left(\frac{Z_{0B} - Z_{0A}}{Z_{0B} + Z_{0A}}\right) + \left(\frac{R_g - Z_{0A}}{R_g + Z_{0A}}\right)\left(\frac{Z_{0B} - Z_{0A}}{Z_{0B} + Z_{0A}}\right)\right]$$

$$\frac{V_A(t = 2 \cdot \tau_A)}{V_{A_1}^+} = 1 + \left(\frac{\mathcal{Z}_{0B} - \mathcal{Z}_{0A}}{\mathcal{Z}_{0B} + \mathcal{Z}_{0A}}\right) + \left(\frac{R_g - \mathcal{Z}_{0A}}{R_g + \mathcal{Z}_{0A}}\right)\left(\frac{\mathcal{Z}_{0B} - \mathcal{Z}_{0A}}{\mathcal{Z}_{0B} + \mathcal{Z}_{0A}}\right)$$

$$\frac{\left[\frac{V_A(t = 2 \cdot \tau_A)}{V_{A_1}^+} - 1\right]}{\left[1 + \frac{R_g - \mathcal{Z}_{0A}}{R_g + \mathcal{Z}_{0A}}\right]} = K = \left(\frac{\mathcal{Z}_{0B} - \mathcal{Z}_{0A}}{\mathcal{Z}_{0B} + \mathcal{Z}_{0A}}\right) \tag{3.12}$$

Rearranging to solve for $\mathcal{Z}_{0B}$ results in

$$\mathcal{Z}_{0B} = \mathcal{Z}_{0A}\left(\frac{1 + K}{1 - K}\right) \tag{3.13}$$

Thus, the measured voltages displayed by the TDR are related to the characteristic impedance of the mock DPF by equation (3.12). The characteristic impedance of the mock DPF is then determinable by the voltage of the TDR V_0, the characteristic impedance of the BNC cable $\mathcal{Z}_{0A}$, and the voltage of the TDR measured at time $2 \cdot \tau_A$ or $V_A(t = 2 \cdot \tau_A)$. In Fig. 3.17, the cable tester is connected to the mock DPF by a BNC cable and wire connected to the anode and cathode at the base.

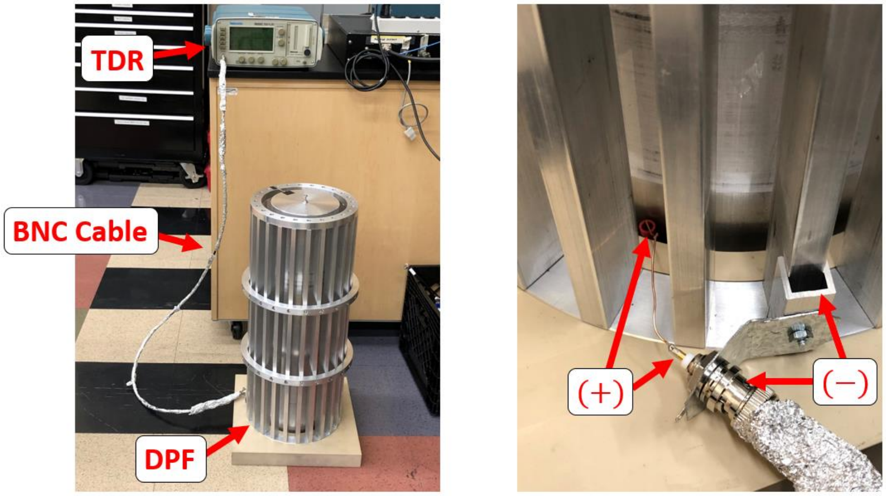

Fig. 3.17 An experiment is set up for connecting a cable tester to a BNC cable wire electrically connected to the base of the mock DPF terminated by a controllable load R_L.

At the pinch-end of the mock DPF, the load R_L can either be shorted, opened, or terminated by a resistive value. Consider the mock DPF termination for the open and short case. The results produced by the cable tester for the open and short case are displayed in Fig. 3.18 and Fig. 3.19. When using the values summarized by Table 3.2, at time $t = 0^+$, recall that the initial voltage displayed on the cable tester must be

$$V_A(t = 0^+) = V_{A_1}^+ = V_0 \frac{\mathcal{Z}_{0A}}{R_g + \mathcal{Z}_{0A}} \approx (540mV) \frac{(50\Omega)}{(49\Omega) + (50\Omega)} \approx 270mV$$

In the open circuit case, as shown in Fig. 3.18, this initial value is demonstratable when compared to the final of V_0 after transients diminish away over time. Similarly, for the short circuit case in Fig. 3.19, the final value approaches $0V$ after transients diminish over time. A consistent voltage drop can be observed by the cable tester at time $t = 2 \cdot \tau_A$ for Fig. 3.18 and Fig. 3.19, indicating the voltage contribution due to reflection of the mismatch point between the mock DPF and the BNC cable. This dip in voltage is $V_A(t = 2 \cdot \tau_A)$.

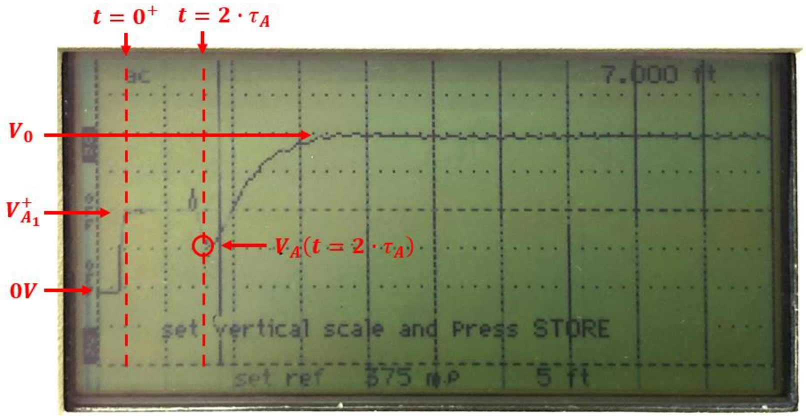

Fig. 3.18 The voltage observed from a cable tester in a two-transmission line system connecting a $1.5m$ length BNC cable to a mock DPF of length $0.59m$ terminated by an open circuited load is presented. Notice that as transients diminish, $V_A(t)$ approaches V_0.

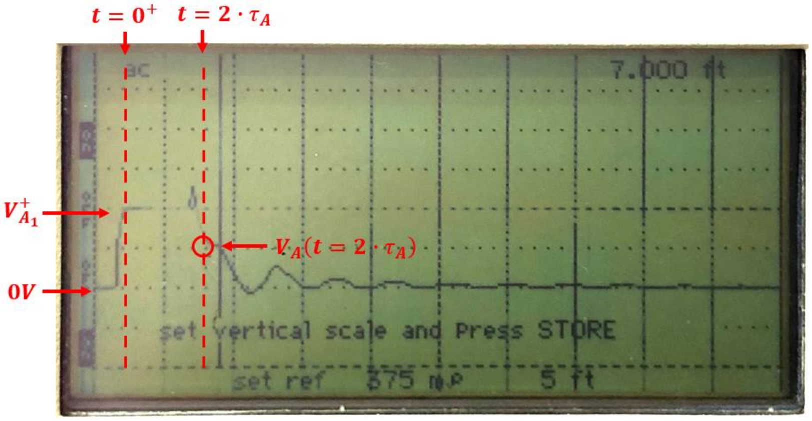

Fig. 3.19 The voltage observed from a cable tester in a two-transmission line system connecting a $1.5m$ length BNC cable to a mock DPF of length $0.59m$ terminated by a short circuit load is presented. Notice that as the transients diminish, $V_A(t)$ approaches $0V$.

Notice from Fig. 3.18 and Fig. 3.19, this dip in voltage occurring at time $t = 2 \cdot \tau_A$ is approximately half of the initial voltage of $V_{A_1}^+$, or

$$V_A(t = 2 \cdot \tau_A) \approx \frac{1}{2} V_{A_1}^+ \approx \frac{1}{2}(270mV) \approx 140mV$$

Using this measured voltage, the value of K can be solved.

$$K = \frac{\left[\frac{V_A(t = 2 \cdot \tau_A)}{V_{A_1}^{+}} - 1\right]}{\left[1 + \frac{R_g - \mathcal{Z}_{0A}}{R_g + \mathcal{Z}_{0A}}\right]} \approx \frac{\left[\frac{(140mV)}{(270mV)} - 1\right]}{\left[1 + \frac{(49\Omega) - (50\Omega)}{(49\Omega) + (50\Omega)}\right]} \approx -0.49$$

Then substituting K into equation (3.13) results in

$$\mathcal{Z}_{0B} = \mathcal{Z}_{0A}\left(\frac{1 + (-0.49)}{1 - (-0.49)}\right) \approx 17\Omega$$

Hence, the characteristic impedance of the mock DPF, as analyzed by a cable tester, is $\mathcal{Z}_{0B} \approx 17\Omega$. To verify this solution, consider a transmission line circuit simulation as the one provided in Fig. 3.20 built on LTspice. When simulating a transient analysis for this schematic with a load of $R_L = 1M\Omega$, the result of Fig. 3.21 is demonstrated. Similarly, simulating a transient analysis for this schematic with a load of $R_L = 0.01\Omega$, the result of Fig. 3.22 is demonstrated. Thus, when the mock DPF is set to a characteristic impedance of $\mathcal{Z}_{0B} \approx 17\Omega$ in simulation, the result appears to be consistent with the result displayed experimentally within the cable tester in Fig. 3.18 and Fig. 3.19. It is worth noting that the rise time in the cable tester appears to rise slowly in comparison to the result simulated in LTspice where the rise time is defined to ramp faster.

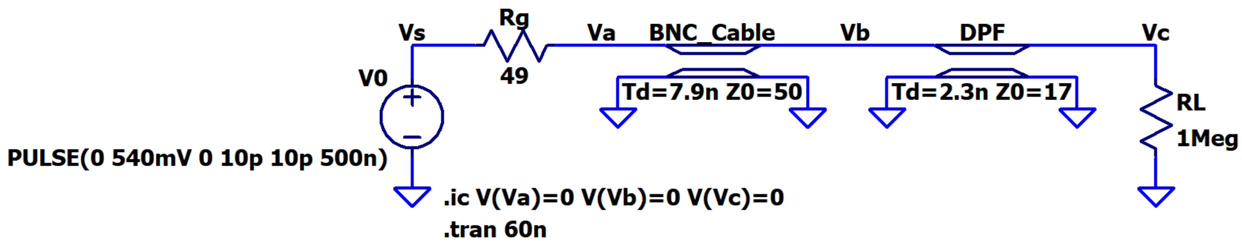

Fig. 3.20 An LTspice model for a two-transmission line circuit representative of a cable tester firing into a BNC cable of $1.5m$ and mock DPF of length $0.59m$ is developed schematically. The load resistance R_L can be controlled ranging between 0 and infinity.

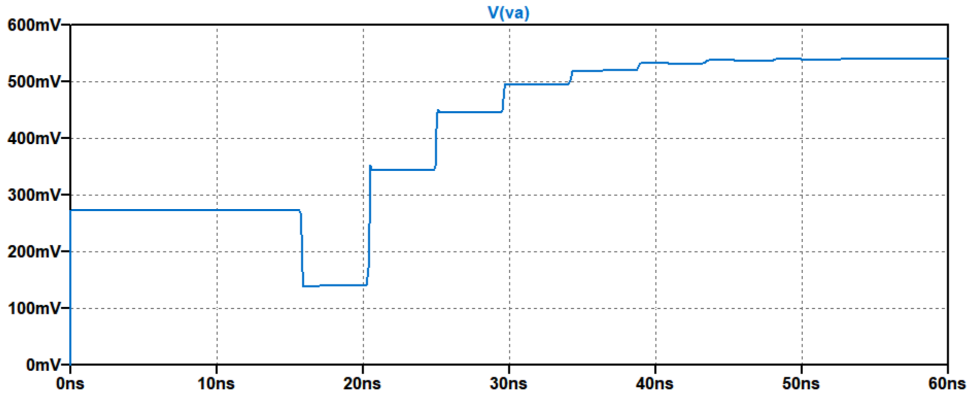

Fig. 3.21 For the two-transmission line circuit model developed in LTspice for a cable tester firing into a BNC cable of $1.5m$ connected to a mock DPF of length $0.59m$ terminated by load $R_L = 1M\Omega$, the transient plot is presented. This simulation provides a comparison to the experiment in Fig. 3.18.

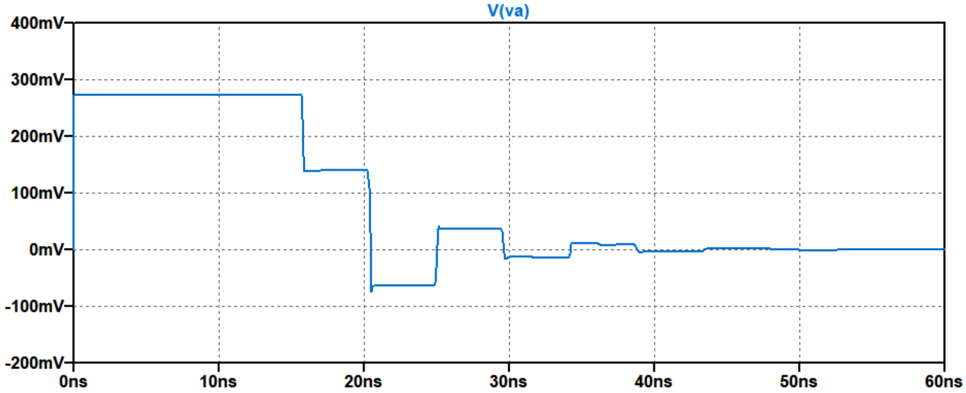

Fig. 3.22 For the two-transmission line circuit model developed in LTspice for a cable tester firing into a BNC cable of $1.5m$ connected to a mock DPF of length $0.59m$ terminated by load $R_L = 0.01\Omega$, the transient plot is presented. This simulation provides a comparison to the experiment in Fig. 3.19.

Now consider another experiment working backwards using the newly determined characteristic impedance of the mock DPF. Allow the LTspice schematic to be terminated by a matched load $R_L = 17\Omega$. Then the transient plot in LTspice is demonstrated in Fig. 3.23.

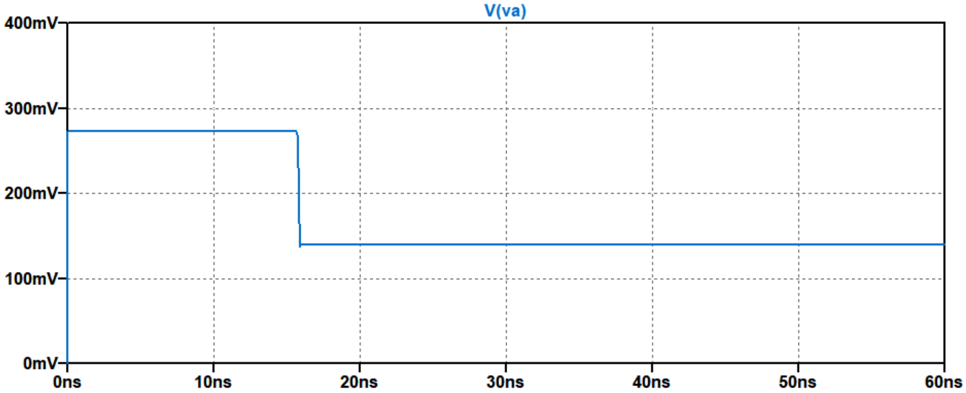

Fig. 3.23 For the two-transmission line circuit model developed in LTspice for a cable tester firing into a BNC cable of $1.5m$ connected to a mock DPF of length $0.59m$ terminated by load $R_L = 17\Omega$, the transient plot is presented.

This is the expected plot seen from the cable tester when the characteristic impedance of the mock DPF is matched to the load $R_L = 17\Omega = \mathcal{Z}_{0B}$. By connecting a 17Ω load resistor across the end of the mock DPF, it is demonstrated that the result of the cable matches similarly to the LTspice simulation as shown in Figure 3.24.

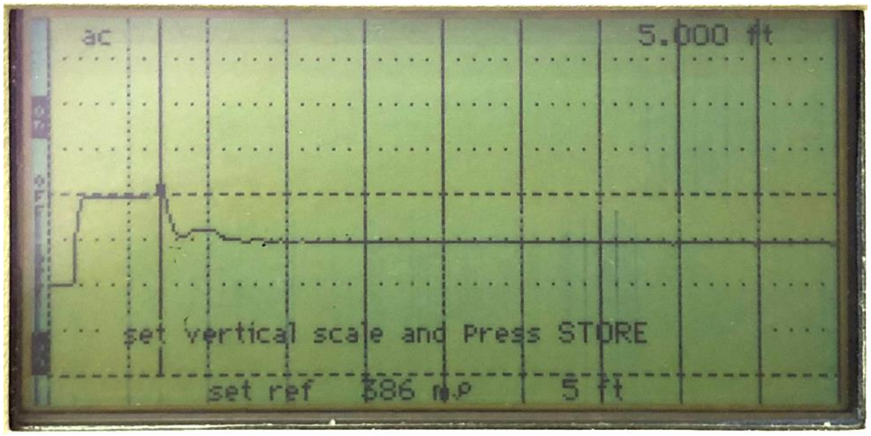

set vertical scale and Press STORE

Fig. 3.24 The voltage observed from a cable tester in a two-transmission line system connecting a $1.5m$ length BNC cable to a mock DPF of length $0.59m$ terminated by a resistor of approximately 17Ω is presented. This experimental result demonstrates consistency to the simulated result in Fig. 3.23.

Thus, the result from the cable tester indicates that the characteristic impedance of the mock DPF must be approximately $\mathcal{Z}_{0B} \approx 17\Omega$. This result differs from the characteristic impedance calculated in section 3.2.1 where an ideal coaxial geometry is assumed. Because the measured length of the mock DPF is known to be $0.59m$, then the VF knob on the cable tester can be adjusted until the measured length by the cable tester is consistent with the experimentally measured length of the mock DPF. This occurs when the velocity factor VF_B is set to 0.69. Then the true velocity of propagation can be calculated for the mock DPF by

$$v_{p,B} = c \cdot VF_B \approx \left(2.99 \cdot 10^8 \frac{m}{s}\right)(0.69) \approx 2.06 \cdot 10^8 \frac{m}{s}$$

Now, by using the Velocity Factor $VF_B = 0.69$ set for the mock DPF, this will result in a transit time for the mock DPF of

$$\tau_B = \frac{l_B}{v_{p,B}} \approx \frac{0.587m}{2.06 \cdot 10^8 \frac{m}{s}} \approx 2.85ns$$

Now that the values for the characteristic impedance and the velocity of propagation for the mock DPF have been determined, the distributed capacitance and distributed inductance are now indirectly able to be determined. Recall the mock DPF as a lossless line that $\bar{R} = \bar{G} = 0$ and with known information, $\mathcal{Z}_{0B} \approx 17\Omega$ and $v_{p,B} \approx 2.06 \cdot 10^8 m/s$. Then with this information, equations (3.1e) and (3.1f) can be worked backwards to obtain the measured distributed capacitance and distributed inductance. Hence,

$$v_{p,B} = \frac{1}{\sqrt{\bar{L}_B \bar{C}_B}} = \frac{\sqrt{\bar{L}_B}}{\sqrt{\bar{L}_B}} \frac{1}{\sqrt{\bar{L}_B \bar{C}_B}} = \frac{1}{\bar{L}_B} \sqrt{\frac{\bar{L}_B}{\bar{C}_B}} = \frac{1}{\bar{L}_B} \mathcal{Z}_{0B}$$

$$\bar{L}_B = \frac{1}{v_{p,B}} \mathcal{Z}_{0B} \approx \frac{1}{\left(2.06 \cdot 10^8 \frac{m}{s}\right)}(16.7\Omega) \approx 80 \frac{nH}{m}$$

$$v_{p,B} = \frac{1}{\sqrt{\bar{L}_B \bar{C}_B}} \rightarrow \sqrt{\bar{C}_B} = \frac{1}{\sqrt{\bar{L}_B}} \frac{1}{v_{phB}}$$

$$\bar{C}_B = \frac{1}{\bar{L}_B \left(v_{phB}\right)^2} \approx \frac{1}{\left(80 \frac{nH}{m}\right)\left(2.06 \cdot 10^8 \frac{m}{s}\right)^2} \approx 290 \frac{pF}{m}$$

These values, though measured indirectly, will be important for the simulation results in LTspice and MATLAB in Chapter 4 of this thesis when comparing experimental data. In Appendix A, the time-domain model can be used as a verification check for the measured parameters for the mock DPF. From Appendix A, Section A.2, it can be shown from Fig. A.1 that the amplitude changes over time for the first few transit times agree with the open load, short load, and matched load cases in Fig. 3.21 – Fig. 3.23. A summary of these measured values is provided in Table 3.3 and Appendix C.

Table 3.3 An extended summary of values for characterizing a cable tester, BNC cable, and the mock DPF is provided.

	Symbol	**Value**	**Unit**
Amplitude of Cable Tester	V_0	540×10^{-3}	V
Internal Input Impedance of Cable Tester	R_g	49	Ω
Length of BNC Cable	l_A	1.5	m
Length of mock DPF	l_B	0.587	m
Characteristic Impedance of BNC Cable	$\mathcal{Z}_{0A}$	50	Ω
Characteristic Impedance of the mock DPF	$\mathcal{Z}_{0B}$	17	Ω
Transit Time of BNC Cable ($\boldsymbol{l_A \approx 1.5m}$)	τ_A	7.7×10^{-9}	s
Transit Time of the mock DPF ($\boldsymbol{l_B \approx 0.587m}$)	τ_B	2.85×10^{-9}	s
Velocity Factor of RG58 BNC Cable ($\boldsymbol{v_{phA} = VF_A * c}$)	VF_A	66% of c (speed of light)	$(Unitless)$
Velocity Factor of the mock DPF ($\boldsymbol{v_{phB} = VF_B * c}$)	VF_A	69% of c (speed of light)	$(Unitless)$

3.3 Intro to Pulsed-Power Signal Analysis for the DPF TL System

For this research effort, two methods are considered for sending a pulse signal along the mock DPF transmission line. Before modeling an input source feeding into the mock DPF system, first let the mock DPF be modeled as a lossless line connected by the load R_L as portrayed in Fig. 3.25. Notice that there are two available terminals for the DPF: the anode (labeled by the positive sign) and the cathode (labeled by the negative sign). Allow the cathode (negative terminal) to be grounded at the base, allowing a path for potentially hazardous stored electrical energy to be shorted. For safety, a shorting stick grounded to the utility ground is used to direct pockets of stored or unreleased electrical energy to ground.

For modeling an input source supplying a pulse signal, one method requires using stored energy in a capacitor bank to be discharged into the DPF by means of a first-order RC circuit configuration. Experimentally, a $3.3\mu F$ *Aerovox* high voltage capacitor bank is available to be used for charging and discharging into the mock DPF. Alternatively, another method requires using a pulse generator to supply a pulse signal into the mock DPF system. Experimentally, a *Bournlea Instruments Ltd Pulse Generator Type 3148* is available to be used to generate a high voltage pulsed signal into the mock DPF. Limitations exist for both models, however, both provide a means to analyzing a pulse signal propagating along the mock DPF.

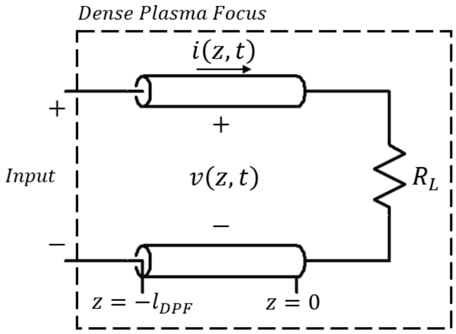

Fig. 3.25 The DPF anode and cathode can be modeled as a lossless transmission line circuit terminated by a load R_L. The input is left open where an RC circuit configuration or pulse generator configuration can be used to connect the anode and cathode (positive and negative terminals).

In section 3.3.1, the characteristics of a pulse signal utilizing a first-order RC circuit is examined. In section 3.3.2, a pulse generator replaced the RC circuit. The characteristics of the mock DPF are examined. In section 3.3.3, the termination load for the mock DPF is presented.

3.3.1 Setting a First-Order RC Circuit as an Input to the Mock DPF

For the first-order RC network approach, an available $3.3\mu F$ *Aerovox* high voltage capacitor bank is utilized with the series path resistance of the DPF circuit. Assume that the resistive load at the end of the DPF transmission line matches the characteristic impedance of the DPF. Then the DPF system can be simplified into the circuit model in Fig. 3.26 where $\mathcal{Z}_0$ is the characteristic impedance of the DPF. This circuit representation is valid since $R_L = \mathcal{Z}_0$ allows for all voltage and current to be absorbed into the load without any sort of reflection back into the DPF System. With this new representation of the circuit, a bandwidth can be determined for the pulsed signal source in the mock DPF system.

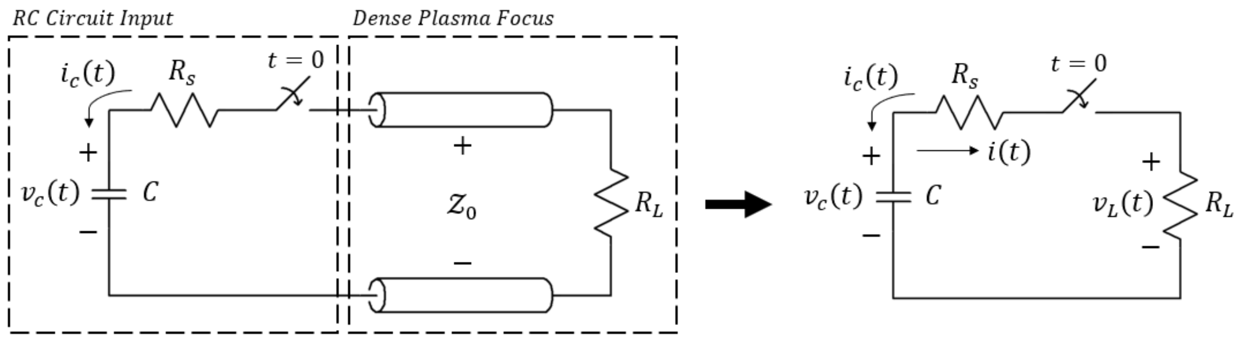

Fig. 3.26 A circuit schematic of the RC network used as an input source to be discharged into the mock DPF transmission line is presented. By allowing the characteristic impedance of the mock DPF and load R_L to be matched, the transmission line circuit can be reduced to a simple circuit model.

Assume that energy has initially been stored in the capacitor bank such that the voltage across it is some constant V_0. Furthermore, there is no excitation to the system until a switch closes the circuit at time $t = 0$. The voltage exponentially decaying function due to the capacitor discharge is represented by Fig. 3.27.

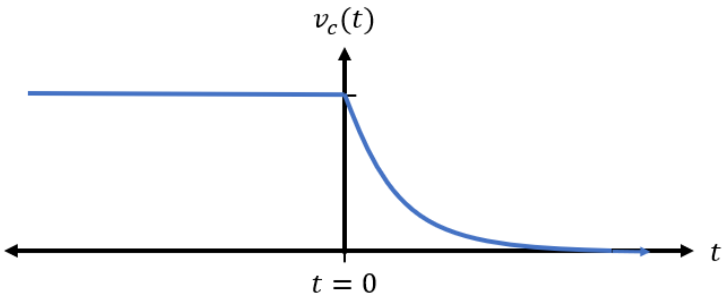

Fig. 3.27 Voltage across a capacitor can be described by the exponentially decaying nature of energy discharged by a capacitor over time where the switch closing the RC circuit configuration closes at time $t = 0$.

When the circuit becomes closed at time $t = 0$, equation (3.14) can be derived by using KVL. Furthermore, the voltage across the load, $v_L(t)$, is related to the current in the circuit by Ohm's Law. Hence

$$v_c(t) = i(t)(R_s + R_L) \tag{3.14}$$

Satisfying the passive device convention, the current flowing into the capacitor, defined by $i_c(t)$, and the current flowing through resistor R_s, $i(t)$ without a subscript, are related by a change in sign as shown in equation (3.15). Refer to Fig. 3.26.

$$i(t) = -i_c(t) \tag{3.15}$$

The voltage across the capacitor, $v_c(t)$, is related to the current flowing into the capacitor, $i_c(t)$, by equation (3.16a) where V_0 represents the initial voltage across the capacitor. Substituting equation (3.15) then produces equation (3.16b) [33].

$$v_c(t) = \frac{1}{C}\int_{0^+}^{t} i_c(t)\,dt + V_0 \tag{3.16a}$$

$$v_c(t) = -\frac{1}{C}\int_{0^+}^{t} i(t)\,dt + V_0 \tag{3.16b}$$

Plugging equation (3.16b) into equation (3.14) then produces

$$\left\{-\frac{1}{C}\int_{0^+}^{t} i(t)\,dt + V_0\right\} = i(t)(R_s + R_L) \tag{3.17a}$$

Differentiating on both sides with respect to time then results in a first-order ordinary differential equation (ODE).

$$-\frac{1}{C}i(t) = (R_s + R_L)\frac{di(t)}{dt}$$

$$\frac{di(t)}{dt} + \frac{1}{(R_s + R_L)C}i(t) = 0 \tag{3.17b}$$

The solution to the first-order differential is an exponentially decaying function with respect to time.

$$i(t) = i(t = 0)e^{\frac{-t}{\tau}} \tag{3.18}$$

where τ is the RC time constant represented by

$$\tau = (R_s + R_L)C \tag{3.19}$$

The initial voltage in the system is related to the properties of the capacitor. Refer to Fig. 3.26 again. The current at $t = 0$ is

$$i(t = 0) = \frac{v_c(t = 0)}{R_s + R_L} = \frac{V_0}{R_s + R_L} \tag{3.20}$$

Substituting equation (3.20) back into equation (3.18) then yields

$$i(t) = \left\{\frac{V_0}{R_s + R_L}\right\} e^{\frac{-t}{\tau}} \tag{3.21}$$

Now that $i(t)$ has been solved for, equation (3.21) can be substituted into equation (3.16b) to obtain a solution for $v_c(t)$. Thus

$$v_c(t) = -\frac{1}{C}\int_{0^+}^{t}\left\{\frac{V_0}{R_s + R_L} e^{\frac{-t}{\tau}}\right\} dt + V_0$$

$$= -\frac{V_0}{(R_s + R_L)C}\int_{0^+}^{t} e^{\frac{-t}{\tau}}\, dt + V_0$$

$$= -\frac{V_0}{\tau}\left[-\tau e^{\frac{-t}{\tau}}\right]_{t=0^+}^{t=t} + V_0$$

$$= V_0\left[e^{\frac{-t}{\tau}} - e^{\frac{-(0^+)}{\tau}}\right] + V_0$$

$$= V_0 \left[e^{\frac{-t}{\tau}} - 1 \right] + V_0$$

$$v_c(t) = V_0 \cdot e^{\frac{-t}{\tau}} \tag{3.22}$$

Now, define the exponentially decaying pulse to be within the 10% to 90% margins of V_0 as shown in Fig. 3.28. This exponentially decaying function is consistent with [33].

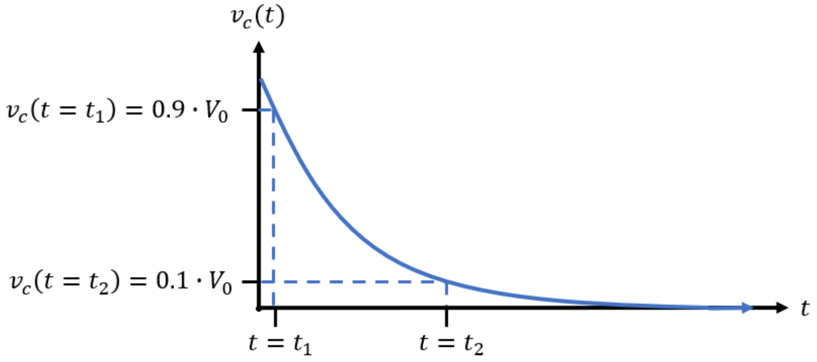

Fig. 3.28 For characterizing a pulse signal as having bandwidth, allow the decaying pulse to be characterized with the 10% and 90% margins of V_0.

Then define $v_c(t = t_1)$ at 90% of V_0 by

$$v_c(t = t_1) = 0.9 \cdot V_0$$

$$\left\{ V_0 \cdot e^{\frac{-t}{\tau}} \right\}_{t=t_1} = 0.9 \cdot V_0$$

$$\left[V_0 \cdot e^{\frac{-t_1}{\tau}} \right] = 0.9 \cdot V_0$$

$$e^{-\frac{t_1}{\tau}} = 0.9$$

$$\frac{-t_1}{\tau} = \ln(0.9)$$

$$t_1 = -\tau \cdot \ln(0.9) \tag{3.23a}$$

Similarly, define $v_c(t = t_2)$ at 10% of V_0 by

$$v_c(t = t_2) = 0.1 \cdot V_0$$

$$t_2 = -\tau \cdot \ln(0.1) \tag{3.23b}$$

Then define the fall time of the pulsed signal by

$$t_{fall} = t_2 - t_1 \tag{3.24a}$$

$$t_{fall} = \{-\tau \cdot \ln(0.1)\} - \{-\tau \cdot \ln(0.9)\}$$

$$t_{fall} = \tau \cdot \ln(0.9) - \tau \cdot \ln(0.1)$$

$$t_{fall} = \tau \cdot \ln\left(\frac{0.9}{0.1}\right) \approx 2.197\tau \tag{3.24b}$$

The corner frequency is defined by

$$\omega_0 = 2\pi f_{3dB} = \frac{1}{\tau} = \frac{1}{(R_s + R_L)C} \tag{3.25}$$

$$t_{fall} \approx 2.197\tau \approx \frac{2.197}{\omega_0} \approx \frac{2.197}{2\pi f_{3dB}} \approx \frac{0.35}{BW}$$

A convenient form written in equation (3.26) for the bandwidth of a first order RC circuit pulse signal can be used provided the fall time, t_{fall}, is known. Alternatively, the time constant τ can be used to determine the pulse signal bandwidth. In section 3.3.2, the transmission line circuit utilizing the pulse generator as the input source, the fall time of the pulse can be used to determine the pulse signal bandwidth.

$$BW = \frac{0.35}{t_{fall}} = \frac{0.35}{t_2 - t_1} = \frac{0.35}{2.197\tau} \tag{3.26}$$

There is some flexibility in being able to control the RC time constant in the DPF system by changing the additional series resistance, R_s. However, the DPF is fixed at a characteristic impedance $\mathcal{Z}_0$ terminated by a load R_L. Adding any additional series resistance will only increase the fall time of the system as indicated by the relation in equation (3.19). Consider the scenario that $R_s = 0$ and $R_L \approx 16.7\Omega$. Then

$$\tau_{min} = (R_s + R_L)C = \big((0) + (16.7\Omega)\big)(3.3\mu F) \approx 55.1\mu s$$

$$t_{fall_1} = \{2.197\tau_{min}\}_{\tau \approx 55.1\mu s} \approx 121\mu s$$

$$BW_1 = \frac{0.35}{t_{fall_1}} \approx 2.9kHz$$

Thus, the smallest time constant that can be achieved in this RC network is approximately $55\mu s$ or a fall time of approximately $121\mu s$. This poses a limitation to the RC network if one is interested in achieving smaller pulse widths.

To demonstrate the $121\mu s$ pulse width signal from the previous analysis, an experiment is set up to recreate the RC configuration from Fig. 3.26. In the experiment, a mock DPF is terminated by an approximately matched load of $R_L \approx 16.7\Omega$. A mechanical relay is then set up in its initial position to connect a voltage source across a $3.3\mu F$ *Aerovox* high voltage capacitor bank. The relay is then switched into its second position by disconnecting the voltage source and connecting the capacitor bank across the base of the mock DPF. A more accurate representation of this circuit experiment is presented later in this chapter in Fig. 3.37. The series resistance will be negligible in comparison to the load ($R_s \ll R_L$) since there is no additional series resistance in the experiment. Further, the stored potential across the capacitor bank will be $12V$ to prevent risk of damaging a high impedance oscilloscope connected across the output load R_L.

Three different instances of the pulse signal from the RC configuration experiment are captured by the oscilloscope provided in Fig. 3.29 (a, b, c). It can be shown that in all instances captured, the signal peaks at $12V$ and exponentially decays. The pulse width appears to be approximately in the range of 100-200μs. Mechanical bounce from the relay is observable at this scale and appears to be random in the three different instances. In the next section, another method is approached for setting up a pulse generator as an input to the mock DPF.

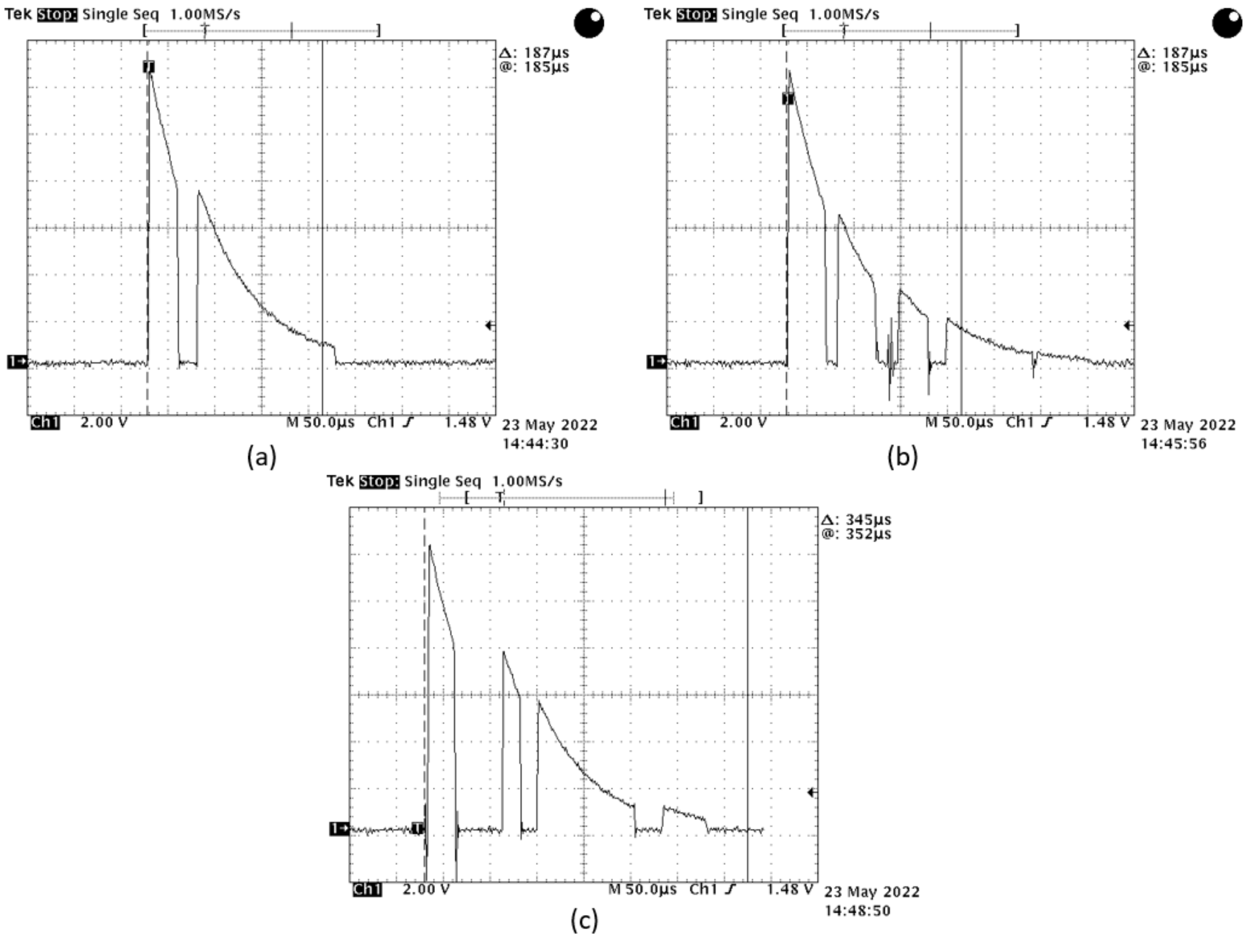

(a) (b) (c)

Fig. 3.29 (a, b, c) An oscilloscope setup in high impedance mode is connected across the load of the mock DPF when the system is connected by an RC configuration as an input where $R_s \approx 0\Omega$, $R_L \approx 16.7\Omega$, and $C = 3.3\mu F$. There are three instances captured by the oscilloscope with the same setup. Mechanical bounce of the switch in the RC configuration is detectable in the $50\mu s$ horizontal scale. However, ignoring mechanical bounce of the relays, the pulse width in the RC setup is close to $t_{fall_1} \approx 121\mu s$.

3.3.2 Setting a Pulse Generator as a Source to the Mock DPF

For the second approach, a pulse generator is used in place of the first-order RC network source as shown in Fig. 3.30. Notice that in the pulse generator circuit, additional resistors R_1 and R_2 are embedded in between the pulse generator and the DPF. In the instruction manual of the *Bournlea Instruments Ltd Pulse Generator Type 3148*, connecting a load impedance different than 50Ω to the pulse generator will introduce reflections at the mismatch point leading to distortion of the output waveform. To prevent this distortion from occurring, the total connected load to the pulse generator, R_{total}, must be equal to 50Ω. It is demonstrated in Fig. 3.31 that matching the load of the output generator minimizes distortion of the output waveform.

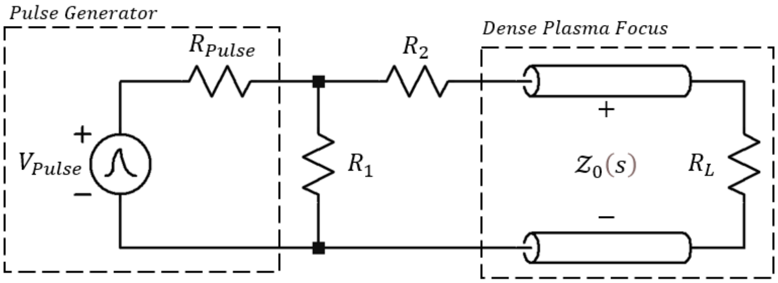

Fig. 3.30 A schematic for connecting the *Bournlea Instruments Ltd Pulse Generator Type 3148* to the mock DPF is presented. Notice that resistors R_1 and R_2 are embedded into the circuit to provide a means to matching the pulse generator to the DPF system in order to reduce distortion.

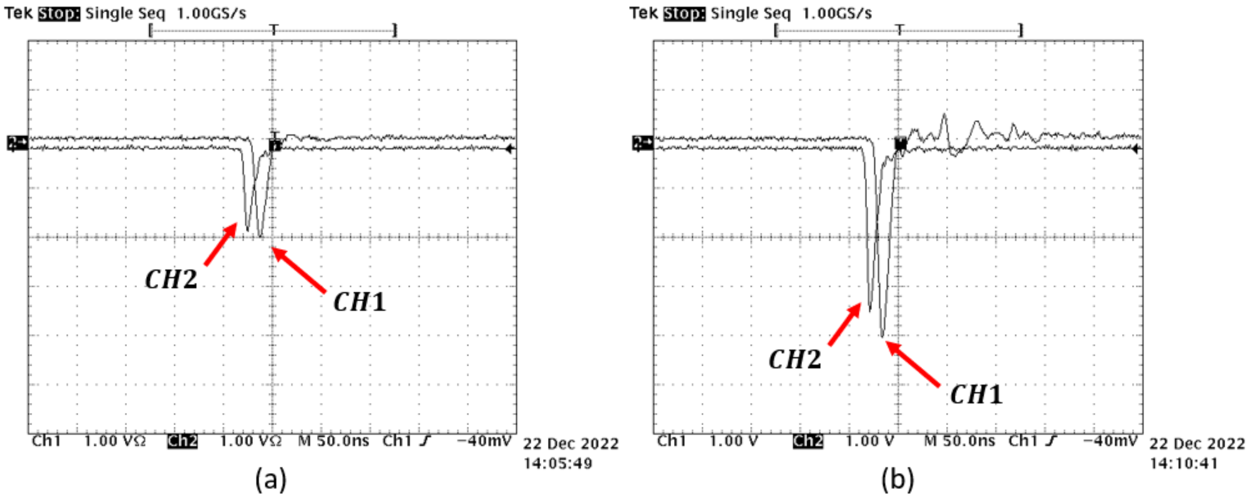

(a) (b)

Fig. 3.31 (a, b) A $60dB$ attenuated pulse signal is fired from a pulse generator into an oscilloscope with load impedance set at (a) 50Ω and (b) High-Z ($1M\Omega$). Channel 1 of the oscilloscope represents a $60dB$ mock signal of the pulse generator output and Channel 2 represents the pulse generator output when attenuated by $60dB$ attenuators. The effects of distortion due to a mismatched load of the pulse generator appear minimal in comparison to the peak of the pulse signal.

The purpose of R_1 and R_2 is to help achieve meeting the 50Ω matched load requirement for the *Bournlea Instruments* pulse generator. Since the DPF is already characterized by $R_L \approx 16.7\Omega$ and R_{total} must be equal to 50Ω, then only R_1 and R_2 need to be solved for in the pulse generator circuit. Disregarding transmission line time delays of the DPF, the total resistive load R_T can be represented by resistances R_1, R_2, and R_L as shown in Fig. 3.32.

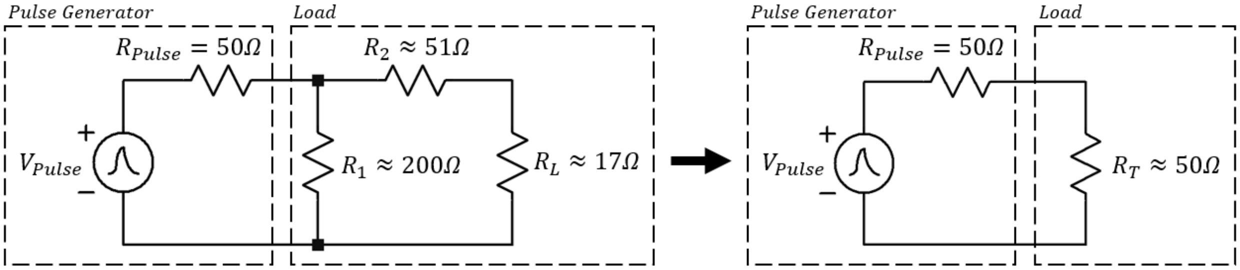

Fig. 3.32 Matching the pulse generator to a 50Ω load requires resistors R_1, R_2, and the DPF, characterized by R_L, to be solved for to satisfy a desired value of $R_L = 50\Omega$.

It can be shown that the total connected load to the pulse generator can be solved for using resistances in series and parallel relations as provided in equation (3.27a).

$$R_T = R_1||(R_2 + R_L) = \frac{R_1 \cdot (R_2 + R_L)}{R_1 + (R_2 + R_L)} \tag{3.27a}$$

Terms can then be rearranged in equation (3.27a) to obtain a solution for R_1 in terms of R_2 as provided in equation (3.27b).

$$R_1 = \frac{(R_2 + R_L) \cdot R_T}{(R_2 + R_L) - R_T} \tag{3.27b}$$

By letting $R_2 \approx 50\Omega$, then $R_1 \approx 200\Omega$. Refer to Fig. 3.27.

The pulse width of the *Bournlea Instruments Ltd Pulse Generator Type 3148* is determined by an internal hardware component referred to as the charge line. The charge line currently installed into the pulse generator provides a fixed pulse width of approximately $10ns$. Then

$$t_{fall_2} = t_1 - t_2 \approx 10ns$$

$$BW_2 = \frac{0.35}{t_{fall_2}} \approx 35MHz$$

Performing an experiment using an open or shorted load condition on the mock DPF will result in distortion where one needs to look at the first pulse and what is driving the pulse in the circuit outside the source and load ends of the line. However, for the matched condition case, this should be enough to demonstrate the redirection of current in a DPF system. A $10ns$ pulse width with $5ns$ to $8ns$ rise time should be fast enough to demonstrate changes in voltage and current due to reflections in the DPF system. Recall that the DPF has a transit time of approximately $2ns$ assuming speed of light velocity of propagation.

$$t_{d,DPF} = \frac{l_{DPF}}{c} = \frac{(0.587375m)}{(2.99 \times 10^8 m/s)} \approx 1.96ns$$

3.3.3 Constructing a Matching Load Condition for the DPF

In order for both approaches in the previous sections to be operable, it was assumed that the load R_L connected to the DPF was matched and lossless. Consequently, $R_L = \mathcal{Z}_0$ and is real. If the load is matched to the line, all of the energy incident upon the load is absorbed by the line with load. Ideally, the load does not reflect energy back into the connecting line or DPF. Fig. 3.33 models the pinch end of the DPF.

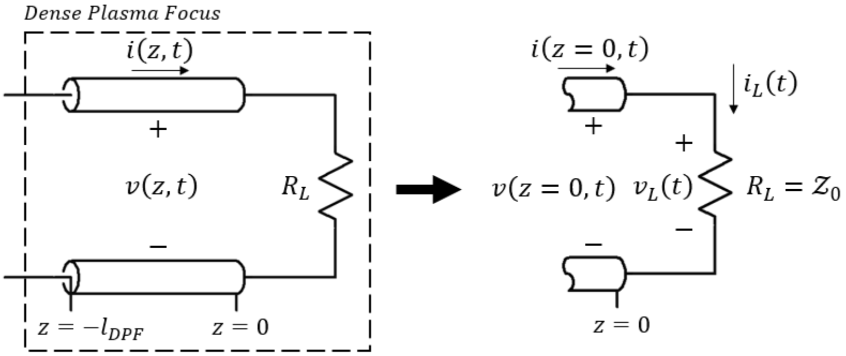

Fig. 3.33 The load resistance R_L is matched to the characteristic impedance of the mock DPF ($R_L = \mathcal{Z}_0$). Ideally, energy incident upon the load is absorbed by the load without reflecting energy back.

For very large voltages and currents generated and launched into the mock DPF, the load R_L must be able to satisfy power requirements in the system. Since a 17Ω high wattage resistor is not practical and readily available for this effort, then constructing a resistive network comprised of high wattage ceramic resistors was approached instead. By focusing attention on the pinch end of the mock DPF as shown in Fig. 3.33, then by Ohm's Law and properties of matching, allow

$$v(z = 0,t) = i(z = 0,t)R_L \Leftrightarrow v_L(t) = i_L(t)R_L \tag{3.28}$$

The total amount of power dissipated into the load R_L is then a consequence of voltage and current incident upon the load. For an exponentially decaying pulse signal, consider analyzing the peak power. Define the peak voltage and current across the connected load by $v_{L,peak}$ and $i_{L,peak}$. Then the peak power absorbed into the load may be defined by

$$P_{L,peak} = v_{L,peak} \cdot i_{L,peak} = \frac{v_{L,peak}^2}{R_L} = i_{L,peak}^2 \cdot R_L \tag{3.29}$$

To match the load R_L with the characteristic impedance of the mock DPF measured in section 3.2.3, then R_L must be approximately 17Ω. Provided a signal is generated and launched into the mock DPF system with a peak voltage of $v_{L,peak} = 1kV$, then the peak current seen at the load is $i_{L,peak} \approx 59.8A$. From equation (3.29), the peak power at the load is then $P_{L,peak} \approx 59.8kW$.

Although the peak power dissipated into the load may be very high, the exposure to this amount is for an instant of time before rapidly decaying exponentially. For this research effort, the characterized pulse width exposure can be within the 10s of nanoseconds and 100s of microseconds range. *TE Connectivity* provides a datasheet for their metal film RR Series resistors listing the pulse characteristics in a logarithmic plot for different power rated resistors [34]. In Fig. 3.34, it can be shown that their $3W$ RR Series resistors can handle up to approximately $P_{max} = 1.5kW$ given a pulse width of approximately $200\mu s$. At least 40 of these resistors would be required to dissipate $60kW$. As the pulse duration decreases, the rated power dissipation increases. It is also worth noting that the pulse duration defined in the datasheet is a constant value unlike the exponentially decaying nature of the pulse within the mock DPF setup.

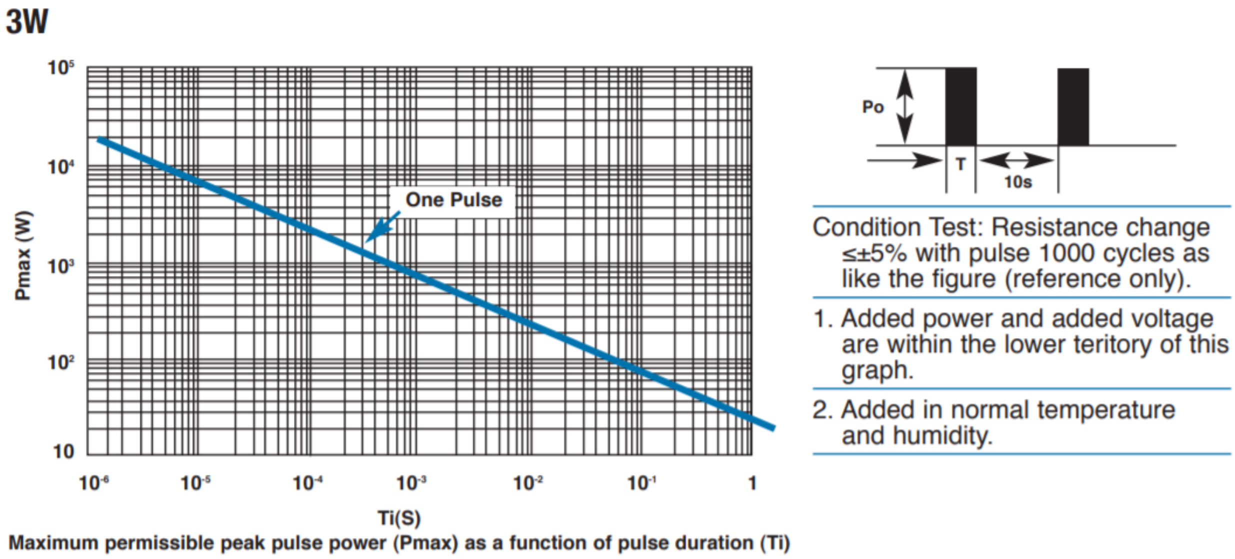

Condition Test: Resistance change ≤±5% with pulse 1000 cycles as like the figure (reference only).

1. Added power and added voltage are within the lower teritory of this graph.
2. Added in normal temperature and humidity.

Maximum permissible peak pulse power (Pmax) as a function of pulse duration (Ti)

Fig. 3.34 A logarithmic graph taken from the datasheet of 3W RR Series conventional resistors provided by *TE Connectivity* lists the maximum permissible peak pulse power as a function of pulse duration [34].

For the purpose of the mock DPF experiment, a resistive network is used to dissipate $60kW$ for a $200\mu s$ pulse. By increasing the number of resistors in this network, the amount of power dissipated into each of the individual resistors should decrease. Each individual resistor must at least be able to absorb power below its maximum permissible peak pulse power, P_{max}. Allow R_L to be characterized by the resistive network circuit in Fig. 3.35. Fig. 3.35 is the load resistance needed for a matched DPF.

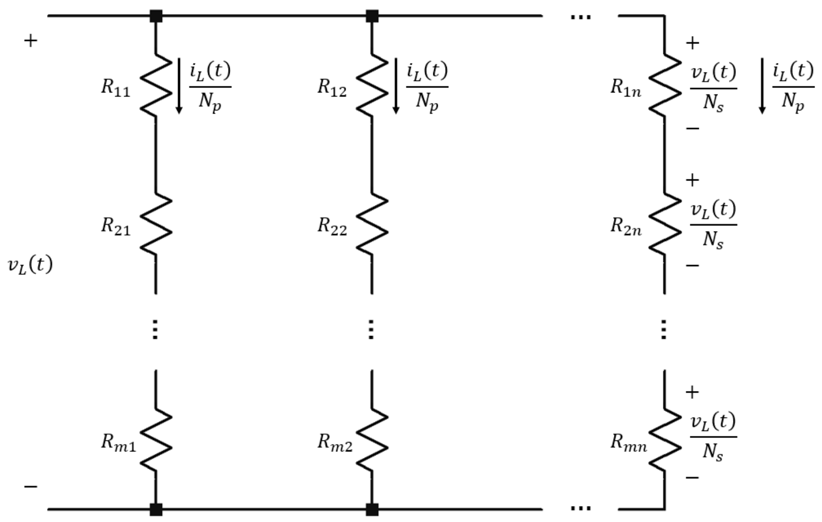

Fig. 3.35 The load resistance R_L can be characterized by a resistive network of series and parallel resistors.

Recall that resistors in series can be added together. Then the equivalent load resistance for resistors in parallel is

$$\frac{1}{R_L} = \frac{1}{(R_{11} + R_{21} + \cdots + R_{m1})} + \frac{1}{(R_{12} + R_{22} + \cdots + R_{m2})} + \cdots + \frac{1}{(R_{1n} + R_{2n} + \cdots + R_{mn})}$$

Assume that each of the resistors in this network have the same value of R_0. Then the equivalent series resistance in each path is just R_0 multiplied by the number of resistors in series N_s. Hence

$$\frac{1}{R_L} = \frac{1}{N_s R_0} + \frac{1}{N_s R_0} + \cdots + \frac{1}{N_s R_0}$$

Similarly, the number of resistors in parallel is just $1/(N_s R_0)$ multiplied by the number of paths in the network N_p. Hence

$$\frac{1}{R_L} = N_p \left(\frac{1}{N_s R_0}\right)$$

$$R_L = \frac{N_s}{N_p} R_0 \tag{3.30a}$$

Now that the equivalent load resistance has been characterized by the number of resistors R_0 in series and parallel, then R_0 can be solved for provided R_L as rearranged in equation (3.30b). Then the number of resistors R_0 required to construct the resistive network R_L is N_{total} as shown in equation (3.30c).

$$R_0 = \frac{N_p}{N_s} R_L \tag{3.30b}$$

$$N_{total} = N_s N_p \tag{3.30c}$$

Note that each individual resistor R_0 can handle up to power P_0. That is

$$P_0 = \frac{v_{L,peak}}{N_s} \cdot \frac{i_{L,peak}}{N_p} = \left(\frac{v_{L,peak}}{N_s}\right)^2 \frac{1}{R_0} = \left(\frac{i_{L,peak}}{N_p}\right)^2 R_0 \tag{3.31a}$$

or

$$P_0 = \frac{1}{N_s N_p} \frac{v_{L,peak}^2}{R_L} = \frac{1}{N_s N_p} i_{L,peak}^2 R_L \tag{3.31b}$$

For the mock DPF set up in the RC configuration in section 3.3.1, the pulse width is defined by $t_{fall_1} \approx 121\mu s$. Using the logarithmic plot for the RR Series resistors, at $200\mu s$, the maximum permissible peak power is $1.5kW$. The power rating is higher for shorter pulse widths.

Consider the case that $R_0 = 200\Omega$, provided $R_L = 16.7\Omega$. Setting $N_s = 2$ results in $N_p = 24$. Then the total amount of resistors for the network, required to build a 16.7Ω load matching impedance, is $N_{total} = 48$ resistors. Assuming $v_{L,peak} = 1kV$ implies a peak power dissipated into an individual resistor in the load resistive network to be $P_0 = 59kW$. By using N_{total}

number of the TE Connectivity RR Series resistors, then $59kW$ can be dissipated into the DPF system using the constructed resistive load network.

A load resistive network is then constructed as shown in Fig. 3.36. The network is electrically connected by four bolts on the outer ring to the external cathode cage of the mock DPF and one bolt on the center plate to the pinch end of the mock DPF anode.

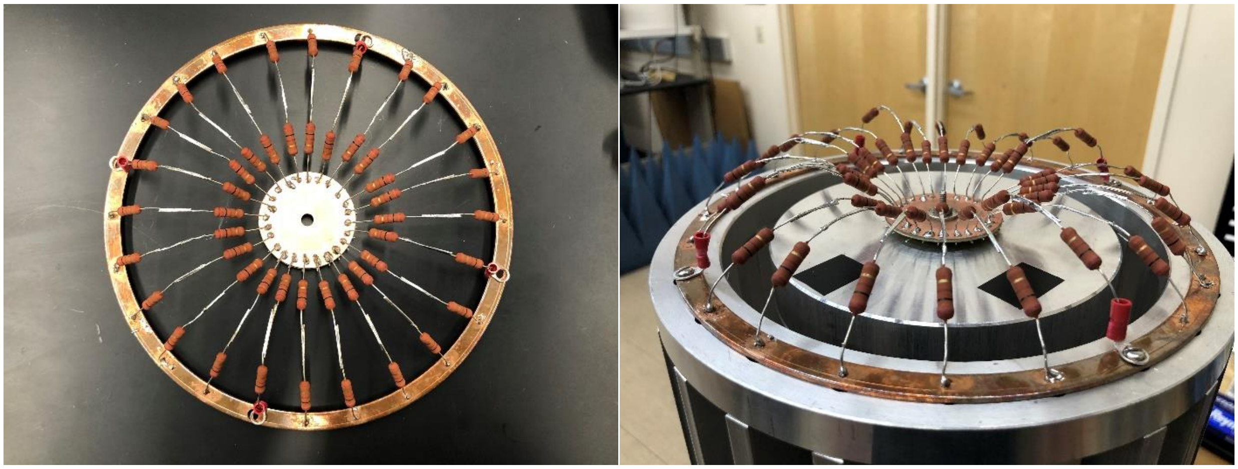

Fig. 3.36 A construction of the resistive load network used to match the characteristic impedance of the DPF is provided.

3.4 Introduction to Connecting Wires to the DPF

Recall that there are two configurations that can be used for the DPF. When recording data, it is important to ensure wires are connected appropriately and that shielding is provided to wires that are prone to be affected by radiation and antenna effects.

3.4.1 Connecting Wires to the DPF using an RC Source Configuration

For characterizing the discharge of a pulse from a capacitor bank into the mock DPF, a simple circuit model presented in Fig. 3.26 was utilized. A more defined circuit model provided in Fig. 3.37 can be utilized for recreating the experimental setup for discharging energy from an *Aerovox* $3.3\mu F$ capacitor bank into the mock DPF. Notice that there is a switch that initially connects a high voltage (HV) DC power supply across the *Aerovox* $3.3\mu F$ capacitor bank defined by C. When the capacitor bank is connected to the HV power supply, the HV supply can be set to charge the capacitor bank to a desired voltage potential.

Further notice in the experimental setup, there are two different grounds defined in Fig. 3.37. The earth ground (Earth GND) is defined as the reference point that connects the circuit to a copper pipe intended to connect directly to earth ground. A common (COM) mode ground is defined to be the signal referenced ground internal to the electrical circuitry inside the HV Power Supply that is unknown. A third ground can be defined by a chassis which is normally represented by an external metal structure that hides internal circuitry of some device such as the HV Power Supply. Since there are different distances between grounds, is it typical to expect COM to eventually become connected to chassis, and then expect the chassis to become connected to earth ground to minimize different paths to different grounds. Mixing grounds can result in possible ground loops within a circuit.

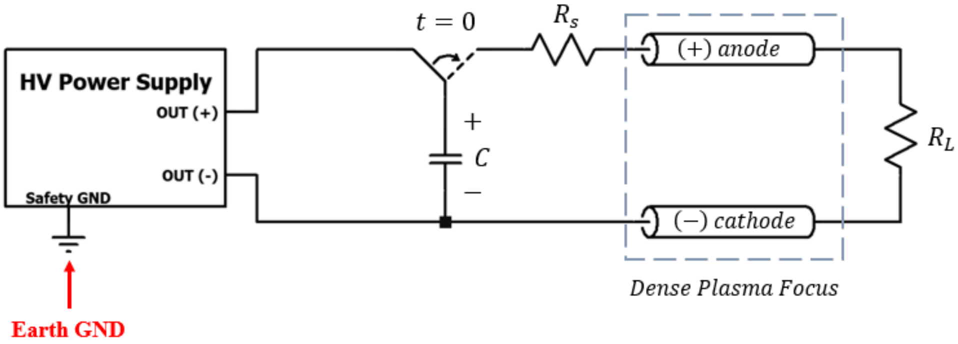

Fig. 3.37 A complete circuit model is presented for recreating the discharge of energy from a capacitor bank into the mock DPF. A switch is shown that is initially connecting a high voltage power supply to the *Aerovox* $3.3\mu F$ capacitor bank for charging. At time $t = 0$, the switch disconnects from the high voltage power supply and connects the capacitor bank to the mock DPF circuit for discharge.

After charging the capacitor bank to a desired voltage potential, at time $t = 0$, the switch connecting the HV power supply is disconnected from the capacitor bank. Instead, the capacitor bank becomes connected to the mock DPF and discharges the stored energy from the capacitor bank into the mock DPF. Experimentally, the connections made on the switch between the capacitor bank, HV power supply, and mock DPF may look like that of Fig. 3.38. The connections made between the capacitor bank, the switch, and the HV power supply may look like that of Fig 3.39. The ground connection is labeled on the capacitor bank, a COM ground of the HV supply is tied to that point and an external earth GND is tied to the same point.

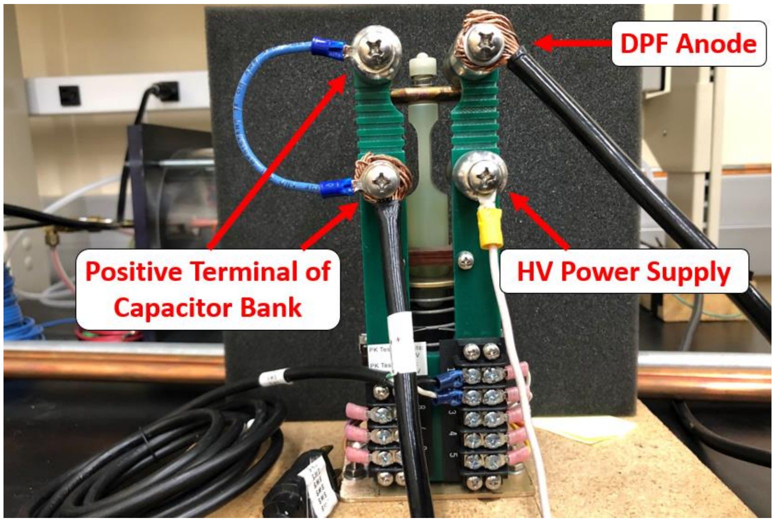

Fig. 3.38 A switch is turned on closing a path connecting a $3.3\mu F$ capacitor bank to a high voltage power supply charging the capacitor up to $1kV$. After the switch is turned off, the capacitor bank is disconnected from the power supply then closing a path between the capacitor and the DPF anode discharging any stored energy.

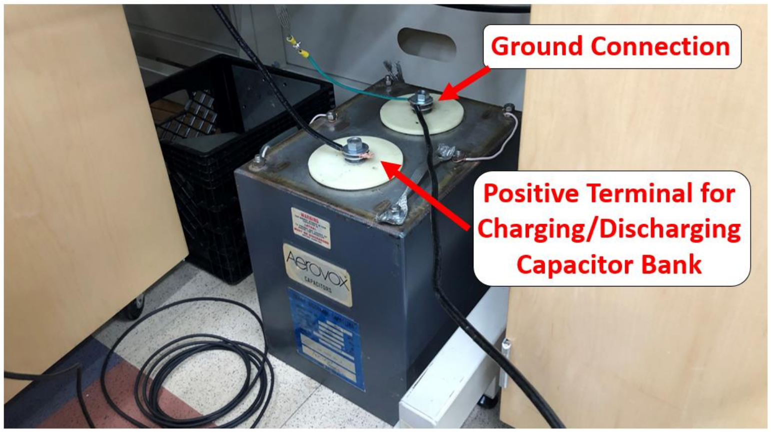

Fig. 3.39 In the natural state, one end of the capacitor is connected to a ground potential and the other end of the capacitor is shorted through a path connecting to the anode of the DPF. After firing the DPF using the RC configuration, it is advised to use a shorting rod on the discharging positive node terminal of the capacitor bank to eliminate residual shocking hazards.

3.4.2 Connecting Wires to the DPF using a Pulse Generator Configuration

Instead of using the RC configuration experimental setup in section 3.4.1, an experimental setup for utilizing the pulse generator can be used to fire a pulse along the mock DPF. A general circuit model provided in Fig. 3.30 was previously used to demonstrate the properties of the pulse in the pulse generator experimental setup. A more defined circuit model found in Fig. 3.40 can be used to obtain a better understanding of the experimental connections between different devices and the mock DPF.

Notice in the experimental setup, a *Model DG535 4 Channel Digital Delay* is used to trigger the *Bournlea Instruments Pulse Generator*. Refer to Fig. 3.40. The purpose of the model DG535 is to fire two different rectangular pulses (pre-pulse trigger and main pulse trigger) at different timed intervals to meet the required specifications of the *Bournlea Instruments Pulse Generator*. Furthermore, three different grounds are demonstrated in the experimental circuit model. The Pulse Generator has an external ground (Chassis) tied directly to internal ground (COM). An external safety ground (presumably Chassis) is tied to earth ground. Moreover, the Output Monitor of the pulse generator is a $60dB$ attenuated signal replica of the HV Output. Hence, if the HV output is 4kV, the output monitor displays a 4V output.

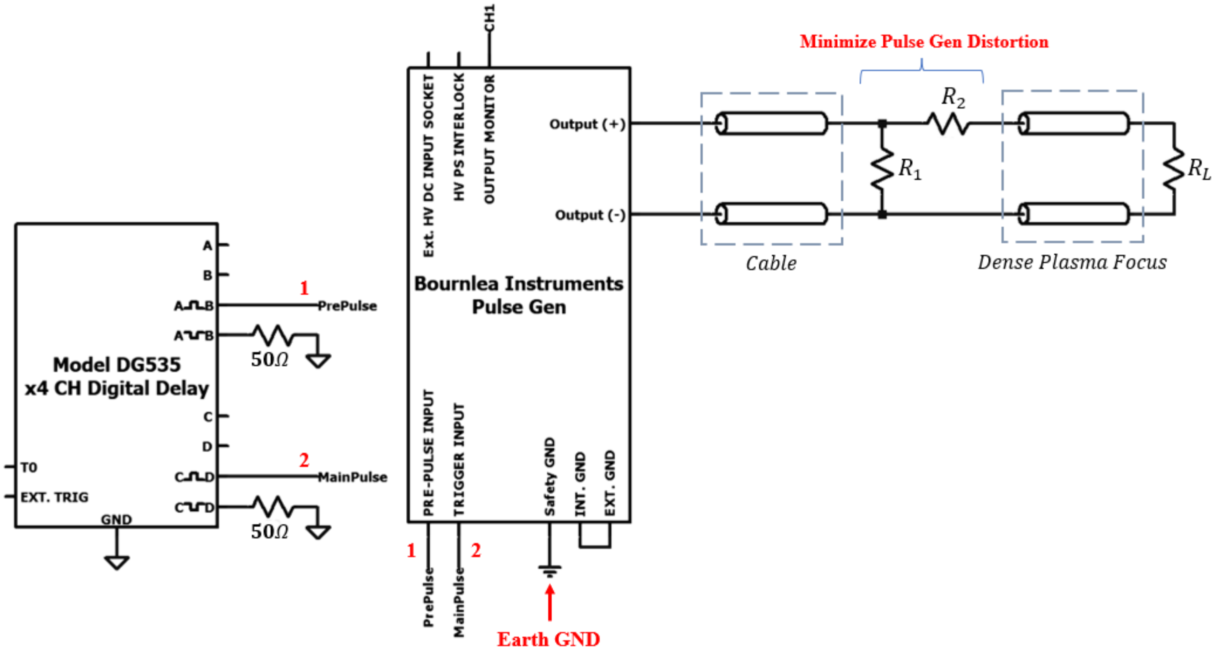

Fig. 3.40 A complete circuit model for firing the *Bournlea Instruments Pulse Generator* into the mock DPF is presented. In order to fire the pulse generator in single pulse or multi-pulse mode, a separate device, the *Model DG535 Digital Delay*, is used to trigger the pulse generator. When the pulse generator is triggered, a pulse is fired from the Output Monitor (60dB attenuated signal replica) and from its HV Output (actual signal).

With the pulse generator configuration, it is important to minimize additional delays to the DPF system. The *Bournlea Instruments Ltd Pulse Generator Type 3148* has an installed charge line to produce a 25ns pulse. This signal is output from the Output Monitor and the HV Output. The output monitor connects directly to a standard BNC cable to Channel 1 of an oscilloscope intended to be used as a trigger. The HV output connects to a cable that connects to the R_1 and R_2 resistor interface of the mock DPF circuit. From this point, the signal then propagates along the mock DPF and gets absorbed into the R_L load resistor if the line is matched.

Based on the instruction manual of the pulse generator, the output monitor has a waveform that is like the HV output of the pulse generator with a $60dB$ internal attenuation (decrease in voltage by a factor of 10^3). When the HV output is connected directly to the oscilloscope with a $60dB$ attenuation and with same length cables for both the output monitor and HV output, then the result in Fig. 3.41 is demonstrated.

Curs1 X Pos -21.76ns
Curs2 X Pos -10.36ns

C1 500mV/div 50Ω BW:16.0G
C2 500mV/div 50Ω BW:16.0G

t1 -21.76ns
t2 -10.36ns
Δt 11.4ns
1/Δt 87.719MHz

A' C1 ∫ -730mV

20.0ns/div 6.25GS/s 160ps/pt
Preview Single Seq
0 acqs RL:1.25k
Auto October 19, 2021 13:52:05

Cursor 1: Ch 1
Cursor 2: Ch 1

Fig. 3.41 The "output monitor" of the Bournlea Instruments Pulse Generator is indicated by channel 1 (yellow) of the oscilloscope. The HV output is indicated by channel 2 (turquoise) of the oscilloscope. The "output monitor" of the pulse generator is internally attenuated by $60dB$ and additionally attenuated with a $20dB$ attenuator ($80dB$ total attenuation). The HV output is forced to be attenuated by $80dB$ using attenuators. There exists a difference in time delay of about $10ns$ between peaks despite having the same length of cable connections. There is also an amplitude difference between pulses of about $500mV$ (or $500V$ non-attenuated) despite having 50Ω terminations on the oscilloscope. For experimental purposes, the HV output is fed into the mock DPF, and the "output monitor" is used as a trigger for the oscilloscope.

To ensure that the signal captured by the DPF is occurring at a time instance relatively close to the time instance of when the pulse generator is fired, then it is important to determine the lengths of the wires connected in the DPF system. Assume that the pulse generator output monitor is connected to channel 1 of the oscilloscope. When the voltage of the output monitor approaches some set triggered value on channel 1, then the oscilloscope will freeze the frame and collect the results captured by all channels during that time instance the voltage is reached. However, this result is not captured instantaneously on the oscilloscope because the pulse from the output monitor must propagate along a $6m$ BNC cable. As a rule of thumb, it takes light approximately $1ns$ to propagate along $0.3m$ $(1ft)$ or

$$\frac{1ft}{c} \approx \frac{(0.3048m)}{c} \approx 1.01ns.$$

This implies that that signal from the output monitor will not reach to the oscilloscope until about $20ns$ after the pulse generator has already been fired. Because changes in voltage are occurring in the nanosecond scale for the anticipated DPF experiments, then it is important to minimize the influence of this delay. Connect the actual output of the pulse generator to the front end of the DPF using a BNC cable of the same length, that is $6m$. Then, the signal propagating from the output monitor will reach the oscilloscope at $20ns$ after the shot is fired and the actual pulse output from the pulse generator will then only reach the base of the DPF approximately the same time instance. Define this time instance to be time $t = 0$.

Now that the wire connections have been defined for the pulse generator configuration, in the next chapter, experiments will be performed using either the RC configuration or pulse generator configuration for generating a signal driving the DPF.

Chapter 4: Results and Discussion

4.1 Introduction to Results

It is of interest to locate current redirection in a high energy Dense Plasma Focus (DPF) device when activated. Energy is redirected somewhere along the length of the DPF. It is anticipated that an antenna sensor can detect the changes in the fields generated throughout the device. In Chapter 2, the field strengths anticipated in a DPF device and how the discharged energy flows were examined. The transmission line theory using Laplace transformation techniques was written into a MATLAB program provided in Appendix B. In the next section, an LTspice model of the circuit was also created to provide a comparison between MATLAB and LTspice software simulations. Section 4.2 will examine these results. From Chapter 3, the setup needed to investigate energy losses in a mock DPF system was built using an RC source configuration and a pulse generator source configuration. A series of experiments are performed to study how a linear antenna responds to a transmitting antenna operating both in the radiating and the non-radiating field regions. The experimental results captured by the mock DPF will be examined and compared to the simulated data in the sections following the rest of this chapter.

4.2 Introduction to Transmission Line Theory and Simulations

In Chapter 2, an analysis was performed to determine the voltage and current along a mock DPF for time $t > 0$ using a two-segment transmission line circuit approach. The equations derived from this analysis were then built into a MATLAB program that has been provided in Appendix B. The intention of this section is to simulate the behavior of a current redirected path in a DPF system. By simulating this scenario will help to offer insight on the field information that one might expect in experimentation as presented later in this chapter.

In this section, it is not enough to assume that the theory and MATLAB program are correct. Thus, an LTspice model has also been developed to simulate the same two-segment transmission line circuit. In Section 4.2.1, an initial simulation is computed using the LTspice and MATLAB program models. This initial simulation is based on an experiment from Chapter 3 Section 3.3.1 for firing a $12V$, $121\mu s$ exponentially decaying pulse signal into the mock DPF using the RC source configuration. This initial simulation will be used to provide a direct comparison to a known experimental result. In Section 4.2.2, different scenarios are then modeled for the two-segment transmission line circuit in LTspice and MATLAB to demonstrate changes in voltage and current behavior along the mock DPF. At least one of these scenarios includes a system with a current redirected path.

Recall in Chapter 2 that the parameters of the two-segment transmission line circuit have been previously defined. These parameters are summarized and are available in Appendix B. Additionally, a copy of the analyzed circuit model from Chapter 2 is presented in Fig. 4.1 for reference. The different scenarios simulated in Section 4.2.2 will be based on modifying resistive paths R_f and R_L.

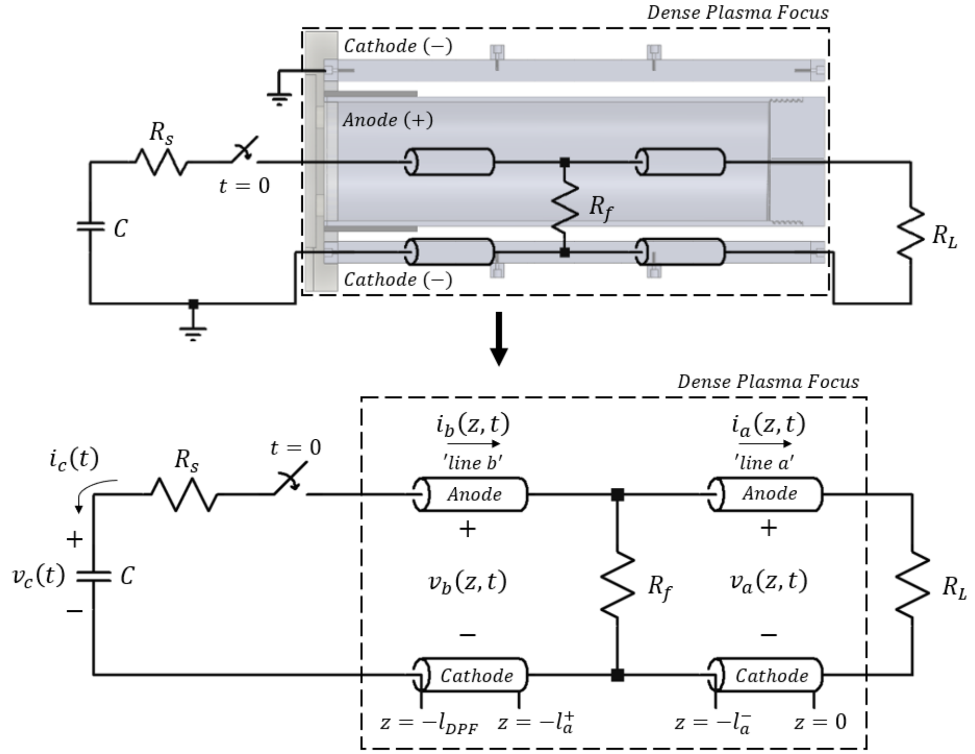

Fig. 4.1 An RC source configuration connects across the mock DPF anode and cathode at the base terminated by a load R_L. Resistor R_f is the resistive path characterizing current redirection in the mock DPF. A two-segment transmission line circuit is used to model this setup.

4.2.1 Pulse Width Simulation Results

From Chapter 2, the mock DPF transmission line theory is based on a circuit design consistent with Fig. 4.1. This circuit can be modeled into LTspice software using the schematic setup shown in Fig. 4.2. From the LTspice model, the circuit parameters have been carefully selected to simulate the experiment examined in Chapter 3 Section 3.3.1. This experiment is the scenario for generating the $12V$, $121\mu s$ exponentially decaying pulse signal from an RC source into the mock DPF as characterized by the load $R_L \approx 17\Omega$.

From the LTspice model in Fig. 4.2, the mock DPF is demarcated within dashed lines. Resistors R_{la} and R_{lb} are implemented into the LTspice schematic solely for measuring current flow at two different points along the mock DPF. These resistors do not represent physical attributes to the experiment. Resistor R_s represents the experimental series resistance in the mock DPF system which is set to $1m\Omega$ for simulation. Resisto/r R_L represents the load resistance terminated by the mock DPF which is approximately $R_L \approx \mathcal{Z}_0 \approx 17\Omega$. Capacitor C represents the $3.3\mu F$ capacitor bank discharging energy into the mock DPF. Switch SW1 is a voltage-controlled switch that switches from $1G\Omega$ to $1\mu\Omega$ at time $t = 0$ by the Vsw1 voltage step response. Refer to Fig. 4.2.

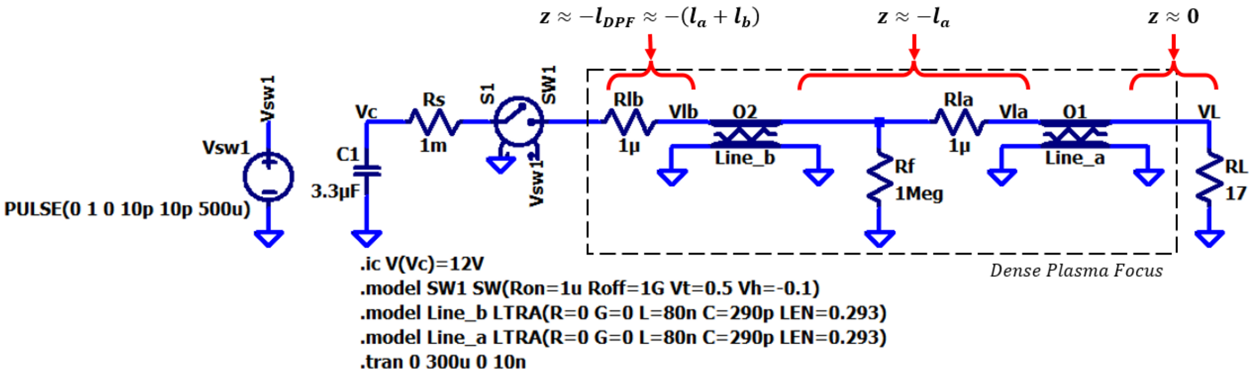

```
.ic V(Vc)=12V
.model SW1 SW(Ron=1u Roff=1G Vt=0.5 Vh=-0.1)
.model Line_b LTRA(R=0 G=0 L=80n C=290p LEN=0.293)
.model Line_a LTRA(R=0 G=0 L=80n C=290p LEN=0.293)
.tran 0 300u 0 10n
```

Fig. 4.2 An LTspice representation of the two-segment transmission line system, as modeled from Chapter 2, is shown. Circuit parameters have been carefully selected in this LTspice model to recreate the exponentially decaying pulse from the experiment in Chapter 3 Section 3.3.1.

Further, from Fig. 4.2, some statements are defined below the schematic. The .ic statement represents an initial condition statement allowing for the capacitor to be initially charged where switch SW1 isolates the capacitor and mock DPF until time $t = 0$. The .model

SW1 statement provides voltage-controlled instructions for the SW1 switch, when to close and open, modeled by resistance values. The .model Line_a and .model Line_b statements define the distributed parameters of the two transmission lines, which are both experimentally the same since they represent similar segments of the mock DPF. The distributed parameters have been values obtained from the TDR experiment in Section 3.2.3 of Chapter 3. That is, $\bar{R} = \bar{G} = 0$, $\bar{L} = 80nH/m$, and $\bar{C} = 290pF/m$. Lastly, the .tran statement defines the transient analysis instructions for how to run the simulation in LTspice. For this simulation, the sample duration is set at $300\mu s$ starting at $t = 0$.

In Fig. 4.3, the transient response of the LTspice model is simulated. It is observed that the pulse peak is at an amplitude of $12V$ (or $0.7A$). Further, the pulse exponentially decays. Between the 90% and 10% voltage margins, the pulse width of the signal is characterized by a $123\mu s$ fall time. Notice that the pulse signal at $z = 0$, $z = -l_a$, and $z = -(l_a + l_b)$ appear to sit on top of one another. Any changes in delay along the mock DPF are expected to occur on the nanoseconds scale. The most prominent simulated component in this $300\mu s$ sample duration is the decaying nature of the RC signal.

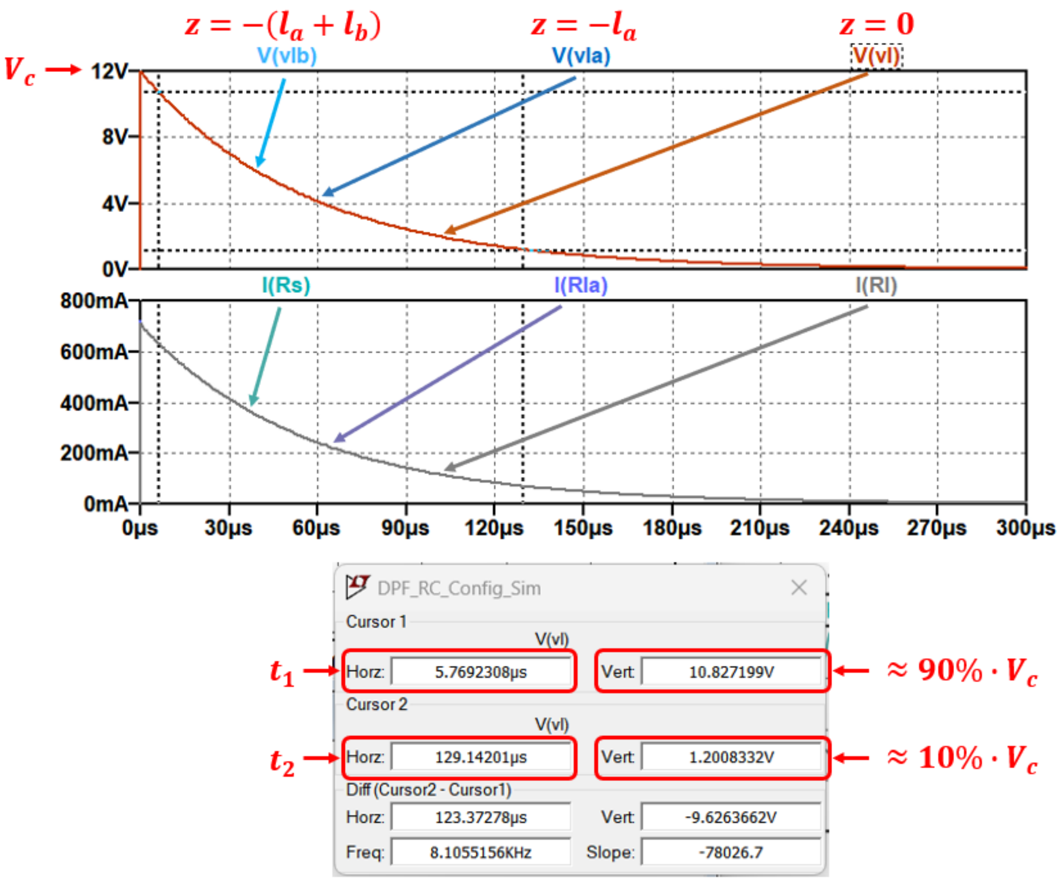

DPF_RC_Config_Sim

Cursor 1

V(vl)

Horz: 5.7692308µs Vert: 10.827199V

Cursor 2

V(vl)

Horz: 129.14201µs Vert: 1.2008332V

Diff (Cursor2 - Cursor1)

Horz: 123.37278µs Vert: -9.6263662V

Freq: 8.1055156KHz Slope: -78026.7

Fig. 4.3 The simulated result of the LTspice schematic from Fig. 4.2 is presented. This simulation is similar to the experimental setup in Section 3.3.1. An RC pulse power signature is released in the mock DPF. The circuit and mock DPF transmission line parameters are defined by $Vc = 12V$, $C1 = 3.3\mu F$, $Rs = 1m\Omega$, $R_L = 17\Omega$, $\bar{R} = \bar{G} = 0$, $\bar{L} = 80nH/m$, $\bar{C} = 290pF/m$. This simulation demonstrates the generation of a $12V_{peak}$ signature with a $121\mu s$ $(t_1 - t_2)$ pulse width.

Now, the same circuit parameters are implemented into the MATLAB transmission line theory program from Appendix B, program file “*dpf_tl_main_file.m*”. Refer to Fig. 4.3. After running the MATLAB program, the simulated plot is shown in Fig. 4.4. From this simulation, the pulse signal peaks at $12V$ (or $0.7A$) and then exponentially decays. At the 90% and 10% voltage margins of the pulse signal, the pulse width of the signal is characterized with a $123\mu s$

fall time. When interpolating both MATLAB and LTspice curves to fit the same number of points and sample length (300 points, 1 point per millisecond), an average error difference of 0.0063% exists between both curves at $z = 0$ (the pinch-end of the DPF). This demonstrates consistency across both LTspice and MATLAB programs.

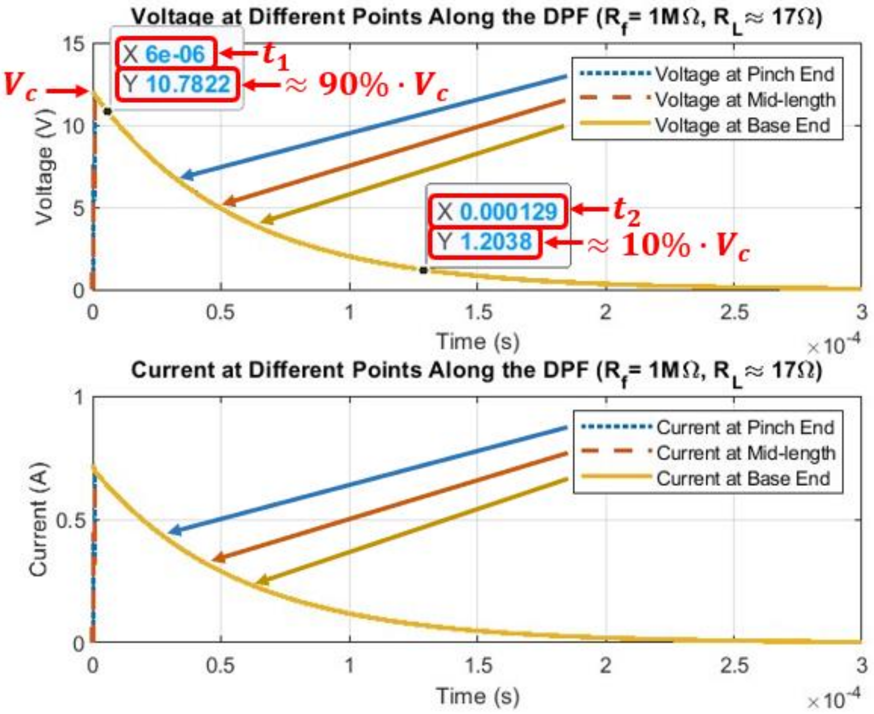

Fig. 4.4 The simulated result of the MATLAB transmission line theory program is presented. There is consistency in peak amplitude and pulse width signal when comparing with the LTspice simulation. Plots are obtained for voltage and current at points $z = -(l_a + l_b) = -0.587m$, $z = -l_a = -0.294m$, and $z = 0$. The plots are shown to lie on top of one another. A $12V$, $121\mu s$ signal was generated internal to the mock DPF when activated. There is consistency in voltage and current data in the mock DPF system when simulated through the Appendix B MATLAB program vs simulated through LTspice.

At the end of Section 3.3.1, an experiment was performed where the results of an exponentially decaying RC pulse signal are measured by an oscilloscope connected at the pinch end of the mock DPF ($z = 0$). An image of the experimental setup is shown in Fig. 4.5. A $3.3\mu F$ capacitor bank connects the input of the mock DPF. The pinch end of the mock DPF is terminated by a matched load resistance network of $R_L \approx 17\Omega$. In experiment, R_f is removed from the circuit to represent an open circuit at $z = -l_a$, but in simulation, R_f is chosen to be very large ($1M\Omega$) to represent the open circuit.

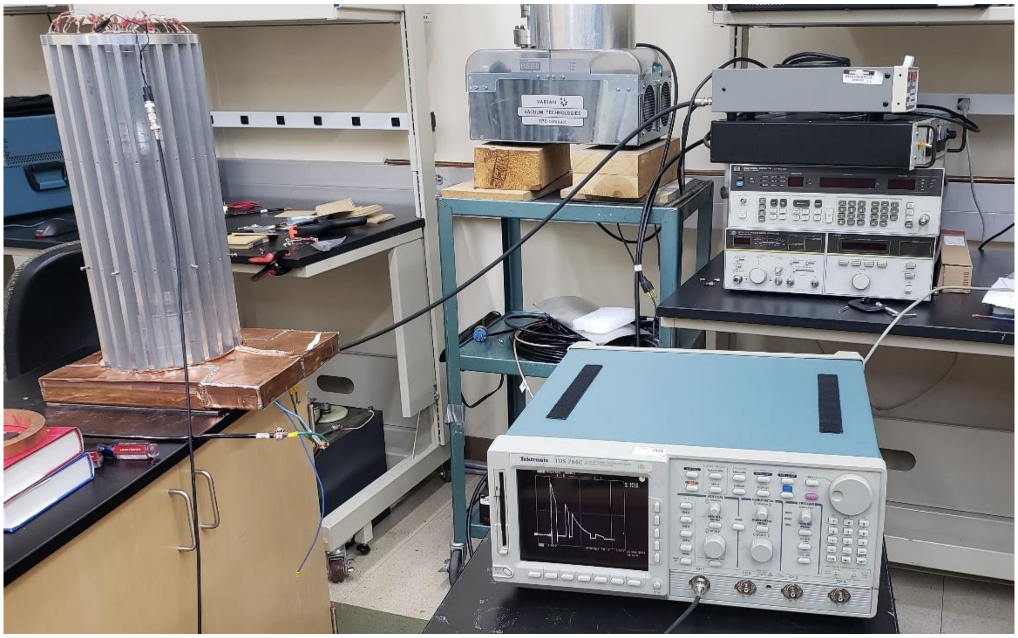

Fig. 4.5 From Section 3.3.1, an experiment was performed to fire a $12V$, $121\mu s$ pulse into the base of the mock DPF. An oscilloscope is connected across the pinch end of the mock DPF with high impedance to measure the pulse signal. This experimental result can be compared to the simulation data seen at the pinch end of the mock DPF.

By using the Curve Fitting application provided in MATLAB, a degree 9 polynomial curve with bi-square robustness is fitted onto one of the captured samples of the experimental setup from Fig. 4.5. The sample measured in the experiment and curve fit are shown in Fig. 4.6. From the experimental data, features of mechanical ground bounce exist in the signal. Thus, there is an expectation of some level of error when comparing the curve fitted data to the LTspice and MATLAB simulated data as shown in Fig. 4.6. While an error analysis can be done to demonstrate the level of error between the experimental and the simulated data, the main take away is to show that the LTspice and MATLAB data demonstrate consistency in simulated results. Further, the simulated data was able to demonstrate an ideal RC decaying pulse signal similar to that from the experiment in Section 3.3.1.

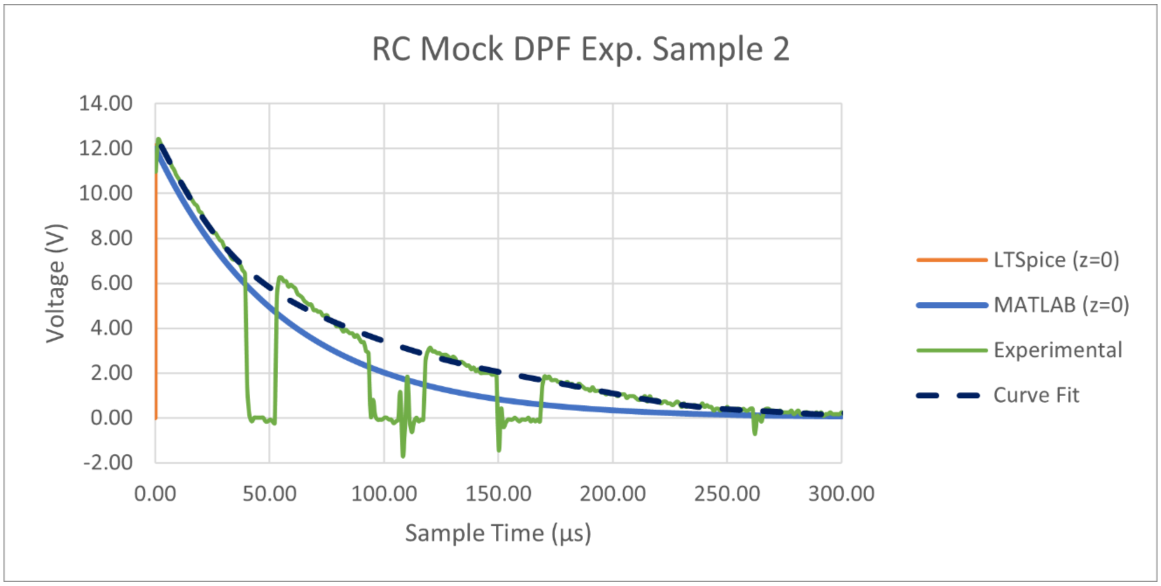

Fig. 4.6 From the Curve Fitting application provided in MATLAB, a degree 9 polynomial curve with bi-square robustness is fitted onto one of the samples (sample 2) of the mock DPF RC configuration experiment in Chapter 3 Section 3.3.1 (the experimental setup in Fig. 4.5). The experimental and curve fit data, as measured from the pinch end of the mock DPF ($z = 0$), are compared to the LTspice and MATLAB simulation data.

In the next section, the MATLAB and LTspice programs will be utilized to simulate data at a time scale closer to the 10s of nanoseconds range. At this scale, an emphasis will be placed on examining the changes that occur along the mock DPF transmission line.

4.2.2 Reflections in a Mock DPF System Simulation Results

In this section, changes in voltage and current along the mock DPF will be examined on the nanosecond time scale to place emphasis on transmission line effects. The LTspice and MATLAB programs have been adjusted for a $30ns$ sample duration. In Fig. 4.7, the LTspice transmission line circuit implements this new change. Further, the initial condition for stored energy in the capacitor has also been modified from $12V$ to $1kV$. In the previous section, a $12V$ pulse signal was used as a source during simulation to provide consistent comparison with experimental results. However, in the following experiments, a higher voltage is needed to better represent the energy levels as found in the MSTS DPF.

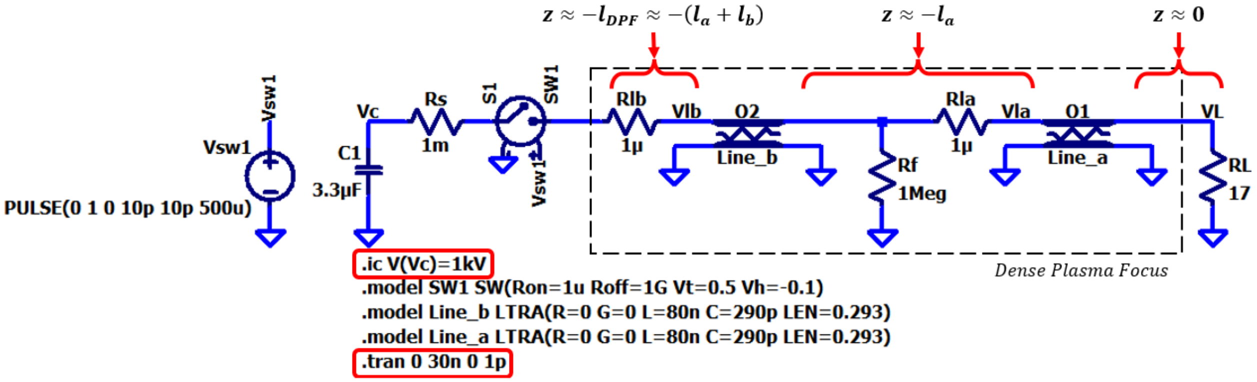

```
.ic V(Vc)=1kV
.model SW1 SW(Ron=1u Roff=1G Vt=0.5 Vh=-0.1)
.model Line_b LTRA(R=0 G=0 L=80n C=290p LEN=0.293)
.model Line_a LTRA(R=0 G=0 L=80n C=290p LEN=0.293)
.tran 0 30n 0 1p
```

Fig. 4.7 The LTspice schematic from Fig. 4.2 has been modified for changes in the sample duration of simulation and the initial voltage across the capacitor bank. For this schematic, resistors R_f and $R_L$will be modified to demonstrate six different case scenarios simulated ($R_f = 1M\Omega$, $R_f = 1m\Omega$, $R_L = 17\Omega$, $R_L = 1M\Omega$, $R_L = 1m\Omega$).

From Fig. 4.7, R_f and R_L will be modified to demonstrate six different scenarios for the mock DPF system ($R_f = 1M\Omega$, $R_f = 1m\Omega$, $R_L = 17\Omega$,$R_L = 1M\Omega$, $R_L = 1m\Omega$). Consider the case for the matched impedance system in Fig. 4.7 where $R_f = 1M\Omega$ and $R_L = 17\Omega \approx \mathcal{Z}_{DPF}$. When running the LTspice schematic using a $30ns$ transient analysis instead of $300\mu s$, different features are present on this scale. In Fig. 4.8, there is a time delay observed at different points along the mock DPF for $z = 0$, $z = -l_a$, and $z = -(l_a + l_b)$. The natural response of the system cannot be seen at the $30ns$ scale because the changes due to the natural response of the system occur very slowly relative to this $30ns$ scale. Thus, the natural response of the system appears to be DC as opposed to exponentially decaying. Further, there is negligible loss through the R_f resistor minimizing loss between both segments of the mock DPF. The time delay features seen in Fig. 4.8 are attributed to the transit time of the mock DPF. It takes time for energy to travel from one point of the mock DPF to the next point. Thus, the initial voltage and current seen at the base of the mock DPF will not be seen by the pinch end until after some time delay, “a transit time of the mock DPF”.

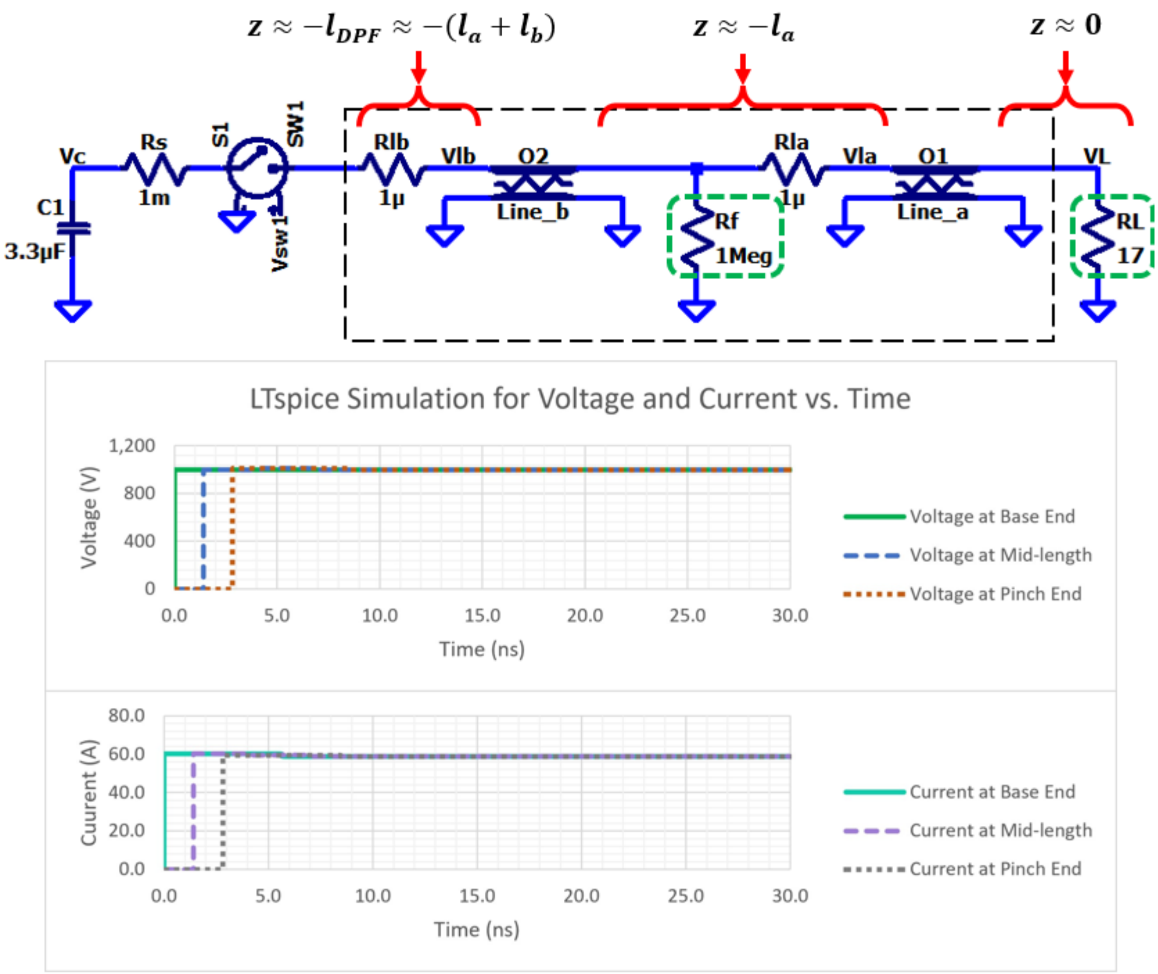

Fig. 4.8 A result is simulated by the LTspice schematic from Fig. 4.7. Resistors $R_f = 1M\Omega$ and $R_L = 17\Omega$ are chosen representing the matched impedance system case. This is similar to the LTspice schematic from Fig. 4.2 except with a smaller sample duration and different initial stored charge across the capacitor. Refer to Fig. 4.1 and Fig. 4.2. Time delay cannot be observed standing at a position of the mock DPF as energy does not reflect back in the matched impedance case. The verification in Appendix A, Section A.3, Fig. A.2 is consistent with this result.

Now consider the scenario for the resistor defined by R_f to continue being fixed at $R_f = 1M\Omega$, but modifying the load resistor R_L for the open load case ($R_L = 1M\Omega$) and the short load case ($R_L = 1m\Omega$).

Running the LTspice model for the open load case ($R_f = 1M\Omega$, $R_L = 1M\Omega$), the plot in Fig. 4.9 is obtained. In this scenario, the load impedance R_L is very large in comparison to the mock DPF characteristic impedance ($R_L \gg \mathcal{Z}_{DPF}$). However, the source impedance represented by R_s is very small in comparison to the mock DPF impedance ($R_s \ll \mathcal{Z}_{DPF}$). Hence, at the pinch end of the mock DPF at $z = 0$, the voltage changes from $0V$ to $2kV$ in a time duration where $\Delta t \approx 2.9ns$. This is a result of reflection ($\rho = +1$) seen at the mock DPF load end during the first signal incidence. The base end of the mock DPF at $z = -(l_a + l_b)$, the voltage changes from $0V$ to $1kV$ at time $t = 0$ and slowly decays but appears to be close to constant at the $30ns$ timescale. At two transits times, the direction of current changes at the base end of the mock DPF resulting in a voltage drop from $2kV$ to $0V$ at the end of the mock DPF after 4 transit times,

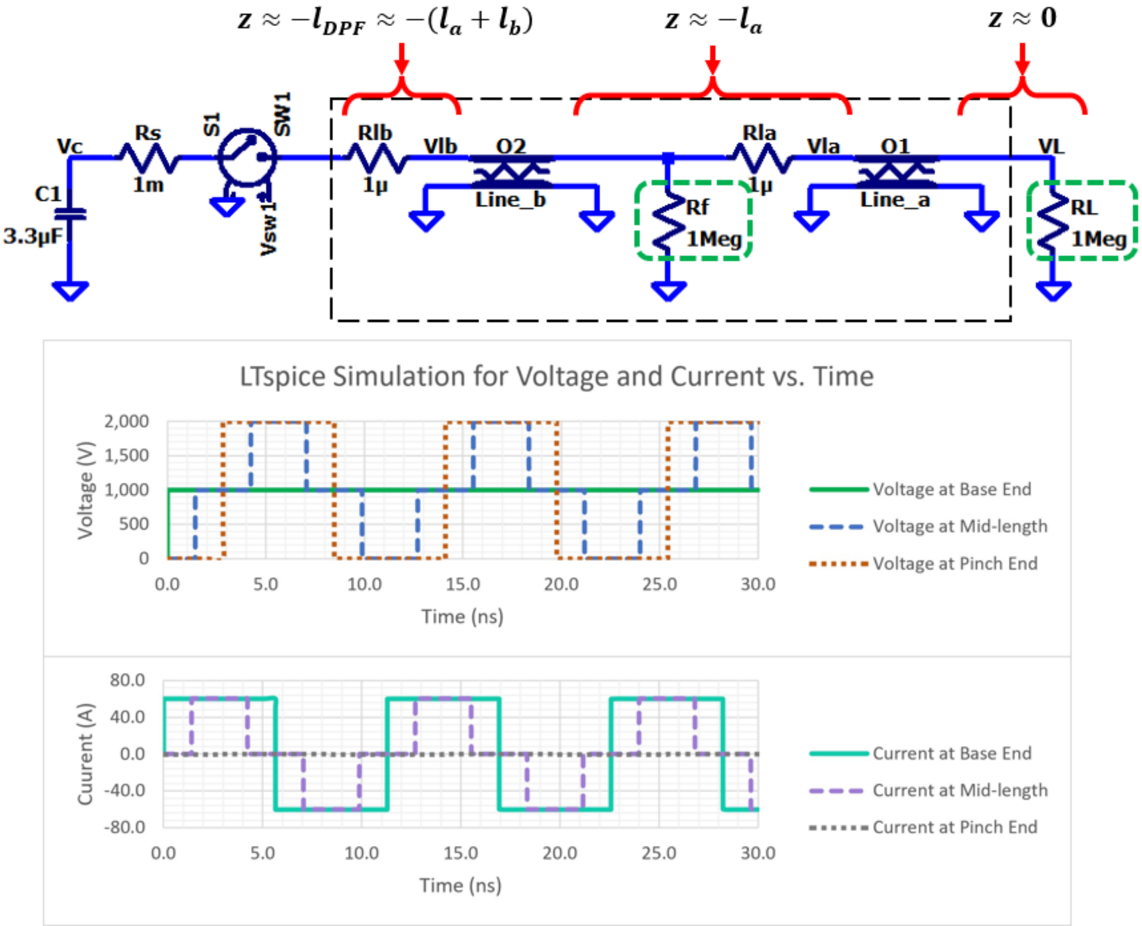

Fig. 4.9 A result is simulated by the LTspice schematic from Fig. 4.7. Resistors $R_f = 1M\Omega$ and $R_L = 1M\Omega$ are chosen representing the open load case. The result simulated by the LTspice schematic from Fig. 4.7 is obtained where resistors $R_f = 1M\Omega$ and $R_L = 1M\Omega$. This plot is representative of the open load case. At the base end of the mock DPF, the voltage changes from $0V$ to $1kV$ and slowly decays but appears approximately constant at the $30ns$ time scale. The verification in Appendix A, Section A.3, Fig. A.3 is consistent with this result.

Running the LTspice model for the short load case ($R_f = 1M\Omega$, $R_L = 1m\Omega$), the plot in Fig. 4.10 is obtained. In this scenario, the load impedance R_L and the source impedance R_s are both very small in comparison to the mock DPF characteristic impedance ($R_L \ll \mathcal{Z}_{DPF}$, $R_s \ll \mathcal{Z}_{DPF}$). At the base end of the mock DPF at $z = 0$, the voltage appears fixed at $0V$ for $t > 0$.

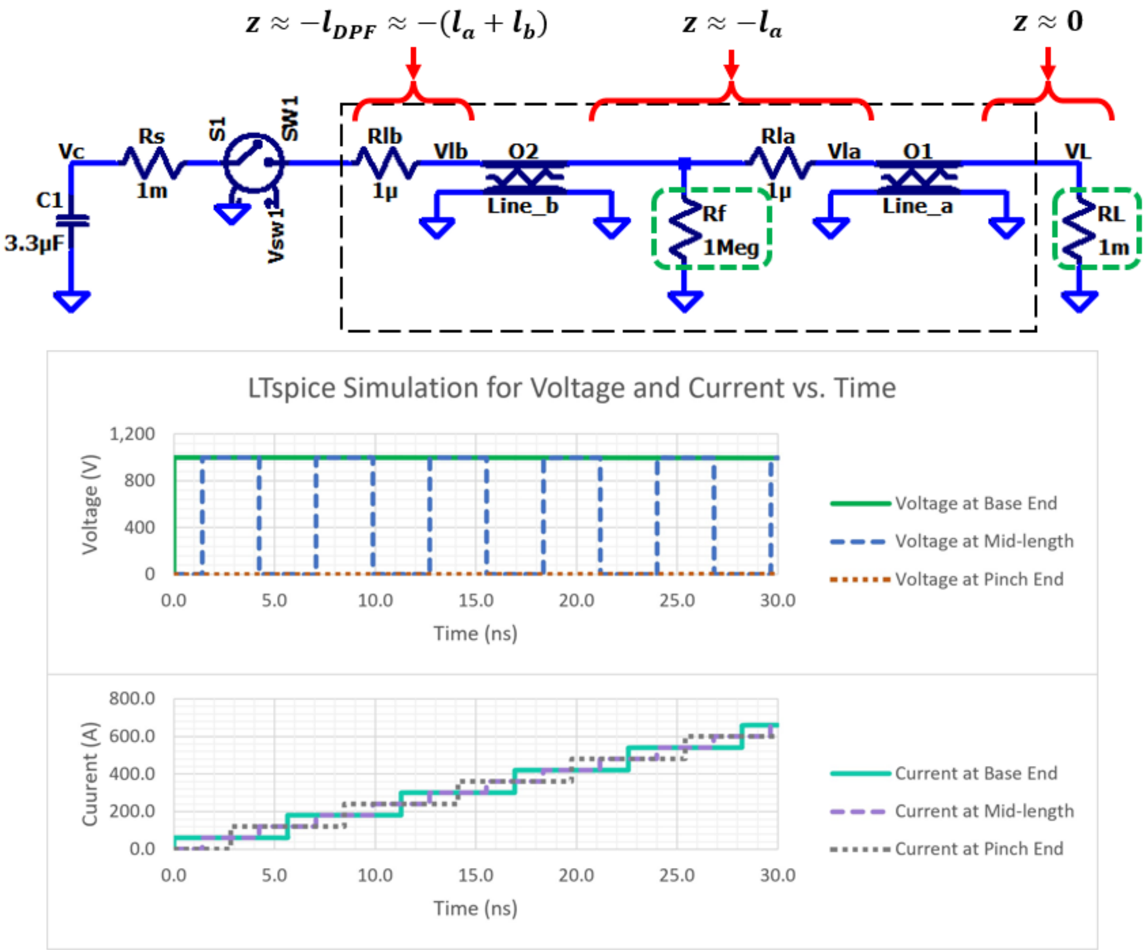

Fig. 4.10 The result simulated by the LTspice schematic from Fig. 4.7 is obtained where resistors $R_f = 1M\Omega$ and $R_L = 1m\Omega$. This plot is representative of the short load case. The current at the mid-length and the pinch end regions of the mock DPF overlap at different intervals of the signal over time. The verification in Appendix A, Section A.3, Fig. A.4 is consistent with this result.

For comparison, the MATLAB transmission line program is simulated with the same LTspice requirements from Fig. 4.8 – 4.10. These simulations are presented in Fig. 4.11 – 4.13. Notice that the results in MATLAB show some agreement in pattern. There is a loss of accuracy in the MATLAB data especially noticeable at later time instances. The simulations from MATLAB are constrained by computation time. Simulations with higher resolution data result in longer computation times that can take the duration of days based on the available resources for this effort. By reducing the computation time for these plots, a lower resolution is selected. This loss of accuracy is consistent with the limitations of the numerical inverse Laplace transform algorithm of the talbot function utilized in the MATLAB program [35]. Regardless, the MATLAB simulations show some agreement when compared to the LTspice simulations overall.

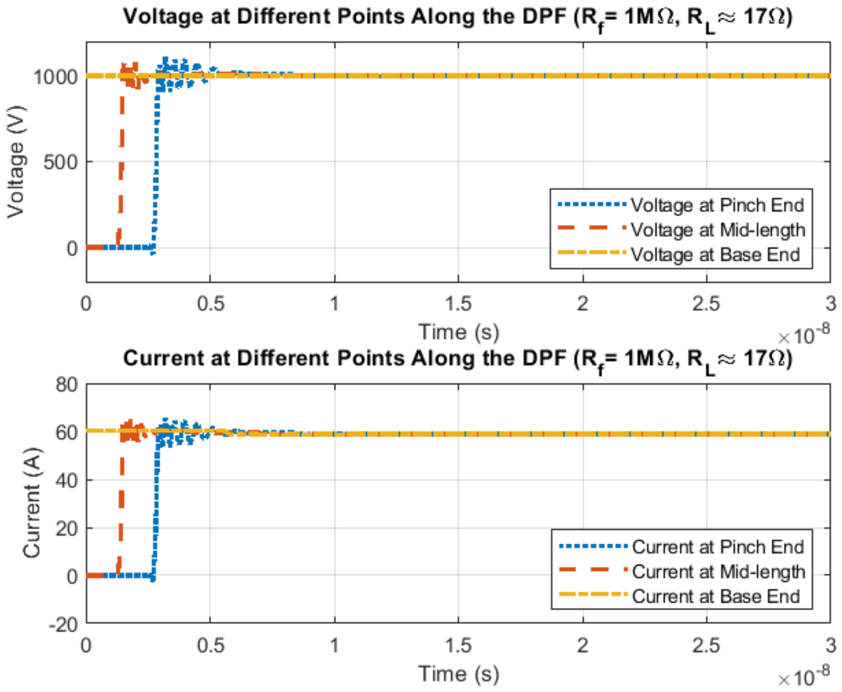

Fig. 4.11 The result simulated by the MATLAB transmission line program is presented where resistors $R_f = 1M\Omega$ and $R_L = 17\Omega$ representing the matched impedance case. Since it is matched, there are no contributions of the reflected wave, and consequently, time delay and transit times are not identifiable. The natural response of the system cannot be seen at the $30ns$ scale because the changes due to the natural response of the system occur very slowly relative to the $30ns$ scale. Thus, the natural response of the system appears to be DC as opposed to exponentially decaying.

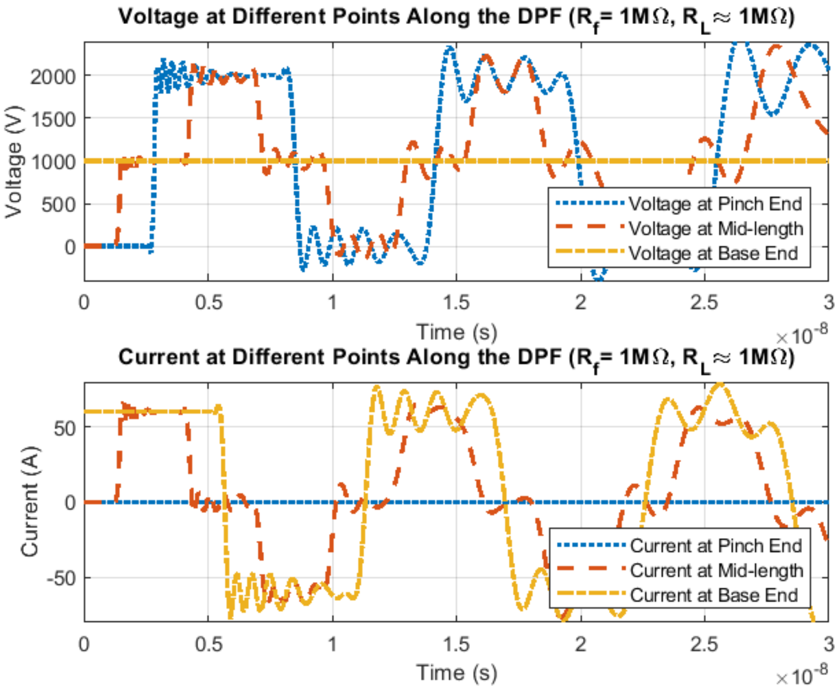

Fig. 4.12 The result simulated by the MATLAB transmission line program is presented where resistors $R_f = 1M\Omega$ and $R_L = 1M\Omega$. Notice that this is for the open load case and that accuracy of data worsens at time instances further away from time $t = 0$. The voltage appears to look like a square wave that is consistent over four transit times. The voltage at the pinch end can be shown changing from $0V$ to $2kV$ at $1\tau_{DPF}$ as a result of the open load condition ($\rho \approx +1$). At $2\tau_{DPF}$, the voltage at the base end is the sum of the initial wave, the reflected wave at the load ($\rho \approx +1$), and the reflected wave at the source ($\rho \approx -1$) resulting in $1kV$ or approximately no change. At $3\tau_{DPF}$, the voltage at the pinch end changes from $2kV$ to $0V$.

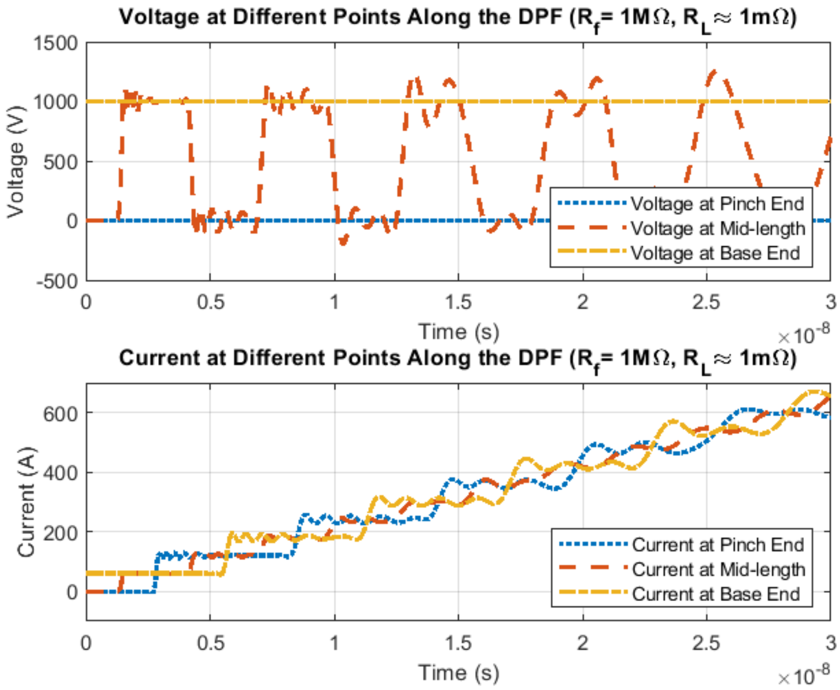

Fig. 4.13 The result simulated by the MATLAB transmission line program is presented where resistors $R_f = 1M\Omega$ and $R_L = 1m\Omega$. Notice that this is for the short load case and that accuracy of data worsens at time instances further away from time $t = 0$. The voltage at the pinch end is shown to be $0V$ at $1\ \tau_{DPF} \approx$ as a result of the short load condition ($\rho \approx -1$). At $2\tau_{DPF}$, the voltage at the base end is the sum of the initial wave, the reflected wave from the load ($\rho \approx +1$), and the reflected wave from the source ($\rho \approx +1$). Since the contribution from the load is close to none, the voltage at the base end appears approximately $1kV$ throughout the $30ns$ sample duration.

The last three scenarios simulated by the LTspice and MATLAB software provide information on the voltage and the current along the mock DPF when modifying the load end of the system R_L. However, the resistor R_f between both segments of the mock DPF was fixed at $1M\Omega$ allowing the transfer of energy from one segment of the mock DPF to the next segment. It is of interest to examine how these results change by implementing a lower impedance path due to R_f representing current loss or current redirection in the mock DPF system. Consider the same last three simulations for changing R_L, but now allow $R_f = 1m\Omega$.

In the LTspice simulation shown in Fig. 4.14, this is the matched case again similar to Fig. 4.8, but now $R_f = 1m\Omega$. Notice that the voltage and current seen at the point of R_f and at the load end R_L are zero. This is an indication that significant energy discharged from the capacitor bank is seen at the front of the mock DPF but is dissipated through the path of R_f. Hence, significant energy is lost in the system before reaching the pinch end of the mock DPF.

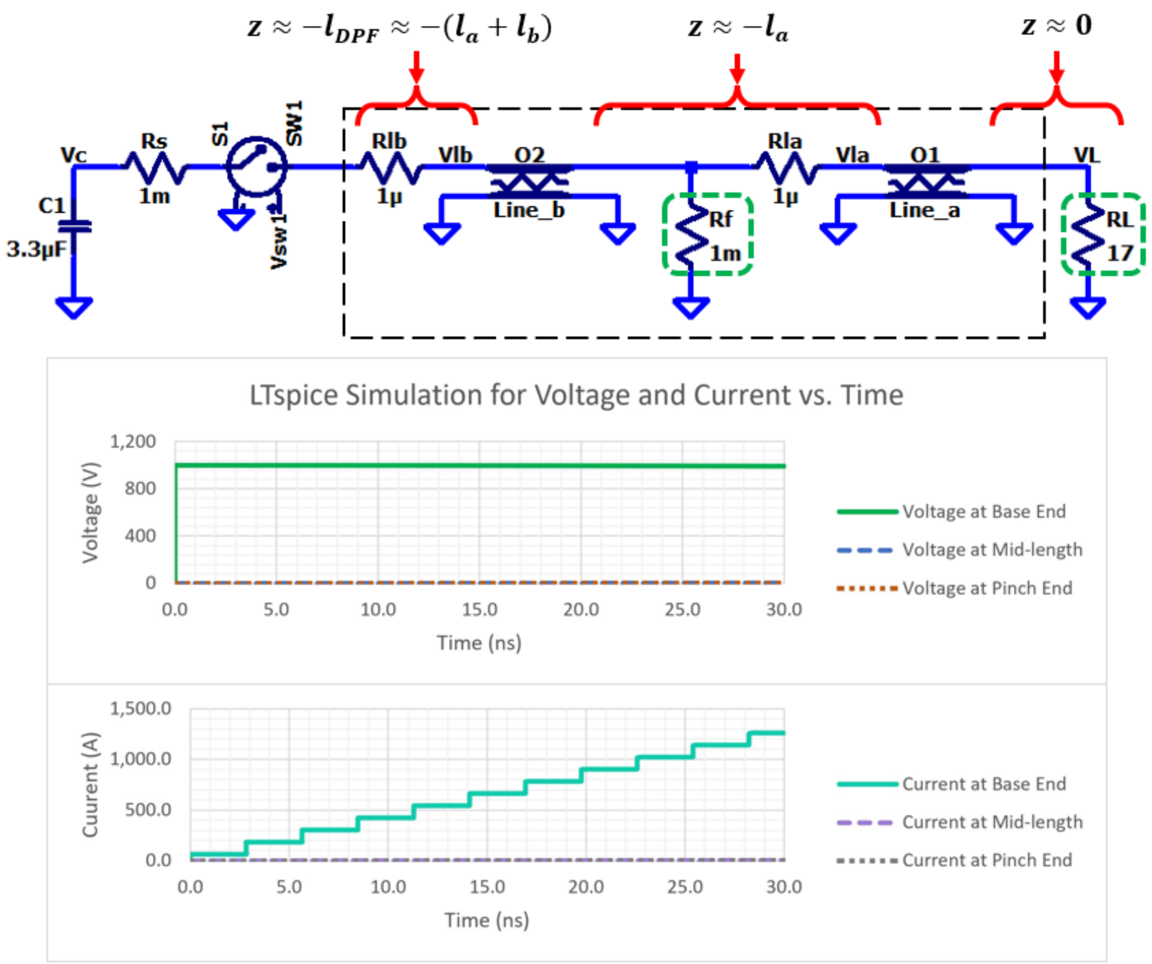

Fig. 4.14 The result simulated by the LTspice schematic from Fig. 4.7 is obtained where resistors $R_f = 1m\Omega$ and $R_L = 17\Omega$ are chosen. Notice that no voltage and current is observed at $z = -l_a$ and $z = 0$ for the mock DPF. The verification in Appendix A, Section A.3, Fig. A.5 is consistent with this result.

In the LTspice simulation shown in Fig. 4.15, this is the open load case again similar to Fig. 4.9, but now $R_f = 1m\Omega$. Notice that the path defined by R_f dissipates current from the capacitor bank. Thus, there is little to no current flow at the pinch end region.

In the LTspice simulation shown in Fig. 4.16, this is the short load case similar to Fig. 4.10. Once again, the path defined by R_f dissipates current from the capacitor bank. Thus, there is little to no current flow at the pinch end region again.

If there is a lack of current flow beyond the position of R_f along the mock DPF (as one approaches the pinch end region), then one should anticipate less field strength near the pinch end.

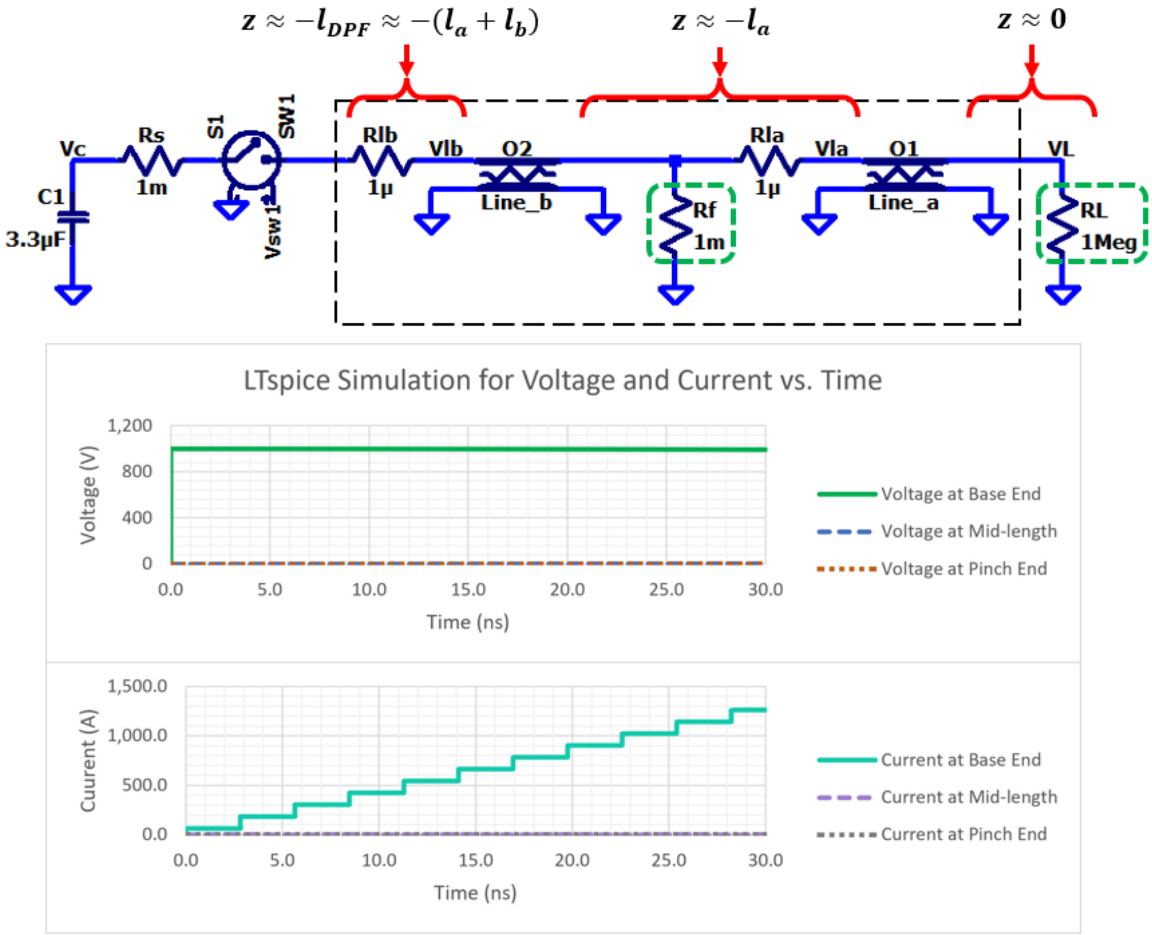

Fig. 4.15 The result simulated by the LTspice schematic from Fig. 4.7 is obtained where resistors $R_f = 1m\Omega$ and $R_L = 1M\Omega$ are chosen. Notice that no voltage and current is observed at $z = -l_a$ and $z = 0$ for the mock DPF. The verification in Appendix A, Section A.3, Fig. A.6 is consistent with this result.

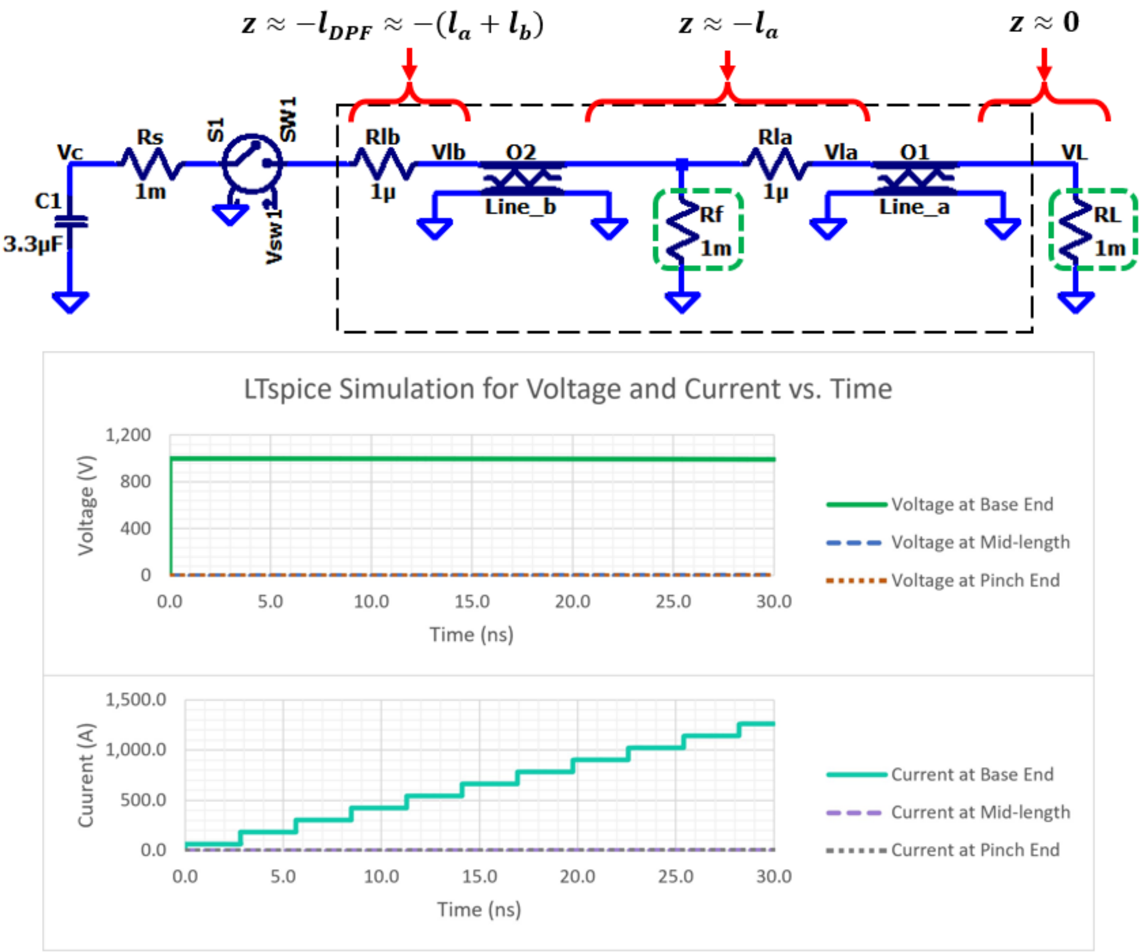

Fig. 4.16 The result simulated by the LTspice schematic from Fig. 4.7 is obtained where resistors $R_f = 1m\Omega$ and $R_L = 1m\Omega$ are chosen. Notice that no voltage and current is observed at $z = -l_a$ and $z = 0$ for the mock DPF. The verification in Appendix A, Section A.3, Fig. A.7 is consistent with this result.

For comparison, the simulations are run once again, but now with the MATLAB transmission line program. These results are provided in Fig. 4.17 – Fig. 4.19. The same conclusions can be extrapolated from the MATLAB results with the understanding that accuracy of the data is lost at time instances further away from $t = 0$.

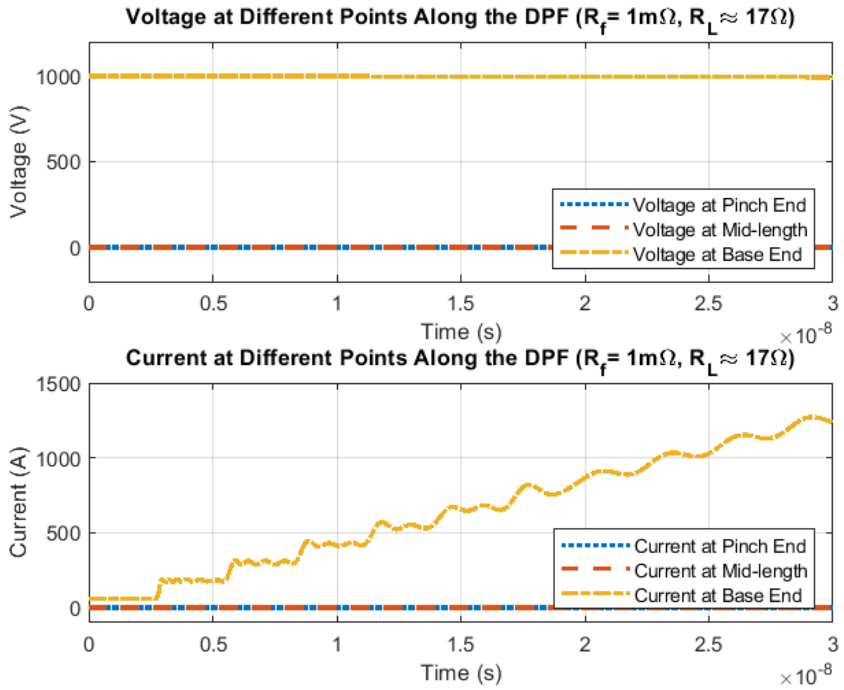

Fig. 4.17 A simulated result of the MATLAB transmission line theory computation program is obtained where resistors $R_f = 1m\Omega$ and $R_L = 17\Omega$. No voltage and current is observed at the mid-length region ($z = -l_a$) and pinch end region ($z = 0$) of the mock DPF simulation.

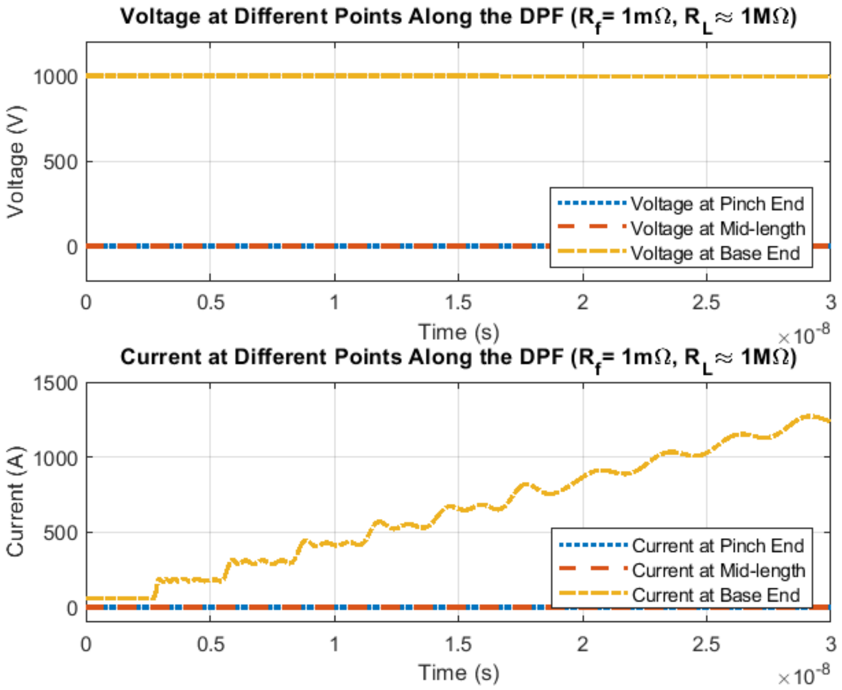

Fig. 4.18 A simulated result of the MATLAB transmission line theory computation program is obtained where resistors $R_f = 1m\Omega$ and $R_L = 1M\Omega$. No voltage and current is observed at the mid-length region ($z = -l_a$) and pinch end region ($z = 0$) of the mock DPF simulation.

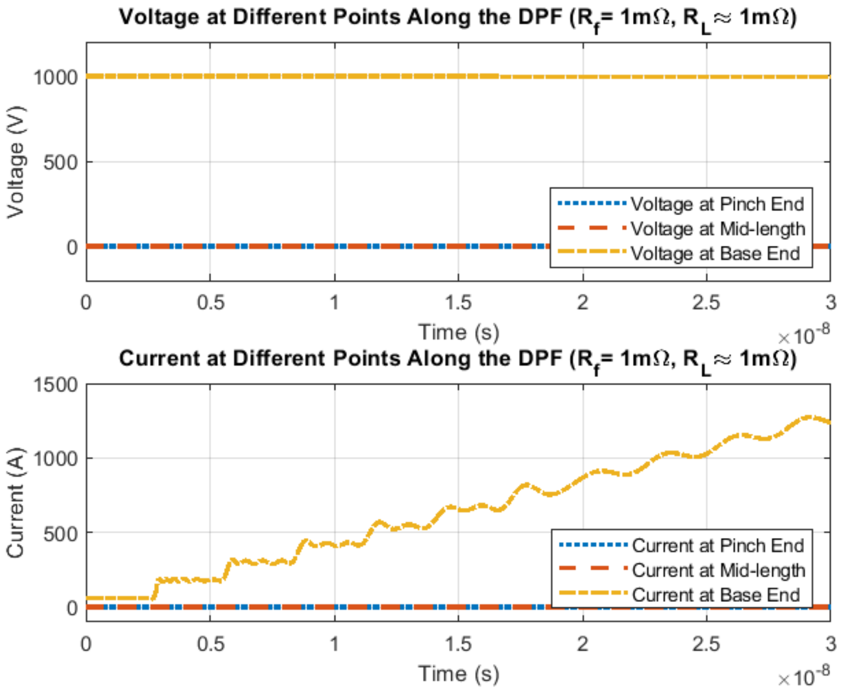

Fig. 4.19 A simulated result of the MATLAB transmission line theory computation program is obtained where resistors $R_f = 1m\Omega$ and $R_L = 1m\Omega$. No voltage and current is observed at the mid-length region ($z = -l_a$) and pinch end region ($z = 0$) of the mock DPF simulation.

The simulated data demonstrates that certain changes in voltage and current are expected along the mock DPF depending on the scenario for characterizing the load on the pinch end of the mock DPF, R_L, and the redirected current path defined by the resistive path R_f. In Section 4.3, information about the linear dipole antenna will be discussed to offer insight of the type of fields expected to be measurable from the mock DPF system. In Section 4.4, experiments using a linear dipole antenna will be examined providing comparison to the simulations explored from the LTspice and MATLAB software.

4.3 Introduction to Mock DPF Magnetic Field Theory and DPF Data

Recall from the previous section that the voltage source is changed from 12V to 1kV to meet higher energy requirements as needed in the MSTS DPF. The voltage and current information for the mock DPF is determinable for all points along the transmission line and for all time $t \geq 0$.

Previously from Chapter 2, an analysis was performed to determine what type of fields are generated from a DPF-like system provided the geometry of the DPF and the supply current is known from the system. With the supply current information now known for all z along the mock DPF and for all time t > 0. The magnetic field data can be determined from this information using the analysis from Chapter 2.

Let the mock DPF be modeled as a sum of straight, finite current filaments composing the mock DPF in a cylindrical coordinate system. Magneto static laws were used to characterize the time variation of the magnetic field. Inherently, this is allowed as long as the source current varies slowly with time. This is the quasi-static approximation. Consequently, under the quasi-static approximation, the current

$$i(\vec{r}) \approx i(\vec{r}, t) \tag{4.1}$$

$$\vec{\boldsymbol{B}}(\vec{\boldsymbol{r}}) \approx \vec{\boldsymbol{B}}(\vec{\boldsymbol{r}}, \boldsymbol{t}) \tag{4.2}$$

It is noted that the quasi-static field solutions do not satisfy Maxwell’s equations and/or boundary conditions.

4.3.1 Biot-Savart Law for a Finite, Straight Current Filament

A $1kV$ source is used to study the properties of the mock DPF. Comparisons between a $12V$ DC source and $1kV$ DC source are. The voltage and current information for the mock DPF is determinable for all points along the transmission line model for all points in time $t \geq 0$. The static magnetic field is characterized by the Biot-Savart law. The static current and static magnetic field are assumed to vary slowly as a function of time. Under this assumption, the Biot-Savart law for a slowly varying current and magnetic field can be written in integral form as

$$\vec{\boldsymbol{B}}(\vec{\boldsymbol{r}}_{\boldsymbol{p}}, \boldsymbol{t}) = \frac{\mu_0}{4\pi}\int \frac{I(\vec{\boldsymbol{r}}_{\boldsymbol{s}}, t)\,d\vec{\boldsymbol{l}}_{\boldsymbol{s}} \times \vec{\boldsymbol{R}}}{R^3} \tag{4.3}$$

where $I(\vec{r}_s, t)$ is a finite current filament; $I(\vec{\boldsymbol{r}}_{\boldsymbol{s}}, t)d\vec{\boldsymbol{l}}_{\boldsymbol{s}}$**.** The following integral forms can be used [36]:

$$\int \frac{dx}{(x^2 + a^2)^{3/2}} = \frac{x}{a^2\sqrt{x^2 - a^2}} \tag{4.4}$$

$$\int \frac{dx}{(a^2 - x^2)^{3/2}} = \frac{x}{a^2\sqrt{a^2 - x^2}} \tag{4.5}$$

$$\int \frac{dx}{(x^2 - a^2)^{3/2}} = -\frac{x}{a^2\sqrt{x^2 - a^2}} \tag{4.6}$$

Consider a finite straight filament of current

$$\vec{\boldsymbol{r}}_{\boldsymbol{p}} = r_p\hat{\boldsymbol{r}}(\boldsymbol{\varphi}_{\boldsymbol{p}}) + z_p\hat{\boldsymbol{z}} \tag{4.7}$$

$$\vec{\boldsymbol{r}}_{\boldsymbol{s}} = z_s\hat{\boldsymbol{z}} \tag{4.8}$$

$$\begin{aligned} \vec{\boldsymbol{R}} &= \vec{\boldsymbol{r}}_{\boldsymbol{p}} - \vec{\boldsymbol{r}}_{\boldsymbol{s}} \\ &= r_p\hat{\boldsymbol{r}}(\boldsymbol{\varphi}_{\boldsymbol{p}}) + z_p\hat{\boldsymbol{z}} - z_s\hat{\boldsymbol{z}} \\ &= r_p\hat{\boldsymbol{r}}(\boldsymbol{\varphi}_{\boldsymbol{p}}) + (z_p - z_s)\hat{\boldsymbol{z}} \end{aligned} \tag{4.9}$$

$$R = |\vec{\boldsymbol{R}}| = [\vec{\boldsymbol{R}} \cdot \vec{\boldsymbol{R}}]^{1/2} = \left[r_p^2 + (z_p - z_s)^2\right]^{1/2} \tag{4.10}$$

$$d\vec{\boldsymbol{l}}_{\boldsymbol{s}} = dr_s\hat{\boldsymbol{r}}(\boldsymbol{\varphi}_{\boldsymbol{p}}) + r_s d\varphi_s\hat{\boldsymbol{\varphi}}(\boldsymbol{\varphi}_{\boldsymbol{s}}) + dz_s\hat{\boldsymbol{z}} \tag{4.11}$$

$$d\vec{\boldsymbol{l}}_{\boldsymbol{s}} = dz_s\hat{\boldsymbol{z}}$$

$$\frac{\vec{\boldsymbol{R}}}{R^3} = \frac{r_p \hat{\boldsymbol{r}}(\boldsymbol{\varphi_p}) + (z_p - z_s)\hat{\boldsymbol{z}}}{\left[r_p^2 + (z_p - z_s)^2\right]^{3/2}}$$

$$\frac{d\vec{\boldsymbol{l}}_{\boldsymbol{s}} \times \vec{\boldsymbol{R}}}{R^3} = \frac{dz_s \hat{\boldsymbol{z}} \times \{r_p \hat{\boldsymbol{r}}(\boldsymbol{\varphi_p}) + (z_p - z_s)\hat{\boldsymbol{z}}\}}{\left[r_p^2 + (z_p - z_s)^2\right]^{3/2}}$$

$$\frac{d\vec{\boldsymbol{l}}_{\boldsymbol{s}} \times \vec{\boldsymbol{R}}}{R^3} = \frac{r_p \hat{\boldsymbol{\varphi}}(\boldsymbol{\varphi_p})}{\left[r_p^2 + (z_p - z_s)^2\right]^{3/2}} dz_s$$

$$d\vec{\boldsymbol{B}}(\vec{\boldsymbol{r}}_{\boldsymbol{p}}) = \frac{\mu_0 I}{4\pi}\left[\frac{r_p \hat{\boldsymbol{\varphi}}(\boldsymbol{\varphi_p})}{\left[r_p^2 + (z_p - z_s)^2\right]^{3/2}}\right] dz_s$$

$$\int d\vec{\boldsymbol{B}}(\vec{\boldsymbol{r}}_{\boldsymbol{p}}) = \vec{\boldsymbol{B}}(\vec{\boldsymbol{r}}_{\boldsymbol{p}}) = \hat{\boldsymbol{\varphi}}(\boldsymbol{\varphi_p}) \frac{\mu_0 I}{4\pi} r_p \int \frac{dz_s}{\left[r_p^2 + (z_p - z_s)^2\right]^{3/2}}$$

Integral Form

$$\int \frac{1}{(a^2 \pm x^2)^{3/2}} dx = \frac{\pm x}{a^2\sqrt{a^2 \pm x^2}} \qquad (4.12)$$

Manipulating

$$\tilde{z} = z_p - z_s \qquad (4.13)$$

$$d\tilde{z} = -dz_s$$

$$a = r_p \qquad (4.14)$$

$$x = z_p - z_s$$

$$\int \frac{dz_s}{\left[r_p^2 + (z_p - z_s)^2\right]^{3/2}} = -\int \frac{d\tilde{z}}{\left[r_p^2 + \tilde{z}^2\right]^{3/2}}$$

$$= \left[-\frac{\tilde{z}}{r_p^2\left[r_p^2 + \tilde{z}^2\right]^{1/2}}\right]_{\tilde{z}_1 = z_p - z_{s1}}^{\tilde{z}_2 = z_p - z_{s2}}$$

$$= -\frac{\tilde{z}_2}{r_p^2\left[r_p^2 + \tilde{z}_2{}^2\right]^{1/2}} + \frac{\tilde{z}_1}{r_p^2\left[r_p^2 + \tilde{z}_1{}^2\right]^{1/2}}$$

$$= -\frac{\left(z_p - z_{s2}\right)}{r_p^2\left[r_p^2 + \left(z_p - z_{s2}\right)^2\right]^{1/2}} + \frac{\left(z_p - z_{s1}\right)}{r_p^2\left[r_p^2 + \left(z_p - z_{s1}\right)^2\right]^{1/2}}$$

Combining,

$$\vec{\boldsymbol{B}}\left(\vec{\boldsymbol{r}}_{\boldsymbol{p}}\right) = \widehat{\boldsymbol{\varphi}}\left(\boldsymbol{\varphi}_{\boldsymbol{p}}\right)\frac{\mu_0 I}{4\pi} r_p \left[\frac{\left(z_{s2} - z_p\right)}{r_p^2\left[r_p^2 + \left(z_p - z_{s2}\right)^2\right]^{1/2}} + \frac{\left(z_p - z_{s1}\right)}{r_p^2\left[r_p^2 + \left(z_p - z_{s1}\right)^2\right]^{1/2}}\right] \tag{4.15}$$

$\vec{\boldsymbol{B}}$-field orientation must satisfy a Biot-Savart law, RHR.

Incorporating time into the problem, $\vec{\boldsymbol{B}}\left(\vec{\boldsymbol{r}}_{\boldsymbol{p}}\right)$ is $\vec{\boldsymbol{B}}\left(\vec{\boldsymbol{r}}_{\boldsymbol{p}}, \boldsymbol{t}\right)$ and I is $I(t)$.

4.3.2 Insight to Field Solution of Maxwell's Equations

From Section 4.2, the mock DPF system was simulated using a $1kV$ source. The voltage and current information along the mock DPF are determinable for all time $t > 0$ as examined by example through LTspice and MATLAB software. However, a linear antenna does not measure this voltage and current directly. Instead, fields are generated by the mock DPF consistent with the voltage and current patterns described in the scenarios from the previous section. This field information is capturable by the linear antenna.

Previously in Chapter 2, an analysis was performed to determine the expected field strength generated by a DPF-like system provided that the geometry of the DPF and the supply current are known in the system. With the supply current information now known for all z along the mock DPF and for all time $t > 0$, the magnetic field data can be determined from this information using the analysis from Chapter 2. However, at this point, it is not entirely known what fields are measurable by the dipole linear antenna.

Consider a simple theory that suggests how to set up the experiment to capture a time harmonic field generated by a straight wire. Consider the straight wire to be of radius $r = a$ and to be a perfect conductor. The current flowing in the z-direction is uniformly distributed in terms of φ on the surface of the wire within a handful of skin depths. That is, as the conductivity of the wire approaches infinity, the skin depth approaches zero. This implies that there is a high concentration of current on the surface of the nearly perfect conductor. Imposing azimuthal symmetry, the magnetic and electric field intensity in the region $r > a$ have the form

$$\vec{H}(\vec{r},t) = \hat{r}(\varphi)H_r(r,z)e^{j\omega t} + \hat{\varphi}(\varphi)H_\varphi(r,z)e^{j\omega t} + \hat{z}H_z(r,z)e^{j\omega t} \tag{4.16}$$

$$\vec{E}(\vec{r},t) = \hat{r}(\varphi)E_r(r,z)e^{j\omega t} + \hat{\varphi}(\varphi)E_\varphi(r,z)e^{j\omega t} + \hat{z}E_z(r,z)e^{j\omega t} \tag{4.17}$$

For $r > a$, Maxwell's Equations for Faraday's Law and Ampere's Law can be rewritten into component form assuming the time harmonic solution above.

$$\vec{\nabla} \times \vec{E}(\vec{r},t) = -\frac{\partial \vec{B}(\vec{r},t)}{\partial t} \tag{4.18}$$

$$\vec{\nabla} \times \vec{H}(\vec{r},t) = \frac{\partial \vec{D}(\vec{r},t)}{\partial t} \tag{4.19}$$

By substituting Eq. (4.16) into Eq. (4.8) and substituting Eq. (4.17) into Eq. (4.19) then produces the following components

$$-\frac{\partial E_\varphi}{\partial z} = -j\omega\mu_o H_r \tag{4.20a}$$

$$\frac{\partial H_r}{\partial z} - \frac{\partial H_z}{\partial r} = j\omega\varepsilon_o E_\varphi \tag{4.20b}$$

$$\frac{1}{r}\frac{\partial\left(rE_\varphi\right)}{\partial r} = -j\omega\mu_o H_z \tag{4.20c}$$

$$-\frac{\partial H_\varphi}{\partial z} = j\omega\varepsilon_o E_r \tag{4.21a}$$

$$\frac{\partial E_r}{\partial z} - \frac{\partial E_z}{\partial r} = -j\omega\mu_o H_\varphi \tag{4.21b}$$

$$\frac{1}{r}\frac{\partial\left(rH_\varphi\right)}{\partial r} = j\omega\varepsilon_o E_z \tag{4.21c}$$

It is observed that the fields H_φ, E_r, and E_z are mutually coupled. Further, it is observed that E_φ, H_r, and H_z are also mutually coupled. If Maxwell's equations can be solved and boundary conditions satisfied, then potential solutions exist. The field components (H_φ, E_r, E_z) are coupled to each other in a cylindrical coordinated system. From boundary conditions and a Poynting vector argument, the straight linear antenna pointing in the radial and/or z-directions may couple one or all three field components. The second set of coupled field components (E_φ, H_r, H_z) are not of interest. Initial experimental studies have indicated that such a coupling does exist. Further, it is most convenient to position the dipole antennas in the radial and/or z-direction. In Section 4.4, a series of experiments are performed to demonstrate the fields measurable by a linear dipole antenna when examining different scenarios.

4.4 Linear Antenna Experiments

A series of experiments are performed throughout this section to demonstrate how a linear antenna responds to a time varying and/or a space varying field operating in the transient, radiating and/or the non-radiating field regions. Previously in Chapter 3, two different methods of generating a pulse signal were examined. One method involved the use of an RC source. Another method involved the use of a pulse generator source. In Chapter 2, an analysis was performed to examine the voltage and current information for a two-segment transmission line for $-l_{DPF} < z < 0$ and all time $t > 0$. The transmission line is modeled by the characteristic impedance and velocity of propagation of the line. Further, a two-dimensional analysis was performed to identify the magnetic flux density external to a DPF-like device when characterizing the anode and cathode cage as line currents.

The goal of this section is to demonstrate how a linear antenna can be used to determine the location of current redirection for energy propagating along a line. These experiments include using the RC circuit and the pulse generator as sources. They also include experiments for modifying the antenna length, antenna orientation, and positioning external to an AWG 4 wire or the mock DPF.

4.4.1 Experiment 1: Modifying Linear Antenna Lengths

The influence of a linear antenna's length when exposed to time varying fields from a pulse power discharge is examined. In Fig. 4.20, an experimental setup is shown for a linear antenna facing radially external to an AWG 4 insulated wire. This linear antenna protrudes from an open-ended straight X-band waveguide that terminates to a BNC connector internally on the opposite end. A BNC cable connects this antenna to an oscilloscope's channel 2. In this experiment, a pulse generator's "output monitor" (60dB attenuated mock signal) is connected to the oscilloscope's channel 1 and used as a trigger source for capturing data.

The pulse generator's positive terminal output connects to one side of the AWG 4 wire. The negative terminal output is connected to a high voltage $R_L = 50\Omega$ ceramic resistor in series to the opposite end of the AWG 4 wire. The intention of this load resistor is to prevent distortion of the pulse generator by providing a matched impedance system. The pulse generator is set to fire an amplitude of up to $4kV$ and a pulse width of approximately $20ns$. The pulse generator is set to $4kV$ to stay within the voltage requirements of the AWG 4 wire, but large enough to be measured by the linear antenna. For experiments using the RC source configuration, $1kV$ source is used as opposed to $4kV$ to minimize damage to equipment. The RC source contains a $121\mu s$ pulse width as opposed to the pulse generator $20ns$ pulse width and thus provides longer exposure to high voltage. The internal inductance of the ceramic resistor in this experiment was not taken into consideration during the time of experiment.

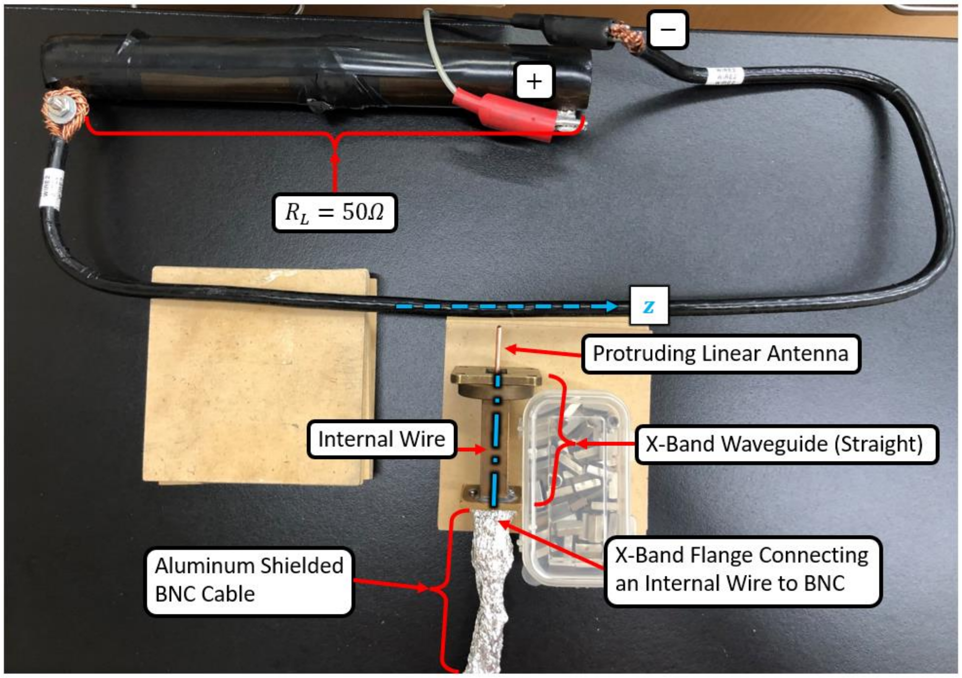

Fig. 4.20 An experimental setup is presented where an oscilloscope is connected to a linear antenna facing radially external to an AWG 4 wire. A pulse generator is set to fire a $4kV$, $20ns$ pulse signal through the AWG 4 wire system.

For this experiment, the protruding linear antenna is modified to different lengths to demonstrate the antenna length's influence when exposed to a pulse current signal from the

AWG 4 wire. Samples are taken in this experiment when the antenna is modified to lengths of: $2.2cm$, $1.0cm$, $0.3cm$, and $0cm$. In Appendix D, Section D.1, images for each antenna length setup are provided for the samples taken from this experiment. Further, oscilloscope captures are also provided for each sample. Fig. 4.21 provides one sample taken from the experiment when using a linear antenna length of $2.2cm$ external to the AWG 4 wire. From this sample, it can be demonstrated that the 60dB attenuated pulse generator signal contains a double pulse feature which is not anticipated from this experiment. It is anticipated the 50Ω wire wound ceramic load resistor in this experiment is influencing the pulse generator signal output. Despite this feature, the pulse generator output remains consistent throughout testing when only modifying the antenna length. For the redirection condition, the overall signal amplitude is anticipated to This is demonstrated in Fig. 4.22 where the pulse generator signal in channel 1 is consistent for the samples captured. In Fig. 4.23, the linear antenna connected to channel 2 demonstrates a decrease in amplitude when decreasing the length of the linear antenna used.

Tek Stopped Single Seq 1 Acqs 29 Apr 21 12:43:50

V1 : -30.0mV
V2 : -3.1V
ΔV : -3.07V

Curs1 Pos -30.0mV

Curs2 Pos -3.1V

Ch1 1.0V Ω Ch2 1.0V Ω M 20.0ns 10.0GS/s 100ps/pt
A Ch1 ⁄ 20.0mV

Fig. 4.21 Channel 1 (yellow) represents a 60dB attenuated 4kV pulse signal from the “output monitor”. Channel 2 (turquoise) represents the 2.2cm protruding linear antenna. A double pulse feature is demonstrated from channel 1 which is not anticipated and may be a result of the wire wound ceramic resistor in the AWG 4 wire circuit for this experiment.

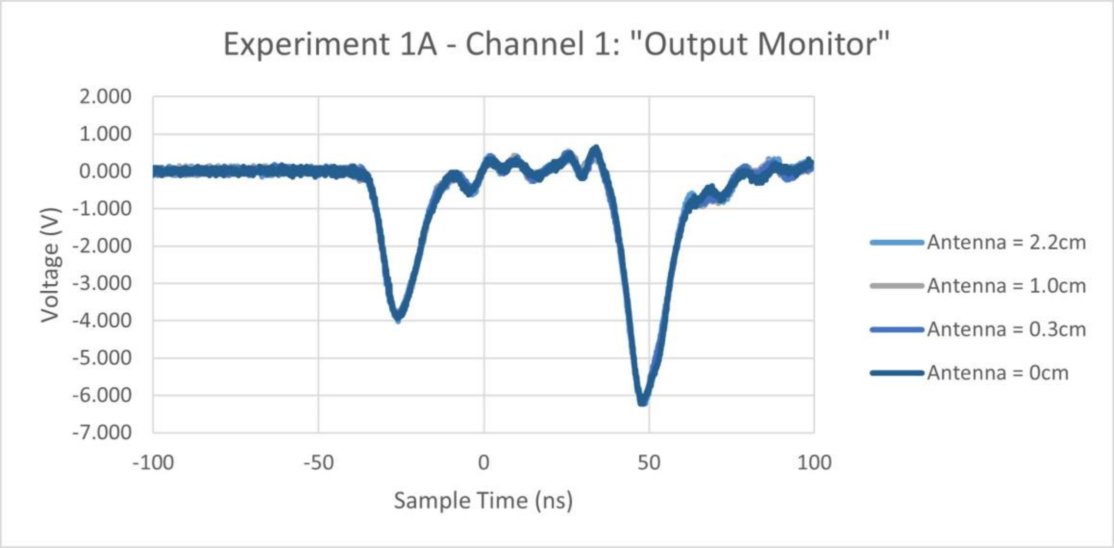

Fig. 4.22 Refer to Appendix D, Section D.1, Experiment 1A. A pulse signal is fired from a pulse generator along an AWG 4 wire. The "output monitor" of the pulse generator (60dB attenuated pulse), as measured by an oscilloscope, is consistent throughout the different samples within this experiment. A double pulse feature exists in the signal which is not anticipated and may be a result of the wire wound ceramic resistor in the AWG 4 wire circuit. In this experiment, $V_{Pulse} \approx 4kV$, $R_{Pulse} \approx 50\Omega$, and $R_L \approx 50\Omega$.

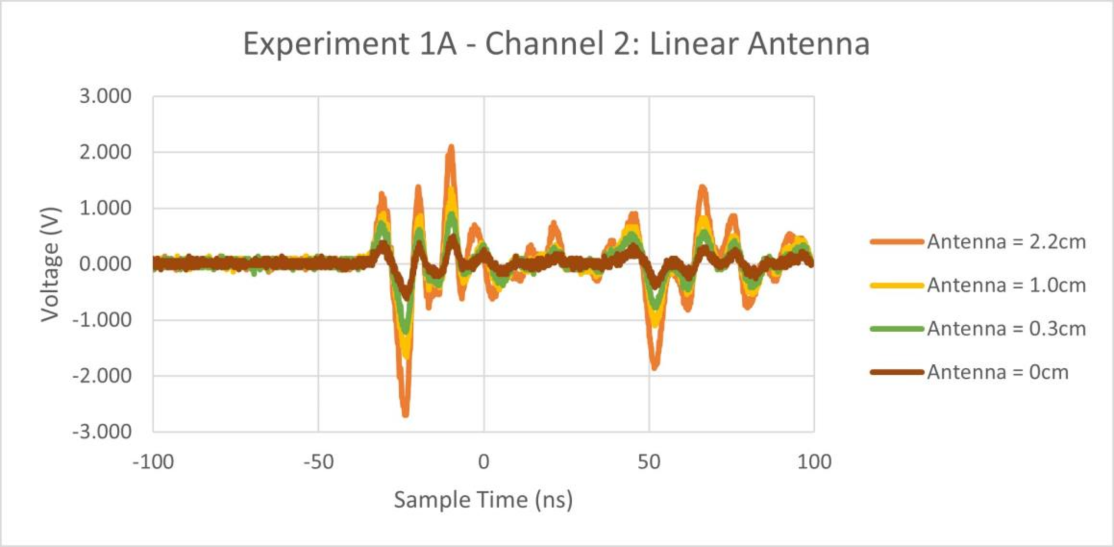

Fig. 4.23 Refer to Appendix D, Section D.1, Experiment 1A. A pulse signal is fired from a pulse generator along an AWG 4 wire. The linear antenna, as measured by an oscilloscope, demonstrates a decrease in amplitude signal when decreasing the length of the antenna. In this experiment, $V_{Pulse} \approx 4kV$, $R_{Pulse} \approx 50\Omega$, and $R_L \approx 50\Omega$.

Now, consider the same experiment, except replacing the AWG 4 wire and $R_L = 50\Omega$ load termination with the pulse generator mock DPF system from Chapter 3. The same experiment is performed again collecting 4 more samples for the different antenna lengths. A thorough collection of experimental images and oscilloscope captures are provided in Appendix D, Section D.1. Refer to Fig. 4.24. Based on channel 1 data, the 60dB pulse generator "output monitor" provides a single pulse feature. In Fig. 4.25, the linear antenna connected to channel 2 can be shown to decrease in amplitude when decreasing the length of the linear antenna. In channel 2, it is worth noting that the time-varying electromagnetic signal captured by the linear antenna appears to be different when generated by the mock DPF as compared to the AWG 4 wire. While there may be potential interest to investigate this feature, the main take away from this experiment is to demonstrate the changes in amplitude in field strength when modifying the linear antenna length. In the next section, an experiment is performed with a fixed antenna length and modifying the orientation of the linear antenna external to the AWG 4 wire.

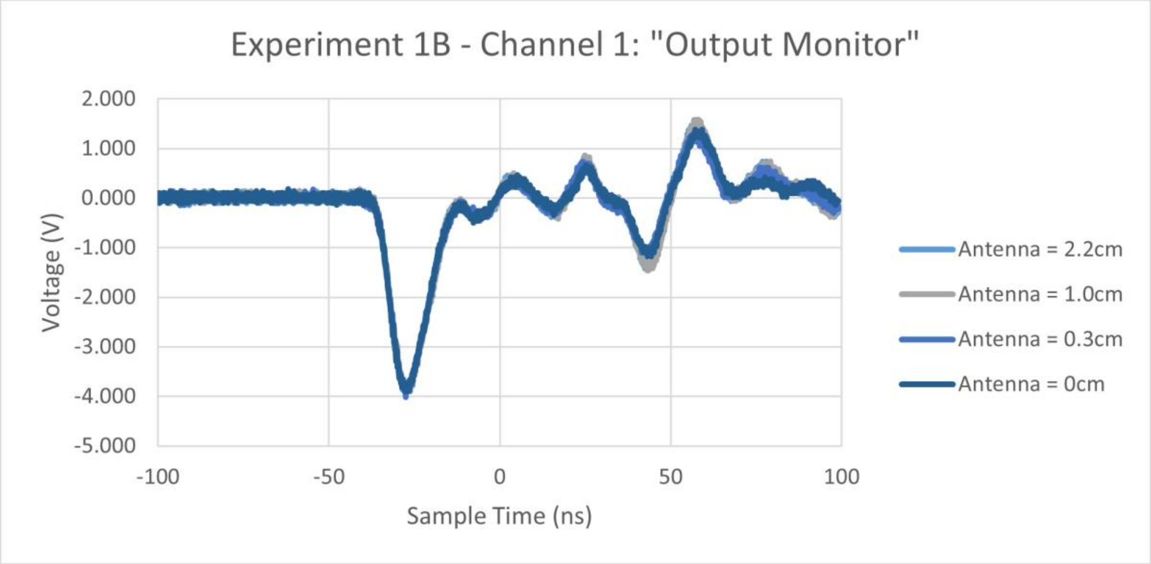

Fig. 4.24 Refer to Appendix D, Section D.1, Experiment 1B. A pulse signal is fired from a pulse generator along the mock DPF. The "output monitor" of the pulse generator (60dB attenuated pulse), as measured by an oscilloscope, is consistent throughout the different samples within this experiment. In this experiment, $V_{Pulse} \approx 4kV$, $R_{Pulse} \approx 50\Omega$, $R_1 \approx 200\Omega$, $R_2 \approx 51\Omega$, and $R_L \approx 17\Omega$. Refer to Chapter 3, Section 3.3.2 for more information on the mock DPF circuit.

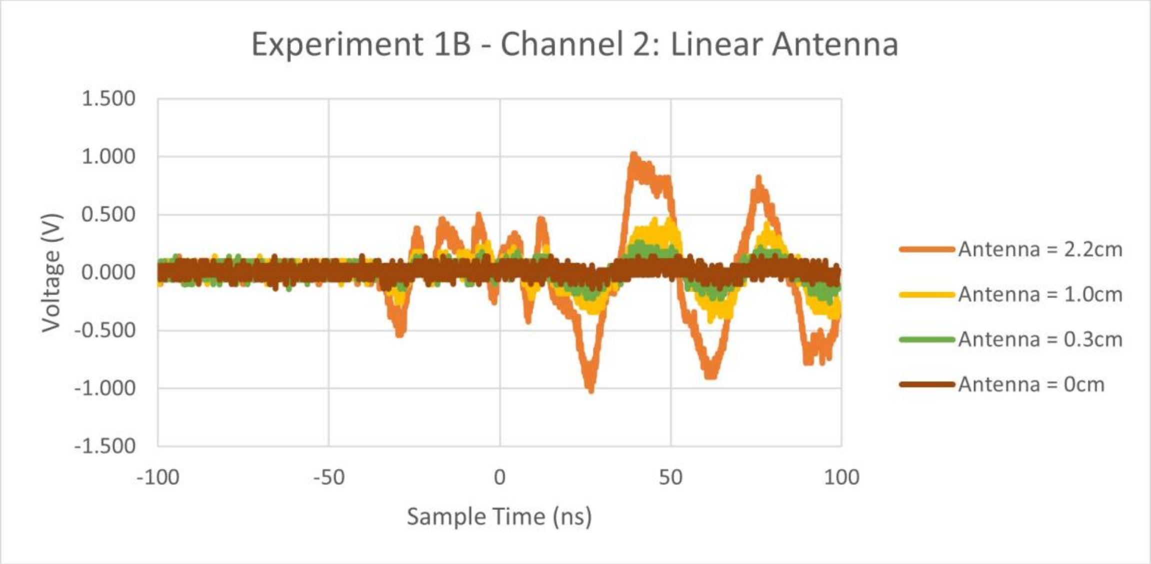

Fig. 4.25 Refer to Appendix D, Section D.1, Experiment 1B. A pulse signal is fired from a pulse generator along the mock DPF. The linear antenna, as measured by an oscilloscope, demonstrates a decrease in amplitude signal when decreasing the length of the antenna. The linear antenna is positioned outside of the cathode cage of the mock DPF. Further, the linear antenna is pointing radially inwards (for a cylindrical coordinate system) towards the mock DPF. In this experiment, $V_{Pulse} \approx 4kV$, $R_{Pulse} \approx 50\Omega$, $R_1 \approx 200\Omega$, $R_2 \approx 51\Omega$, and $R_L \approx 17\Omega$. Refer to Chapter 3, Section 3.3.2 for more information on the mock DPF circuit.

4.4.2 Experiment 2: Modifying Linear Antenna Orientations

In this section, an experiment is performed to demonstrate the influence of a linear antenna's orientation when exposed to time varying electromagnetic fields generated from a pulse discharge. The pulse discharge is generated by the *Bournlea Instruments* pulser. The current flows from the pulser through the AWG 4 insulated wire. Samples are taken by an oscilloscope when the linear antenna orientation is pointed radially towards and pointed parallel to the direction of current along the AWG 4 wire. Samples are captured for two different distances between the antenna and AWG 4 wire, that is $+2.5cm$ and $+8.3cm$.

First, an X-band waveguide structure is constructed as shown in Fig. 4.26. In this structure, a linear antenna protrudes from one of the wide walls of a straight X-band waveguide segment. Underneath the protrusion, internal to the waveguide, the linear antenna is an insulated wire that is positioned along the center of the waveguide through a curved path connecting to a flange end terminated by a BNC connector. On the opposite end of the waveguide structure is an internal antenna-based flange terminated by an SMA connector.

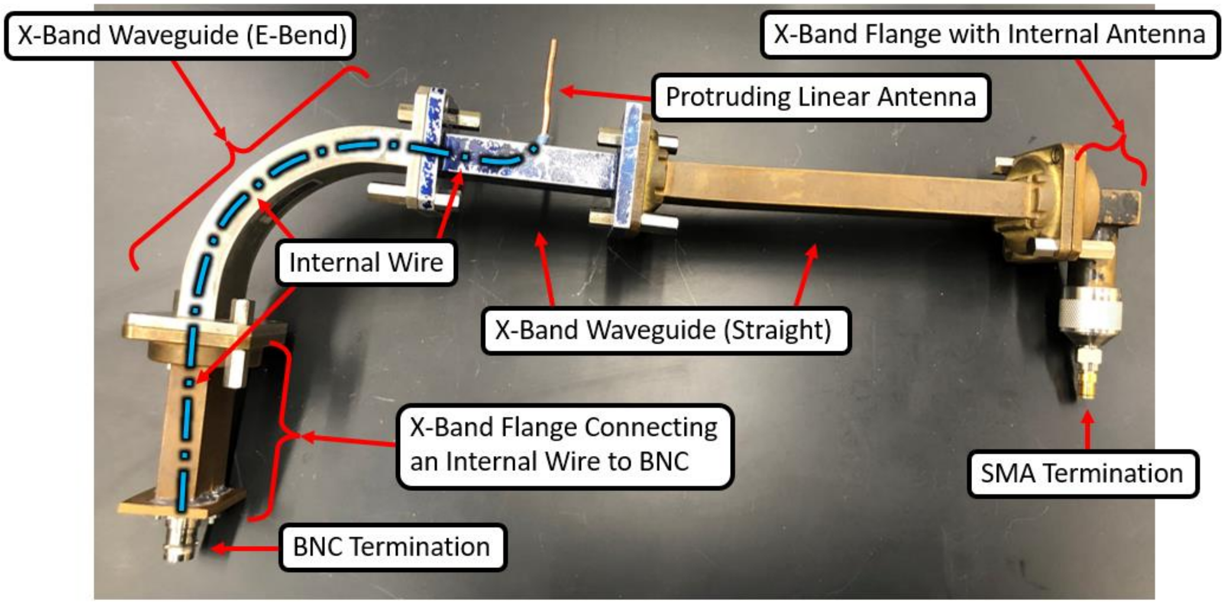

Fig. 4.26 A waveguide structure is constructed of various X-Band waveguide segments. On one flange end of the structure, a BNC termination connects to an internal insulated wire that is positioned along the center of the waveguide that is then protruded from one of the wide walls of a straight waveguide segment. On the other flange end of the structure, an SMA termination connects to an internal antenna inside the waveguide.

Similarly, to the AWG 4 wire setup from the previous section, the positive terminal of the pulse generator is connected to one side of the AWG 4 black wire connected in series with a resistor $R_L = 50\Omega$ connecting to the negative terminal of the pulse generator. Refer to Fig. 4.27. The "output monitor" of the pulse generator ($60dB$ attenuated output) is setup as a trigger source for the oscilloscope on channel 1. Allow channel 2 of the oscilloscope to connect to the SMA connector end of the waveguide structure. Channel 2 is set up to measure field changes from the internal waveguide antenna. This internal antenna faces perpendicular from the wide wall of the X-band flange. Allow channel 3 of the oscilloscope to connect to the BNC connector end of the waveguide structure. Channel 3 is set up to measure field changes from the linear antenna protruding externally to the waveguide structure. Refer to Fig. 4.26 to view the protruding linear antenna. The lengths of both cables between the antenna flanges and the oscilloscope are the same.

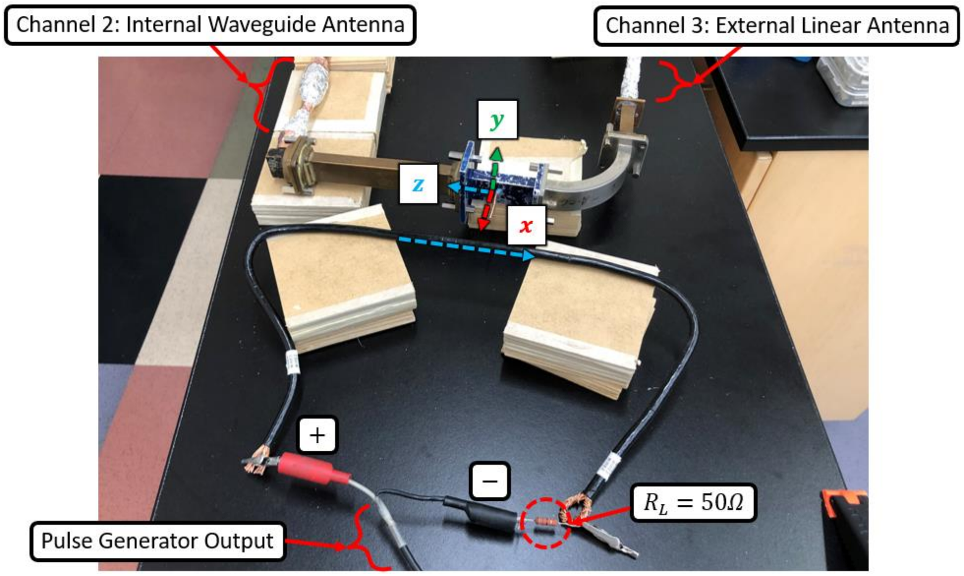

Fig. 4.27 An experimental setup is shown for generating a pulse by a pulse generator along an AWG 4 insulated wire to be observed by a linear antenna protruding externally from an X-band waveguide structure. The direction of current in the wire flows along the direction of z.

Notice that in Fig. 4.27, axes are defined in the x, y, and z directions. The z-axis is intended to be in parallel to the flow of current in the AWG 4 wire. The x and y axes are then orthogonal to the defined z-axis. For this experiment, a $4kV$, $20ns$ pulse signal is output by the pulse generator. Samples are taken by the oscilloscope when modifying the relative orientation of the linear antenna and the AWG 4 wire.

In Fig. 4.28, an example oscilloscope capture is provided by the setup presented in Fig. 4.27. From the oscilloscope capture, channel 2 connected to the internal waveguide antenna is negligible in amplitude compared to the externally protruding linear antenna. This is consistent throughout the captures in this experiment. In Fig. 4.29 (a, b), alternate setups are provided for the different relative orientations of the linear antenna to the AWG 4 wire. Samples are taken at two distances for all three provided orientations totaling up to 6 oscilloscope captures within this experiment.

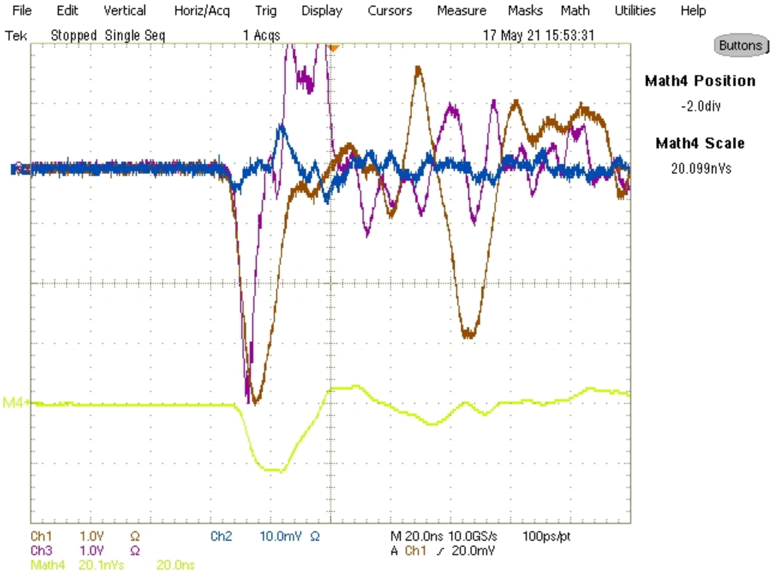

Fig. 4.28 An oscilloscope capture is provided for the experimental setup from Fig. 4.27. Channel 1 represents the 60dB attenuated pulse generator "output monitor". Channel 2 represents the antenna internal to the waveguide. Channel 3 represents the external linear antenna. Math 4 represents an integration of the channel 3 measurement.

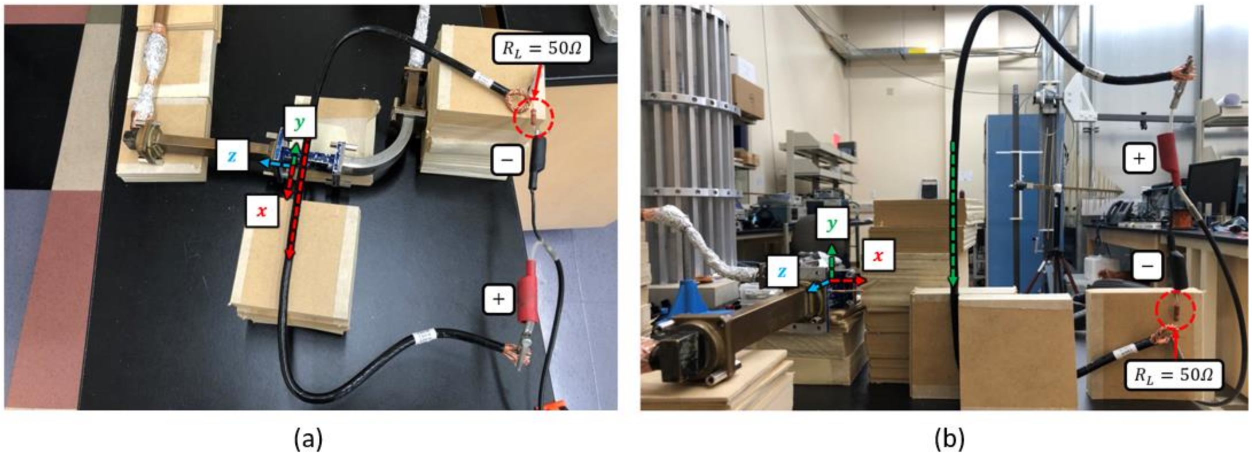

Fig. 4.29 (a, b) In addition to the experimental set up from Fig. 4.27, samples are also taken when orienting the linear antenna (a) parallel to the direction of current in the AWG 4 wire and (b) pointing radially towards the direction of current in the AWG 4 wire again.

In Fig. 4.30 – Fig. 4.32, the results for channel 3 connected to the linear antenna are provided for different orientations at two different distances. The results captured by the protruding linear antenna connected to channel 3 are summarized into plots in Fig. 4.30 – Fig. 4.32. Each plot is representative of the linear antenna orientation defined by Fig. 4.27 and Fig. 4.29 (a, b) for two different distances. Upon examination of the results, an increase in distance between the linear antenna and source current results in a decrease in amplitude measurements.

From Fig. 4.30 – Fig. 4.32, the signal measured by the linear antenna has a peak amplitude at $2.5cm$ distance between the antenna and AWG 4 wire. At $8.3cm$ distance, the peak amplitude is decreased, but the features of the signal remain similar. However, for the redirection condition, almost total attenuation is anticipated from the signal. Thus, this experiment is not an indicator of recreating a redirection condition.

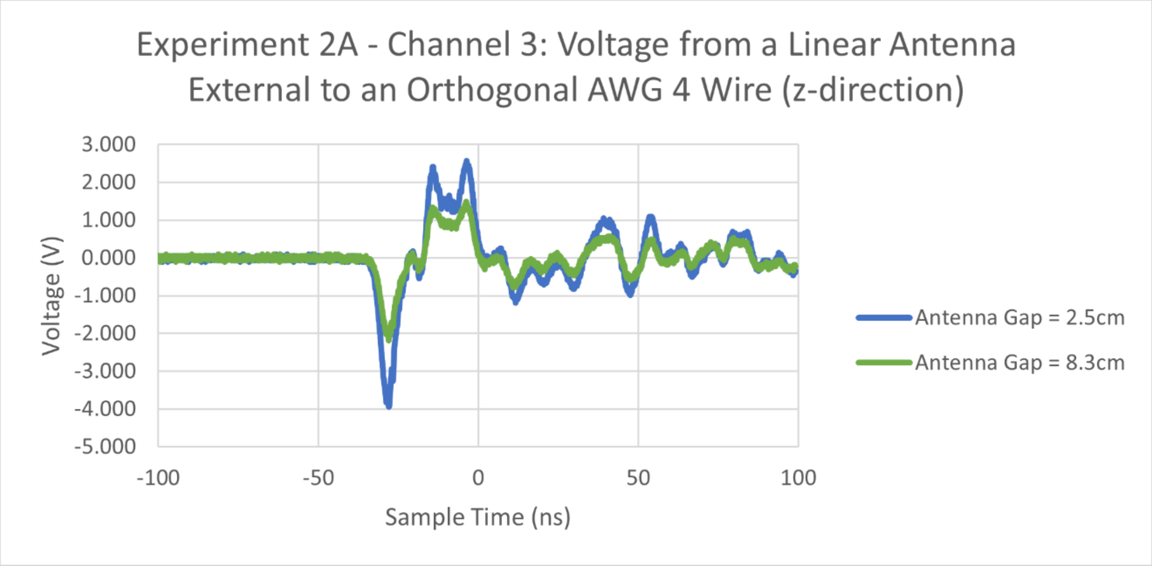

Fig. 4.30 Within this experiment, there is a decrease in amplitude signal when increasing the gap between the linear antenna and the AWG 4 wire. The AWG 4 wire is oriented orthogonally (in the z-direction) to the linear antenna.

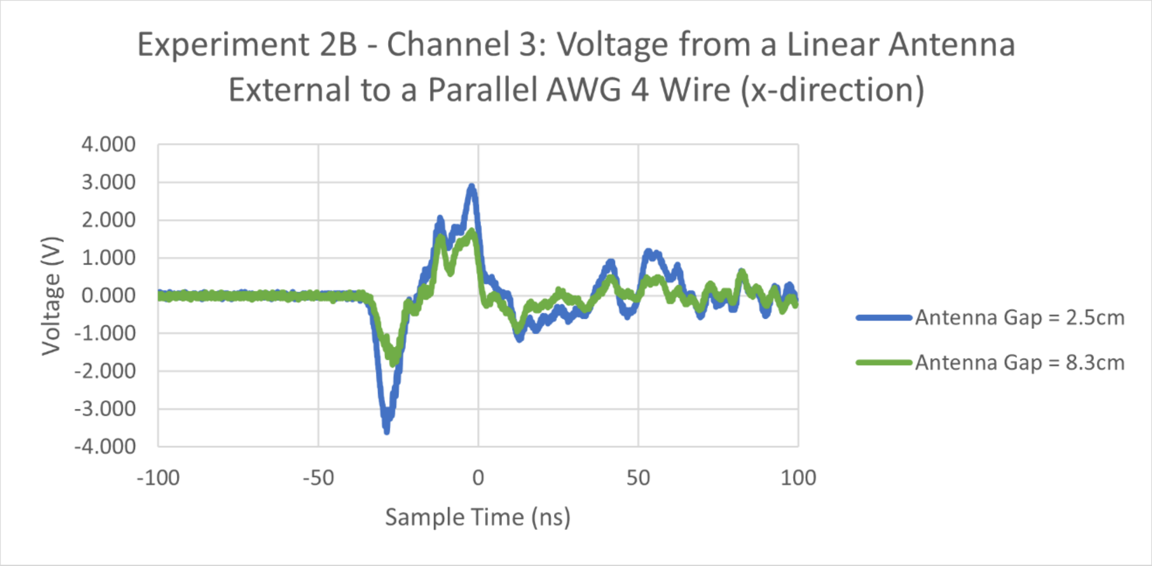

Fig. 4.31 Within this experiment, there is a decrease in amplitude signal when increasing the gap between the linear antenna and the AWG 4 wire. The AWG 4 wire is oriented in parallel (x-direction) to the linear antenna.

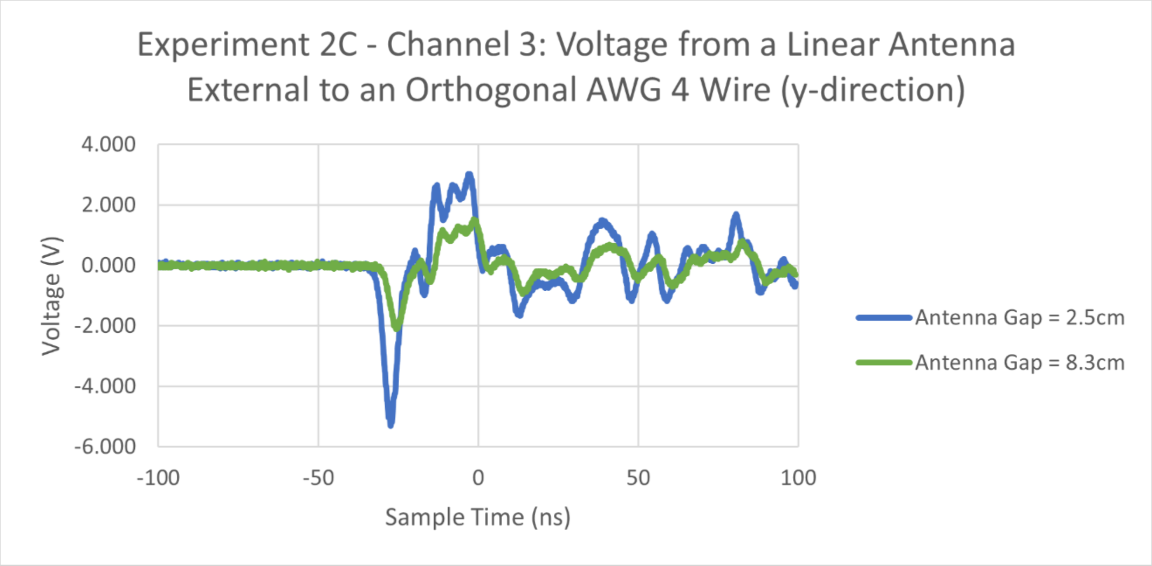

Fig. 4.32 Within this experiment, there is a decrease in amplitude signal when increasing the gap between the linear antenna and the AWG 4. The AWG 4 wire is oriented orthogonally (in the y-direction) to the linear antenna.

To summarize the results captured within this experiment, data has been recorded into Table 4.1 for all channels when arranging the wire in the different orientations and distances relative to the linear antenna. From the data captured in this experiment, it is demonstrated that a signal is measurable from the linear antenna when facing radially towards the AWG 4 wire or in parallel. This information is consistent with the theory from Section 4.3 in which fields are expected to be seen by a linear antenna when facing radially towards the source current. For the rest of the experiments in this section, a linear antenna will be used to face radially towards the current source for measurements. Field data observed by a linear antenna when in parallel to the direction of source current in a mock DPF may present an opportunity for future investigation involving different modes of the linear antenna.

In the next section, an experiment is performed when positioning the linear antenna orthogonal to the AWG 4 wire at different points along a fixed axis where the AWG 4 wire has a bend.

Table 4.1 A $4kV$, $20ns$ pulse is generated through an AWG 4 wire system in which measurements are captured by an external linear antenna and internal waveguide antenna. A summary of the results is provided.

		Experiment 2: Changing Orientation of a Linear Antenna External to an AWG 4 Wire		
		Channel 1	Channel 2	Channel 3
Antenna to AWG 4 Wire Orientation	Antenna and AWG 4 Wire Gap	Pulse Generator (60dB Attenuated) "Output Monitor"	Internal Waveguide Linear Antenna	External Linear Antenna
Orthogonal (z-direction)	+2.5cm	-3.9V (Min)	0.1mV (Mean)	-3.9V (Min)
	+8.3cm	-4.0V (Min)	0.0mV (Mean)	-2.2V (Min)
Parallel (x-direction)	+2.5cm	-4.0V (Min)	0.1mV (Mean)	-3.6V (Min)
	+8.3cm	-4.0V (Min)	0.1mV (Mean)	-1.8V (Min)
Orthogonal (y-direction)	+2.5cm	-4.0V (Min)	0.1mV (Mean)	-5.3V (Min)
	+8.3cm	-4.0V (Min)	0.1mV (Mean)	-2.1V (Min)

4.4.3 Experiment 3: Modifying Linear Antenna Positioning Along an AWG 4 Wire (Pulse Generator)

Similar to the waveguide linear antenna structure used in the previous section, another experiment is performed to demonstrate diversion of current when translating a linear antenna along a fixed axis in the z-direction. In Fig. 4.33, the protruding linear antenna is vertically aligned along an approximate 90° bend of the AWG 4 wire. The linear antenna from this position will then be translated along a fixed axis in the z-direction. At the 90° bend, this position will be identified as the $z = 0$ position. Samples are taken along the fixed axis in the z-direction for $z = 0$, $z = 2.5cm$, $z = 7.6cm$, and $z = 15.2cm$. When firing a $4kV$, $20ns$ pulse from the pulse generator into the AWG 4 wire system, then the linear antenna channel 3 results are captured and provided in Fig. 4.34 for the different positions. The voltage readings for channels 1 – 3 are recorded in Table 4.2. Additionally, in Appendix D, Section D.3, images for the experiment and oscilloscope captures are provided.

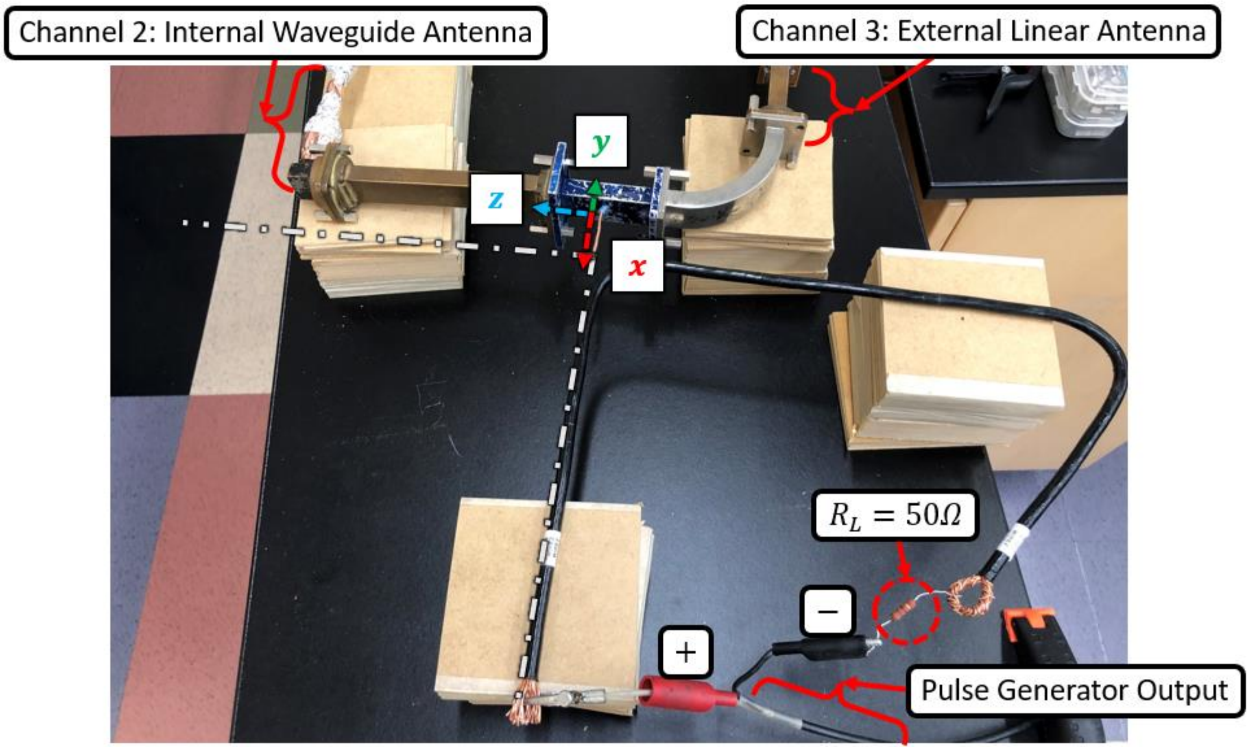

Fig. 4.33 The experimental setup is shown for generating a pulse by a pulse generator along an AWG 4 wire to be observed by a protruding external linear antenna from the X-band waveguide structure. Samples are taken when translating the linear antenna along a fixed axis in the z-direction.

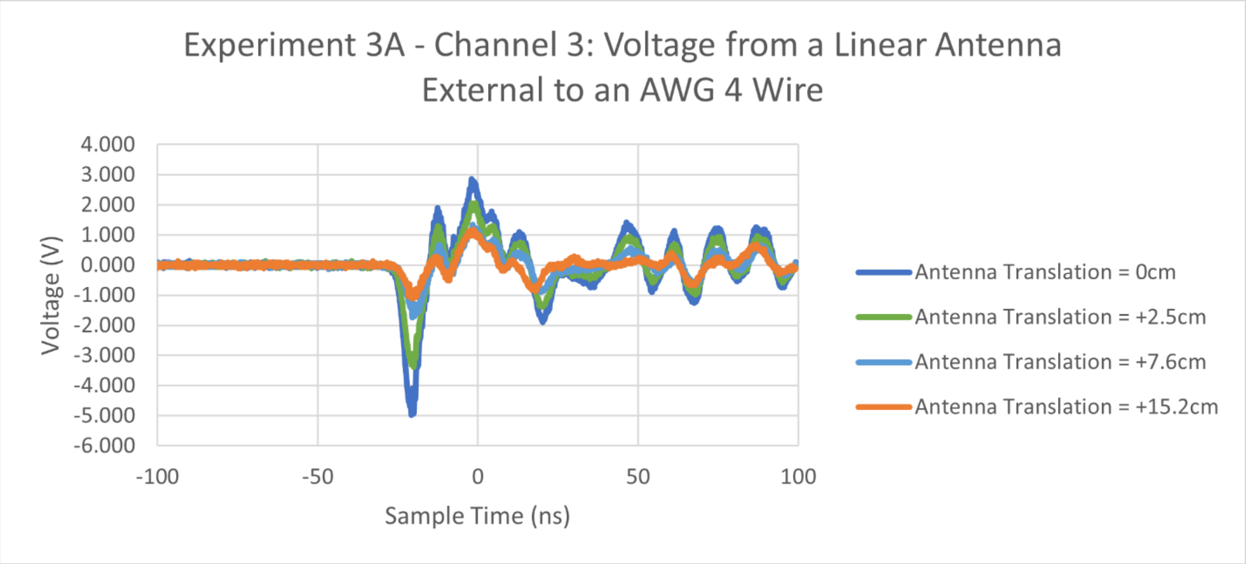

Fig. 4.34 The results captured by the linear antenna, external to the AWG 4 wire system and translated along a fixed axis in the z-direction, are provided. As the antenna moves further away from the AWG 4 wire, the measured signal decreases in amplitude.

Table 4.2 A linear antenna aligns with the radial axis of an AWG 4 current source and is translated along a fixed axis parallel to the direction of current. The AWG 4 wire has a 90° bend defined as the $z = 0$ position for this experiment. From this experiment, a trend of decreasing amplitude signal from channel 3 can be extrapolated when translating the linear antenna on a fixed axis further away from the AWG 4 wire during pulse fire.

	Experiment 3A: Translating Linear Antenna along z-direction w/ approximate +2.5cm Linear Antenna length and AWG 4 Wire Gap		
	Channel 1	Channel 2	Channel 3
Antenna z-direction Translation	Pulse Generator (60dB Attenuated) “Output Monitor”	Internal Waveguide Linear Antenna	External Linear Antenna
0cm	-3.9V (Min)	0.1mV (Mean)	-5.0V (Min)
+2.5cm	-3.9V (Min)	0.1mV (Mean)	-3.4V (Min)
+7.6cm	-3.9V (Min)	0.1mV (Mean)	-1.7V (Min)
+15.2cm	-4.0V (Min)	0.1mV (Mean)	-1.1V (Min)

In line with physics, the captured data suggests that as the linear antenna aligns with the radial axis of the AWG 4 wire current source and is translated further away along a fixed axis, there is a decrease in the measured signal amplitude as demonstrated by the oscilloscope channel 3 results. As the antenna translation in the z-direction moves further away from the AWG 4 wire, the measured signal decreases in negative peak voltage amplitude. From channel 1, the measured voltage has a consistent negative voltage peak (minimum) of about $-3.9V$ or a source voltage of $-3.9kV$ without attenuation. From channel 2, a small voltage mean signal is measured by the antenna internal to the waveguide indicating a measurement of evanescent waves.

Now consider the same experiment, except that the linear antenna is measuring from the opposite side closer to the negative terminal of the pulse generator. There is an added gap between the axis of the AWG 4 source current, but samples are collected when translating the linear antenna along a fixed axis. This experimental setup is provided in Fig. 4.35 and results collected and provided into Fig. 4.36 for the linear antenna. Additionally, results are summarized in Table 4.3.

From the Table 4.3 oscilloscope channel 3 results, the linear antenna aligning with the radial axis of the AWG 4 wire current source is translated along the z-axis closer to the AWG 4 wire. As the linear antenna approaches the AWG 4 wire, there is an increase in the measured signal peak amplitude from $-2.2V$ to $-4.9V$. When the linear antenna radially external to the AWG 4 wire continues to translate, there is a small increase in voltage from $-4.9V$ to $-5.2V$. From channel 1, the measured voltage has a consistent negative voltage peak (minimum) of about $-4.0V$ or a source voltage of $-4.0kV$ without attenuation. From channel 2, a small voltage mean signal is measured by the antenna internal to the waveguide indicating a measurement of evanescent waves.

From the results, it can be shown that when external to the AWG 4 wire, the amplitude is almost consistent. When moving away from the AWG 4 wire along the fixed axis, then the amplitude begins to decrease again. This suggests that the linear antenna is able to detect this change when current is being diverted in direction due to the bend in the AWG 4 wire. This will be similar to the case in which current redirection will occur in a dense plasma focus system as energy is lost through an alternate path in the system.

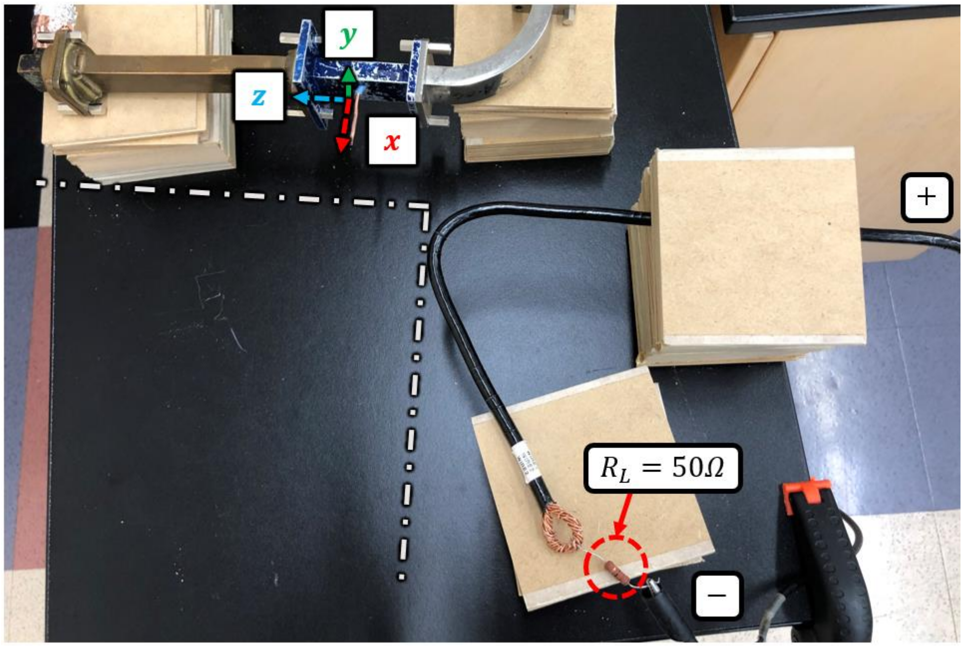

Fig. 4.35 The experimental setup is shown for generating a pulse by a pulse generator along an AWG 4 wire to be observed by a protruding external linear antenna from the X-band waveguide structure. Samples are taken when translating the linear antenna along a fixed axis in the z-direction.

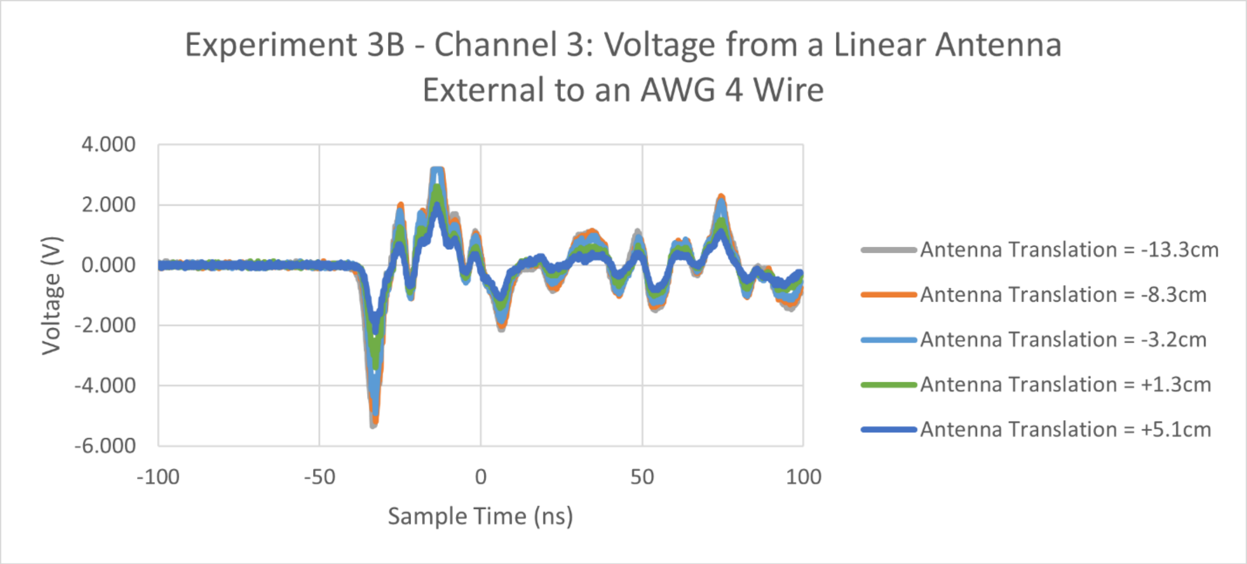

Fig. 4.36 The results captured by the linear antenna, external to the AWG 4 wire system and translated along a fixed axis in the z-direction, are provided. As the antenna moves further away from the AWG 4 wire, the measured signal decreases in amplitude.

Table 4.3 A linear antenna aligns with the radial axis of an AWG 4 current source and is translated along a fixed axis parallel to the direction of current. The AWG 4 wire has a $< 90°$ bend defined as the $z = 0$ position for this experiment. From this experiment, there is a decrease in amplitude signal when translating the linear antenna on a fixed axis further away from the AWG 4 wire during firing a pulse signal.

	Experiment 3B: Translating Linear Antenna along z-direction w/ approximate +2.5cm Linear Antenna length and AWG 4 Wire Gap		
	Channel 1	Channel 2	Channel 3
Antenna z-direction Translation	Pulse Generator (60dB Attenuated) “Output Monitor”	Internal Waveguide Linear Antenna	External Linear Antenna
+5.1cm	-4.0V (Min)	0.0mV (Mean)	-2.2V (Min)
+1.3cm	-4.0V (Min)	0.0mV (Mean)	-3.4V (Min)
-3.2cm	-4.0V (Min)	0.0mV (Mean)	-4.9V (Min)
-8.3cm	-4.0V (Min)	0.0mV (Mean)	-5.2V (Min)
-13.3cm	-4.0V (Min)	0.0mV (Mean)	-5.3V (Min)

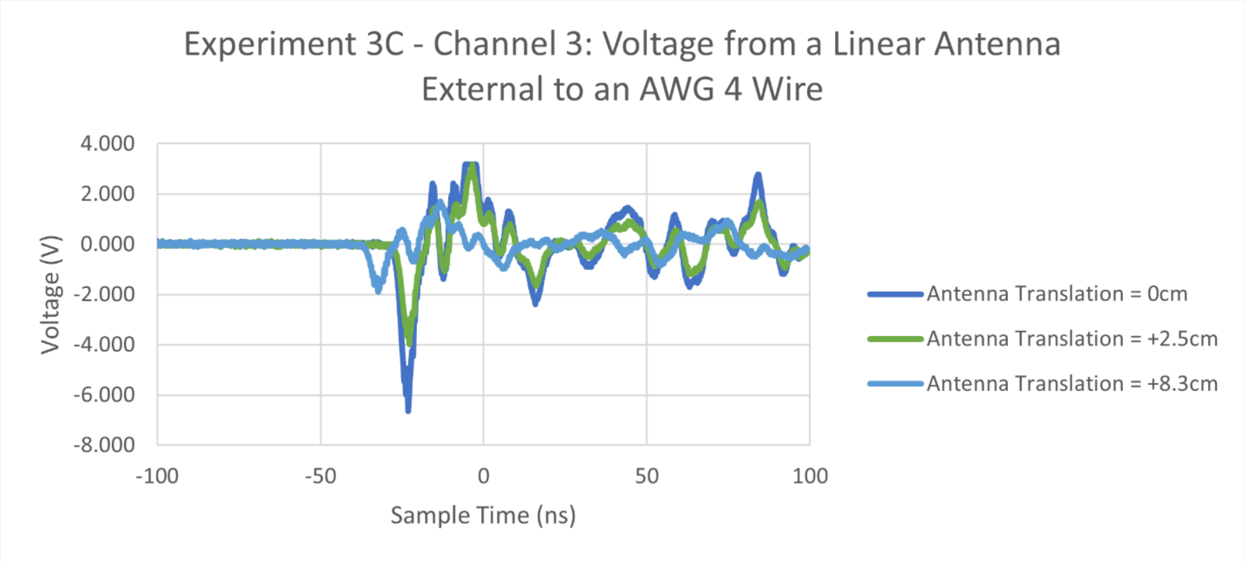

Fig. 4.37 The results captured by the linear antenna, external to the AWG 4 wire system and translated along a fixed axis in the z-direction, are provided. As the antenna moves further away from the AWG 4 wire, the measured signal decreases in amplitude.

Table 4.4 From this experiment, there is a decrease in amplitude signal when translating the linear antenna on a fixed axis further away from the AWG 4 wire during firing a pulse signal.

	Experiment 3C: Translating Linear Antenna along z-direction w/ approximate +2.5cm Linear Antenna length and AWG 4 Wire Gap		
	Channel 1	Channel 2	Channel 3
Antenna z-direction Translation	Pulse Generator (60dB Attenuated) “Output Monitor”	Internal Waveguide Linear Antenna	External Linear Antenna
0cm	-4.0V (Min)	0.1mV (Mean)	-6.6V (Min)
+2.5cm	-4.0V (Min)	0.0mV (Mean)	-4.0V (Min)
+8.3cm	-4.0V (Min)	0.1mV (Mean)	-1.9V (Min)

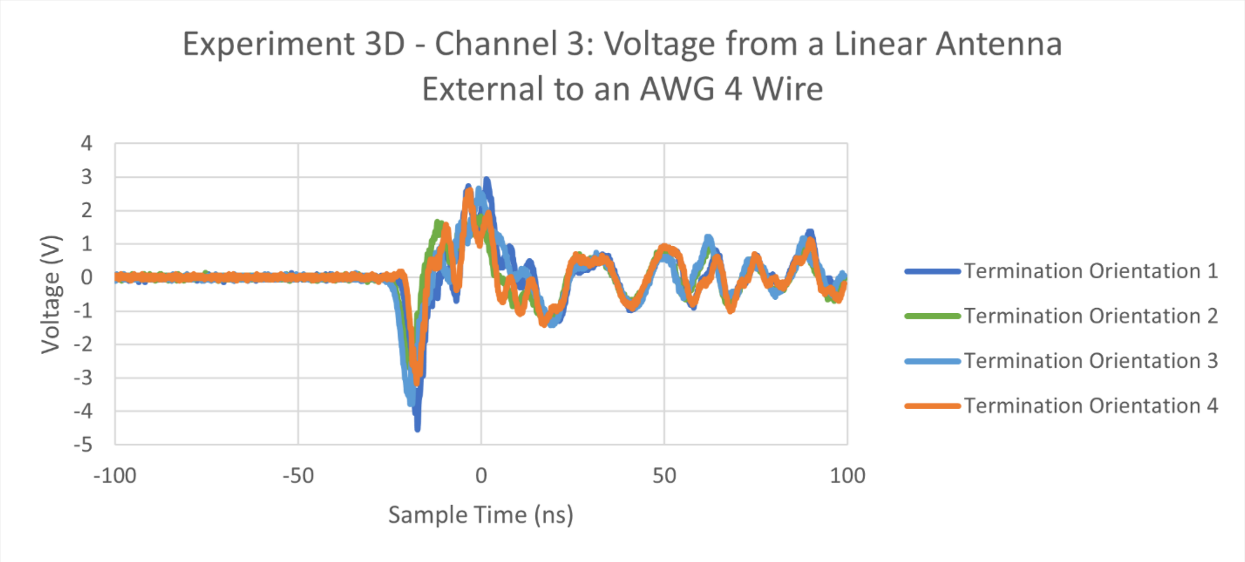

Fig. 4.38 The results captured by the linear antenna, external to the AWG 4 wire system and translated along a fixed axis in the z-direction, are provided. As the antenna moves further away from the AWG 4 wire, the measured signal decreases in amplitude.

Table 4.5 From this experiment, there is a decrease in amplitude signal when translating the linear antenna on a fixed axis further away from the AWG 4 wire during firing a pulse signal.

			Experiment 3D: Translating Linear Antenna along z-direction w/ approximate +2.5cm Linear Antenna length and AWG 4 Wire Gap		
Termination Orientation			Channel 1	Channel 2	Channel 3
#	Positive Terminal of Pulse Gen	R_L Load Termination Location	Pulse Generator (60dB Attenuated) “Output Monitor”	Internal Waveguide Linear Antenna	External Linear Antenna
1	90° Bend	Sharp Bend	-4.1V (Min)	0.0mV (Mean)	-4.5V (Min)
2	Sharp Bend	Sharp Bend	-3.9V (Min)	0.0mV (Mean)	-2.7V (Min)
3	Sharp Bend	90° Bend	-4.1V (Min)	0.1mV (Mean)	-3.8V (Min)
4	90° Bend	90° Bend	-3.9V (Min)	0.1mV (Mean)	-3.2V (Min)

To conclude the results from this section, Table 4.2 – Table 4.4 provide similar test scenarios demonstrating the same effect. That is, as the linear antenna translates away along a fixed axis parallel to the direction of current flow in the AWG 4 wire, there is a decrease in signal amplitude. In Table 4.5, additional scenarios were presented for connecting the pulse generator terminals and the R_L termination at different positions where the linear antenna is fixed. The amplitudes are shown to differ depending on how the system is wired together.

4.4.4 Experiment 4: Modifying Linear Antenna Positioning Along an AWG 4 Wire (RC Source)

In Section 4.4.3, a pulse generator was used as a source for the input to the AWG 4 wire. However, the transmission line theory in Chapter 2 is based on an RC source configuration feeding into a mock DPF. Using the same exact setup from the previous section except replacing the pulse generator input configuration for the RC source configuration as provided in Chapter 3, then samples are taken by the antenna waveguide structure along a fixed axis in the z-direction. The antenna waveguide structure is not translated in the x or y direction and is held constant with respect to z. From Fig. 4.39, the $z = 0$ position is identified. As the antenna is further away from the bend, the antenna position grows in the negative z-direction. As the antenna approaches closer to the wire, the antenna position grows in the positive z-direction. Measurements are recorded for antenna positions at $z = -17.8cm$, $z = 10.2cm$, $z = -2.5cm$, $z = 0$, $z = +2.5cm$, and $z = +7.6cm$.

When firing a $1kV$, $120\mu s$ pulse from the RC source via relay switch into the AWG 4 wire system, then the linear antenna channel 3 results are captured and provided in Fig. 4.39 for the different positions. The voltage readings for channels 1 – 3 are recorded in Table 4.6. Additionally, in Appendix D, Section D.4, images for the experiment and oscilloscope captures are provided.

From the results, the same phenomenon is demonstrated in that the signal amplitude measured by the linear antenna facing radially to the AWG 4 wire, the amplitude is consistent until the linear antenna begins to move away from the AWG 4 wire along a fixed axis. From the previous section, a clean single pulse is captured, as where in this experiment, a ripple is captured from the signal. The RC source utilizes a relay switch that has previously demonstrated mechanical bounce, which may be a potential cause to this feature. Otherwise, current diversion is demonstrated within this setup using the RC source as a source to the AWG 4 wire system.

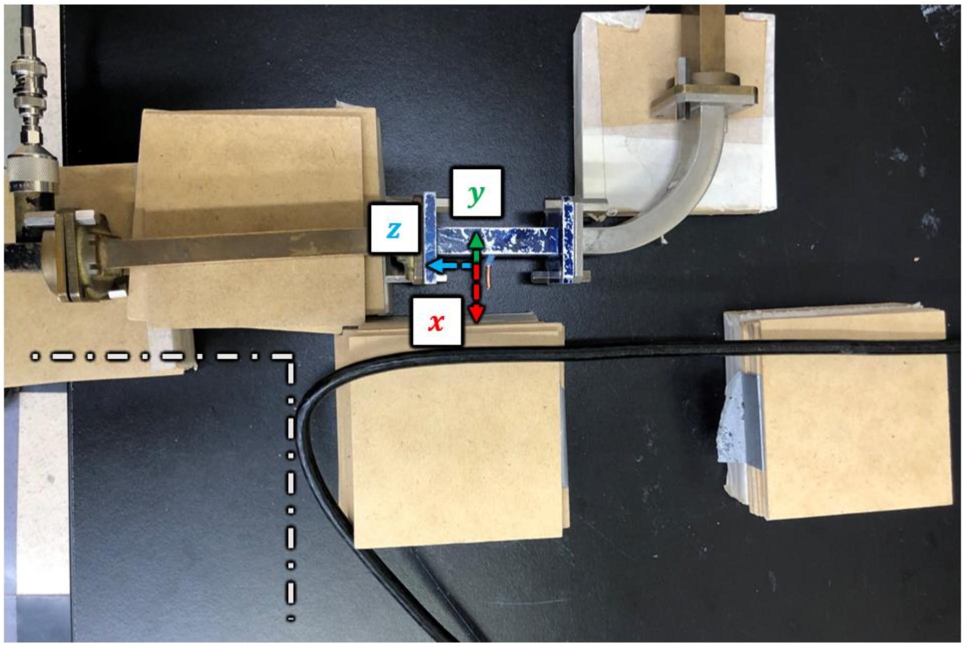

Fig. 4.39 The experimental setup is shown for generating a pulse by an RC source along an AWG 4 wire to be observed by a protruding external linear antenna from the X-band waveguide structure. Samples are taken when translating the linear antenna along a fixed axis in the z-direction.

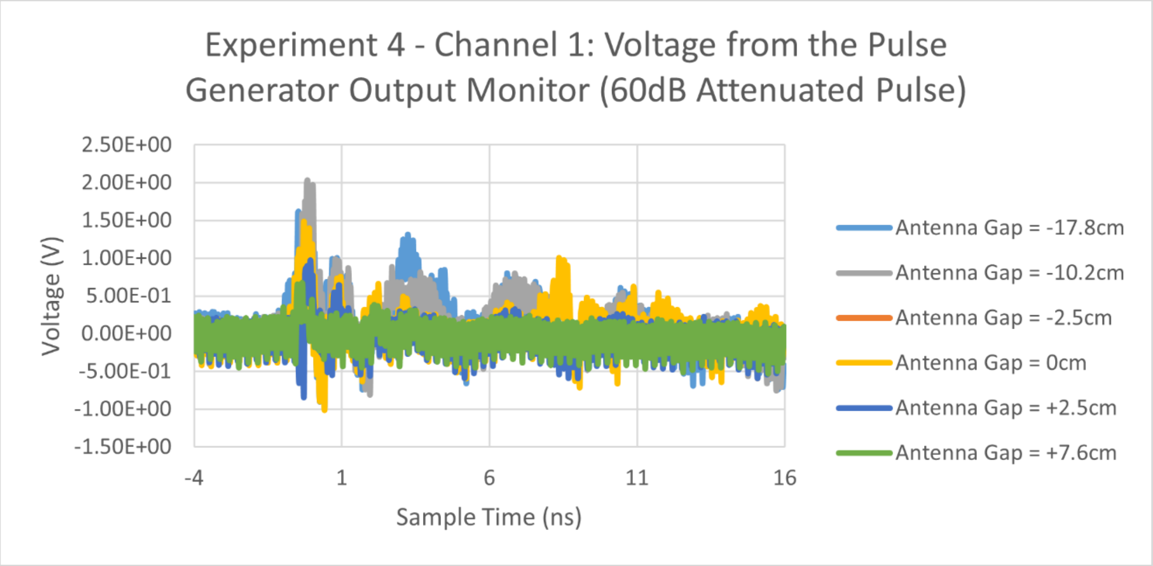

Fig. 4.40 The results captured by the linear antenna, external to the AWG 4 wire system and translated along a fixed axis in the z-direction, are provided. As the antenna moves further away from the AWG 4 wire, the measured signal decreases in amplitude.

Table 4.6 It can be shown within this experiment that there is a decrease in amplitude signal when translating the linear antenna on a fixed axis further away from the AWG 4 wire during firing a pulse signal.

	Experiment 4: Translating Linear Antenna along z-direction w/ approximate +1.0cm Linear Antenna length and AWG 4 Wire Gap	
	Channel 1	Channel 2
Antenna z-direction Translation	External Linear Antenna	Internal Waveguide Diode Antenna
-17.8cm	-1.0V (Min)	0.0mV (Mean)
-10.2cm	-0.8V (Min)	0.1mV (Mean)
-2.5cm	-0.9V (Min)	0.1mV (Mean)
0cm	-1.0V (Min)	0.0mV (Mean)
+2.5cm	-0.8V (Min)	0.1mV (Mean)
+7.6cm	-0.5V (Min)	0.1mV (Mean)

4.4.5 Experiment 5: Mock DPF Time of Flight from a Linear Antenna (Pulse Generator)

In this section, instead of using the AWG 4 wire to demonstrate current diversion, the mock DPF is used to fire a pulse signal through. In this experiment, the linear antenna waveguide structure is still used except, now the antenna faces radially external to the mock DPF. In this experiment, a time-of-flight experiment is performed. That is, when firing a pulse through the pulse generator, the linear antenna will be used to detect delay when measuring at the base end of the mock DPF and the pinch end of the mock DPF. A $4kV$, $20ns$ pulse signal is fired into the mock DPF system. From the results, relative to the pulse output trigger source, there is a measured delay about $3ns$ between the peak pulse from the mock DPF base and mock DPF pinch end. From Chapter 3, the transit time of the mock DPF is expected to be approximately $2.85ns$. Thus, there is some agreement between measured result and calculated result.

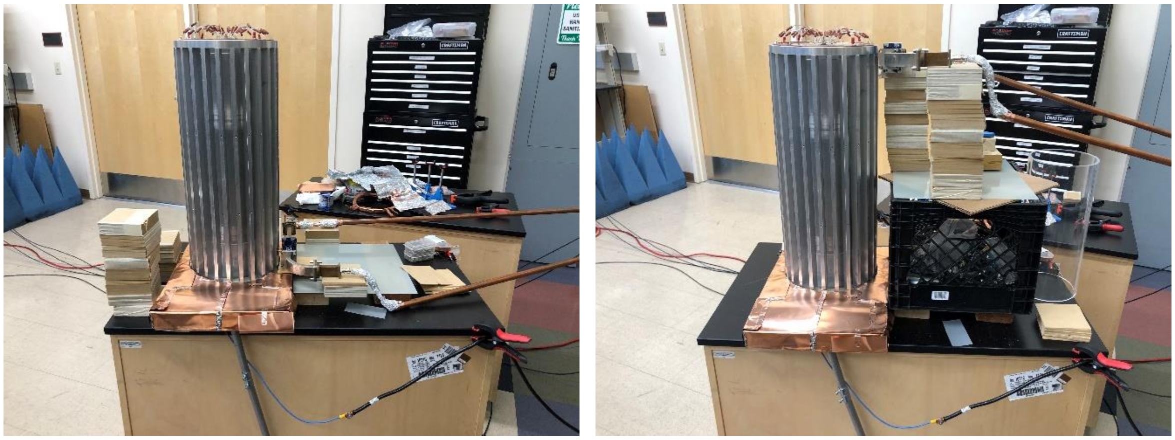

Fig. 4.41 The experimental setup is shown for generating a pulse by a pulse generator input along the mock DPF as observed by a protruding external linear antenna from the X-band waveguide structure near the base and pinch end of the mock DPF.

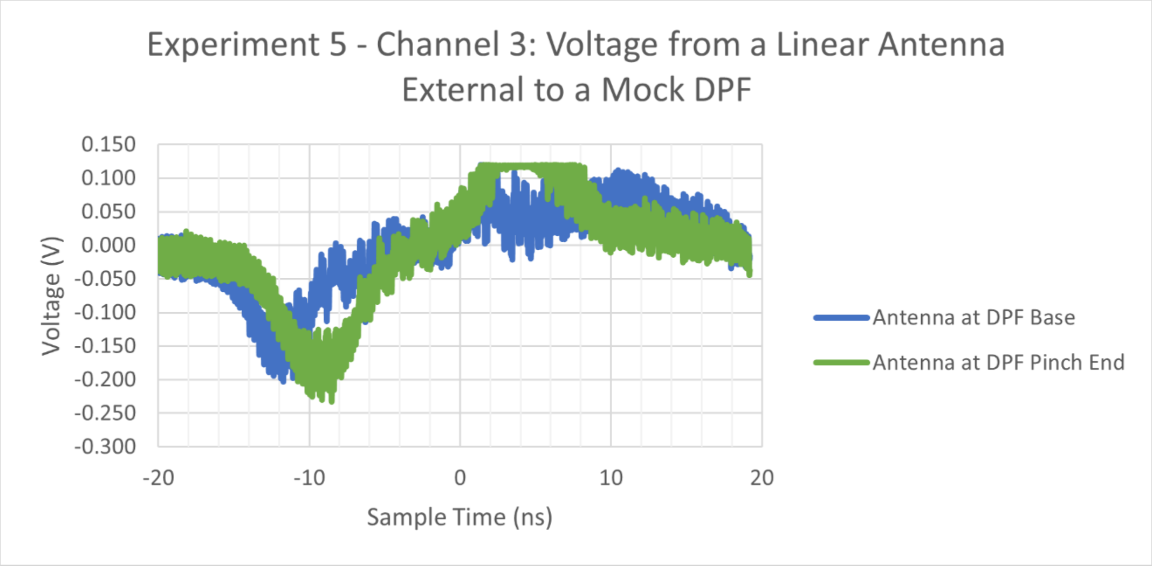

Fig. 4.42 The experimental setup is shown for generating a pulse by a pulse generator along the mock DPF at the base and pinch end as observed by a protruding external linear antenna from the X-band waveguide structure.

4.4.6 Experiment 6: Mock DPF Current Redirection (RC Source)

For the final experiment, the linear antenna waveguide structure is still used again, but is fixed at a position midway between the base and pinch end of the mock DPF. The RC configuration input is used in this experiment. Samples are taken when no short is implemented into the mock DPF system, when a short is placed above the antenna, and when a short is placed below the antenna. With the short placed below the antenna, current redirection is anticipated to occur in the system. Fig. 4.43 portrays the three different scenarios for the experimental setup. Results measured by the linear antenna are provided in Fig. 4.44 and summarized into Table 4.7. Peak-to-Peak measures in Table 4.7 demonstrate that when the linear antenna is placed above the location of the short, energy is lost and attenuated in the system. However, when the linear antenna is placed below the short or not short in the system, the signal appears to be almost consistent in amplitude and signal features, Thus, to conclude the experiment, a linear antenna facing radially towards a line current source, such as the AWG 4 wire or the mock DPF structure, can be used to detect signal changes of current diversion in a system. Where these signal changes occur provide a clue on determining the location of current diversion or redirection in a transmission line based system.

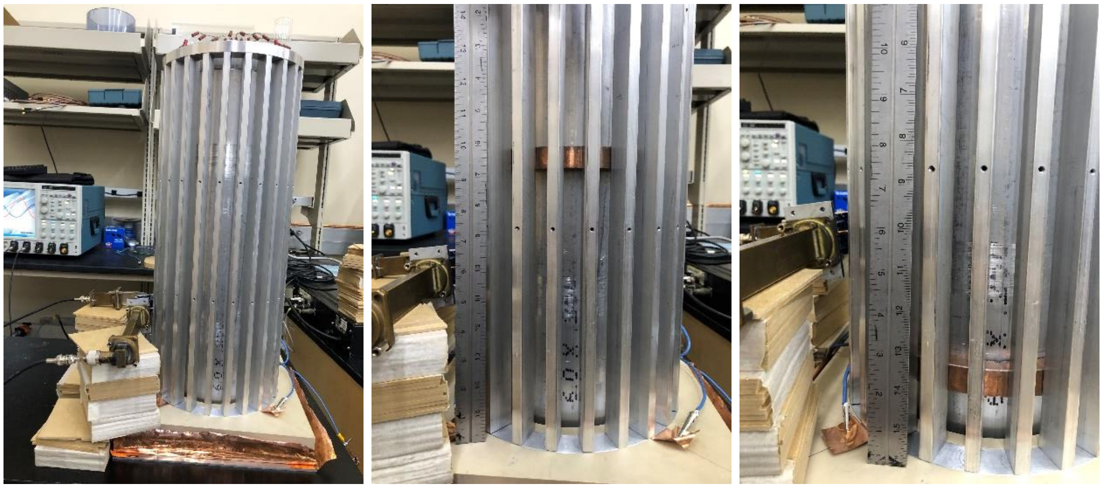

Fig. 4.43 The experimental setup is shown for generating a pulse by an RC source along the mock DPF as observed by a protruding external linear antenna from the X-band waveguide structure at a fixed height. Three images are shown where a short represented by R_f is not used (left image), a short is positioned below the antenna position (middle image), and a short is positioned above the antenna position (right image).

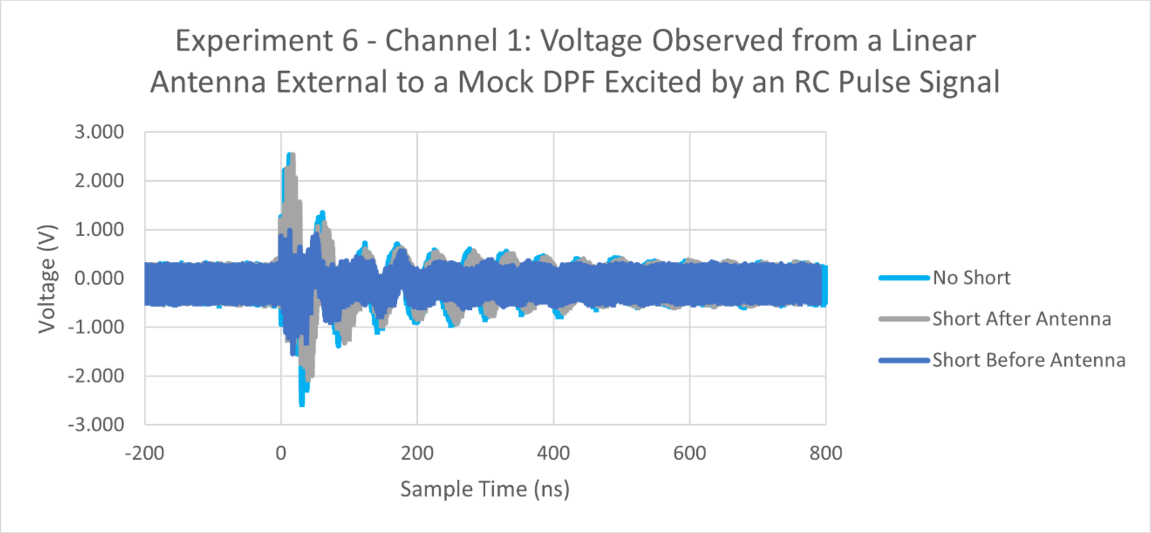

Fig. 4.44 The experimental setup is shown for generating a pulse by an RC source alongthe mock DPF to be observed by a protruding external linear antenna from the X-band waveguide structure.

Table 4.7 It can be shown within this experiment that there is a decrease in amplitude signal when translating the linear antenna on a fixed axis further away from the AWG 4 wire during firing a pulse signal.

	Experiment 6: Fixed Linear Antenna External to Mock DPF w/ 2kV RC Source	
	Channel 1	Channel 2
Setup	External Linear Antenna	Internal Waveguide Diode Antenna
No Short	5.1V (Peak-Peak)	1.0V (Peak-Peak)
Short After Antenna	4.5V (Peak-Peak)	0.9V (Peak-Peak)
Short Before Antenna	2.5V (Peak-Peak)	0.8V (Peak-Peak)

4.5 Discussion

From the experiments performed Section 4.4, it was demonstrated how a linear dipole antenna can be used to capture fields generated through an AWG 4 insulated wire and through the mock DPF when fired by an RC source or pulse generator as a source. From the experiments, it was examined that a decrease in the linear antenna length resulted in decrease in amplitude data. Further, regardless of the linear antenna orientation relative to the flow of current in a straight wire, fields were measured thus supporting the coupling of fields as discussed in Section 4.3.

In Section 4.2, it was examined in simulation that introducing a low resistive path of current, represented by R_f, into the mock DPF system at the mid-length region resulted in little to no current flow at the pinch end region of the mock DPF. From the mock DPF experiment in Section 4.4.6, it was demonstrated that there was a loss in signal amplitude when placing the linear antenna at a position between the pinch end region and the region of R_f.

Chapter 5: Conclusion and Future

5.1 Conclusion

To summarize this thesis, in chapter 1, literature was examined to provide an overview in the topic of dense plasma focus research and potential causes of energy loss in the mock DPF. In chapter 2, theory was examined for characterizing fields generated by the mock DPF using a 2-dimensional model and a transmission line analysis for characterizing energy fired into the mock DPF. In chapter 3, an experimental model was built for characterizing a mock DPF system. In chapter 4, LTspice and MATLAB simulations provided a foundation for understanding field data generated by the mock DPF. Further, a linear antenna was used to examine data captured in different scenarios involving current through an AWG 4 insulated wire and through the mock DPF.

Experiments in Section 4.4 demonstrated that a linear antenna or antenna stub can be used to capture fields generated by an AWG 4 insulated wire and through the mock DPF when activated. It was shown that a decrease in linear antenna length results in a decrease in amplitude strength.

The linear antenna orientation relative to the flow of current in a straight wire supports field coupling discussions in Section 4.3. Experiment #3 [Fig. 4.33 and 4.35], experiment #4 [Fig. 4.39], and experiment #6 [Fig. 4.43] represent experiments in which the current carrying AWG 4 wire has gradual and/or sharp bends for studying redirection studies.

The current carrying wire represents the redirected current path. It was examined that a path of current loss represented by R_f introduced into the mock DPF simulation resulted in significant energy loss through or along the path. Placement of the stub linear wire antenna array in a two-dimensional configuration should, with triangular techniques, locate the place where redirection occurs.

5.2 Future Work

While this thesis only provides a basis for determining the location of current redirection in a DPF system, there is opportunity for more exploration in this field of research. Some areas that can further be explored include examining the transmission line model as a multi-state system analysis. In this thesis, the path defined by R_f was either selected as high impedance or low impedance. However, from Chapter 1, it was discussed that the DPF pinch dynamics were modeled by different phases. A multi-state system analysis could better characterize changes in voltage and current along the DPF where restrike can be released in a particular state. The MATLAB program modeling the two-segment transmission line system in Chapter 2 was constrained to computation time resulting in loss of accuracy in simulation. Optimization for this MATLAB program can further be explored to understand the constraints with the numerical inverse Laplace transformation algorithms. Another area of research that can be explored in this topic includes the characterization of the linear dipole antenna. Previous discussion in Chapter 4, Section 4.3.2 has shown that two sets of fields are coupled with one another for the linear dipole antenna. Further characterization of the antenna may shed insight to the signal measured by the mock DPF. While the application of these explorative efforts are not entirely defined, they do provide possible areas of research to continue expanding upon for the topic of identifying current redirection in a Dense Plasma Focus based system.

Appendix A: Transmission Line Verification Program

A.1 Introduction to the Transmission Line Verification Program

From Chapter 2, a two-segment transmission line system is analyzed to model voltage and current along a DPF system using Laplace transformation techniques in the analysis. However, solving voltage and current along a two-segment transmission line system is also possible through analysis strictly in the time-domain as exercised by [29]. In this appendix, MATLAB scripts are developed based on the time-domain model following the analysis from [29]. These scripts are designed to verify experiments performed in Chapter 3 and Chapter 4 of this thesis. However, the voltage and current data computed from these scripts are constrained to up to a few transit times ($t > 0$) without further increasing the complexity of the scripts.

Following the analysis from [29], at $t = 0^+$, $z = 0^+$

$$V_1^+ = \frac{\mathcal{Z}_a V_s}{\mathcal{Z}_a + R_g} \tag{A.1}$$

At $z = 0^+$

$$V(z = 0^+, 0 < t < 2\tau_a)$$

Through KVL

$$V_{aj}^+ + V_{aj}^- = V_b = V_{tj}^+ \tag{A.2}$$

Through KCL

$$I_{aj}^+ + I_{aj}^- = I_b + I_{tj}^+ \tag{A.3}$$

Let

$$\rho_{va} = \frac{V_{aj}^-}{V_{aj}^+}, \qquad \rho_{ia} = \frac{I_{aj}^-}{I_{aj}^+}$$

Then

$$I_{aj}^{+} + I_{aj}^{-} = I_b + I_{tj}^{+}$$

$$\frac{V_{aj}^{+}}{\mathcal{Z}_a} - \frac{V_{aj}^{-}}{\mathcal{Z}_a} = \frac{V_b}{R_b} + \frac{V_{tj}^{+}}{\mathcal{Z}_c} = \left[\frac{1}{R_b} + \frac{1}{\mathcal{Z}_c}\right] V_{tj}^{+}$$

$$\frac{1}{\mathcal{Z}_a}\left[V_{aj}^{+} - V_{aj}^{-}\right] = \left[\frac{1}{R_b} + \frac{1}{\mathcal{Z}_c}\right][1 + \rho_{va}]$$

$$\rho_{va} = \frac{V_{aj}^{-}}{V_{aj}^{+}} = \frac{\frac{1}{\mathcal{Z}_a} - \left[\frac{1}{R_b} + \frac{1}{\mathcal{Z}_{ac}}\right]}{\frac{1}{\mathcal{Z}_a} + \frac{1}{\mathcal{Z}_c} + \frac{1}{R_b}} \tag{A.4}$$

Now consider the transmission coefficients defined as

$$\tau_{vab} = \frac{V_{tj}^{+}}{V_{aj}^{+}}, \qquad \tau_{iab} = \frac{I_{tj}^{+}}{I_{aj}^{+}}$$

From KVL

$$V_{aj}^{+} + V_{aj}^{-} = V_{tj}^{+}$$

$$1 + \rho_{va} = \frac{V_{tj}^{+}}{V_{aj}^{+}} = \tau_{iab} \tag{A.5}$$

Since $V_{tj}^{+} = \mathcal{Z}_c I_{tj}^{+}$ and $V_{aj}^{+} = \mathcal{Z}_a I_{aj}^{+}$,

$$V_{aj}^{+} + V_{aj}^{-} = V_{tj}^{+}$$

$$1 + \rho_{va} = \frac{\mathcal{Z}_c}{\mathcal{Z}_a}\frac{I_{tj}^{+}}{I_{cj}^{+}} \tag{A.6}$$

Furthermore

$$\rho_{va} = -\rho_{ia} \tag{A.7}$$

$$[1-\rho_{ia}]\frac{\mathcal{Z}_a}{\mathcal{Z}_c} = \frac{I_{tj}^{+}}{I_{cj}^{+}} = \tau_{iac} \tag{A.8}$$

Between both transmission line segments from [29], through KVL

$$V_{cj}^{-} + V_{c(j+1)}^{+} = V_b = V_{tj}^{-} \tag{A.9}$$

From KCL

$$I_{cj}^{-} + I_{c(j+1)}^{+} + I_b = I_{tj}^{-} \tag{A.10}$$

Let

$$\rho_{vc} = \frac{V_{c(j+1)}^{+}}{V_{cj}^{-}}, \qquad \rho_{ic} = \frac{I_{a(j+1)}^{+}}{I_{cj}^{-}}$$

Then

$$I_{cj}^{-} + I_{c(j+1)}^{+} + I_b = I_{tj}^{-}$$

$$-\frac{V_{cj}^{-}}{\mathcal{Z}_c} + \frac{V_{c(j+1)}^{+}}{\mathcal{Z}_c} + \frac{V_b}{R_b} = -\frac{V_{tj}^{-}}{\mathcal{Z}_a}$$

$$-\frac{V_{cj}^{-}}{\mathcal{Z}_c} + \frac{V_{c(j+1)}^{+}}{\mathcal{Z}_c} + \frac{V_b}{R_b} = -\left[\frac{1}{R_b} + \frac{1}{\mathcal{Z}_a}\right]\left[V_{cj}^{-} + V_{c(j+1)}^{+}\right]$$

$$-\frac{1}{\mathcal{Z}_c}[1-\rho_{vc}] = +\left[\frac{1}{R_b} + \frac{1}{\mathcal{Z}_a}\right][1+\rho_{vc}]$$

$$\rho_{vc} = \frac{V_{c(j+1)}^{+}}{V_{cj}^{-}} = \frac{\frac{1}{\mathcal{Z}_c} - \left[\frac{1}{R_b} + \frac{1}{\mathcal{Z}_a}\right]}{\frac{1}{c} + \frac{1}{R_b} + \frac{1}{\mathcal{Z}_a}} \tag{A.11}$$

Since $V_{c(j+1)}^{+} = \mathcal{Z}_c I_{c(j+1)}^{+}$ and $V_{cj}^{-} = -\mathcal{Z}_c I_{cj}^{-}$,

$$\rho_{ic} = -\rho_{vc} \tag{A.12}$$

Now consider the transmission coefficients defined as

$$\tau_{vca} = \frac{V_{tj}^-}{V_{cj}^-}, \qquad \tau_{ica} = \frac{I_{tj}^-}{I_{cj}^-}$$

From KVL

$$V_{cj}^- + V_{c(j+1)}^+ = V_{tj}^-,$$

$$1 + \rho_{vc} = \frac{V_{tj}^-}{V_{cj}^-} = \tau_{vca} \tag{A.13}$$

Furthermore, $\rho_{vc} = -\rho_{ic}$, $V_{tj}^- = -\mathcal{Z}_c I_{tj}^-$, and $V_{cj}^- = -\mathcal{Z}_c Y_{cj}^-$, then

$$\rho_{vl} = -\rho_{il} = \frac{R_l - \mathcal{Z}_c}{R_l + \mathcal{Z}_c} \tag{A.14}$$

$$\tau_{vs} = 1 + \rho_{vs} \tag{A.15}$$

$$\tau_{is} = 1 + \rho_{is} \tag{A.16}$$

A.2 Chapter 3 Verification for Cable Tester, BNC Cable, and Mock DPF System

The code provided in this section is used to simulate the voltage measured from a cable tester when connected to a BNC cable to a mock DPF terminated by a load as analyzed by the two-segment transmission line cable tester system in Chapter 3 Section 3.2.3. Running the code from this section will result in plotting Fig. A.1. This plot is simulated up to a few transit times and is consistent with amplitude changes for the open load, short load, and matched load scenarios.

```
% Written: Rocky Y. Gonzalez (11/29/2023)
% University of Nevada Las Vegas
% Department of Electrical and Computer Engineering
% Electromagnetics and High-Energetic Physics Lab
% Program: This program is used to simulate Voltage at the Cable Tester
%  front end up to a few transit times referencing a time-domain analysis
%  approach from S.R. Seshadri, "Fundamentals of Transmission Lines and
%  Electromagnetic Fields,"Addison-Wesley Publishing Company, Copyright
%  1971, Chapter 1, pp. 1-33 (Book) and Transmission Line notes from
%  Robert A. Schill, Jr.

clear all, close all, clc

% -------------------------------------------------------------------------
% Variables ---------------------------------------------------------------
% -------------------------------------------------------------------------
Vs = 0.54;                  % Supplied Voltage of Cable Tester System
Rs = 49;                    % Internal Resistance of Cable Tester
Rb = 1e6;                   % Resistance of Rb (open) between BNC cable and Mock DPF
RL = [1e6, 1e-6, 17];       % Resistance of Load RL (matched case, open case, short case)

Za  = 50;                   % Characteristic Impedance of BNC Cable (Line A)
Zc  = 17;                   % Characteristic Impedance of Mock DPF (Line C)

time = [0:100e-12:25e-9];   % time duration
transit_a = 7.9e-9;         % transit time of BNC Cable 'line a'
transit_b = 2.3e-9;         % transit time of Mock DPF 'line b' (-l_dpf < z < 0)

% -------------------------------------------------------------------------
% Call Functions ----------------------------------------------------------
% -------------------------------------------------------------------------
% Call function to simulate Chapter 3 Cable Tester Voltage for a BNC Cable
% and Mock DPF connect system:
[v_L, v_f, v_tdr1] = two_TL_voltage(Vs, Rs, Rb, RL(1,1), Za, Zc, ...
                                    time, transit_a, transit_b);
[v_L, v_f, v_tdr2] = two_TL_voltage(Vs, Rs, Rb, RL(1,2), Za, Zc, ...
                                    time, transit_a, transit_b);
[v_L, v_f, v_tdr3] = two_TL_voltage(Vs, Rs, Rb, RL(1,3), Za, Zc, ...
                                    time, transit_a, transit_b);

% -------------------------------------------------------------------------
% Plot --------------------------------------------------------------------
% -------------------------------------------------------------------------
% Create Plot for Mock DPF Chapter 3 Cable Tester system:
% Cable Tester connected to BNC Cable to Mock DPF to Load
figure(1)
set(gcf, 'Position',  [500, 100, 550, 650])

% Scenario 1: Fig. 3.21 (Rb = 1e6, RL = 1e6)
subplot(3,1,1), grid on, grid minor, xlim([0 60e-9]), ylim([0 0.6])
title(strcat("Voltage at the Cable Tester front end (R_b = ", ...
```

```
                 string(Rb), "\Omega, R_L = ", string(RL(1,1)), "\Omega)"))
    xlabel("Time (s)"), ylabel("Voltage (V)"),
    hold on
    plot(time, v_tdr1),
    hline = findobj(gcf, 'type', 'line');
    set(hline,'LineWidth',2);
    hold off

    % Scenario 2: Fig. 3.22 (Rb = 1e6, RL = 1e-6)
    subplot(3,1,2), grid on, grid minor, xlim([0 60e-9]), ylim([-0.2 0.4])
    title(strcat("Voltage at the Cable Tester front end (R_b = ", ...
                 string(Rb), "\Omega, R_L = ", string(RL(1,2)), "\Omega)"))
    xlabel("Time (s)"), ylabel("Voltage (V)"),
    hold on
    plot(time, v_tdr2),
    hline = findobj(gcf, 'type', 'line');
    set(hline,'LineWidth',2);
    hold off

    % Scenario 3: Fig. 3.23 (Rb = 1e6, RL = 17)
    subplot(3,1,3), grid on, grid minor, xlim([0 60e-9]), ylim([0 0.4])
    title(strcat("Voltage at the Cable Tester front end (R_b = ", ...
                 string(Rb), "\Omega, R_L = ", string(RL(1,3)), "\Omega)"))
    xlabel("Time (s)"), ylabel("Voltage (V)"),
    hold on
    plot(time, v_tdr3),
    hline = findobj(gcf, 'type', 'line');
    set(hline,'LineWidth',2);
    hold off
```

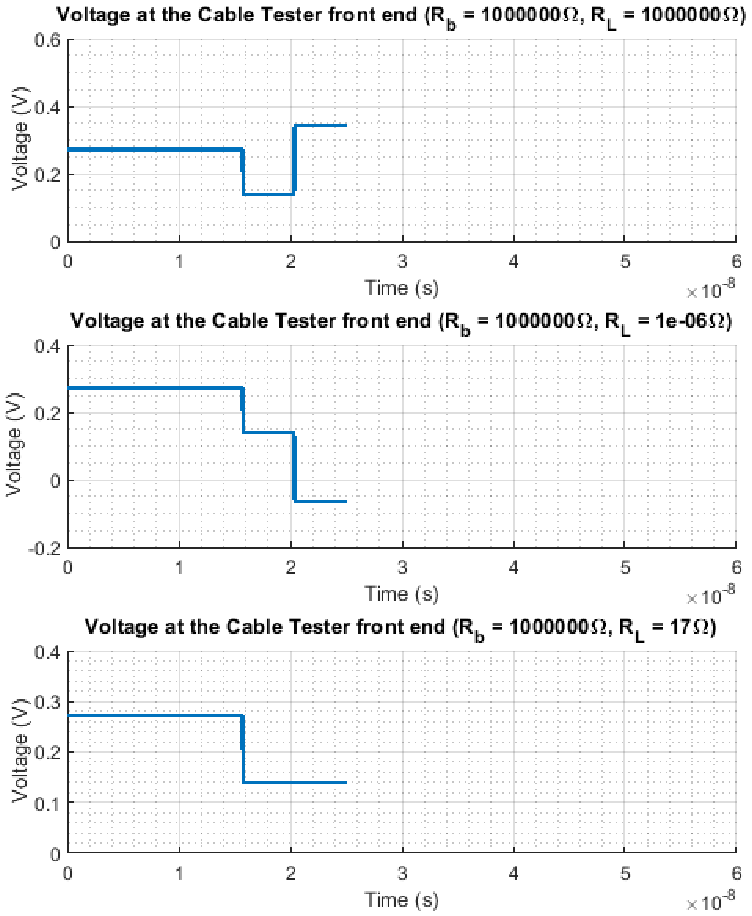
Voltage at the Cable Tester front end (R_b = 1000000Ω, R_L = 1000000Ω)

Voltage at the Cable Tester front end (R_b = 1000000Ω, R_L = 1e-06Ω)

Voltage at the Cable Tester front end (R_b = 1000000Ω, R_L = 17Ω)

Fig. A.1 Three different plots are shown each representing the expected voltage to be measured from the cable tester system in Chapter 3 Section 3.2.3 when modifying the load termination R_L to $1M\Omega$ (open load case), $1\mu\Omega$ (short load case), and 17Ω (matched load to mock DPF case). The plots are simulated up to a few transit times due to constraint of the time-domain model. Based on these plots, there is agreement with the model extracted from [29] and the results measured and simulated from Chapter 3 Section 3.2.3.

A.3 Chapter 4 Verification for the Two-Transmission Line Mock DPF System

The code provided in this section is used to simulate the voltage and current of the mock DPF at the base end, mid-length, and pinch end regions, where the fault path R_f is defined to be at the mid-length region or half of the length of the mock DPF. These simulations are used to verify the two-segment transmission line simulations in Chapter 4 Section 4.2.2. Running the code from this section will result in plotting Fig. A.2 – Fig. A.7. These plots are simulated up to a few transit times and are consistent with amplitude changes for the open load ($R_L = 1M\Omega$), short load ($R_L = 1\mu\Omega$), and matched load ($R_L = 17\Omega$) scenarios when implementing $R_f = 1M\Omega$ and $R_f = 1\mu\Omega$.

```
% Written: Rocky Y. Gonzalez (11/29/2023)
% University of Nevada Las Vegas
% Department of Electrical and Computer Engineering
% Electromagnetics and High-Energetic Physics Lab
% Program: This program is used to simulate Voltage and Current at the Base
%  End, Mid-length, and Pinch End regions of a DPF up to a few transit
%  times referencing a time-domain analysis approach from S.R. Seshadri,
%  "Fundamentals of Transmission Lines and Electromagnetic Fields,"
%  Addison-Wesley Publishing Company, Copyright 1971, Chapter 1, pp. 1-33
%  (Book) and Transmission Line notes from Robert A. Schill, Jr.

clear all, close all, clc

% -----------------------------------------------------------------------
% Variables -------------------------------------------------------------
% -----------------------------------------------------------------------
Vs = 1000;                  % Supplied Voltage to DPF System
Rs = 1e-6;                  % Source Resistance of DPF
Rb = [1e6, 1e-6];           % Resistance of Rf (short, open) at DPF Mid-length Region
RL = [17, 1e6, 1e-6];       % Resistance of Load RL (matched case, open case, short case)

Za  = 17;                   % Characteristic Impedance of Mock DPF (Line A)
Zc  = 17;                   % Characteristic Impedance of Mock DPF (Line C)

time = [0:10e-12:8.5e-9];   % time duration
transit_a = 1.43e-9;        % transit time of 'line a' (-l_a   < z < 0)
transit_b = 1.43e-9;        % transit time of 'line b' (-l_dpf < z < -l_a)
```

```

% -----------------------------------------------------------------------
% Call Functions -----------------------------------------------------
% -----------------------------------------------------------------------
% Call function to simulate Chapter 4 Voltage along the Mock DPF for 6
% different resistor combination scenarios:
[v_L1, v_f1, v_b1] = two_TL_voltage(Vs, Rs, Rb(1,1), RL(1,1), Za, Zc, ...
                                    time, transit_a, transit_b);
[v_L2, v_f2, v_b2] = two_TL_voltage(Vs, Rs, Rb(1,1), RL(1,2), Za, Zc, ...
                                    time, transit_a, transit_b);
[v_L3, v_f3, v_b3] = two_TL_voltage(Vs, Rs, Rb(1,1), RL(1,3), Za, Zc, ...
                                    time, transit_a, transit_b);
[v_L4, v_f4, v_b4] = two_TL_voltage(Vs, Rs, Rb(1,2), RL(1,1), Za, Zc, ...
                                    time, transit_a, transit_b);
[v_L5, v_f5, v_b5] = two_TL_voltage(Vs, Rs, Rb(1,2), RL(1,2), Za, Zc, ...
                                    time, transit_a, transit_b);
[v_L6, v_f6, v_b6] = two_TL_voltage(Vs, Rs, Rb(1,2), RL(1,3), Za, Zc, ...
                                    time, transit_a, transit_b);

volt_L      = [v_L1, v_L2, v_L3, v_L4, v_L5, v_L6]; % Voltage at Pinch End Region
volt_f      = [v_f1, v_f2, v_f3, v_f4, v_f5, v_f6]; % Voltage at Mid-Length Region
volt_base   = [v_b1, v_b2, v_b3, v_b4, v_b5, v_b6]; % Voltage at Base End Region

% Call function to simulate Chapter 4 Current along the Mock DPF for 6
% different resistor combination scenarios:
[i_L1, i_f1, i_b1] = two_TL_current(Vs, Rs, Rb(1,1), RL(1,1), Za, Zc, ...
                                    time, transit_a, transit_b);
[i_L2, i_f2, i_b2] = two_TL_current(Vs, Rs, Rb(1,1), RL(1,2), Za, Zc, ...
                                    time, transit_a, transit_b);
[i_L3, i_f3, i_b3] = two_TL_current(Vs, Rs, Rb(1,1), RL(1,3), Za, Zc, ...
                                    time, transit_a, transit_b);
[i_L4, i_f4, i_b4] = two_TL_current(Vs, Rs, Rb(1,2), RL(1,1), Za, Zc, ...
                                    time, transit_a, transit_b);
[i_L5, i_f5, i_b5] = two_TL_current(Vs, Rs, Rb(1,2), RL(1,2), Za, Zc, ...
                                    time, transit_a, transit_b);
[i_L6, i_f6, i_b6] = two_TL_current(Vs, Rs, Rb(1,2), RL(1,3), Za, Zc, ...
                                    time, transit_a, transit_b);

curr_L      = [i_L1, i_L2, i_L3, i_L4, i_L5, i_L6]; % Current at Pinch End Region
curr_f      = [i_f1, i_f2, i_f3, i_f4, i_f5, i_f6]; % Current at Mid-Length Region
curr_base   = [i_b1, i_b2, i_b3, i_b4, i_b5, i_b6]; % Current at Base End Region

% -----------------------------------------------------------------------
% Plot ---------------------------------------------------------------
% -----------------------------------------------------------------------
% Create Plot for Mock DPF Chapter 4 Scenario 1 (Rf = 1e6, RL = 17)
figure(1)
two_TL_plotter(Rb(1,1), RL(1,1), time, volt_L(:,1), volt_f(:,1), volt_base(:,1), ...
               curr_L(:,1), curr_f(:,1), curr_base(:,1))
subplot(2,1,1), xlim([0 30e-9]), ylim([-200 1200])
subplot(2,1,2), xlim([0 30e-9]), ylim([-20 80])
```

```matlab

% Create Plot for Mock DPF Chapter 4 Scenario 2 (Rf = 1e6, RL = 1e6)
figure(2)
two_TL_plotter(Rb(1,1), RL(1,2), time, volt_L(:,2), volt_f(:,2), volt_base(:,2), ...
               curr_L(:,2), curr_f(:,2), curr_base(:,2))
subplot(2,1,1), xlim([0 30e-9]), ylim([-500 2500])
subplot(2,1,2), xlim([0 30e-9]), ylim([-80 80])

% Create Plot for Mock DPF Chapter 4 Scenario 3 (Rf = 1e6, RL = 1e-6)
figure(3)
two_TL_plotter(Rb(1,1), RL(1,3), time, volt_L(:,3), volt_f(:,3), volt_base(:,3), ...
               curr_L(:,3), curr_f(:,3), curr_base(:,3))
subplot(2,1,1), xlim([0 30e-9]), ylim([-500 1500])
subplot(2,1,2), xlim([0 30e-9]), ylim([-100 700])

% Create Plot for Mock DPF Chapter 4 Scenario 4 (Rf = 1e-6, RL = 17)
figure(4)
two_TL_plotter(Rb(1,2), RL(1,1), time, volt_L(:,4), volt_f(:,4), volt_base(:,4), ...
               curr_L(:,4), curr_f(:,4), curr_base(:,4))
subplot(2,1,1), xlim([0 30e-9]), ylim([-200 1200])
subplot(2,1,2), xlim([0 30e-9]), ylim([-100 1500])

% Create Plot for Mock DPF Chapter 4 Scenario 5 (Rf = 1e-6, RL = 1e6)
figure(5)
two_TL_plotter(Rb(1,2), RL(1,2), time, volt_L(:,5), volt_f(:,5), volt_base(:,5), ...
               curr_L(:,5), curr_f(:,5), curr_base(:,5))
subplot(2,1,1), xlim([0 30e-9]), ylim([-200 1200])
subplot(2,1,2), xlim([0 30e-9]), ylim([-100 1500])

% Create Plot for Mock DPF Chapter 4 Scenario 6 (Rf = 1e-6, RL = 1e-6)
figure(6)
two_TL_plotter(Rb(1,2), RL(1,3), time, volt_L(:,6), volt_f(:,6), volt_base(:,6), ...
               curr_L(:,6), curr_f(:,6), curr_base(:,6))
subplot(2,1,1), xlim([0 30e-9]), ylim([-200 1200])
subplot(2,1,2), xlim([0 30e-9]), ylim([-100 1500])
```

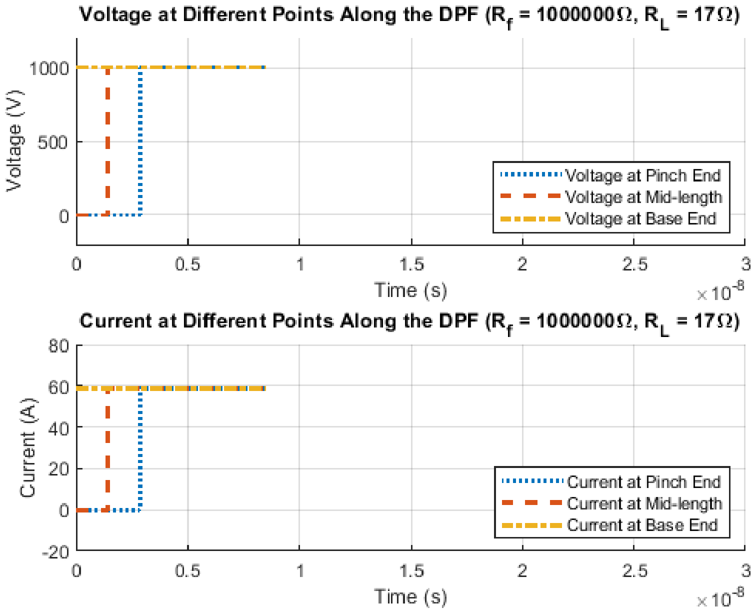

Voltage at Different Points Along the DPF (R_f = 1000000Ω, R_L = 17Ω)

Current at Different Points Along the DPF (R_f = 1000000Ω, R_L = 17Ω)

Fig. A.2 Three different plots are shown for the expected voltage (top plot) and expected current (bottom plot) from the mock DPF at the base end, mid-length, and pinch end regions using the parameters from Chapter 3 Section 4.2.2. For this scenario, $R_L = 17\Omega$ (matched load case) and $R_f = 1M\Omega$. The plots are simulated up to a few transit times due to constraint of the time-domain model. Based on these plots, there is agreement with the model extracted from [29] and the results measured and simulated from Chapter 4, Section 4.2.2, Fig. 4.11.

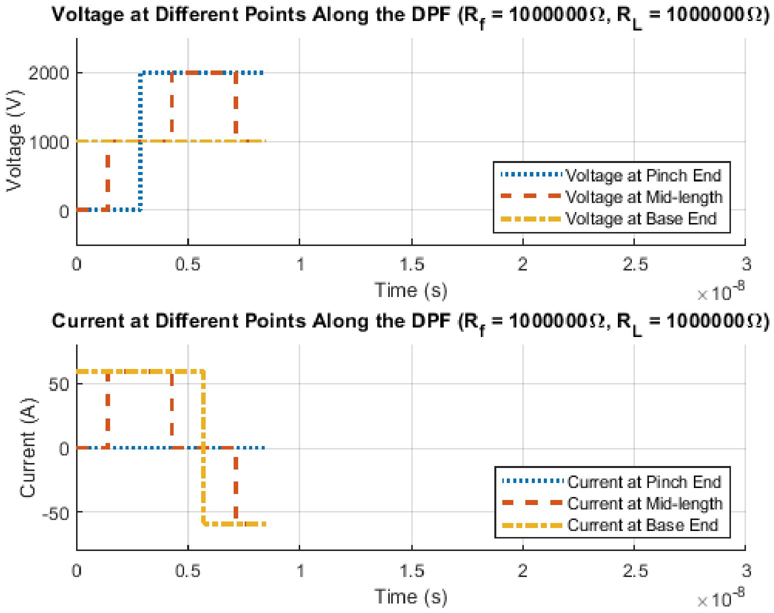

Fig. A.3 Three different plots are shown for the expected voltage (top plot) and expected current (bottom plot) from the mock DPF at the base end, mid-length, and pinch end regions using the parameters from Chapter 3 Section 4.2.2. For this scenario, $R_L = 1M\Omega$ (open load case) and $R_f = 1M\Omega$. The plots are simulated up to a few transit times due to constraint of the time-domain model. Based on these plots, there is agreement with the model extracted from [29] and the results measured and simulated from Chapter 4, Section 4.2.2, Fig. 4.12.

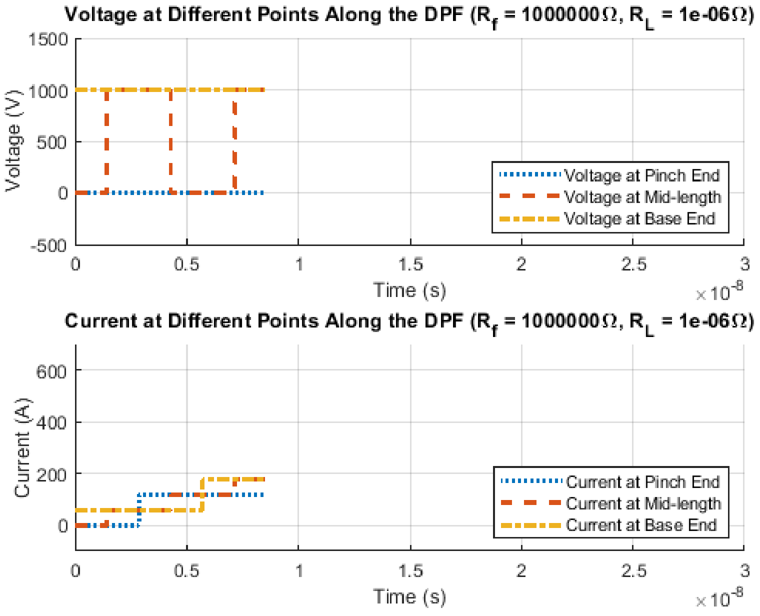

Fig. A.4 Three different plots are shown for the expected voltage (top plot) and expected current (bottom plot) from the mock DPF at the base end, mid-length, and pinch end regions using the parameters from Chapter 3 Section 4.2.2. For this scenario, $R_L = 1\mu\Omega$ (short load case) and $R_f = 1M\Omega$. The plots are simulated up to a few transit times due to constraint of the time-domain model. Based on these plots, there is agreement with the model extracted from [29] and the results measured and simulated from Chapter 4, Section 4.2.2, Fig. 4.13.

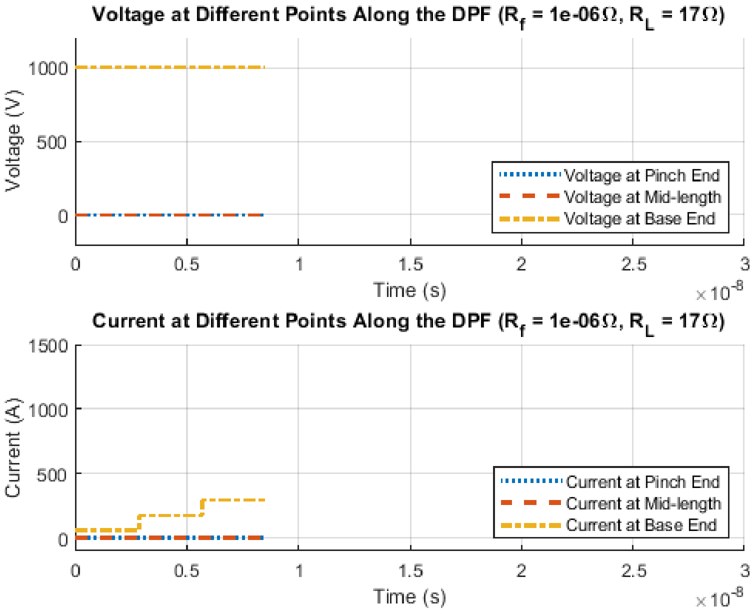

Fig. A.5 Three different plots are shown for the expected voltage (top plot) and expected current (bottom plot) from the mock DPF at the base end, mid-length, and pinch end regions using the parameters from Chapter 3 Section 4.2.2. For this scenario, $R_L = 17\Omega$ (matched load case) and $R_f = 1\mu\Omega$. The plots are simulated up to a few transit times due to constraint of the time-domain model. Based on these plots, there is agreement with the model extracted from [29] and the results measured and simulated from Chapter 4, Section 4.2.2, Fig. 4.17.

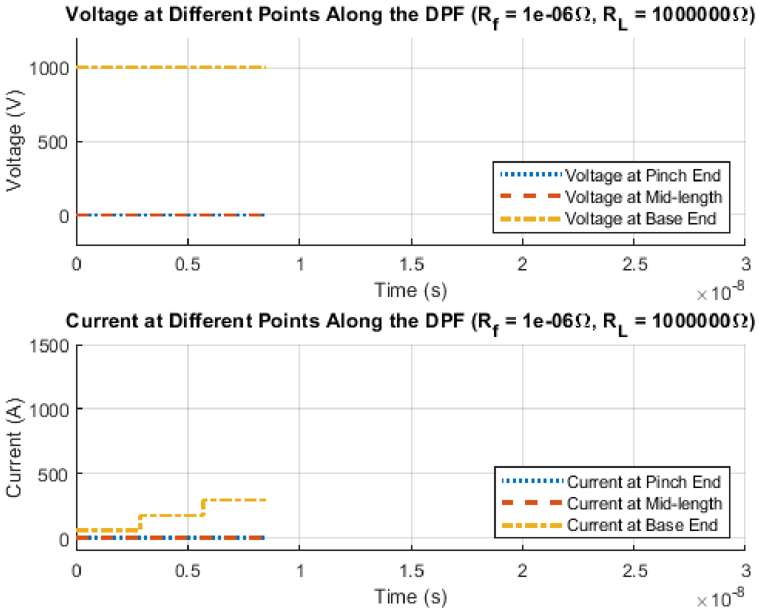

Fig. A.6 Three different plots are shown for the expected voltage (top plot) and expected current (bottom plot) from the mock DPF at the base end, mid-length, and pinch end regions using the parameters from Chapter 3 Section 4.2.2. For this scenario, $R_L = 1M\Omega$ (open load case) and $R_f = 1\mu\Omega$. The plots are simulated up to a few transit times due to constraint of the time-domain model. Based on these plots, there is agreement with the model extracted from [29] and the results measured and simulated from Chapter 4, Section 4.2.2, Fig. 4.18.

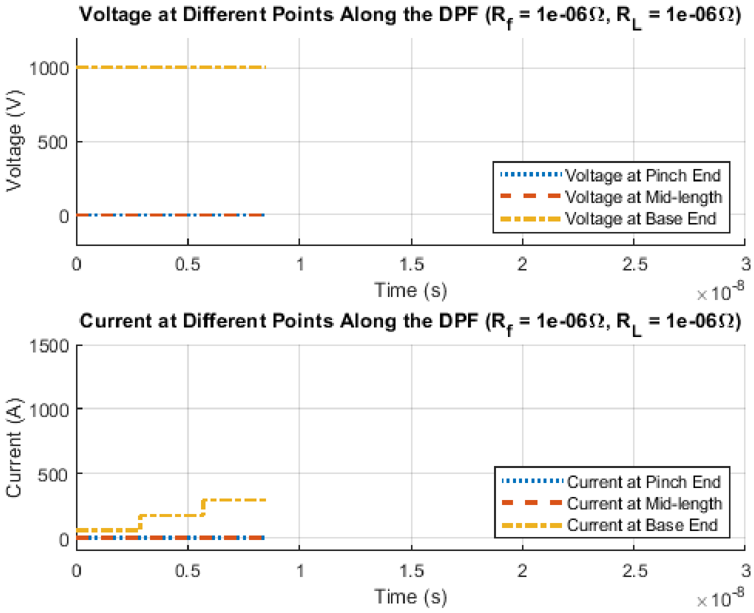

Fig. A.7 Three different plots are shown for the expected voltage (top plot) and expected current (bottom plot) from the mock DPF at the base end, mid-length, and pinch end regions using the parameters from Chapter 3 Section 4.2.2. For this scenario, $R_L = 1\mu\Omega$ (short load case) and $R_f = 1\mu\Omega$. The plots are simulated up to a few transit times due to constraint of the time-domain model. Based on these plots, there is agreement with the model extracted from [29] and the results measured and simulated from Chapter 4, Section 4.2.2, Fig. 4.19.

A.4 Additional Functions Required for Time-Domain Transmission Line Verification Programs

In the MATLAB scripts written in Section A.2 and Section A.3, functions are called to perform the computation and plotting for the formulas following Section A.1 or notes from [29]. These functions are provided in this section.

“*two_TL_voltage.m*”

```
% Written: Rocky Y. Gonzalez (11/29/2023)
% University of Nevada Las Vegas
% Department of Electrical and Computer Engineering
% Electromagnetics and High-Energetic Physics Lab
% Program: This function is used to simulate Voltage at the Base End,
%  Mid-length, and Pinch End regions of a DPF up to a few transit times
%  referencing a time-domain analysis approach from S.R. Seshadri,
%  "Fundamentals of Transmission Lines and Electromagnetic Fields,"
%  Addison-Wesley Publishing Company, Copyright 1971, Chapter 1, pp. 1-33
%  (Book) and Transmission Line notes from Robert A. Schill, Jr.
% -------------------------------------------------------------------------
% -------------------------------------------------------------------------

function [amp_L, amp_f, amp_base] = two_TL_voltage(Vs, Rs, Rb, RL, Za, Zc, ...
                                                   time, t1, t2)
    % ---------------------------------------------------------------------
    % Reflection and Transmission Coefficients ----------------------------
    % ---------------------------------------------------------------------
    Rho_Vs  = (Rs-Za)/(Rs+Za);
    Rho_VL  = (RL-Zc)/(RL+Zc);
    Rho_Va  = ((1/Za)-(1/Rb+1/Zc))/(1/Za+1/Zc+1/Rb);
    Rho_Vc  = ((1/Zc)-(1/Rb+1/Za))/(1/Zc+1/Rb+1/Za);

    Tau_Vac = 1 + Rho_Va;
    Tau_Vca = 1 + Rho_Vc;

    % ---------------------------------------------------------------------
    % Wavelet Contributions  ----------------------------------------------
    % ---------------------------------------------------------------------
    Va1_p   = Vs*Za/(Za+Rs);
    Va1_m   = Va1_p*Rho_Va;
    Va2_p   = Va1_p*Rho_Va*Rho_Vs;
    Va2_m   = Va1_p*Rho_Va^2*Rho_Vs;
    Va3_p   = Va1_p*Rho_Va^2*Rho_Vs^2;
    Va3_m   = Va1_p*Rho_Va^3*Rho_Vs^2;

    Vb1_p   = Va1_p*Tau_Vac;
    Vb1_m   = Va1_p*Tau_Vac*Rho_VL;
    Vb2_p   = Va1_p*Tau_Vac*Rho_VL*Rho_Vc;
    Vb2_m   = Va1_p*Tau_Vac*Rho_VL^2*Rho_Vc;
    Vb3_p   = Va1_p*Tau_Vac*Rho_VL^2*Rho_Vc^2;
    Vb3_m   = Va1_p*Tau_Vac*Rho_VL^3*Rho_Vc^2;

    Vc1_p   = Va1_p*Tau_Vac*Rho_VL*Tau_Vca;
    Vc1_m   = Va1_p*Tau_Vac*Rho_VL*Tau_Vca*Rho_Vs;
    Vc2_p   = Va1_p*Tau_Vac*Rho_VL*Tau_Vca*Rho_Vs*Rho_Va;

    Vd1_p   = Va1_p*Rho_Va*Rho_Vs*Tau_Vac;
```

```
        Vd1_m   = Va1_p*Rho_Va*Rho_Vs*Tau_Vac*Rho_VL;
        Vd2_p   = Va1_p*Rho_Va*Rho_Vs*Tau_Vac*Rho_VL*Rho_Vc;

        Ve1_p   = Va1_p*Tau_Vac*Rho_VL^2*Rho_Vc*Tau_Vca;

        Vf1_p   = Va1_p*Rho_Va^2*Rho_Vs^2*Tau_Vac;

        Vg1_p   = Va1_p*Rho_Va*Rho_Vs*Tau_Vac*Rho_VL*Tau_Vca;

        Vh1_p   = Va1_p*Tau_Vac^2*Rho_VL*Tau_Vca*Rho_Vs;

        % ---------------------------------------------------------------------
        % Voltage at Different Regions ----------------------------------------
        % ---------------------------------------------------------------------
        % Voltage at the DPF Base End Region (z = -l_dpf; 'Line 1')
        Vbase = [Va1_p, ...                                         % 0 < t < 2*t1
                 Va1_p + Va1_m + Va2_p, ...                         % 2*t1 < t < 4*t1
                 Va1_p + Va1_m + Va2_p + Va2_m + Va3_p, ...         % 4*t1 < t < 6*t1
                 Vc1_p + Vc1_m];                                    % (1*t1 + 2*t2 + 1*t1) < t < (1*t1 + 2*t2 + 3*t1)

        % Voltage at the DPF Mid-length Region (z = -l_dpf/2; 'Line 1')
        Vf1   = [0, ...                                             % 0 < t < 1*t1
                 Va1_p + Va1_m, ...                                 % 1*t1 < t < 3*t1
                 Va1_p + Va1_m + Va2_p + Va2_m, ...                 % 3*t1 < t < 5*t1
                 Vc1_p, ...                                         % (1*t1 + 2*t2) < t < 1*t1 + 2*t2 + 2*t1)
                 Va1_p + Va1_m + Va2_p + Va2_m + Va3_p + Va3_m, ... % 5*t1 < t < 7*t1
                 Vc1_p + Vc1_m + Vc2_p, ...                         % (1*t1 + 2*t2 + 2*t1) < t < (1*t1 + 2*t2 + 4*t1)
                 Ve1_p, ...                                         % (1*t1 + 4*t2) < t < (3*t1 + 4*t2)
                 Vg1_p];                                            % (3*t1 + 2*t2) < t < 3*t1 + 2*t2 + 2*t1)

        % Voltage at the DPF Mid-length Region (z = -l_dpf/2; 'Line 2')
        Vf2   = [0, ...                                             % 0 < t < 1*t1
                 Vb1_p, ...                                         % 1*t1 < t < 3*t1
                 Vb1_p + Vb1_m + Vb2_p, ...                         % 3*t1 < t < 5*t1
                 Vd1_p, ...                                         % (1*t1 + 2*t2) < t < (1*t1 + 2*t2 + 2*t1)
                 Vb1_p + Vb1_m + Vb2_p + Vb2_m + Vb3_p, ...         % 5*t1 < t < 7*t1
                 Vd1_p + Vd1_m + Vd2_p, ...                         % (1*t1 + 2*t2 + 2*t1) < t < (1*t1 + 2*t2 + 4*t1)
                 Vf1_p, ...                                         % (1*t1 + 4*t2) < t < (3*t1 + 4*t2)
                 Vh1_p];                                            % (3*t1 + 2*t2) < t < (3*t1 + 2*t2 + 2*t1)

        % Voltage at the DPF Pinch End Region (z = 0; 'Line 2')
        VL    = [0, ...                                             % 0 < t < (1*t1 + 1*t2)
```

```
             Vb1_p + Vb1_m, ...                                 % (1*t1 + 1*t2) < t < (1*t1 + 3*t2)
             Vb1_p + Vb1_m + Vb2_p + Vb2_m, ...                 % (1*t1 + 3*t2) < t < (1*t1 + 5*t2)
             Vb1_p + Vb1_m + Vb2_p + Vb2_m + Vb3_p + Vb3_m, ... % (1*t1 + 5*t2) < t < (1*t1 + 7*t2)
             Vd1_p + Vd1_m];                                    % (3*t1 + 1*t2) < t < (3*t1 + 3*t2)

    % ------------------------------------------------------------------
    % Organize Data ----------------------------------------------------
    % ------------------------------------------------------------------
    for i = 1:length(time)
        amp_base(i,1) = 0;  % Initialize Amplitude Value (Base End)
        amp_f(i,1)    = 0;  % Initialize Amplitude Value (Mid-length)
        amp_L(i,1)    = 0;  % Initialize Amplitude Value (Pinch End)

        % Voltage Contributions at Base End over time ('Line 1')
        if (time(i) >= 0) && (time(i) < 2*t1)
            amp_base(i,1)   = amp_base(i,1) + Vbase(1);
        end
        if (time(i) >= 2*t1) && (time(i) < 4*t1)
            amp_base(i,1)   = amp_base(i,1) + Vbase(2);
        end
        if (time(i) >= 4*t1) && (time(i) < 6*t1)
            amp_base(i,1)   = amp_base(i,1) + Vbase(3);
        end
        if (time(i) >= 1*t1 + 2*t2 + 1*t1) && (time(i) < 1*t1 + 2*t2 + 3*t1)
            amp_base(i,1)   = amp_base(i,1) + Vbase(4);
        end

        % Voltage Contributions between 'Line 1' and 'Line 2' over time
        if (time(i) >= 0) && (time(i) < 1*t1)
            amp_f(i,1)      = amp_f(i,1)    + Vf1(1);
        end
        if (time(i) >= 1*t1) && (time(i) < 3*t1)
            amp_f(i,1)      = amp_f(i,1)    + Vf1(2);
        end
        if (time(i) >= 3*t1) && (time(i) < 5*t1)
            amp_f(i,1)      = amp_f(i,1)    + Vf1(3);
        end
        if (time(i) >= 1*t1 + 2*t2) && (time(i) < 1*t1 + 2*t2 + 2*t1)
            amp_f(i,1)      = amp_f(i,1)    + Vf1(4);
        end
        if (time(i) >= 5*t1) && (time(i) < 7*t1)
            amp_f(i,1)      = amp_f(i,1)    + Vf1(5);
        end
        if (time(i) >= 1*t1 + 2*t2 + 2*t1) && (time(i) < 1*t1 + 2*t2 + 4*t1)
            amp_f(i,1)      = amp_f(i,1)    + Vf1(6);
        end
        if (time(i) >= 1*t1 + 4*t2) && (time(i) < 3*t1 + 4*t2)
```

```
            amp_f(i,1)      = amp_f(i,1)    + Vf1(7);
        end
        if (time(i) >= 3*t1 + 2*t2) && (time(i) < 3*t1 + 2*t2 + 2*t1)
            amp_f(i,1)      = amp_f(i,1)    + Vf1(8);
        end

        % Voltage Contributions at Load End region over time ('Line 2')
        if (time(i) >= 0) && (time(i) < 1*t1 + 1*t1)
            amp_L(i,1)   = amp_L(i,1) + VL(1);
        end
        if (time(i) >= 1*t1 + 1*t2) && (time(i) < 1*t1 + 3*t2)
            amp_L(i,1)   = amp_L(i,1) + VL(2);
        end
        if (time(i) >= 1*t1 + 3*t2) && (time(i) < 1*t1 + 5*t2)
            amp_L(i,1)   = amp_L(i,1) + VL(3);
        end
        if (time(i) >= 1*t1 + 5*t2) && (time(i) < 1*t1 + 7*t2)
            amp_L(i,1)   = amp_L(i,1) + VL(4);
        end
        if (time(i) >= 3*t1 + 1*t2) && (time(i) < 3*t1 + 3*t2)
            amp_L(i,1)   = amp_L(i,1) + VL(5);
        end
    end
    % ---------------------------------------------------------------------
end

% -------------------------------------------------------------------------
% -------------------------------------------------------------------------
```

“*two_TL_current.m*”

```
% Written: Rocky Y. Gonzalez (11/29/2023)
% University of Nevada Las Vegas
% Department of Electrical and Computer Engineering
% Electromagnetics and High-Energetic Physics Lab
% Program: This function is used to simulate Current at the Base End,
%  Mid-length, and Pinch End regions of a DPF up to a few transit times
%  referencing a time-domain analysis approach from S.R. Seshadri,
%  "Fundamentals of Transmission Lines and Electromagnetic Fields,"
%  Addison-Wesley Publishing Company, Copyright 1971, Chapter 1, pp. 1-33
%  (Book) and Transmission Line notes from Robert A. Schill, Jr.
% -------------------------------------------------------------------------
% -------------------------------------------------------------------------

function [amp_L, amp_f, amp_base] = two_TL_current(Vs, Rs, Rb, RL, Za, Zc, ...
                                                   time, t1, t2)
    % ---------------------------------------------------------------------
```

```
% Reflection and Transmission Coefficients ----------------------------
% ---------------------------------------------------------------------
Rho_Is  = -(Rs-Za)/(Rs+Za);
Rho_IL  = -(RL-Zc)/(RL+Zc);
Rho_Ia  = -((1/Za)-(1/Rb+1/Zc))/(1/Za+1/Zc+1/Rb);
Rho_Ic  = -((1/Zc)-(1/Rb+1/Za))/(1/Zc+1/Rb+1/Za);

Tau_Iac = Za/Zc*(1 - Rho_Ia);
Tau_Ica = Zc/Za*(1 - Rho_Ic);

% ---------------------------------------------------------------------
% Wavelet Contributions  ----------------------------------------------
% ---------------------------------------------------------------------
Ia1_p   = Vs/(Za+Rs);
Ia1_m   = Ia1_p*Rho_Ia;
Ia2_p   = Ia1_p*Rho_Ia*Rho_Is;
Ia2_m   = Ia1_p*Rho_Ia^2*Rho_Is;
Ia3_p   = Ia1_p*Rho_Ia^2*Rho_Is^2;
Ia3_m   = Ia1_p*Rho_Ia^3*Rho_Is^2;

Ib1_p   = Ia1_p*Tau_Iac;
Ib1_m   = Ia1_p*Tau_Iac*Rho_IL;
Ib2_p   = Ia1_p*Tau_Iac*Rho_IL*Rho_Ic;
Ib2_m   = Ia1_p*Tau_Iac*Rho_IL^2*Rho_Ic;
Ib3_p   = Ia1_p*Tau_Iac*Rho_IL^2*Rho_Ic^2;
Ib3_m   = Ia1_p*Tau_Iac*Rho_IL^3*Rho_Ic^2;

Ic1_p   = Ia1_p*Tau_Iac*Rho_IL*Tau_Ica;
Ic1_m   = Ia1_p*Tau_Iac*Rho_IL*Tau_Ica*Rho_Is;
Ic2_p   = Ia1_p*Tau_Iac*Rho_IL*Tau_Ica*Rho_Is*Rho_Ia;

Id1_p   = Ia1_p*Rho_Ia*Rho_Is*Tau_Iac;
Id1_m   = Ia1_p*Rho_Ia*Rho_Is*Tau_Iac*Rho_IL;
Id2_p   = Ia1_p*Rho_Ia*Rho_Is*Tau_Iac*Rho_IL*Rho_Ic;

Ie1_p   = Ia1_p*Tau_Iac*Rho_IL^2*Rho_Ic*Tau_Ica;

If1_p   = Ia1_p*Rho_Ia^2*Rho_Is^2*Tau_Iac;

Ig1_p   = Ia1_p*Rho_Ia*Rho_Is*Tau_Iac*Rho_IL*Tau_Ica;

Ih1_p   = Ia1_p*Tau_Iac^2*Rho_IL*Tau_Ica*Rho_Is;

% ---------------------------------------------------------------------
% Current at Different Regions ----------------------------------------
% ---------------------------------------------------------------------
% Current at the DPF Base End Region (z = -l_dpf; 'Line 1')
Ibase = [Ia1_p, ...                                         % 0 < t < 2*t1
         Ia1_p + Ia1_m + Ia2_p, ...                         % 2*t1 < t < 4*t1
         Ia1_p + Ia1_m + Ia2_p + Ia2_m + Ia3_p, ...         % 4*t1 < t < 6*t1
         Ic1_p + Ic1_m];                                    % (1*t1 + 2*t2 + 1*t1) <
```

```
t < (1*t1 + 2*t2 + 3*t1)

    % Current at the DPF Mid-length Region (z = -l_dpf/2; 'Line 1')
    If1   = [0, ...                                                 % 0 < t < 1*t1
             Ia1_p + Ia1_m, ...                                     % 1*t1 < t < 3*t1
             Ia1_p + Ia1_m + Ia2_p + Ia2_m, ...                     % 3*t1 < t < 5*t1
             Ic1_p, ...                                             % (1*t1 + 2*t2) < t <
(1*t1 + 2*t2 + 2*t1)
             Ia1_p + Ia1_m + Ia2_p + Ia2_m + Ia3_p + Ia3_m, ... % 5*t1 < t < 7*t1
             Ic1_p + Ic1_m + Ic2_p, ...                             % (1*t1 + 2*t2 + 2*t1) <
t < (1*t1 + 2*t2 + 4*t1)
             Ie1_p, ...                                             % (1*t1 + 4*t2) < t <
(3*t1 + 4*t2)
             Ig1_p];                                                % (3*t1 + 2*t2) < t <
(3*t1 + 2*t2 + 2*t1)

    % Current at the DPF Mid-length Region (z = -l_dpf/2; 'Line 2')
    If2   = [0, ...                                                 % 0 < t < 1*t1
             Ib1_p, ...                                             % 1*t1 < t < 3*t1
             Ib1_p + Ib1_m + Ib2_p, ...                             % 3*t1 < t < 5*t1
             Id1_p, ...                                             % (1*t1 + 2*t2) < t <
(1*t1 + 2*t2 + 2*t1)
             Ib1_p + Ib1_m + Ib2_p + Ib2_m + Ib3_p, ...             % 5*t1 < t < 7*t1
             Id1_p + Id1_m + Id2_p, ...                             % (1*t1 + 2*t2 + 2*t1) <
t < (1*t1 + 2*t2 + 4*t1)
             If1_p, ...                                             % (1*t1 + 4*t2) < t <
(3*t1 + 4*t2)
             Ih1_p];                                                % (3*t1 + 2*t2) < t <
(3*t1 + 2*t2 + 2*t1)

    % Current at the DPF Pinch End Region (z = 0; 'Line 2')
    IL    = [0, ...                                                 % 0 < t < (1*t1 + 1*t2)
             Ib1_p + Ib1_m, ...                                     % (1*t1 + 1*t2) < t <
(1*t1 + 3*t2)
             Ib1_p + Ib1_m + Ib2_p + Ib2_m, ...                     % (1*t1 + 3*t2) < t <
(1*t1 + 5*t2)
             Ib1_p + Ib1_m + Ib2_p + Ib2_m + Ib3_p + Ib3_m, ... % (1*t1 + 5*t2) < t <
(1*t1 + 7*t2)
             Id1_p + Id1_m];                                        % (3*t1 + 1*t2) < t <
(3*t1 + 3*t2)

    % ---------------------------------------------------------------------
    % Organize Data -------------------------------------------------------
    % ---------------------------------------------------------------------
    for i = 1:length(time)
        amp_base(i,1) = 0;  % Initialize Amplitude Value (Base End)
        amp_f(i,1)    = 0;  % Initialize Amplitude Value (Mid-length)
        amp_L(i,1)    = 0;  % Initialize Amplitude Value (Pinch End)

        % Voltage Contributions at Base End over time ('Line 1')
        if (time(i) >= 0) && (time(i) < 2*t1)
```

```
                amp_base(i,1)   = amp_base(i,1) + Ibase(1);
            end
            if (time(i) >= 2*t1) && (time(i) < 4*t1)
                amp_base(i,1)   = amp_base(i,1) + Ibase(2);
            end
            if (time(i) >= 4*t1) && (time(i) < 6*t1)
                amp_base(i,1)   = amp_base(i,1) + Ibase(3);
            end
            if (time(i) >= 1*t1 + 2*t2 + 1*t1) && (time(i) < 1*t1 + 2*t2 + 3*t1)
                amp_base(i,1)   = amp_base(i,1) + Ibase(4);
            end

            % Voltage Contributions between 'Line 1' and 'Line 2' over time
            if (time(i) >= 0) && (time(i) < 1*t1)
                amp_f(i,1)      = amp_f(i,1)    + If2(1);
            end
            if (time(i) >= 1*t1) && (time(i) < 3*t1)
                amp_f(i,1)      = amp_f(i,1)    + If2(2);
            end
            if (time(i) >= 3*t1) && (time(i) < 5*t1)
                amp_f(i,1)      = amp_f(i,1)    + If2(3);
            end
            if (time(i) >= 1*t1 + 2*t2) && (time(i) < 1*t1 + 2*t2 + 2*t1)
                amp_f(i,1)      = amp_f(i,1)    + If2(4);
            end
            if (time(i) >= 5*t1) && (time(i) < 7*t1)
                amp_f(i,1)      = amp_f(i,1)    + If2(5);
            end
            if (time(i) >= 1*t1 + 2*t2 + 2*t1) && (time(i) < 1*t1 + 2*t2 + 4*t1)
                amp_f(i,1)      = amp_f(i,1)    + If2(6);
            end
            if (time(i) >= 1*t1 + 4*t2) && (time(i) < 3*t1 + 4*t2)
                amp_f(i,1)      = amp_f(i,1)    + If2(7);
            end
            if (time(i) >= 3*t1 + 2*t2) && (time(i) < 3*t1 + 2*t2 + 2*t1)
                amp_f(i,1)      = amp_f(i,1)    + If2(8);
            end

            % Voltage Contributions at Load End region over time ('Line 2')
            if (time(i) >= 0) && (time(i) < 1*t1 + 1*t1)
                amp_L(i,1)   = amp_L(i,1) + IL(1);
            end
            if (time(i) >= 1*t1 + 1*t2) && (time(i) < 1*t1 + 3*t2)
                amp_L(i,1)   = amp_L(i,1) + IL(2);
            end
            if (time(i) >= 1*t1 + 3*t2) && (time(i) < 1*t1 + 5*t2)
                amp_L(i,1)   = amp_L(i,1) + IL(3);
            end
            if (time(i) >= 1*t1 + 5*t2) && (time(i) < 1*t1 + 7*t2)
                amp_L(i,1)   = amp_L(i,1) + IL(4);
            end
```

```
        if (time(i) >= 3*t1 + 1*t2) && (time(i) < 3*t1 + 3*t2)
            amp_L(i,1)   = amp_L(i,1) + IL(5);
        end
    end
    % ---------------------------------------------------------------------
end

% -------------------------------------------------------------------------
% -------------------------------------------------------------------------
```

“*two_TL_plotter.m*”

```
% Written: Rocky Y. Gonzalez (11/29/2023)
% University of Nevada Las Vegas
% Department of Electrical and Computer Engineering
% Electromagnetics and High-Energetic Physics Lab
% Program: This is function is used clean up and create labels to voltage
%  and current plots for the DPF transmission line time-domain analysis.
% -------------------------------------------------------------------------
% -------------------------------------------------------------------------

function two_TL_plotter(Rb, RL, time, V_L, V_f, V_base, I_L, I_f, I_base)
    % ---------------------------------------------------------------------
    % Plot Voltage at Pinch End, Mid-length, Base End Regions -------------
    % ---------------------------------------------------------------------
    subplot(2,1,1), grid on
    title(strcat("Voltage at Different Points Along the DPF (R_f = ", ...
                 string(Rb), "\Omega, R_L = ", string(RL), "\Omega)"))
    xlabel("Time (s)"), ylabel("Voltage (V)"),

    hold on
    plot(time, V_L), plot(time, V_f), plot(time, V_base)
    hold off

    legend('Voltage at Pinch End', 'Voltage at Mid-length', ...
           'Voltage at Base End', 'Location', 'southeast')

    hline = findobj(gcf, 'type', 'line');
    set(hline,'LineWidth',2);
    hline(1,1).LineStyle = '-.';
    hline(2,1).LineStyle = '--';
    hline(3,1).LineStyle = ':';

    % ---------------------------------------------------------------------
    % Plot Current at Pinch End, Mid-length, Base End Regions -------------
    % ---------------------------------------------------------------------
    subplot(2,1,2), grid on
```

```
        title(strcat("Current at Different Points Along the DPF (R_f = ", ...
                     string(Rb), "\Omega, R_L = ", string(RL), "\Omega)"))
        xlabel("Time (s)"), ylabel("Current (A)")

        hold on
        plot(time, I_L), plot(time, I_f), plot(time, I_base)
        hold off

        legend('Current at Pinch End', 'Current at Mid-length', ...
               'Current at Base End', 'Location', 'southeast')

        hline = findobj(gcf, 'type', 'line');
        set(hline,'LineWidth',2);
        hline(1,1).LineStyle = '-.';
        hline(2,1).LineStyle = '--';
        hline(3,1).LineStyle = ':';

    % -------------------------------------------------------------------------
    % -------------------------------------------------------------------------
```

Appendix B: MATLAB DPF Transmission Line Theory Program

B.1 Overview of the Chapter 2 Transmission Line Theory Program

From Chapter 2, a two-segment transmission line system is analyzed to model voltage and current along a DPF system using Laplace transformation techniques in the analysis. The benefit of this approach gives rise to a simpler solution for voltage and current along the two-segment transmission line model for time $t > 0$ as compared to the analysis in Appendix A. In this appendix, MATLAB scripts are then developed based on the Chapter 2 analysis. These scripts are designed to verify experiments performed in Chapter 3 and Chapter 4 of this thesis. However, the data simulated from these MATLAB scripts are constrained to numerical computation inverse Laplace Transform algorithms consistent with [35].

From the MATLAB script "*dpf_tl_main_file.m*", lines 10 through 33 provide a list of variables that can be modified to adjust the parameters of the two-segment transmission line circuit from Chapter 2. The mock DPF distributed parameters are defined in lines 13-16. Notice the distributive resistance and distributive conductance are set to zero consistent with the lossless assumption made on the mock DPF. The distributed capacitance and distributed inductance are defined by values characterized by the TDR experiment in Chapter 3, Section 3.2.3.

The circuit parameters of the mock DPF system are defined in lines 18-23. Notice that the initial voltage supplied by the capacitor is set to $12V$ and the capacitor is set at $3.3\mu F$. The initial voltage and capacitance are set to reflect the same values used in the experiment at the end of Section 3.3.1. The series resistance is set to $1m\Omega$ ($R_s \ll R_L$) and the load resistance to 17Ω which is approximately the characteristic impedance of the mock DPF. These values were selected to simulate data that can be compared to a known experiment as captured at the end of Section 3.3.1.

The length of the mock DPF is defined by lines 24 and 25. The sum of these two variables results in the total length of the mock DPF. The fault path defined by variable Rf is positioned at the location in which ‘line a’ length ends. The variable z_div defined in line 26 divides the total length of the mock DPF by the set value. For example, this value is important for determining the spatial step size simulated along the mock DPF transmission line. In the example of defining z_div by 2, a total of 3 spatial points along the line will be simulated starting at zero and taking a spatial step until the total length of the mock DPF is reached. In other words, data is simulated for points at $z = 0$, $z = l_{DPF}/2$, and $z = l_{DPF}$.

In lines 28-32 of the MATLAB program, the resolution of the simulated data can be modified. However, the higher the resolution of the data, the longer it takes for the program to compute simulation results. In Fig. B.1, the program is set to simulate $300\mu s$ worth of data starting at time $t = 0 + 1ps$ with data sampled every $1\mu s$. A $1ps$ offset is implemented into the sample length of data to prevent division by zero in the numerical inverse Laplace transforms algorithms that are part of the MATLAB program implementation. For a larger sample rate, the resolution of the simulated data will increase, but will take longer to run. For a smaller sample rate, the resolution of the simulated data will begin to decrease. Running the program at higher speeds results in less accurate computation.

dpf_tl_main_file.m

```
% Created: Rocky Y. Gonzalez (03/15/2021)
% Updated: Rocky Y. Gonzalez (09/12/2022)
% University of Nevada Las Vegas
% Department of Electrical and Computer Engineering
% Electromagnetics and High-Energetic Physics Lab
% Program: Original Main File for computing DPF TL Problem.

clear all, clc, close all

% --------------------------------------------------------------------------
% Variables ----------------------------------------------------------------
% --------------------------------------------------------------------------
Rd = 0;             % Distributed Resistance  of DPF Transmission Line
Gd = 0;             % Distributed Conductance of DPF Transmission Line
Ld = 80E-9;         % Distributed Inductance  of DPF Transmission Line
Cd = 290E-12;       % Distributed Capacitance of DPF Transmission Line

V0 = 12;            % Initial Voltage Supplied to DPF '(z=-l_dpf, t=0)'
Rs = 1e-3;          % Series Resistance Connected to DPF
C = 3.3e-6;         % Discharge Capacitor Value of DPF
Rf = 1e6;           % Fault Resistance of DPF
RL = 17;            % Load  Resistance of DPF (Assuming infinite/open load)

la = 0.2936875;     % Length between fault and end of the DPF Line (meters)
lb = 0.2936875;     % Length between source and fault (meters)
z_div = 2;          % Divide DPF Length by 'z_div' ('z' points of DPF)

os = 1e-12;         % Very Small Offset to Prevent Division by Zero in Program
t1 = 0 + os;        % Start sampling data at time -> 0ns
t0 = 300e-6 + os;   % End of State 1 Sampling
t2 = t0;            % Total length of Sampling Time (For State 2 Sampling)
ts = 1e-6;          % Sample Voltage/Current every '0.1ns'

% --------------------------------------------------------------------------
% Program Start ------------------------------------------------------------
% --------------------------------------------------------------------------
% NOTE: The Program can be broken into 4 different parts -------------------
% --------------------------------------------------------------------------
% (1) Obtain the voltage and current for all 'z' and all 't' in the DPF
%     when 't < t0' (during State 1). Extract this voltage and current
%     information from State 1.
% --------------------------------------------------------------------------
TL_prop    = [Rd, Gd, Ld, Cd];      % Transmission Line (TL) Properties
Circuit    = [V0, Rs, C, Rf, RL];   % Circuit Components in TL
TL_spatial = [la, lb, z_div];       % Spatial Variation in TL
TL_time    = [t1, t0, t2, ts];      % Time Variation in TL State 1

[v1,i1] = collect_state1_sym(Circuit, TL_prop, TL_spatial, TL_time);
```

```

figure(2),
subplot(2,1,1), plot(t1:ts:t2, v1)
title(['DPF Voltage in State 1 at \{0 < Z < ',num2str(-la-lb),'\}'])
xlabel('Time (s)'), ylabel('Voltage on Line a,b (V)')
subplot(2,1,2), plot(t1:ts:t2, i1)
title(['DPF Current in State 1 at \{0 < Z < ',num2str(-la-lb),'\}'])
xlabel('Time (s)'), ylabel('Current on Line a,b (A)')
```

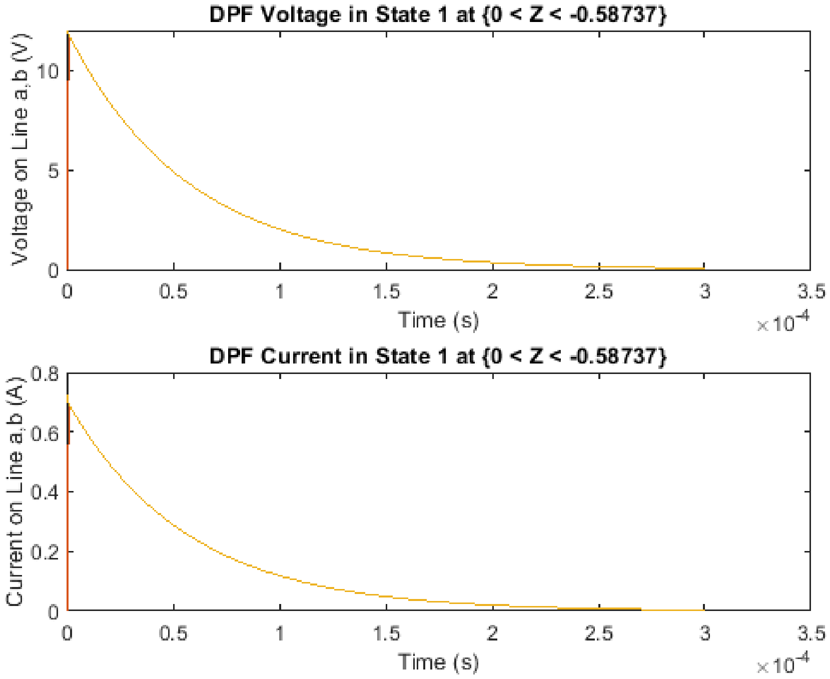

Fig. B.1 From Chapter 3, Section 3.3.1, an experiment was performed to measure the bandwidth of the pulse signal for an RC source type configuration connecting to the mock DPF. Using the parameters from this experiment into the MATLAB "*dpf_tl_main_file.m*" script, the provided voltage and current data is plotted. Ignoring mechanical ground bounce from the experiment, the simulated data demonstrates a $12V$ peak signal exponentially decaying with an approximate $120\mu s$ pulse width consistent with the experiment.

From the main MATLAB program script "*dpf_tl_main_file.m*", a custom function is called "*collect_state1_sym.m*". This script comprises of the formulas from the two-segment transmission line analysis in Chapter 2. The parameters listed in the main script are used to perform the computation. In the "*collect_state1_sym.m*" script, additional functions "*euler_inversion.m*" and "*talbot_inversion.m*" are called to compute the numerical inverse Laplace transformations for the analysis [37]. These functions are available through the MathWorks website [37]. From these functions, division of zero is not allowed. To prevent this division of zero, a small offset variable "*os*" is added into the program variable list. Notice on line 29 of the "*collect_state1_sym.m*" program, this offset is set to 1e-12. This offset is set to be very small such that the first data point is very close to time $t = 0$ but avoids division by zero errors in the program. Further, in the program, the "*euler_inversion.m*" and the "*talbot_inversion.m*" functions have been slightly modified to prevent the loss of data due to division by zero rounding errors.

collect_state1_sym.m

```
% Created: Rocky Y. Gonzalez (10/01/2020)
% Updated: Rocky Y. Gonzalez (08/16/2021)
% University of Nevada Las Vegas
% Department of Electrical and Computer Engineering
% Electromagnetics and High-Energetic Physics Lab
% Program: Collect the Voltage/Current Datasets from State 1 of DPF TL.
%
% -------------------------------------------------------------------------
% -------------------------------------------------------------------------

function [v1,i1] = collect_state1_sym(Circuit, TL_prop, TL_spatial, TL_time)

    % ---------------------------------------------------------------------
    % Variables -----------------------------------------------------------
    % ---------------------------------------------------------------------
    % Extract Individual Variables from 'Grouped Variables'
    [Rd, Gd, Ld, Cd]     = deal(TL_prop(1),TL_prop(2),TL_prop(3),TL_prop(4));
    [V01, Rs, C, Rf, RL] = deal(Circuit(1),Circuit(2),Circuit(3),Circuit(4),Circuit(5));
    [la, lb, z_div]      = deal(TL_spatial(1),TL_spatial(2),TL_spatial(3));
    [t1, t0, t2, ts]     = deal(TL_time(1),TL_time(2),TL_time(3),TL_time(4));

    % Extra Derivable Variables
    l_DPF = la+lb;          % Total Axial Length of DPF
    time = t1:ts:t0;        % Sampling between times 't1' to 't0' (State 1)

    % ---------------------------------------------------------------------
    % State 2 - Preliminary Equations -------------------------------------
    % ---------------------------------------------------------------------
    % Characterist Impedance/Propagation Constant
    Z0a = @(s) sqrt((s*Ld+Rd)/(s*Cd+Gd));
    Z0b = @(s) Z0a(s);
    gam_a = @(s) sqrt((s*Ld+Rd)*(s*Cd+Gd));
    gam_b = @(s) gam_a(s);

    % Input/Load Impedances Seen by TL
    Zina1 = @(s) Z0a(s)*(RL*cosh(gam_a(s)*la) + Z0a(s)*sinh(gam_a(s)*la))/...
                        (RL*sinh(gam_a(s)*la) + Z0a(s)*cosh(gam_a(s)*la));

    ZLb1  = @(s) Rf*Zina1(s)/(Rf+Zina1(s));

    Zinb1 = @(s) Z0b(s)*(ZLb1(s)*cosh(gam_b(s)*lb) + Z0b(s)*sinh(gam_b(s)*lb))/...
                        (ZLb1(s)*sinh(gam_b(s)*lb) + Z0b(s)*cosh(gam_b(s)*lb));

    %----------------------------------------------------------------------
    % State 1 - Preliminary Laplace Domain Coupled Equations --------------
    %----------------------------------------------------------------------
    Q0b1_plus = @(s) (V01*(ZLb1(s)+Z0b(s))*Z0b(s)*C)/...
              ((1+s*(Rs+Zinb1(s))*C)*(ZLb1(s)*sinh(gam_b(s)*lb) +
```

```
Z0b(s)*cosh(gam_b(s)*lb)));

    Q0b1_minus = @(s) Q0b1_plus(s)*(ZLb1(s)-Z0b(s))/(ZLb1(s)+Z0b(s));

    Q0a1_plus = @(s) Q0b1_plus(s)*ZLb1(s)*(RL+Z0a(s))/...
              ((ZLb1(s)+Z0b(s))*(RL*cosh(gam_a(s)*la) + Z0a(s)*sinh(gam_a(s)*la)));

    Q0a1_minus = @(s) Q0a1_plus(s)*(RL-Z0a(s))/(RL+Z0a(s));

    %----------------------------------------------------------------------
    % Inverse Laplace Transforming / Plotting -----------------------------
    %----------------------------------------------------------------------
    for k = 1:(z_div+1)                 % Index Position of DPF TL Space
        z = (k-1)*(-l_DPF/z_div);       % Actual Position of DPF TL [m]
        ext_time = t1:ts:t2;            % Extend Sampling from 't1' to 't2'
        fpass = 0.1;
        M = 16;

        figure(1)
        if z >= -la
            Va1 = @(s) (Q0a1_plus(s)*exp(-gam_a(s)*z) + ...
                        Q0a1_minus(s)*exp(gam_a(s)*z))/2;

            Ia1 = @(s) (Q0a1_plus(s)*exp(-gam_a(s)*z) - ...
                        Q0a1_minus(s)*exp(gam_a(s)*z))/(2*Z0a(s));

            va1(:,k) = euler_inversion_sym(Va1, ext_time, M);
%            va1(:,k) = lowpass(va1(:,k),fpass);
            hold on, subplot(2,1,1), plot(ext_time, transpose(va1(:,k))), hold off
            ia1(:,k) = euler_inversion_sym(Ia1, ext_time, M);
%            ia1(:,k) = lowpass(ia1(:,k),fpass);
            hold on, subplot(2,1,2), plot(ext_time, transpose(ia1(:,k))), hold off

        else
            Vb1 = @(s) (Q0b1_plus(s)*exp(-gam_b(s)*(z+la)) + ...
                        Q0b1_minus(s)*exp(gam_b(s)*(z+la)))/2;

            Ib1 = @(s) (Q0b1_plus(s)*exp(-gam_b(s)*(z+la)) - ...
                        Q0b1_minus(s)*exp(gam_b(s)*(z+la)))/(2*Z0b(s));

            vb1(:,k) = euler_inversion_sym(Vb1, ext_time, M);
%            vb1(:,k) = lowpass(vb1(:,k),fpass);
            hold on, subplot(2,1,1), plot(ext_time, transpose(vb1(:,k))), hold off
            ib1(:,k) = euler_inversion_sym(Ib1, ext_time, M);
%            ib1(:,k) = lowpass(ib1(:,k),fpass);
            hold on, subplot(2,1,2), plot(ext_time, transpose(ib1(:,k))), hold off

        end
    end

    figure(1), subplot(2,1,1)
```

```
    title(['DPF Voltage in State 1 at \{0 < Z < ',num2str(z),'\}'])
    xlabel('Time (s)'), ylabel('Voltage on Line a,b (V)')

    figure(1), subplot(2,1,2)
    title(['DPF Current in State 1 at \{0 < Z < ',num2str(z),'\}'])
    xlabel('Time (s)'), ylabel('Current on Line a,b (A)')

    %----------------------------------------------------------------------
    % Datasets and Final Notes --------------------------------------------
    %----------------------------------------------------------------------
    % Note1: The last two equations of this section represent the dataset
    % for voltage/current anywhere on the DPF TL from time 't1 < t < t0'.
    % The 'm-th'-row represents voltage/current at fixed time from
    % '0:-(la+lb)/z_div:-(la+lb)'. The 'n-th' column represents the
    % voltage/current at fixed space from 't1:ts:t0'.
    %
    % Note2: v1(k1,k2) and i1(k1,k2)...
    %        -> 't = (k1-1)/ts + t1' for 'k1 = 1,2,3,...,(t0/ts+1)
    %        -> 'z = -l_DPF*((k2-1)/z_div)' for 'k2 = 1,2,3,...,(z_div+1)'
    %
    % Examples with numbers
    % Ex1: v1(:,5)     -> Voltages at 'z = -5*(la+lb)/z_div (m)' & 't1 < t < t0'
    % Ex2: v1(5,:)     -> Voltages for all 'z' at 'time = 5*ts (s)'
    %
    % Examples of Special Cases
    % Ex3: v1(:,1)       -> Voltages at the End of the DPF, for 't1 < t < t0'
    % Ex4: i1(:,z_div+1) -> Current at the Base of the DPF, for 't1 < t < t0'
    % Ex5: i1(t0/ts+1,:) -> Current for all 'z' at time of the fault/state change
    v1 = [va1(:,:), vb1(:,(size(va1,2)+1):end)];
    i1 = [ia1(:,:), ib1(:,(size(ia1,2)+1):end)];
end
%--------------------------------------------------------------------------
```

Appendix C: DPF Machine Parameters

C.1 DPF Machine Parameters Summary

From Chapter 3, parameters for the mock DPF experimental apparatus are characterized through measurement and experimentation. This appendix provides a summarization of the measured information characterizing the mock DPF system.

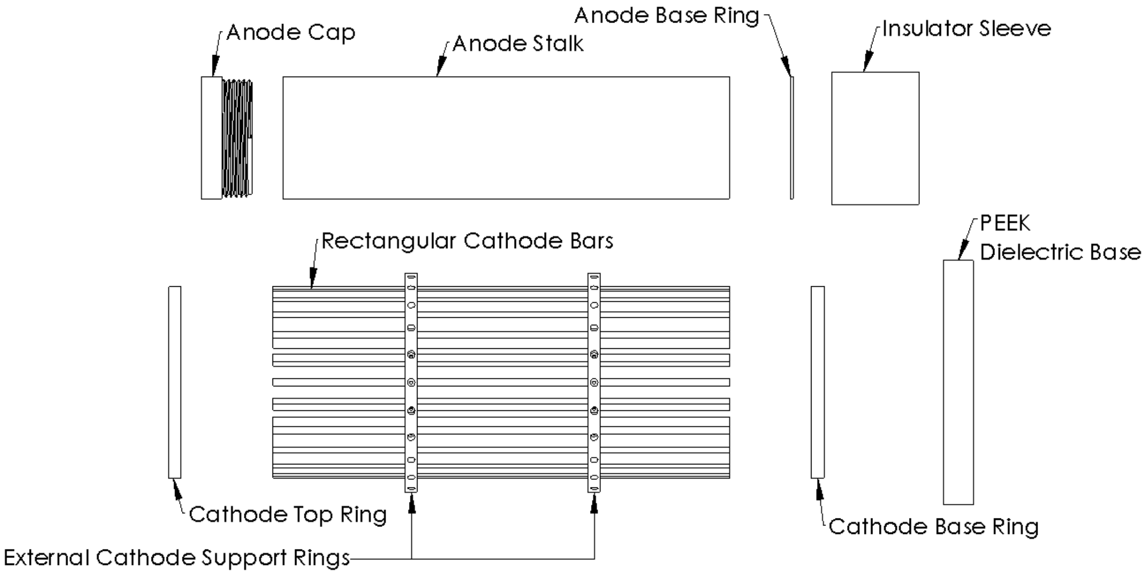

Fig. C.1 A schematic is shown depicting the different components used to assemble the mock DPF for this research.

Table C.1 The physical dimensions of the mock DPF parts, required for assembly and transmission line characterization, have been measured and organized into a table.

Quantity	Symbol	Ideal Value	Tolerance	Measured Value
Total length of the DPF coaxial structure	l_{DPF}	$23.125''$ $(0.587375m)$	$1/32''$	$23.1''$ $(0.588m)$
Total number of cathode bars	N	24	-	24
Length of rectangular cathode bars w/ dimensions of $0.375''\ x\ 1''$ $(0.953\ cm\ x\ 2.54\ cm)$	$l_{c,bar}$	$21.875''$ $(0.555625m)$	$1/32''$	$21.9''$ $(0.556m)$
Length of cathode base ring and top ring w/ $OD = 9.4375''\ (0.240m)$, $ID = 7.4375''\ (0.189m)$	$l_{c,ring}$	$0.625''$ $(15.875\ mm)$	$1/32''$	$0.6''$ $(15mm)$
Length of external cathode support rings w/ $OD = 10.75''\ (0.273\ m)$, $ID = 9.4375''\ (0.240\ m)$	$l_{c,ext\ ring}$	0.625” $(15.875\ mm)$	$1/32''$	0.6” $(15mm)$
Total cathode length	$l_{DPF} = 2 \cdot l_{c,ring} + l_{c,bar}$	23.125” $(0.587375\ m)$	$1/32''$	23.1” $(0.587m)$
Length of anode cap protrusion (non-threaded) w/ $OD = 6$” $(0.152\ m)$	$l_{a,cap}$	1” $(2.54\ cm)$	$1/32''$	1” $(2.5cm)$
Length of anode tube w/ $OD = 6$” $(0.152\ m)$, $ID = 5.5$” $(0.140\ m)$	$l_{a,tube}$	22” $(0.559\ m)$	$1/32''$	22” $(0.559m)$
Length of anode ring w/ $OD = 6$” $(0.152\ m)$, $ID = 5.5$” $(0.140\ m)$	$l_{a,ring}$	0.125” $(3.175\ mm)$	$1/32''$	0.13” $(3mm)$

Total anode length	$l_{DPF} = l_{a,cap} + l_{a,tube} + \cdots \dots + l_{a,ring}$	23.125” $(0.587375\ m)$	$1/32"$	23.1” $(0.587m)$
DPF base insulator sleeve w/ $OD = 6.5”\ (0.165\ m)$, $ID = 6”\ (0.152\ m)$	l_{ins}	4.3" $(0.109\ m)$	$1/32"$	4.3" $(0.1m)$

Table C.2 The transmission line properties of the mock DPF have organized into a table as extracted from experimentation in Chapter 3.

Quantity	Symbol	Ideal Value
Distributed Resistance of the mock DPF	$\bar{R}$	$0\,\frac{\Omega}{m}$
Distributed Conductance of the mock DPF	$\bar{G}$	$0\,\frac{S}{m}$
Measured Distributed Capacitance of the mock DPF	$\bar{C}$	$290\,\frac{pF}{m}$
Measured Distributed Inductance of the mock DPF	$\bar{L}$	$80\,\frac{nH}{m}$
Outer Radius of mock DPF Anode	a	6.0"
Inner Radius of mock DPF Cathode	b	7.4"
Permittivity Between the Anode and Cathode of the mock DPF	ε_0	$8.85 \cdot 10^{-12}\,\frac{F}{m}$
Permeability of Conductors for the Anode and Cathode of the mock DPF	μ_0	$4\pi \cdot 10^{-7}\,\frac{H}{m}$
Characteristic Impedance of the mock DPF modeled as a coaxial cable	$\mathcal{Z}_{DPF} = \left[\frac{s\bar{L} + \bar{R}}{s\bar{C} + \bar{G}}\right]^{1/2}$	13Ω
Measured Characteristic	$\mathcal{Z}_{DPF}$	16.7Ω

Impedance of the mock DPF using a Cable Tester		
Measured Capacitor bank used to discharge a pulse into the DPF	C	$3.30uF$
Series resistance in the DPF system	R_s	0Ω
Matching Load Termination Resistance of the mock DPF	R_L	16.7Ω
Resistor 1 used to match the Pulse Generator onto a 50 Ω load	R_1	200Ω
Resistor 2 used to match the Pulse Generator onto a 50 Ω load	R_2	51Ω
Transit Time of a $5ft$ BNC Cable	$t_{d,DPF} = \frac{l_{DPF}}{c}$	$7.3ns$
Transit Time of the mock DPF	τ_{DPF}	$2.85ns$

Appendix D: Mock DPF Experiments

D.1 Experiment 1: Modifying Linear Antenna Lengths

In Chapter 4, Section 4.4.1, an experiment is documented in which a pulse generator is utilized to discharge a $4kV$, $20ns$ pulse signal into an AWG 4 insulated wire terminated by a ceramic load resistor of $R_L = 50\Omega$. A linear antenna is positioned perpendicularly external to an AWG 4 wire. Oscilloscope captures are then taken from the pulse generator output connected to channel 1 (attenuated by 60dB) and the linear antenna connected to channel 2 in the experiment.

In Section 4.4.1, graphs are presented for oscilloscope channels 1 and 2 separately providing direct signal comparison when modifying the linear antenna's length in the experiment. This section is intended to provide the oscilloscope captures where the data is extrapolated from. The data from this experiment was captured on April 29th, 2021. Further information about this experiment can be referred back to in Chapter 4, Section 4.4.1.

In Fig. D.1 (a, b, c, d), images are provided for linear antennas of different lengths as measured by a ruler. In Fig. D.2 (a, b, c, d), images are provided for each setup when using the different antenna lengths in this experiment. For each setup representing the different antenna lengths, oscilloscope captures are then provided in Fig. D.3 – Fig. D.6.

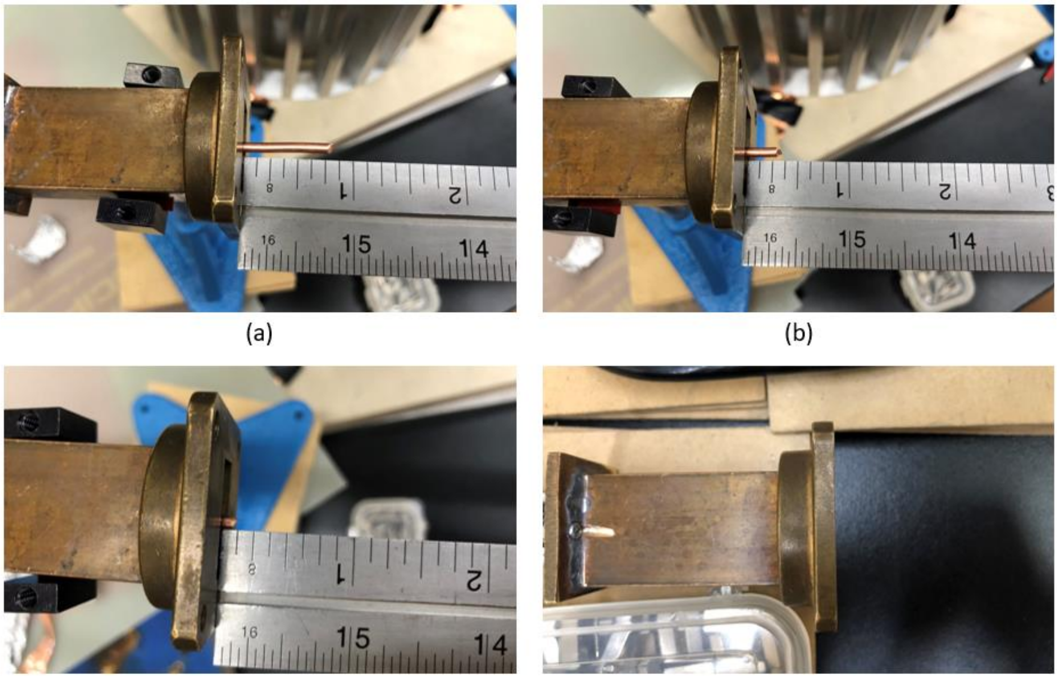

(a) (b)

(c) (d)

Fig. D.1 (a, b, c, d) A wire is centered along a straight X-band waveguide that can be shown protruding from its opening side with different linear antenna lengths as measured by a ruler: (a) $+2.2cm$, (b) $+1.0cm$, (c) $+0.3cm$, and (d) $0cm$. On the other side of the waveguide, a BNC termination connects its center pin to the internal wire and its outer termination to the waveguide. This antenna structure is then connected to a BNC cable connected to oscilloscope channel 2.

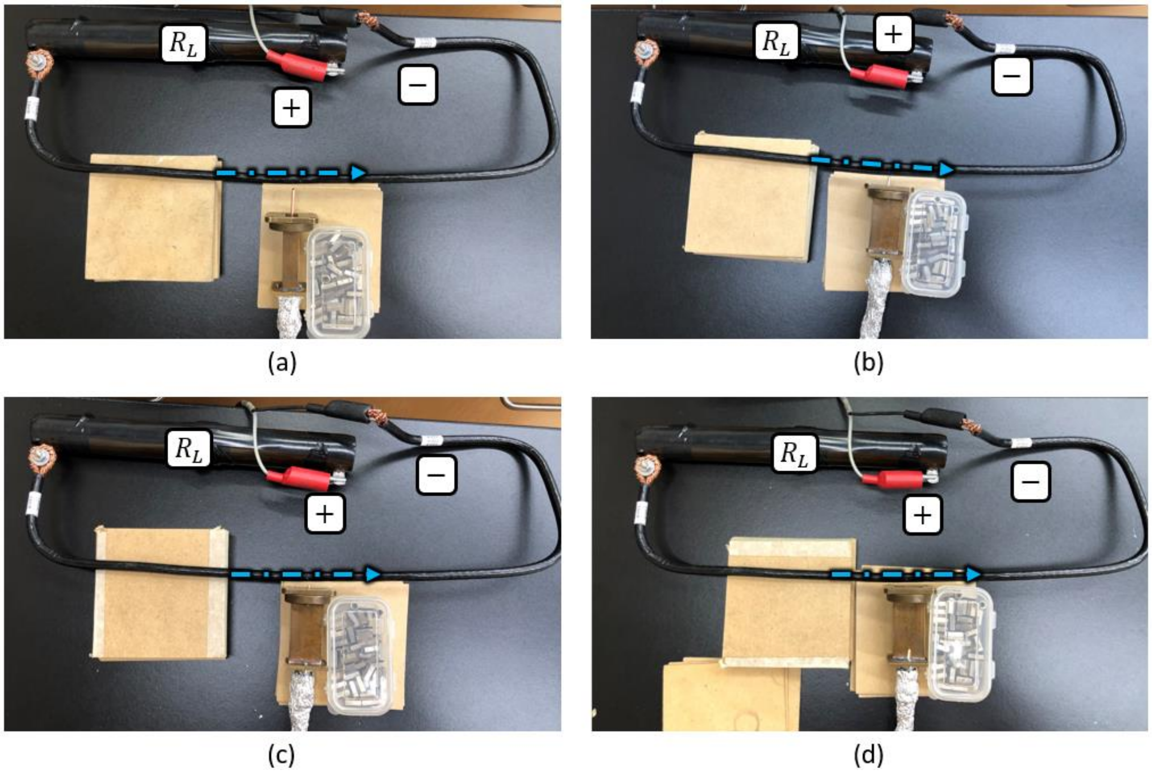

(a) (b) (c) (d)

Fig. D.2 (a, b, c, d) In this experiment, a pulse generator is used to fire a $4kV$, $20ns$ pulse signal into an AWG 4 insulated wire with a 50Ω ceramic load resistor termination. Oscilloscope channel 1 is connected to the pulse generator output monitor (60dB attenuated pulse signal replica) and channel 2 to the linear antenna waveguide structure. The experimental setup is shown for each of the antenna lengths: (a) $+2.2cm$, (b) $+1.0cm$, (c) $+0.3cm$, and (d) $0cm$.

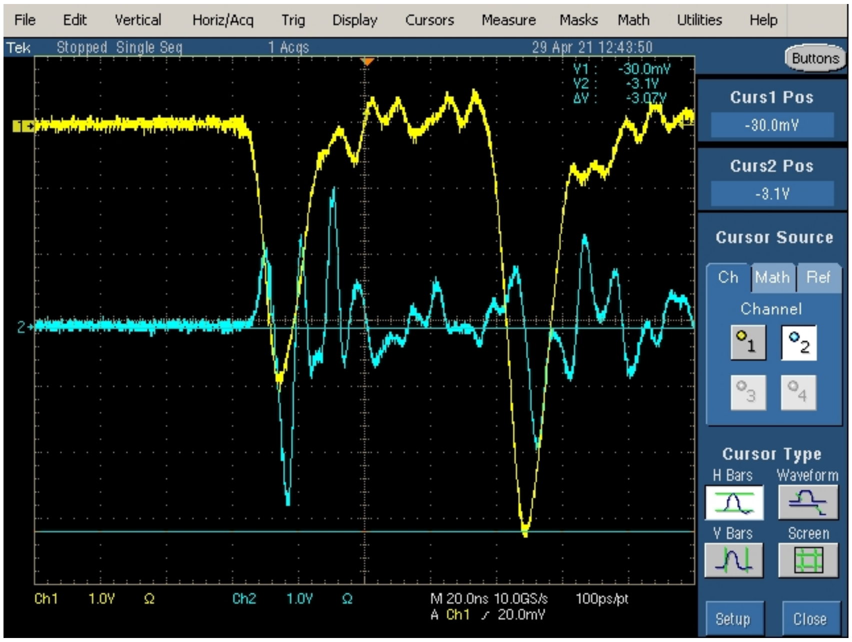

Fig. D.3 A $4kV$, $20ns$ pulse is fired into an AWG 4 insulated wire where channel 1 of the oscilloscope capture represents the $60dB$ attenuated pulse signal replica. Channel 2 represents the signal captured by the linear antenna waveguide structure with a $+2.2cm$ protruding length.

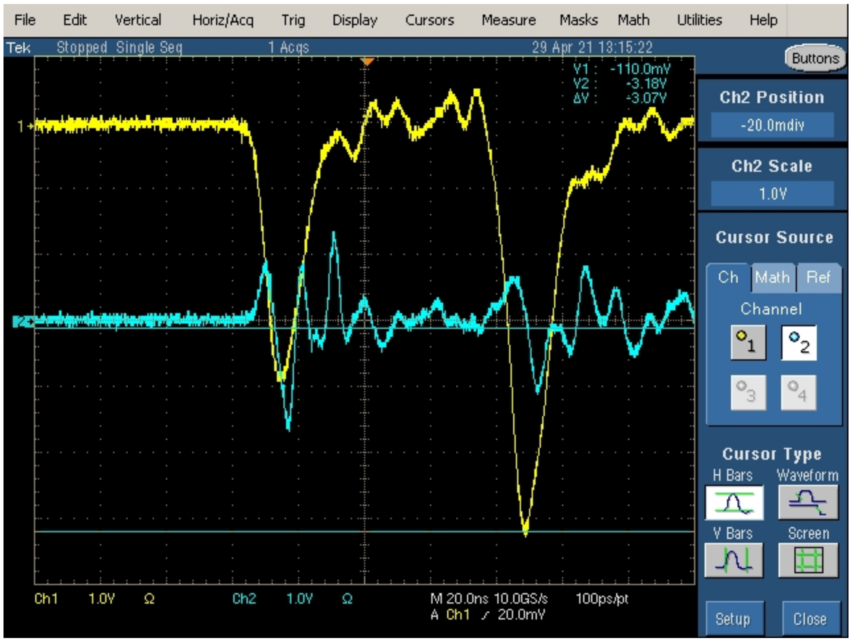

Fig. D.4 A $4kV$, $20ns$ pulse is fired into an AWG 4 insulated wire where channel 1 of the oscilloscope capture represents the $60dB$ attenuated pulse signal replica. Channel 2 represents the signal captured by the linear antenna waveguide structure with a $+1.0cm$ protruding length.

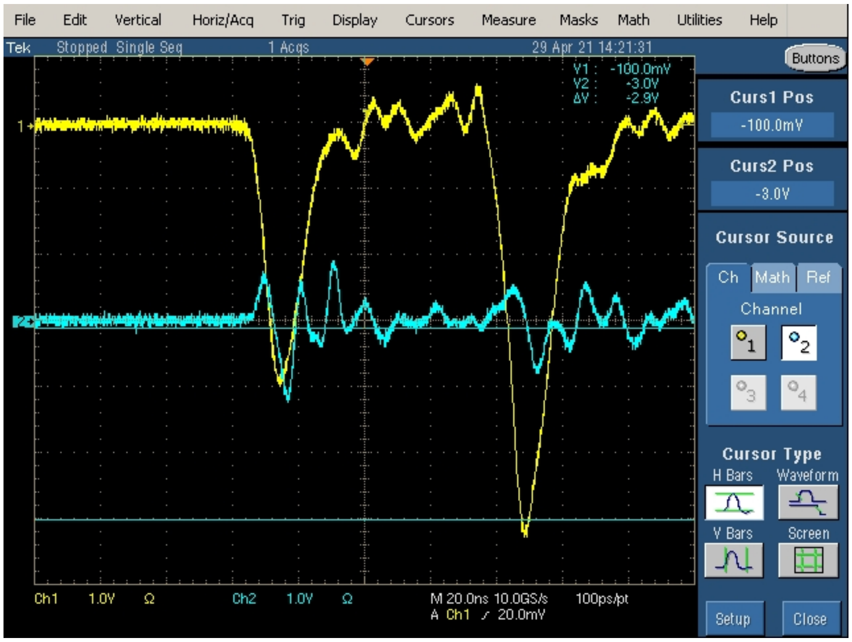

Tek Stopped Single Seq 1 Acqs 29 Apr 21 14:21:31

V1 : -100.0mV
V2 : -3.0V
ΔV : -2.9V

Curs1 Pos -100.0mV

Curs2 Pos -3.0V

Ch1 1.0V Ω Ch2 1.0V Ω M 20.0ns 10.0GS/s 100ps/pt
A Ch1 ⁄ 20.0mV

Fig. D.5 A $4kV$, $20ns$ pulse is fired into an AWG 4 insulated wire where channel 1 of the oscilloscope capture represents the $60dB$ attenuated pulse signal replica. Channel 2 represents the signal captured by the linear antenna waveguide structure with a $+0.3cm$ protruding length.

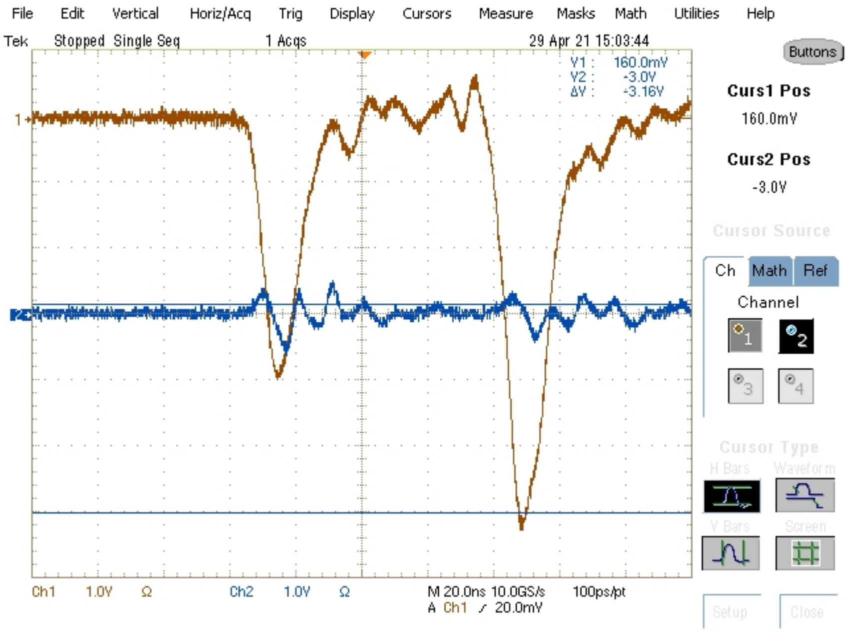

Tek Stopped Single Seq 1 Acqs 29 Apr 21 15:03:44

V1 : 160.0mV
V2 : -3.0V
ΔV : -3.16V

Curs1 Pos 160.0mV

Curs2 Pos -3.0V

Ch1 1.0V Ω Ch2 1.0V Ω M 20.0ns 10.0GS/s 100ps/pt
A Ch1 ⁄ 20.0mV

Fig. D.6 A $4kV$, $20ns$ pulse is fired into an AWG 4 insulated wire where channel 1 of the oscilloscope capture represents the $60dB$ attenuated pulse signal replica. Channel 2 represents the signal captured by the linear antenna waveguide structure with a $0cm$ protruding length.

Notable takeaways from the oscilloscope captures in Fig. D.3 – Fig. D.6 show that a double pulse feature can be observed from channel 1 (the $60dB$ attenuated pulse signal replica from the pulse generator output monitor). It has been deduced that the 50Ω ceramic load resistor termination used in this experiment is potentially influencing the pulse generator signal output. The next experiment in this section, a clean single pulse signal is achieved and demonstrated when using the 50Ω mock DPF termination as characterized by the setup in Chapter 3 Section 3.3.3. Regardless, the pulse signal fired by the pulse generator in Fig. D.3 – Fig. D.6 are consistent. Another notable takeaway from this experiment is that the signal captured by channel 2 (connecting the linear antenna waveguide structure) can be shown decreasing in amplitude when decreasing the length of the linear antenna. Thus, a longer exposed antenna length is preferred for capturing larger signal amplitudes.

In Section 4.4.1, a continuation of this experiment is performed except replacing the AWG 4 insulated wire terminated by the 50Ω ceramic load resistor with the mock DPF setup as characterized by the circuit in Chapter 3 Section 3.3.3. In this setup, two resistors at the input of the mock DPF are required to match the impedance of the pulse generator. In Fig. D.7 (a, b), images are provided for two setups of the linear antenna waveguide structure at a fixed height external to the mock DPF with a difference in modified antenna lengths. It should be noted that the antenna waveguide structure does not touch the external cathode cage of the mock DPF. Oscilloscope captures are provided in Fig. D.8 – Fig. D.11 when modifying the antenna lengths in this experiment for: $2.2cm$, $1.0cm$, $0.3cm$, and $0cm$.

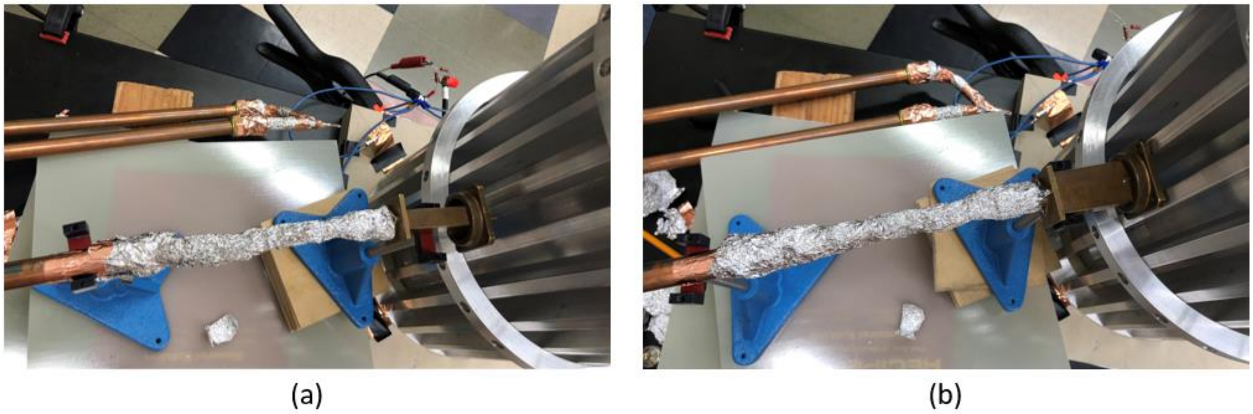

Fig. D.7 (a, b) A pulse generator is used to fire a $4kV$, $20ns$ pulse signal into a mock DPF with two input resistors and load for impedance matching. Oscilloscope channel 1 is connected to the pulse generator output monitor (60dB attenuated pulse signal replica) and channel 2 connects to the linear antenna waveguide structure. Setups are shown for antenna lengths (a) $+2.2cm$ and (b) $0cm$. Measurements are also taken with $+1.0cm$ and $+0.3cm$ antenna lengths but not shown.

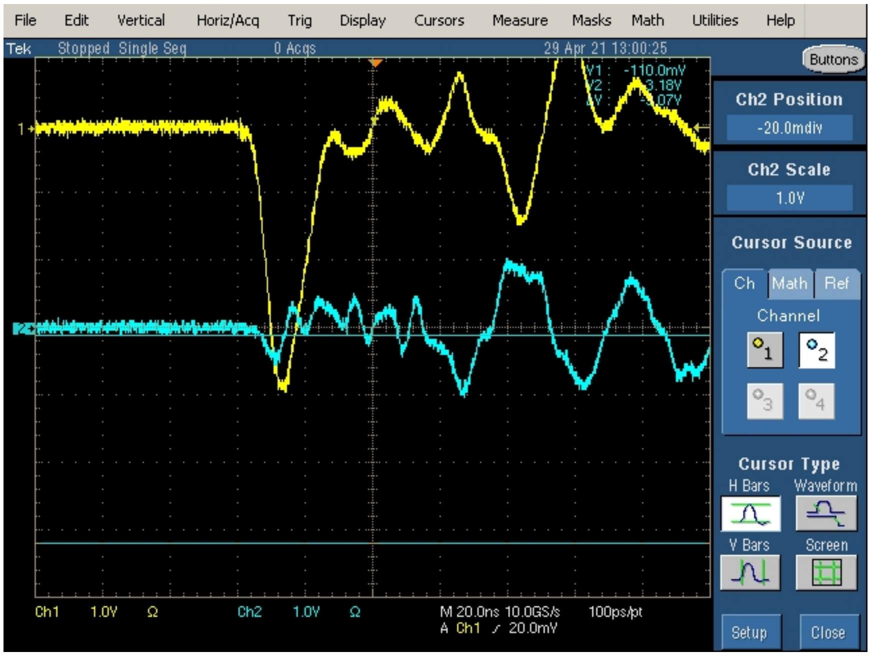

Fig. D.8 A $4kV$, $20ns$ pulse is fired into the mock DPF where channel 1 of the oscilloscope capture represents the $60dB$ attenuated pulse signal replica. Channel 2 represents the signal captured by the linear antenna waveguide structure with a $+2.2cm$ protruding length.

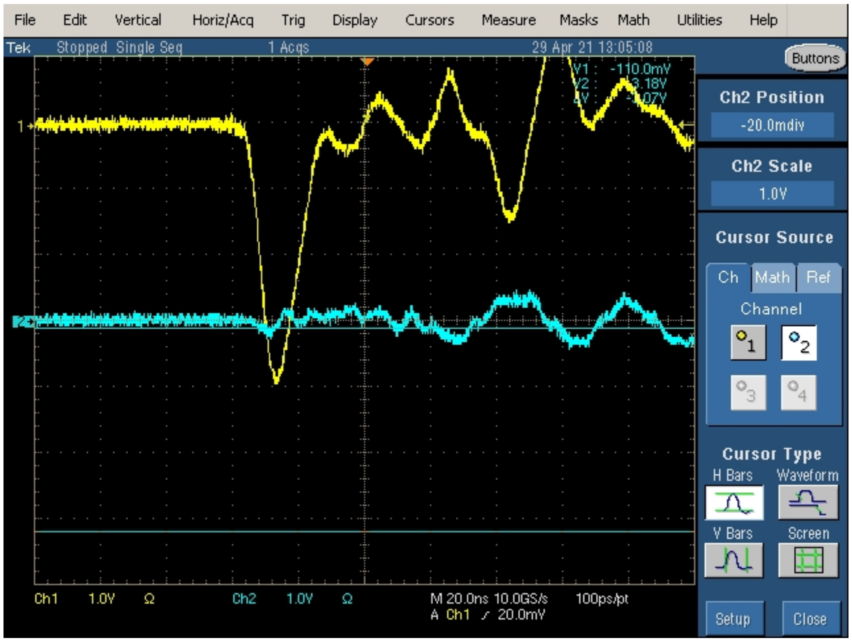

Stopped Single Seq 1 Acqs 29 Apr 21 13:05:08

V1 : -110.0mV
V2 : -3.18V
ΔV : -3.07V

Ch2 Position -20.0mdiv

Ch2 Scale 1.0V

Ch1 1.0V Ω Ch2 1.0V Ω M 20.0ns 10.0GS/s 100ps/pt
A Ch1 ⁄ 20.0mV

Fig. D.9 A $4kV$, $20ns$ pulse is fired into the mock DPF where channel 1 of the oscilloscope capture represents the $60dB$ attenuated pulse signal replica. Channel 2 represents the signal captured by the linear antenna waveguide structure with a $+1.0cm$ protruding length.

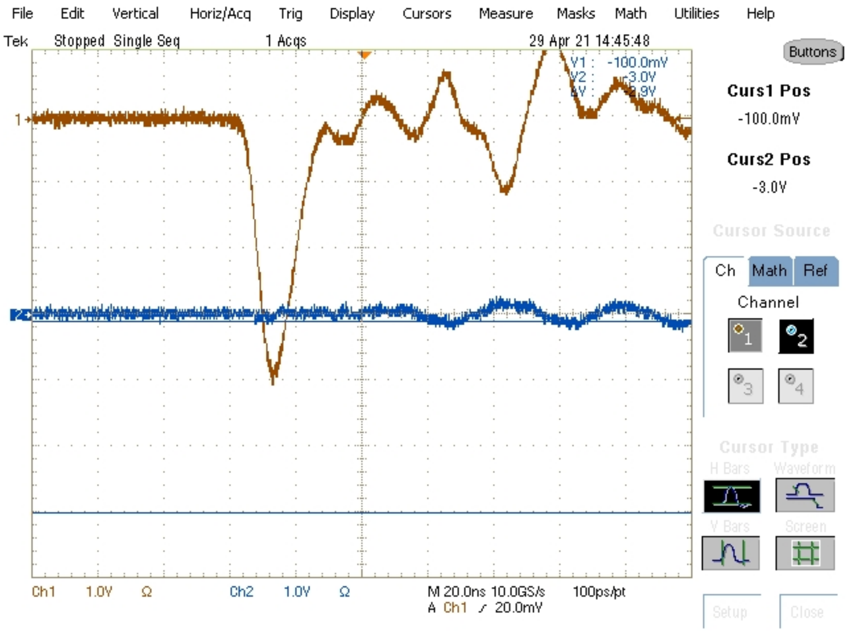

Stopped Single Seq 1 Acqs 29 Apr 21 14:45:48

V1 : -100.0mV
V2 : -3.0V
ΔV : -2.9V

Curs1 Pos -100.0mV

Curs2 Pos -3.0V

Ch1 1.0V Ω Ch2 1.0V Ω M 20.0ns 10.0GS/s 100ps/pt
A Ch1 ⁄ 20.0mV

Fig. D.10 A $4kV$, $20ns$ pulse is fired into the mock DPF where channel 1 of the oscilloscope capture represents the $60dB$ attenuated pulse signal replica. Channel 2 represents the signal captured by the linear antenna waveguide structure with a $+0.3cm$ protruding length.

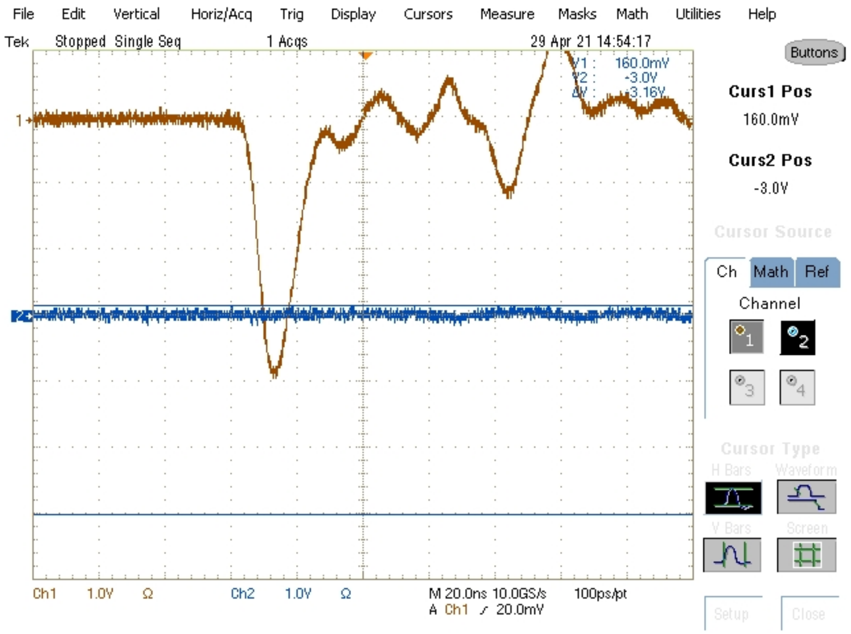

Tek Stopped Single Seq 1 Acqs 29 Apr 21 14:54:17

V1 : 160.0mV
V2 : -3.0V
ΔV : 3.16V

Curs1 Pos
160.0mV

Curs2 Pos
-3.0V

Ch1 1.0V Ω Ch2 1.0V Ω M 20.0ns 10.0GS/s 100ps/pt
A Ch1 ⟋ 20.0mV

Fig. D.11 A $4kV$, $20ns$ pulse is fired into the mock DPF where channel 1 of the oscilloscope capture represents the $60dB$ attenuated pulse signal replica. Channel 2 represents the signal captured by the linear antenna waveguide structure with a $0cm$ protruding length.

Notice that from this version of the experiment, channel 1 connecting the output monitor of the pulse generator demonstrates a better performing single pulse. This helps verify that the ceramic resistor in the previous setup has distorted the pulse generator signal. This information also helps verify that a matched system reduces distortion in the pulse generator. Secondly, consistent with the AWG 4 insulated wire setup, channel 2 connecting the linear antenna can be shown to decrease in amplitude when decreasing the length of the linear antenna. Thus, a longer antenna length is preferred to capture larger signal amplitudes as shown in both the AWG 4 wire and mock DPF setup.

D.2 Experiment 2: Modifying Linear Antenna Orientations

In Chapter 4, Section 4.4.2, an experiment is documented in which a pulse generator is utilized to discharge a $4kV$, $20ns$ pulse into an AWG 4 insulated wire terminated by a high-wattage through-hole load resistor of $R_L = 50\Omega$. Similar to the previous section, a linear antenna is positioned external to an AWG 4 wire. Oscilloscope captures are then taken for three different antenna orientations relative to the AWG 4 wire after a pulse signal is fired into the system.

For the oscilloscope captures provided in this section, channel 1 is representative of a $60dB$ attenuated $4kV$, $20ns$ pulse signal replica from the output monitor of the pulse generator. Channel 2 is representative of an internal waveguide diode antenna. Channel 3 is representative of a linear antenna protruding externally from one of the wide walls of a waveguide structure. The Math 4 channel represents the integration of the channel 3 signal.

In Section 4.4.2, graphs are presented for each antenna orientation relative to the AWG 4 insulated wire for oscilloscope channel 3. From the graphs, direct signal comparison is shown for two different distances in each orientation. This section is intended to provide the oscilloscope captures where the data is extrapolated from. The data from this experiment was captured on May 17th, 2021. Further information about this experiment can be referred back to in Chapter 4, Section 4.4.2.

In Fig. D.12 (a, b, c, d), images are taken for an experimental setup in which a linear antenna faces perpendicularly to the direction of current flowing along the AWG 4 wire. Oscilloscope captures are then provided for two different distances between the linear antenna and the AWG 4 wire as shown in Fig. D.13 – Fig. D.14. The experimental setup and oscilloscope captures for two other antenna orientations are then provided throughout Fig. D.15 – Fig. D.20.

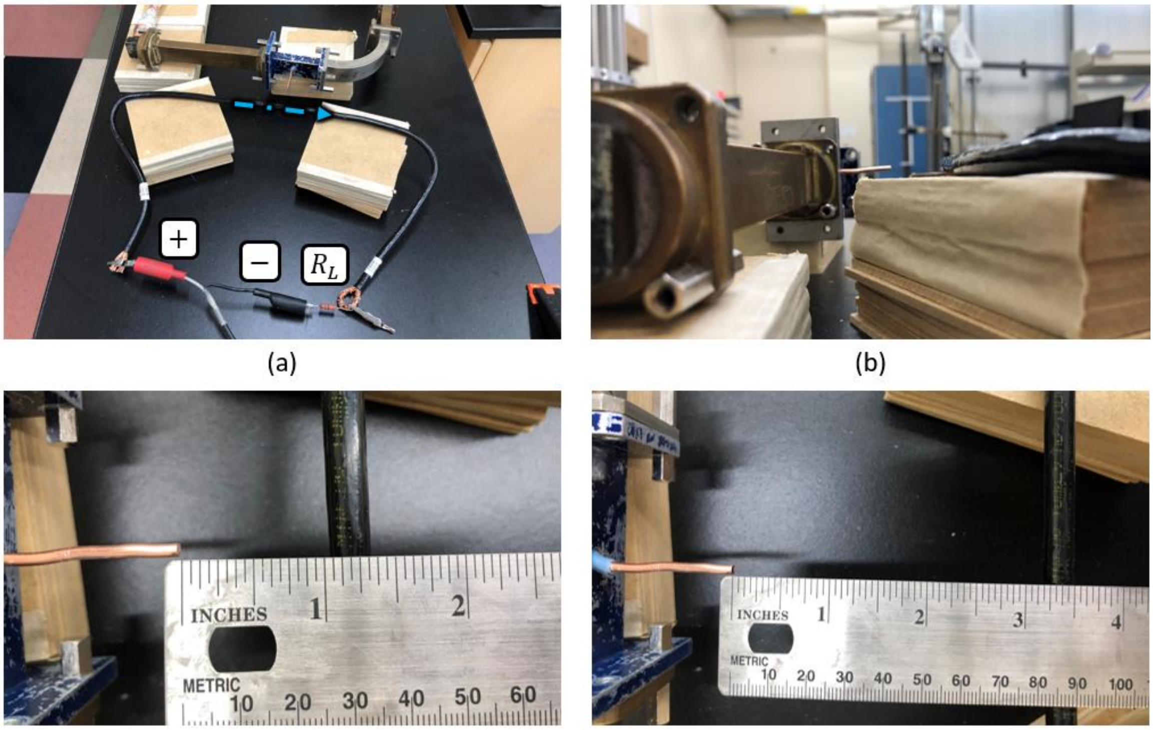

(a) (b)

(c) (d)

Fig. D.12 (a, b, c, d) An X-band waveguide structure with a linear antenna protruding from one of the wide walls is shown placed external to an AWG 4 wire, perpendicular in direction to the current along the wire. A top view of the experimental setup is shown in (a) and a side view of the setup in (b). Two oscilloscope captures are taken at different measured distances with the same orientation: (c) $+2.5cm$ and (d) $+8.3cm$.

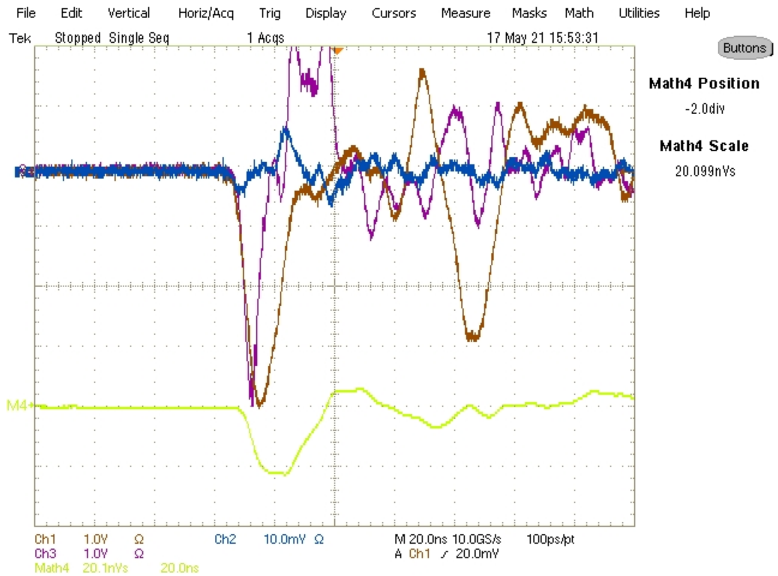

Tek Stopped Single Seq 1 Acqs 17 May 21 15:53:31

Math4 Position
-2.0div

Math4 Scale
20.099nVs

Ch1 1.0V Ω Ch2 10.0mV Ω M 20.0ns 10.0GS/s 100ps/pt
Ch3 1.0V Ω A Ch1 ⁄ 20.0mV
Math4 20.1nVs 20.0ns

Fig. D.13 An oscilloscope capture is taken from the experimental setup demonstrated in Fig. D.12 where the protruding linear antenna tip is placed at a distance of $+2.5cm$ away from the AWG 4 wire.

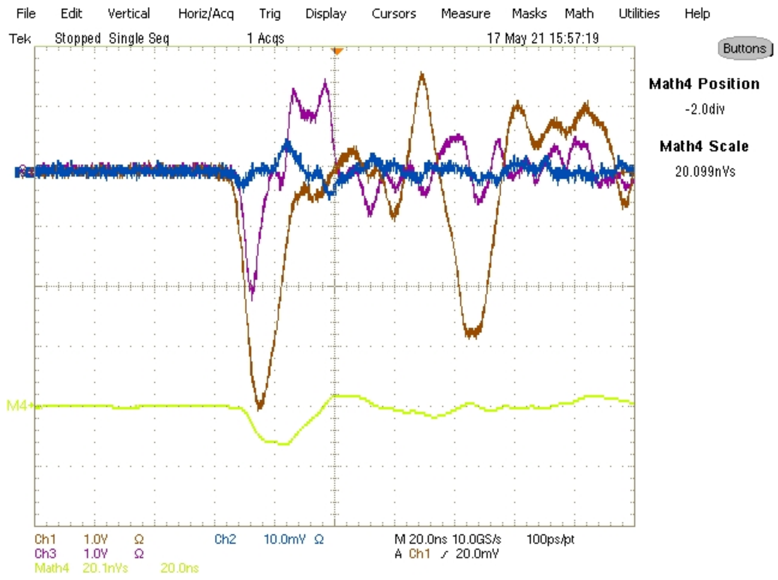

Tek Stopped Single Seq 1 Acqs 17 May 21 15:57:19

Math4 Position
-2.0div

Math4 Scale
20.099nVs

Ch1 1.0V Ω Ch2 10.0mV Ω M 20.0ns 10.0GS/s 100ps/pt
Ch3 1.0V Ω A Ch1 ⁄ 20.0mV
Math4 20.1nVs 20.0ns

Fig. D.14 An oscilloscope capture is taken from the experimental setup demonstrated in Fig. D.12 where the protruding linear antenna tip is placed at a distance of $+8.3cm$ away from the AWG 4 wire.

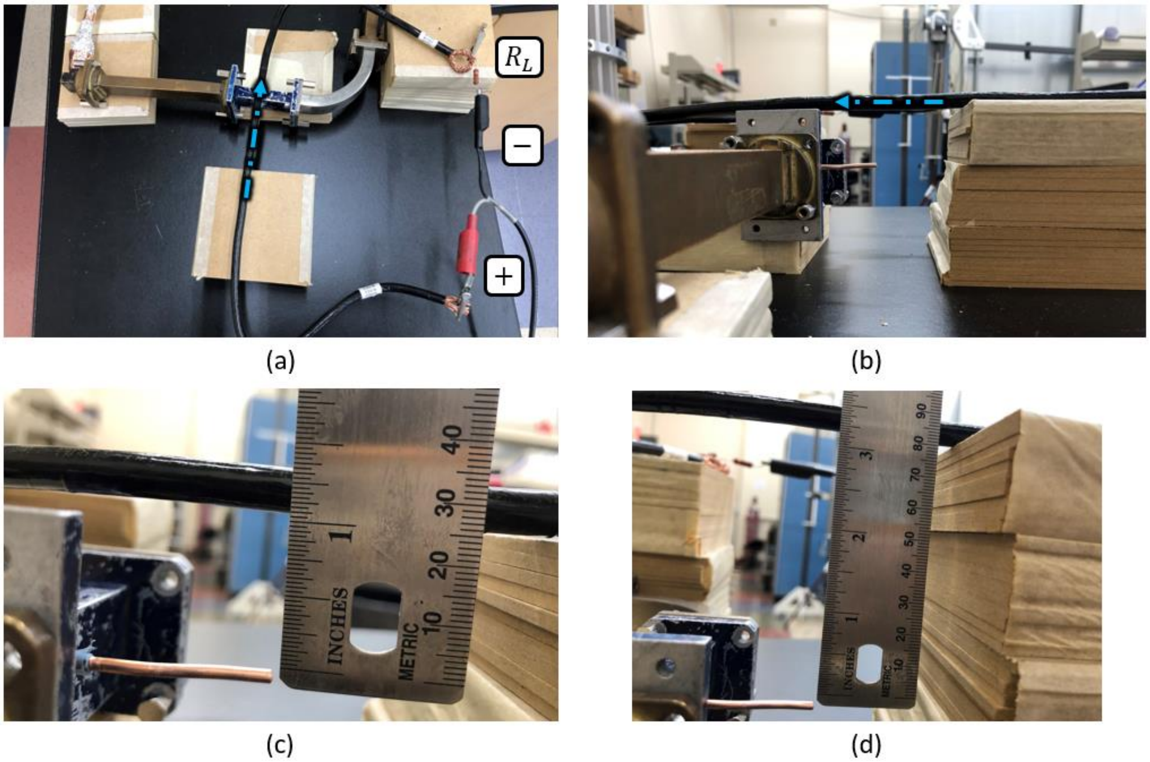

(a) (b)

(c) (d)

Fig. D.15 (a, b, c, d) An X-band waveguide structure with a linear antenna protruding from one of the wide walls is shown placed external to an AWG 4 wire, parallel in direction to the current along the wire. A top view of the experimental setup is shown in (a) and a side view of the setup in (b). Two oscilloscope captures are taken at different measured distances with the same orientation: (c) $+2.5cm$ and (d) $+8.3cm$.

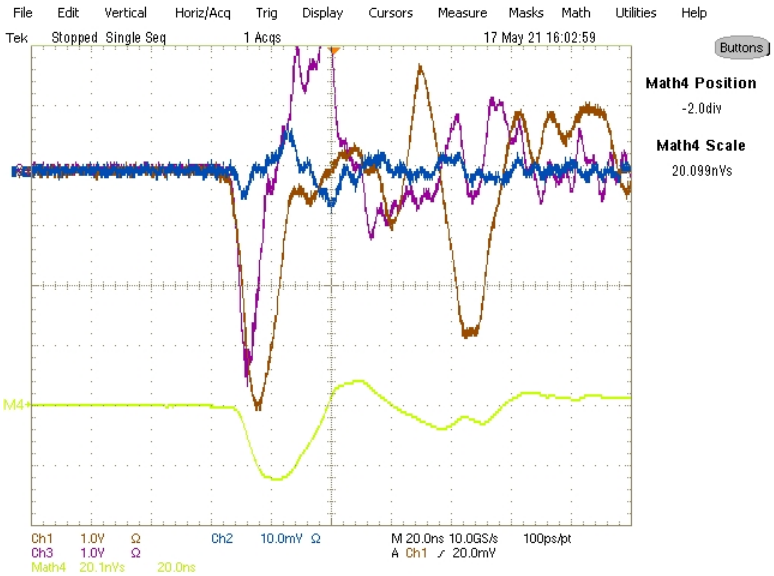

Fig. D.16 An oscilloscope capture is taken from the experimental setup demonstrated in Fig. D.15 where the protruding linear antenna is placed at a distance of $+2.5cm$ away from the AWG 4 wire.

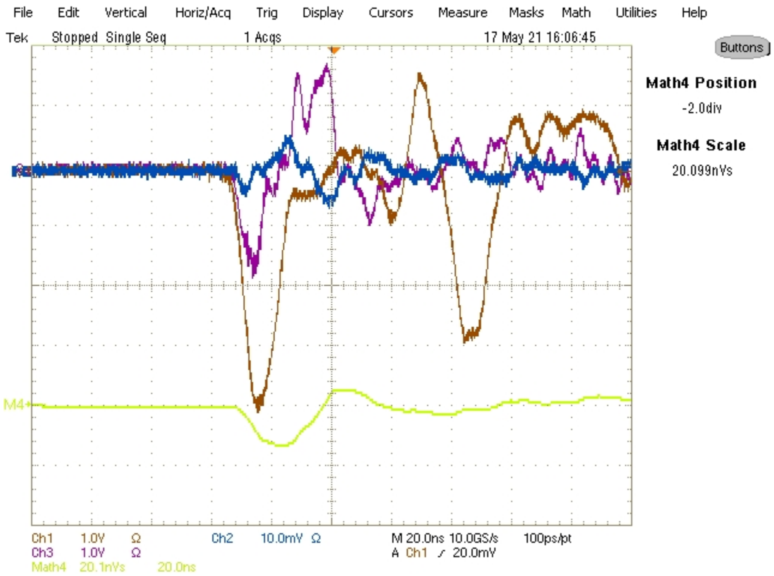

Fig. D.17 An oscilloscope capture is taken from the experimental setup demonstrated in Fig. D.15 where the protruding linear antenna is placed at a distance of $+8.3cm$ away from the AWG 4 wire.

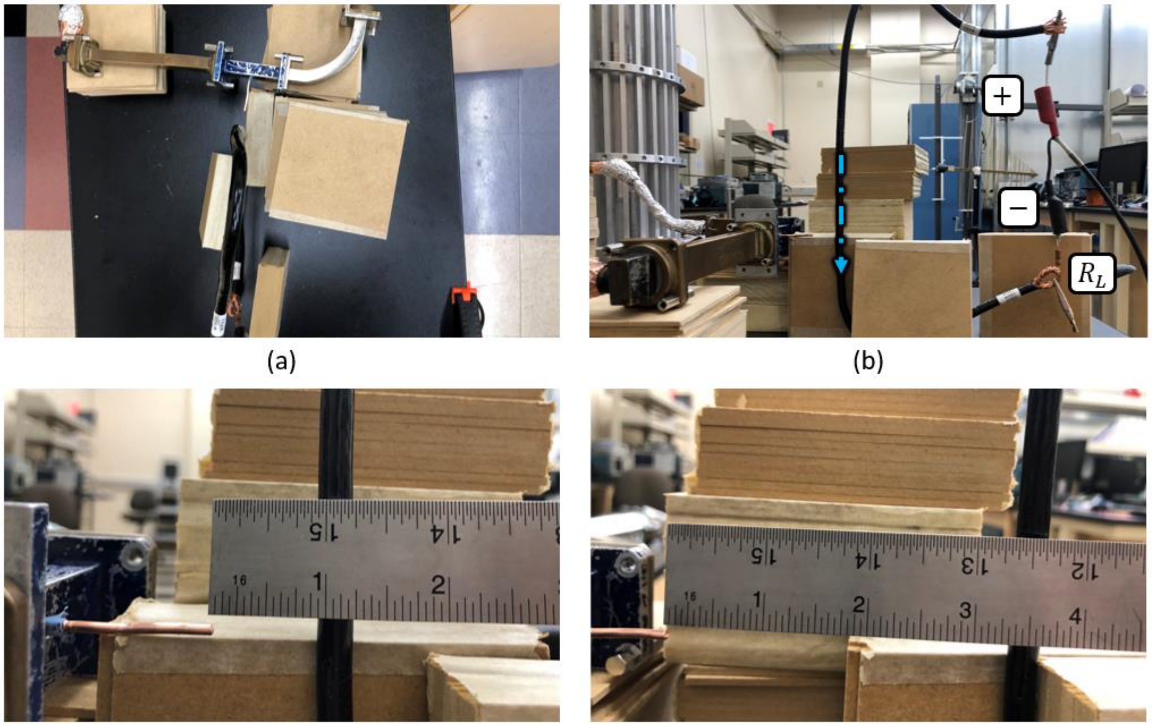

(a) (b)

(c) (d)

Fig. D.18 (a, b, c, d) An X-band waveguide structure with a linear antenna protruding from one of the wide walls is shown placed external to an AWG 4 wire, perpendicular in direction to the current along the wire. A top view of the experimental setup is shown in (a) and a side view of the setup in (b). Two oscilloscope captures are taken at different measured distances with the same orientation: (c) $+2.5cm$ and (d) $+8.3cm$.

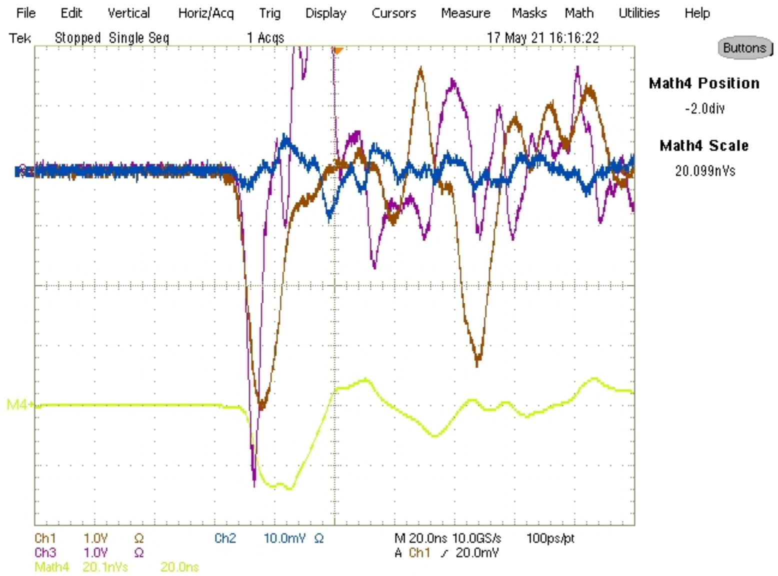

Fig. D.19 An oscilloscope capture is taken from the experimental setup demonstrated in Fig. D.18 where the protruding linear antenna tip is placed at a distance of $+2.5cm$ away from the AWG 4 wire.

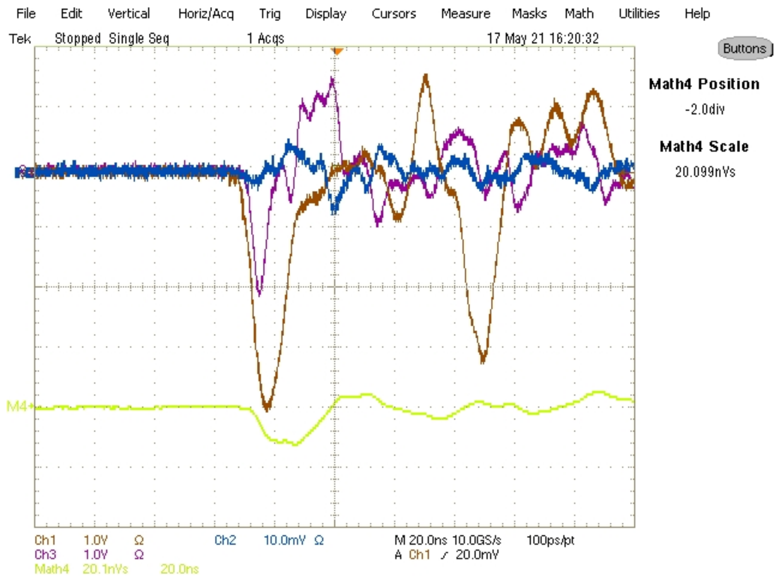

Fig. D.20 An oscilloscope capture is taken from the experimental setup demonstrated in Fig. D.18 where the protruding linear antenna tip is placed at a distance of $+8.3cm$ away from the AWG 4 wire.

D.3 Experiment 3: Modifying Linear Antenna Positioning Along an AWG 4 Wire (Pulse Generator)

In Chapter 4, Section 4.4.3, an experiment is documented in which a pulse generator is utilized to discharge a $4kV$, $20ns$ pulse into an AWG 4 insulated wire terminated by a high-wattage through-hole load resistor of $R_L = 50\Omega$. Similar to previous experiments in this Appendix, a linear antenna is positioned perpendicularly external to an AWG 4. Oscilloscope captures are then taken for different scenarios involving the translation of a linear antenna along a fixed axis relative to the AWG 4 wire.

For the oscilloscope captures provided in this section, channel 1 (brown) is representative of a $60dB$ attenuated $4kV$, $20ns$ pulse signal replica from the output monitor of the pulse generator. Channel 2 (blue) is representative of an internal waveguide diode antenna. Channel 3 (magenta) is representative of a linear antenna protruding externally from one of the wide walls of a waveguide structure. The Math 4 (yellow) channel represents the integration of the channel 3 signal.

In Section 4.4.3, graphs are presented for oscilloscope channel 3 providing direct signal comparison when translating the linear antenna along a fixed axis for different distances. This section is intended to provide the oscilloscope captures where the data is extrapolated from. The data from this experiment was captured on May 17th, 2021, and May 18th, 2021. Further information about this experiment can be referred back to in Chapter 4, Section 4.4.3.

In Fig. D.21 (a, b), two images are taken for an experimental setup in which a linear antenna is placed external to an AWG 4 wire approximately near the 90° bend. In Fig. D.21 – D.22, define the $z = 0$ position at the 90° bend of the AWG 4 wire. In Fig. D.22 (a, b, c, d), images are provided for each setup when translating the linear antenna waveguide structure along a fixed axis at positions: (a) $z = 0cm$, (b) $z = +2.5cm$, (c) $z = +7.6cm$, and (d) $z = +15.2cm$. Oscilloscope captures are then provided for the four different positions of the linear antenna waveguide structure as shown in Fig. D.23 – D.26.

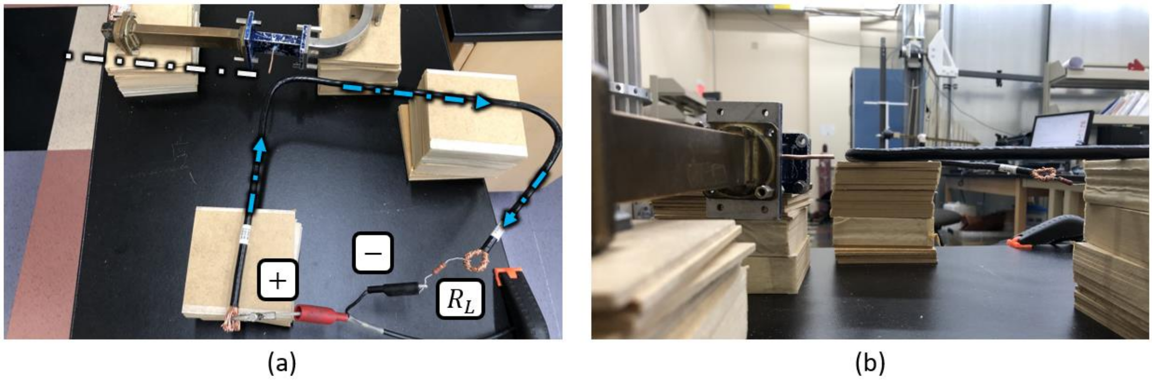

Fig. D.21 (a, b) An X-band waveguide structure with a linear antenna protruding from one of the wide walls is shown placed external to an AWG 4 wire approximately near the 90° bend. A top view of the experimental setup is shown in (a) and a side view in (b). In this setup, the position of the linear antenna is fixed on an axis and positioned at (c) $z = 0cm$ with a gap (d) $0cm$ between the linear antenna tip and the AWG 4 wire.

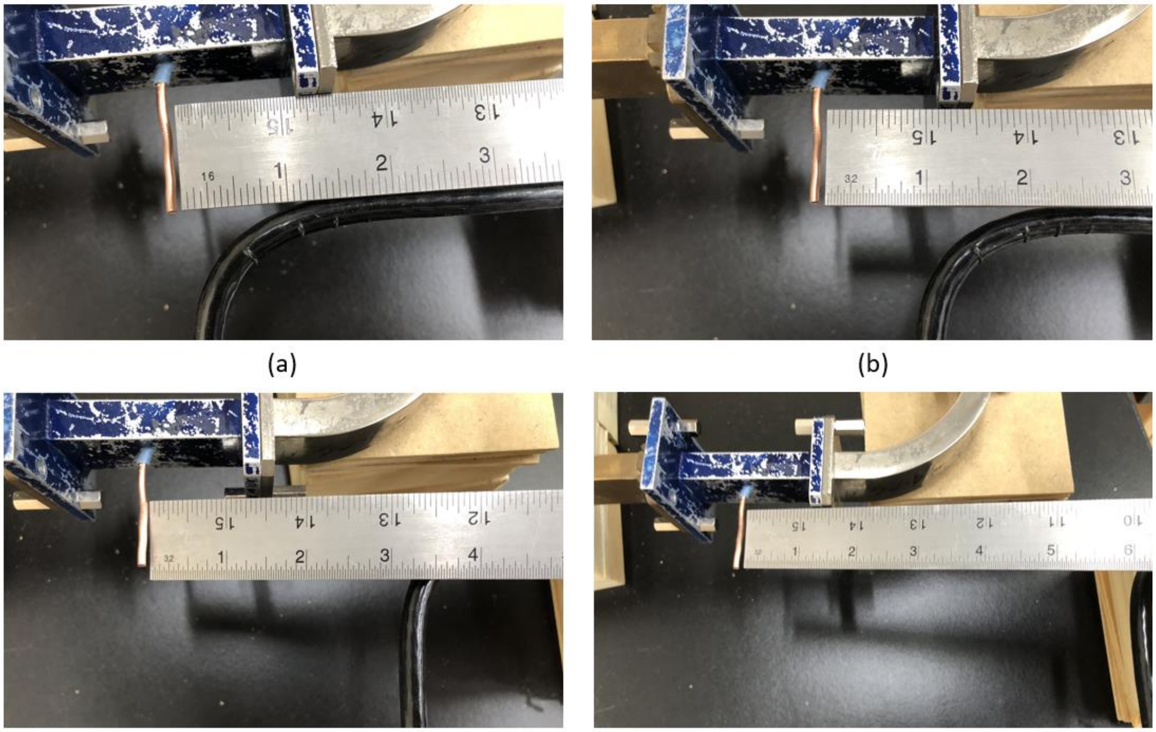

(a) (b)

(c) (d)

Fig. D.22 (a, b, c, d) In this experiment, a pulse generator is used to fire a $4kV$, $20ns$ pulse signal into an AWG 4 insulated wire with a 50Ω high wattage through-hole resistor termination. Oscilloscope channel 1 is connected to the pulse generator output monitor (60dB attenuated pulse signal replica), channel 2 an internal waveguide diode antenna, and channel 3 to the external protruding linear antenna. The experimental setup is shown when translating the linear antenna waveguide structure along an axis at: (a) $0cm$, (b) $+2.5cm$, (c) $+7.6cm$, and (d) $+15.2cm$.

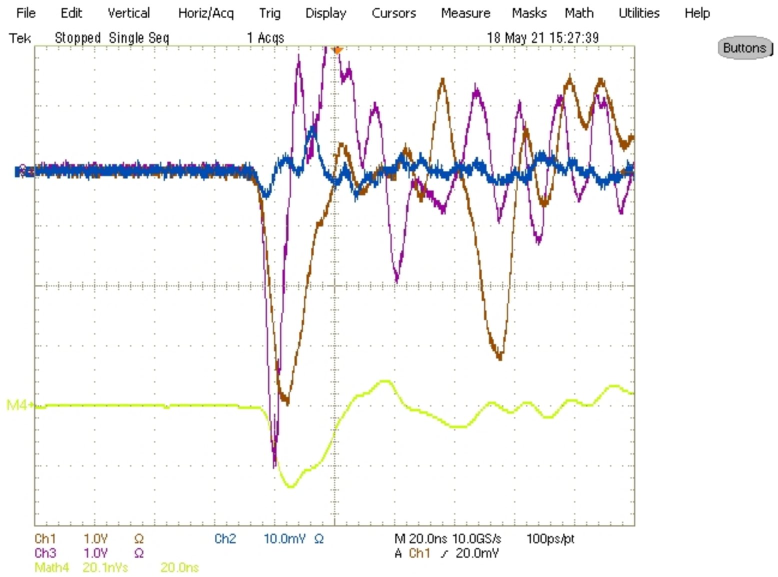

Tek Stopped Single Seq 1 Acqs 18 May 21 15:27:39

Ch1 1.0V Ω Ch2 10.0mV Ω M 20.0ns 10.0GS/s 100ps/pt
Ch3 1.0V Ω A Ch1 ⁄ 20.0mV
Math4 20.1nVs 20.0ns

Fig. D.23 An oscilloscope capture is taken from the experimental setup demonstrated in Fig. D.21 where the linear antenna waveguide structure is placed external to an AWG 4 wire at an initial position of a fixed axis defined at $z = 0$.

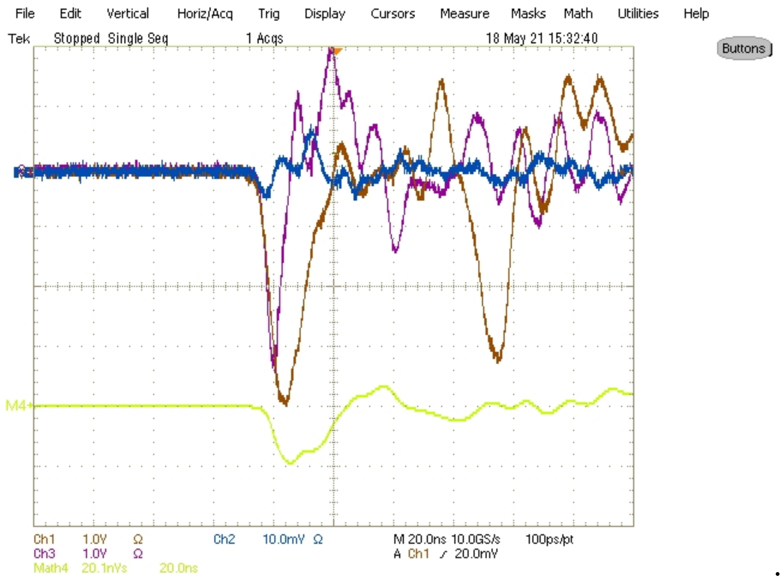

Tek Stopped Single Seq 1 Acqs 18 May 21 15:32:40

Ch1 1.0V Ω Ch2 10.0mV Ω M 20.0ns 10.0GS/s 100ps/pt
Ch3 1.0V Ω A Ch1 ⁄ 20.0mV
Math4 20.1nVs 20.0ns

Fig. D.24 An oscilloscope capture is taken from the experimental setup demonstrated in Fig. D.21 where the linear antenna waveguide structure is placed external to an AWG 4 on a fixed axis translated at $z = +2.5cm$.

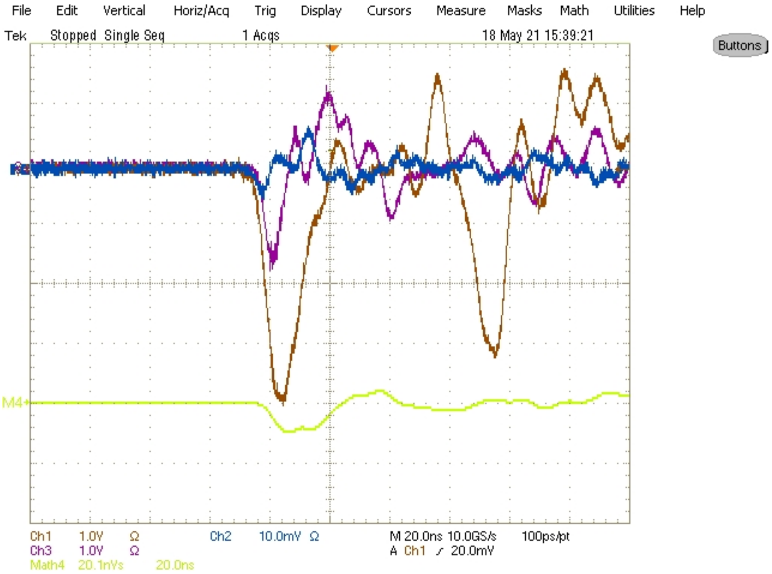

Tek Stopped Single Seq 1 Acqs 18 May 21 15:39:21

Ch1 1.0V Ω Ch2 10.0mV Ω M 20.0ns 10.0GS/s 100ps/pt
Ch3 1.0V Ω A Ch1 ⁄ 20.0mV
Math4 20.1nVs 20.0ns

Fig. D.25 An oscilloscope capture is taken from the experimental setup demonstrated in Fig. D.21 where the linear antenna waveguide structure is placed external to an AWG 4 on a fixed axis translated at $z = +7.6cm$.

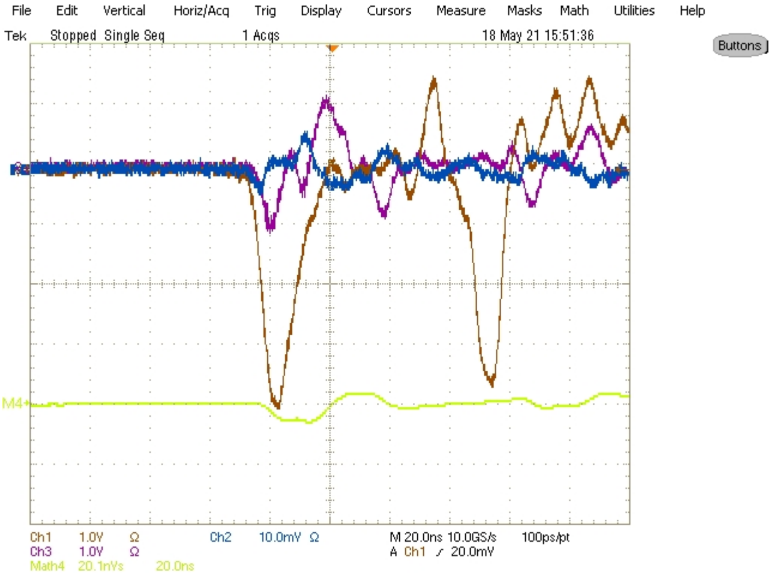

Tek Stopped Single Seq 1 Acqs 18 May 21 15:51:36

Ch1 1.0V Ω Ch2 10.0mV Ω M 20.0ns 10.0GS/s 100ps/pt
Ch3 1.0V Ω A Ch1 ⁄ 20.0mV
Math4 20.1nVs 20.0ns

Fig. D.26 An oscilloscope capture is taken from the experimental setup demonstrated in Fig. D.21 where the linear antenna waveguide structure is placed external to an AWG 4 on a fixed axis translated at $z = +15.2cm$.

In Fig. D.27 (a, b, c, d), images are taken for a similar experiment when translating the linear antenna waveguide structure along a fixed axis. Previously, the linear antenna was translated away from the $90°$ bend and the rest of the AWG 4 wire. In Fig. D.27 – D.28, define the $z = 0$ position at the sharp bend of the AWG 4 wire. The linear antenna in Fig. D.27 (a, b, c, d) is placed at a position $z = -13.3cm$ between the $90°$ bend and sharp bend ($\theta < 90°$) of the AWG 4 wire. Further, there is a $+2.5cm$ gap between the linear antenna tip and the AWG 4 wire. In Fig. D.28 (a, b, c, d), images are provided for each setup when translating the linear antenna waveguide structure along a fixed axis at positions: (a) $z = +5.1cm$, (b) $z = +1.3cm$, (c) $z = -3.2cm$, and (d) $z = -8.3cm$. Oscilloscope captures are then provided for the five different positions of the linear antenna waveguide structure as shown in Fig. D.29 – D.33.

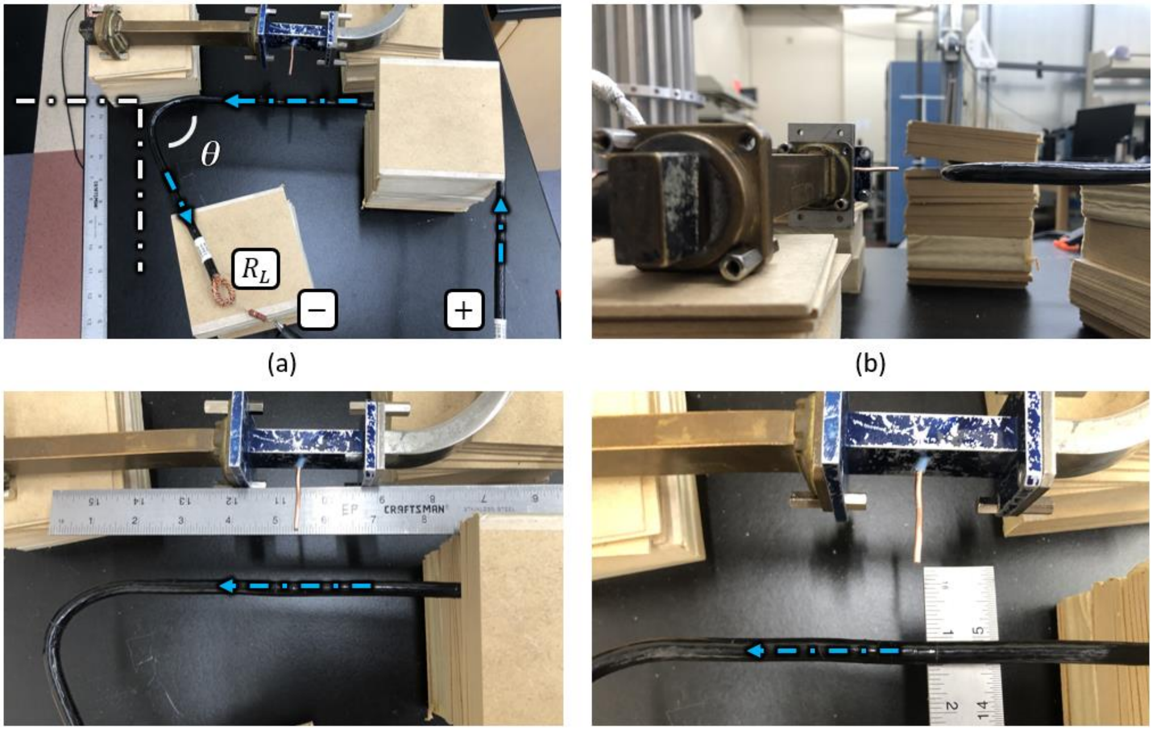

(a) (b)

(c) (d)

Fig. D.27 (a, b, c, d) An X-band waveguide structure with a linear antenna protruding from one of the wide walls is shown placed external to an AWG 4 wire approximately between the 90° bend and sharp bend ($\theta < 90°$). A top view of the experimental setup is shown in (a) and a side view in (b). In this setup, the linear antenna is fixed on an axis and positioned at (c) $z = -13.3cm$ with a gap (d) $2.5cm$ between the linear antenna tip and the AWG 4 wire.

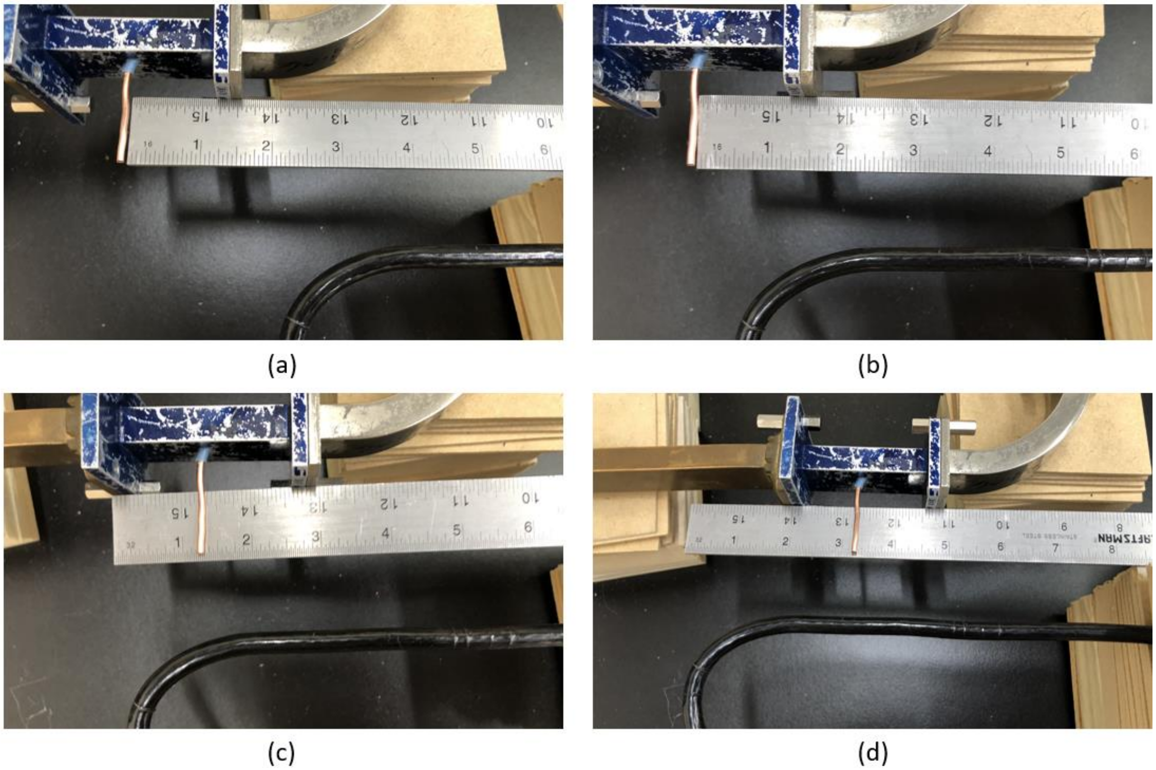

Fig. D.28 (a, b, c, d) In this experiment, a pulse generator is used to fire a $4kV$, $20ns$ pulse signal into an AWG 4 insulated wire with a 50Ω high wattage through-hole resistor termination. Oscilloscope channel 1 is connected to the pulse generator output monitor (60dB attenuated pulse signal replica), channel 2 an internal waveguide diode antenna, and channel 3 to the external protruding linear antenna. The experimental setup is shown when translating the linear antenna waveguide structure along an axis at: (a) $+5.1cm$, (b) $+1.3cm$, (c) $-3.2cm$, and (d) $-8.3cm$.

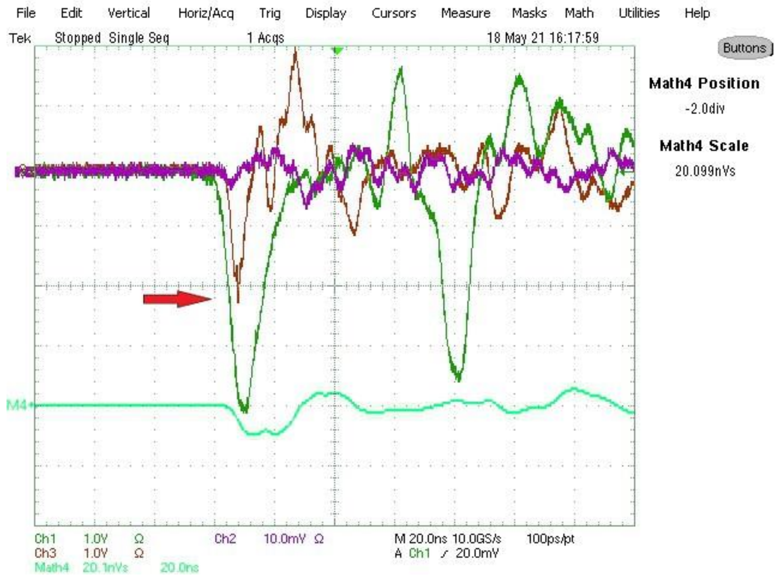

Tek Stopped Single Seq 1 Acqs 18 May 21 16:17:59

Math4 Position
-2.0div

Math4 Scale
20.099nVs

Ch1 1.0V Ω Ch2 10.0mV Ω M 20.0ns 10.0GS/s 100ps/pt
Ch3 1.0V Ω A Ch1 ⁄ 20.0mV
Math4 20.1nVs 20.0ns

Fig. D.29 An oscilloscope capture is taken from the experimental setup demonstrated in Fig. D.27 where the linear antenna waveguide structure is placed external to an AWG 4 on a fixed axis translated at $z = +5.1cm$.

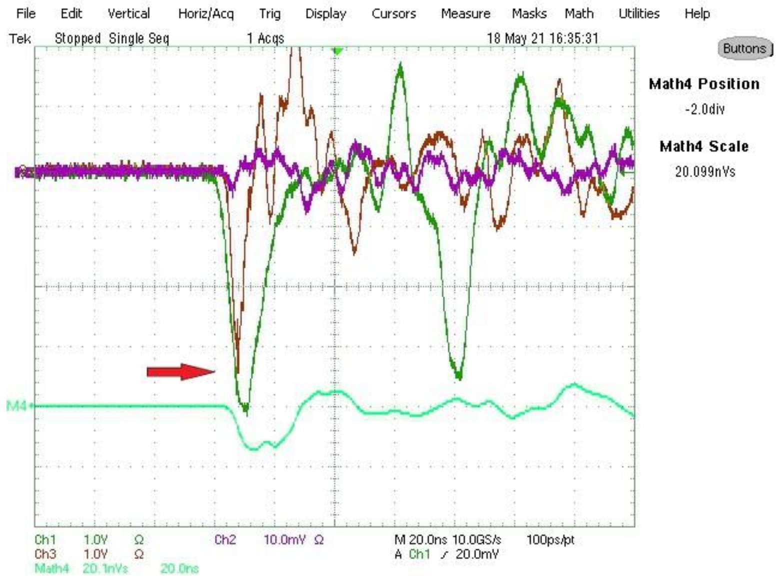

Tek Stopped Single Seq 1 Acqs 18 May 21 16:35:31

Math4 Position
-2.0div

Math4 Scale
20.099nVs

Ch1 1.0V Ω Ch2 10.0mV Ω M 20.0ns 10.0GS/s 100ps/pt
Ch3 1.0V Ω A Ch1 ⁄ 20.0mV
Math4 20.1nVs 20.0ns

Fig. D.30 An oscilloscope capture is taken from the experimental setup demonstrated in Fig. D.27 where the linear antenna waveguide structure is placed external to an AWG 4 on a fixed axis translated at $z = +1.3cm$.

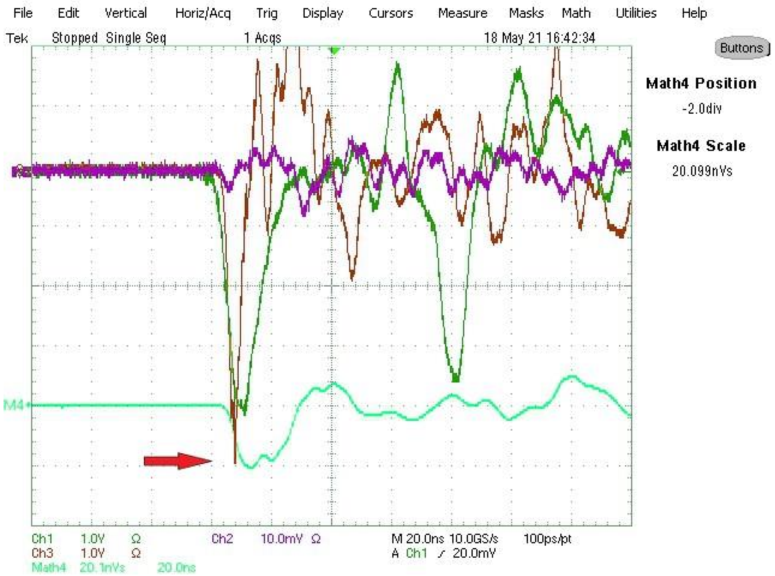

Fig. D.31 An oscilloscope capture is taken from the experimental setup demonstrated in Fig. D.27 where the linear antenna waveguide structure is placed external to an AWG 4 on a fixed axis translated at $z = -3.2cm$.

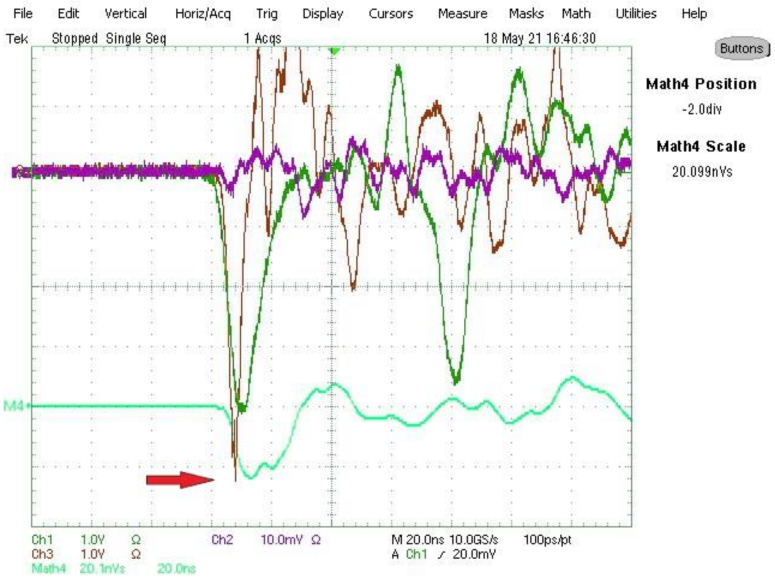

Fig. D.32 An oscilloscope capture is taken from the experimental setup demonstrated in Fig. D.27 where the linear antenna waveguide structure is placed external to an AWG 4 on a fixed axis translated at $z = -8.3cm$.

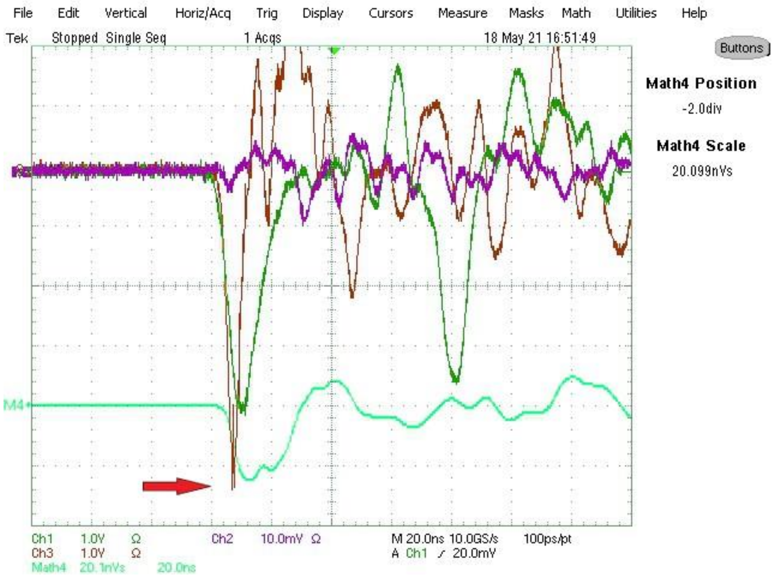

Tek Stopped Single Seq 1 Acqs 18 May 21 16:51:49

Math4 Position
-2.0div

Math4 Scale
20.099nVs

Ch1 1.0V Ω Ch2 10.0mV Ω M 20.0ns 10.0GS/s 100ps/pt
Ch3 1.0V Ω A Ch1 ⁄ 20.0mV
Math4 20.1nVs 20.0ns

Fig. D.33 An oscilloscope capture is taken from the experimental setup demonstrated in Fig. D.27 where the linear antenna waveguide structure is placed external to an AWG 4 on a fixed axis translated at $z = -13.3cm$.

In Fig. D.34 (a, b), images are taken for an experiment similar to the previous, except the $+2.5cm$ gap between the linear antenna tip and the AWG 4 wire is reduced to $0cm$. The linear antenna is then translated away from the sharp bend ($\theta < 90°$) and the rest of the AWG 4 wire. In Fig. D.34 – D.35, define the $z = 0$ position at the sharp bend of the AWG 4 wire again. The linear antenna in Fig. D.34 (a, b) is placed at a position $z = 0cm$ at the sharp bend ($\theta < 90°$) of the AWG 4 wire. In Fig. D.35 (a, b, c), images are provided for each setup when translating the linear antenna waveguide structure along a fixed axis at positions: (a) $z = 0cm$, (b) $z = +2.5cm$, (c) $z = +8.3cm$. Oscilloscope captures are then provided for the three different positions of the linear antenna waveguide structure as shown in Fig. D.36 – D.38.

(a) (b)

Fig. D.34 (a, b) An X-band waveguide structure with a linear antenna protruding from one of the wide walls is shown placed external to an AWG 4 wire approximately near the sharp bend ($\theta < 90°$). A top view of the experimental setup is shown in (a) and a side view in (b). In this setup, the position of the linear antenna is fixed on an axis and positioned at $z = 0cm$ with a gap of $0cm$ between the linear antenna tip and the AWG 4 wire.

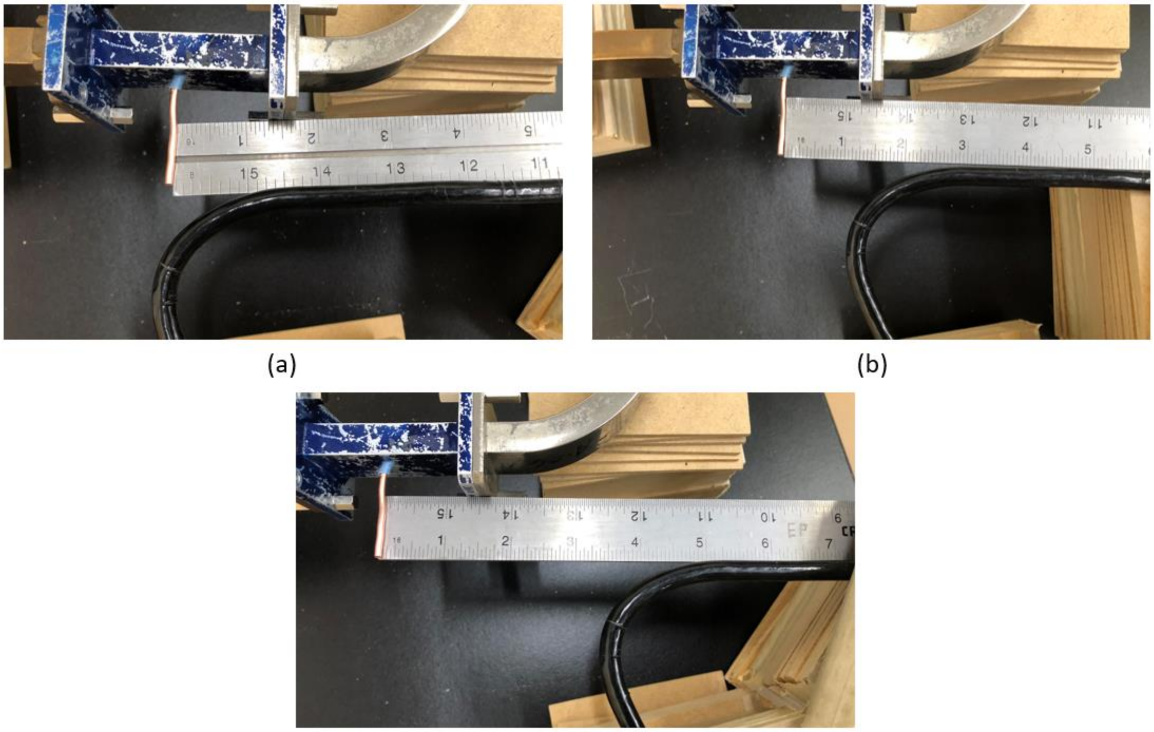

(a) (b)

(c)

Fig. D.35 (a, b, c) In this experiment, a pulse generator is used to fire a $4kV$, $20ns$ pulse signal into an AWG 4 insulated wire with a 50Ω high wattage through-hole resistor termination. Oscilloscope channel 1 is connected to the pulse generator output monitor (60dB attenuated pulse signal replica), channel 2 an internal waveguide diode antenna, and channel 3 to the external protruding linear antenna. The experimental setup is shown when translating the linear antenna waveguide structure along an axis at: (a) $0cm$, (b) $+2.5cm$, (c) $+8.3cm$.

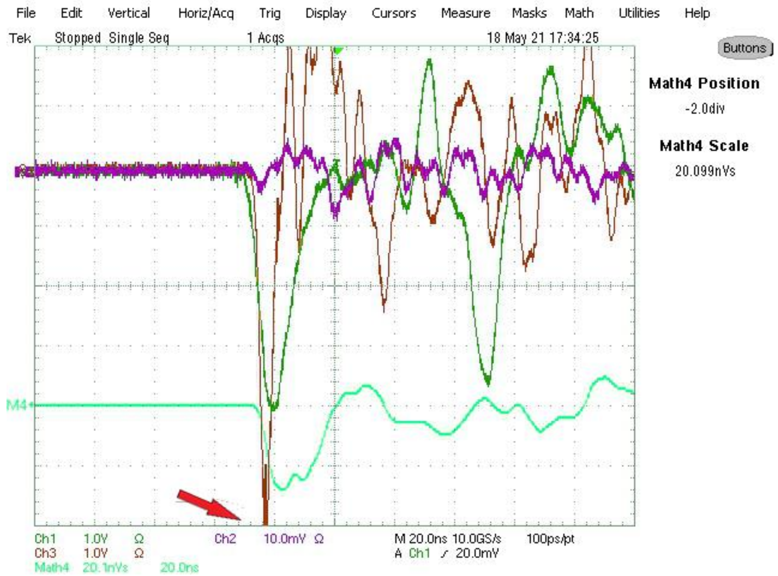

Fig. D.36 An oscilloscope capture is taken from the experimental setup demonstrated in Fig. D.34 where the linear antenna waveguide structure is placed external to an AWG 4 on a fixed axis translated at $z = 0cm$.

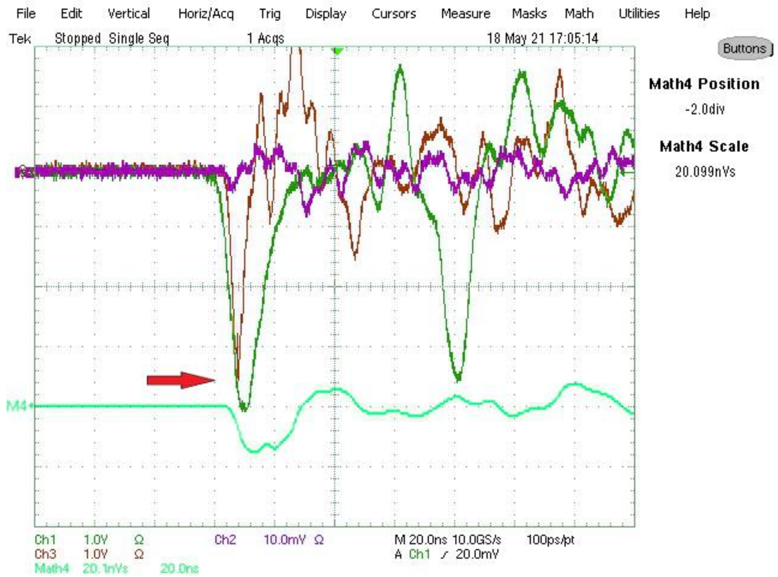

Fig. D.37 An oscilloscope capture is taken from the experimental setup demonstrated in Fig. D.34 where the linear antenna waveguide structure is placed external to an AWG 4 on a fixed axis translated at $z = 2.5cm$.

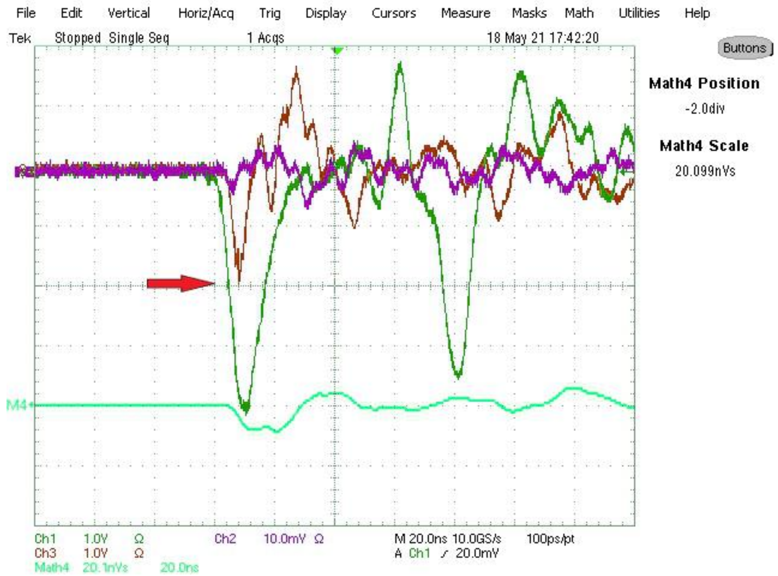

Fig. D.38 An oscilloscope capture is taken from the experimental setup demonstrated in Fig. D.34 where the linear antenna waveguide structure is placed external to an AWG 4 on a fixed axis translated at $z = +8.3cm$.

In Fig. D.39, a similar experiment is performed except now the linear antenna is placed at a fixed position near the sharp bend of the AWG 4 wire without being translated. Four different scenarios are presented in Fig. D.39: (a) the positive terminal of the pulse generator is connected at the 90° bend of the AWG 4 wire and resistor termination at the sharp bend ($\theta < 90°$), (b) a positive terminal of the pulse generator connected at the sharp bend ($\theta < 90°$) of the AWG 4 wire and resistor termination at the sharp bend ($\theta < 90°$), (c) a positive terminal of the pulse generator connected at the sharp bend ($\theta < 90°$) of the AWG 4 wire and resistor termination at the 90° bend, and (d) a positive terminal of the pulse generator terminal connected at the 90° bend of the AWG 4 wire and resistor termination at the 90° bend.

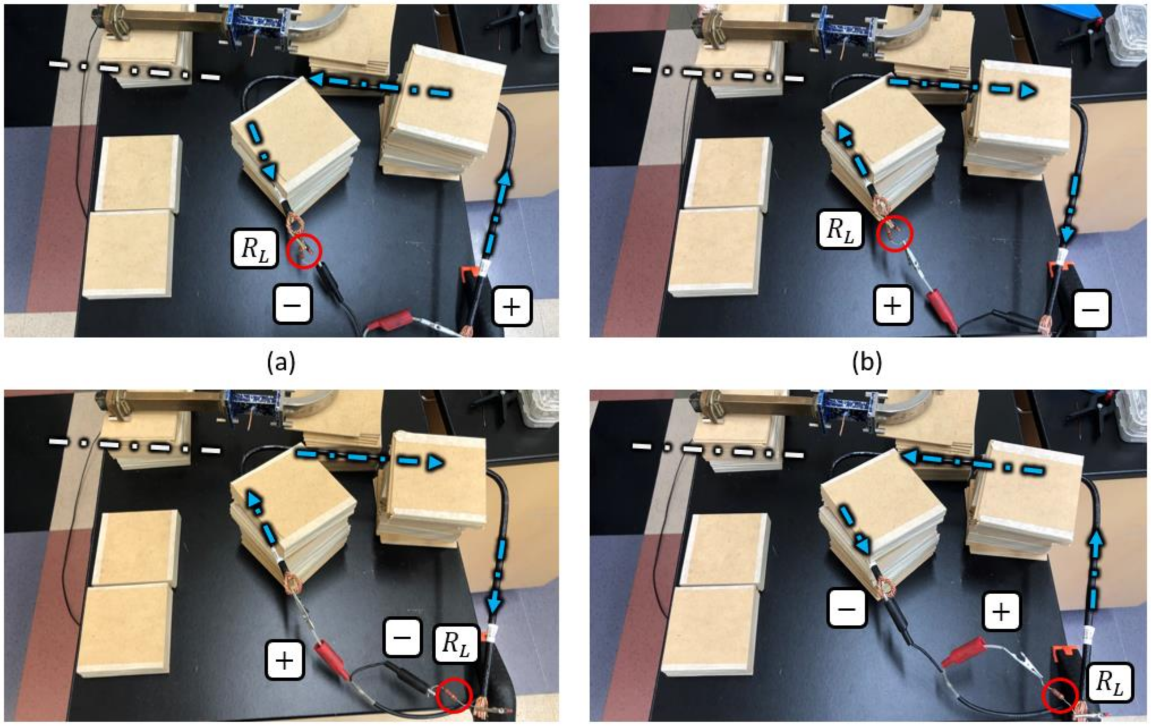

(a) (b)

(c) (d)

Fig. D.39 (a, b, c, d) Four different scenarios are presented for a fixed linear antenna: (a) positive pulse generator terminal at the 90° bend of the AWG 4 wire and resistor termination at the sharp bend ($\theta < 90°$), (b) positive pulse generator terminal at the sharp bend ($\theta < 90°$) of the AWG 4 wire and resistor termination at the sharp bend ($\theta < 90°$), (c) positive pulse generator terminal at the sharp bend ($\theta < 90°$) of the AWG 4 wire and resistor termination at the 90° bend, and (d) positive pulse generator terminal at the 90° bend of the AWG 4 wire and resistor termination at the 90° bend.

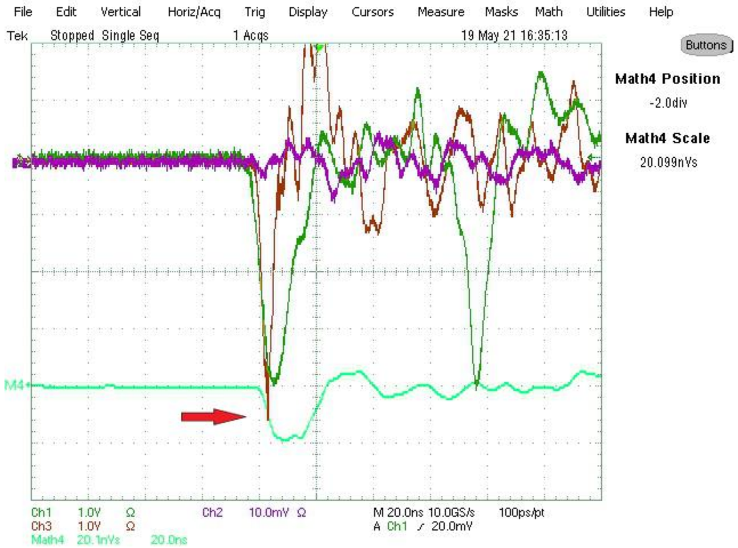

Tek Stopped Single Seq 1 Acqs 19 May 21 16:35:13

Math4 Position
-2.0div

Math4 Scale
20.099nVs

Ch1 1.0V Ω Ch2 10.0mV Ω M 20.0ns 10.0GS/s 100ps/pt
Ch3 1.0V Ω A Ch1 ⁄ 20.0mV
Math4 20.1nVs 20.0ns

Fig. D.40 An oscilloscope capture is taken from the experimental setup demonstrated in Fig. D.39 where the linear antenna waveguide structure is placed external to an AWG 4 near the sharp bend at a fixed position. The positive pulse generator terminal is connected at the 90° bend of the AWG 4 wire and resistor termination at the sharp bend ($\theta < 90°$) or otherwise denoted termination orientation 1.

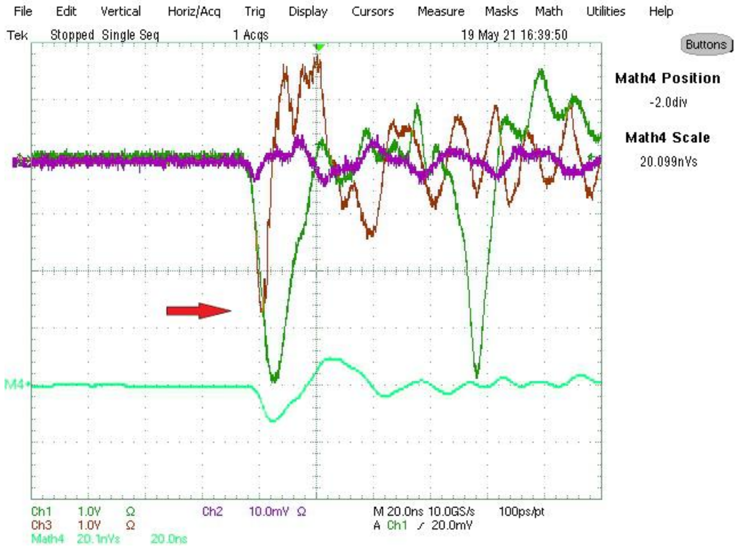

Tek Stopped Single Seq 1 Acqs 19 May 21 16:39:50

Math4 Position
-2.0div

Math4 Scale
20.099nVs

Ch1 1.0V Ω Ch2 10.0mV Ω M 20.0ns 10.0GS/s 100ps/pt
Ch3 1.0V Ω A Ch1 ⁄ 20.0mV
Math4 20.1nVs 20.0ns

Fig. D.41 An oscilloscope capture is taken from the experimental setup demonstrated in Fig. D.39 where the linear antenna waveguide structure is placed external to an AWG 4 near the sharp bend at a fixed position. The positive pulse generator terminal is connected at the sharp bend ($\theta < 90°$) of the AWG 4 wire and resistor termination at the sharp bend ($\theta < 90°$) or otherwise denoted termination orientation 2.

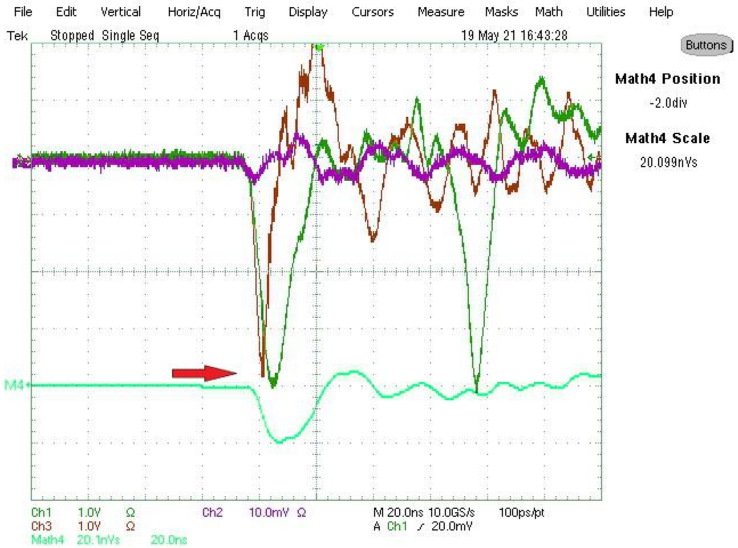

Fig. D.42 An oscilloscope capture is taken from the experimental setup demonstrated in Fig. D.39 where the linear antenna waveguide structure is placed external to an AWG 4 near the sharp bend at a fixed position. The positive pulse generator terminal is connected at the sharp bend ($\theta < 90°$) of the AWG 4 wire and resistor termination at the 90° bend or otherwise denoted termination orientation 3.

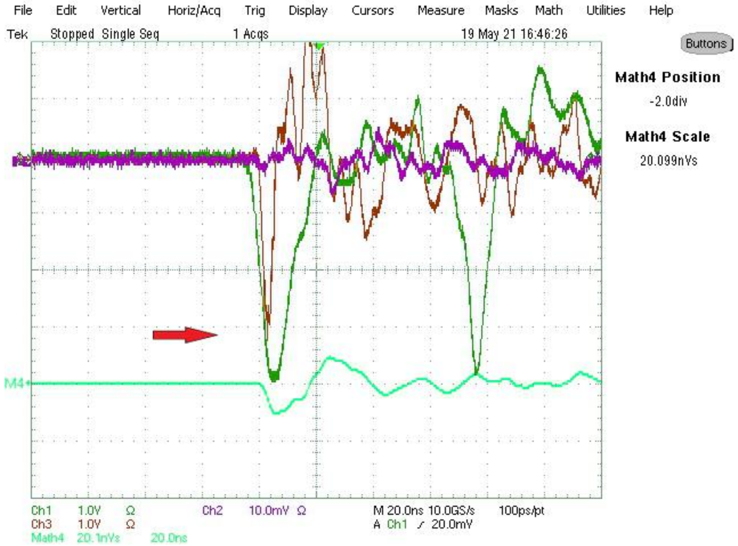

Fig. D.43 An oscilloscope capture is taken from the experimental setup demonstrated in Fig. D.39 where the linear antenna waveguide structure is placed external to an AWG 4 near the sharp bend at a fixed position. The positive pulse generator terminal is connected at the 90° bend of the AWG 4 wire and resistor termination at the 90° bend or otherwise denoted termination orientation 4.

D.4 Experiment 4: Modifying Linear Antenna Positioning Along an AWG 4 Wire (RC Source)

In Chapter 4, Section 4.4.4, an experiment is documented in which an RC configured circuit is utilized to discharge a $1kV$, $120\mu s$ pulse into an AWG 4 insulated wire terminated by a high-wattage through-hole load resistor of $R_L = 50\Omega$. A linear antenna is positioned perpendicularly external to the AWG 4 wire with a gap of $2.5cm$ of separation as shown in Fig. D.44. Oscilloscope captures are then taken for different scenarios involving the translation of a linear antenna along a fixed axis relative to the AWG 4 wire as demonstrated in Fig. D.45.

For the oscilloscope captures provided in this section, channel 1 (yellow) is representative of the linear antenna protruding externally from one of the wide walls of the waveguide structure. Channel 2 (turquoise) is representative of the internal waveguide diode antenna.

In Section 4.4.4, a graph is presented for oscilloscope channel 1 providing direct signal comparison when translating the linear antenna along a fixed axis for different distances. This section is intended to provide the oscilloscope captures where the data is extrapolated from. The data from this experiment was captured on March 17th, 2023. Further information about this experiment can be referred back to in Chapter 4, Section 4.4.4.

In Fig. D.44 (a, b, c, d), images are taken for an experimental setup in which a linear antenna is placed external to an AWG 4 wire. In Fig. D.44 – D.45, define the $z = 0$ position near the sharp bend ($\theta < 90°$) of the AWG 4 wire. In Fig. D.45 (a, b, c, d), images are provided for each setup when translating the linear antenna waveguide structure along a fixed axis at positions: (a) $z = -10.2cm$, (b) $z = -2.5cm$, (c) $z = 0cm$, and (d) $z = +7.6cm$. While not shown in Fig. D.45, oscilloscope captures are provided for the listed positions as well as positions at $z = -17.8cm$ and $z = +2.5cm$ of the linear antenna waveguide structure as shown in Fig. D.46 – D.51.

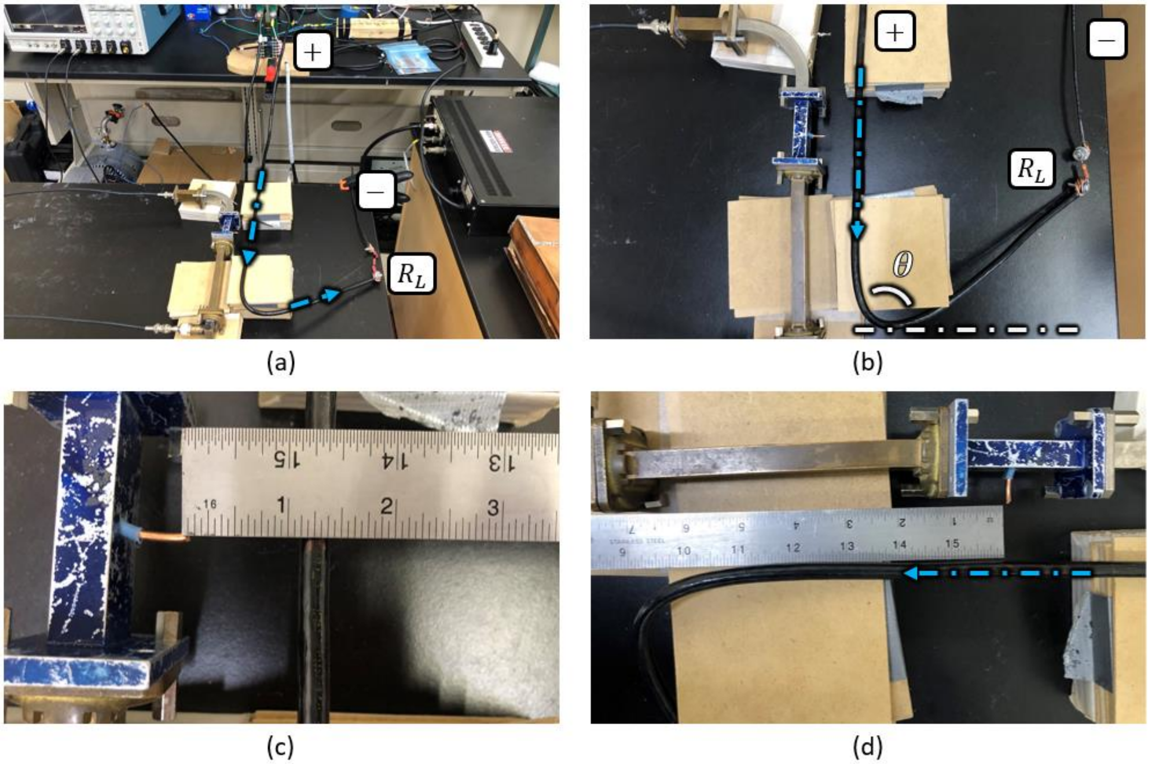

Fig. D.44 A linear antenna is positioned perpendicularly external to an AWG 4 wire with a gap of $2.5cm$ of separation. Different perspectives of the experimental setup is shown in (a), (b), (c), and (d).

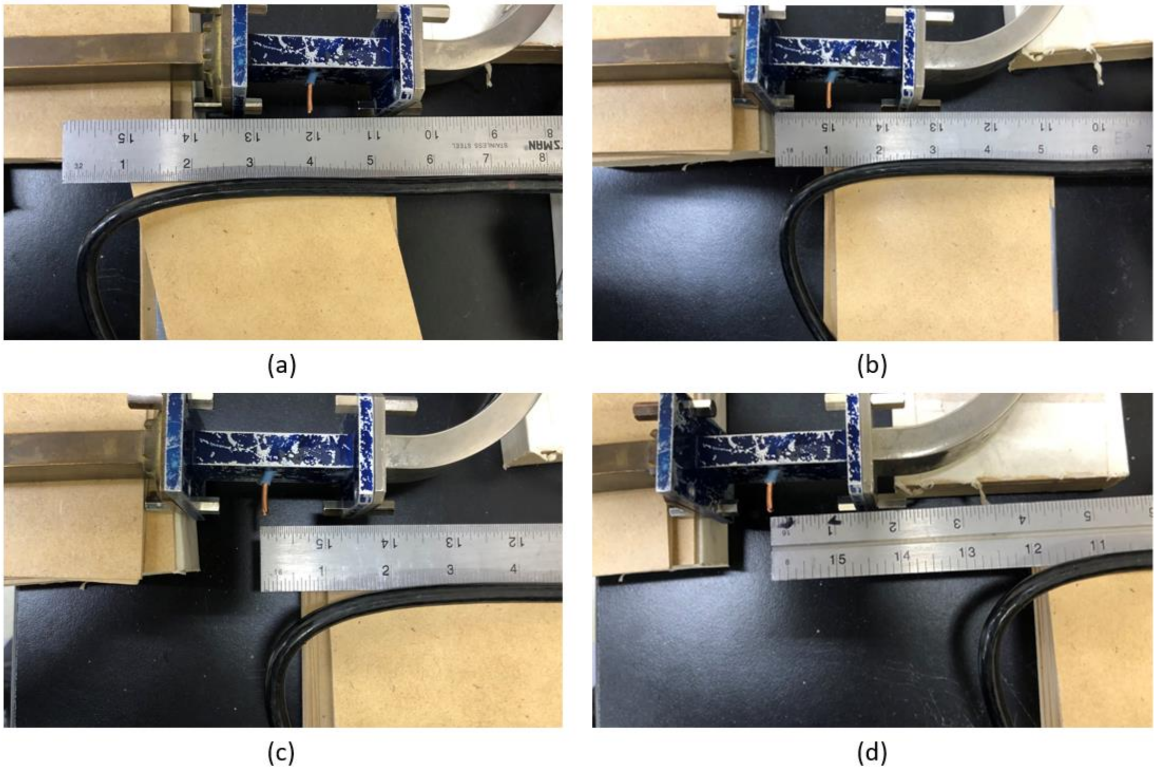

(a) (b)

(c) (d)

Fig. D.45 When a pulse signal is fired by the RC input, an oscilloscope capture is taken when displacing the linear antenna at different points along the direction of current in the AWG 4 wire. Measurements are taken at displacements: $-17.8cm$, (a) $-10.2cm$, (b) $-2.5cm$, (c) $0cm$, $+2.5cm$, and (d) $+7.6cm$.

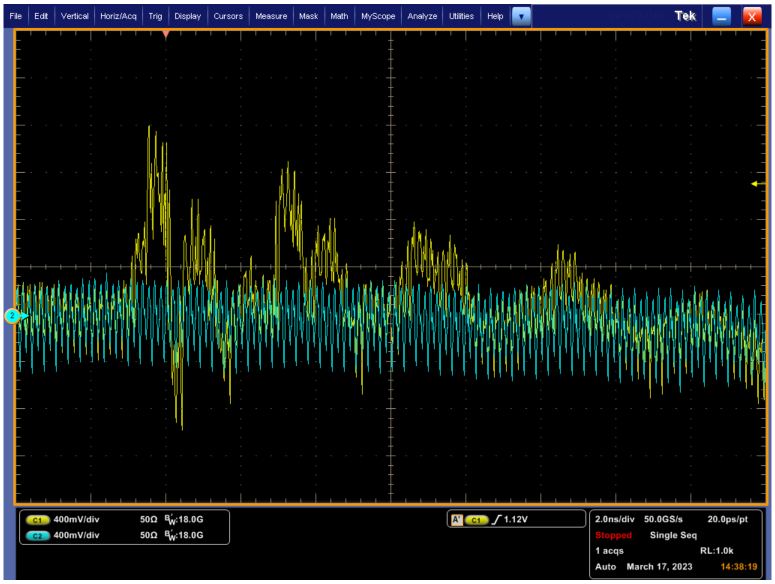

C1 400mV/div 50Ω BW:18.0G
C2 400mV/div 50Ω BW:18.0G
A' C1 ∫ 1.12V
2.0ns/div 50.0GS/s 20.0ps/pt
Stopped Single Seq
1 acqs RL:1.0k
Auto March 17, 2023 14:38:19

Fig. D.46 An oscilloscope capture is taken from the experimental setup demonstrated in Fig. D.44 where the linear antenna waveguide structure is placed external to an AWG 4 on a fixed axis translated at $z = -17.8cm$.

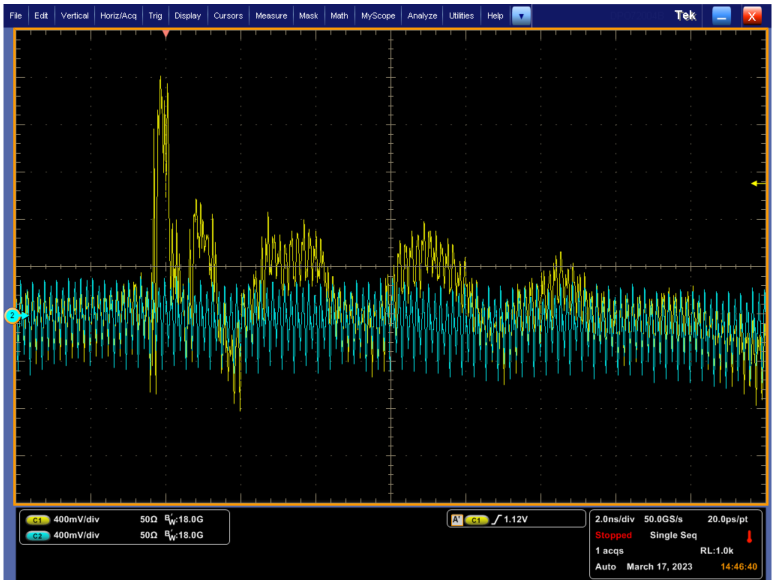

C1 400mV/div 50Ω BW:18.0G
C2 400mV/div 50Ω BW:18.0G
A' C1 ∫ 1.12V
2.0ns/div 50.0GS/s 20.0ps/pt
Stopped Single Seq
1 acqs RL:1.0k
Auto March 17, 2023 14:46:40

Fig. D.47 An oscilloscope capture is taken from the experimental setup demonstrated in Fig. D.44 where the linear antenna waveguide structure is placed external to an AWG 4 on a fixed axis translated at $z = -10.2cm$.

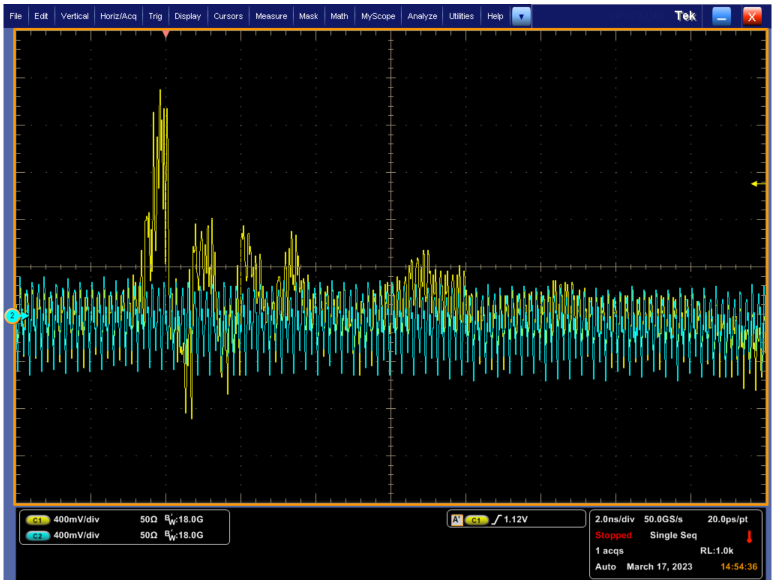

C1 400mV/div 50Ω BW:18.0G
C2 400mV/div 50Ω BW:18.0G
A' C1 1.12V
2.0ns/div 50.0GS/s 20.0ps/pt
Stopped Single Seq
1 acqs RL:1.0k
Auto March 17, 2023 14:54:36

Fig. D.48 An oscilloscope capture is taken from the experimental setup demonstrated in Fig. D.44 where the linear antenna waveguide structure is placed external to an AWG 4 on a fixed axis translated at $z = -2.5cm$.

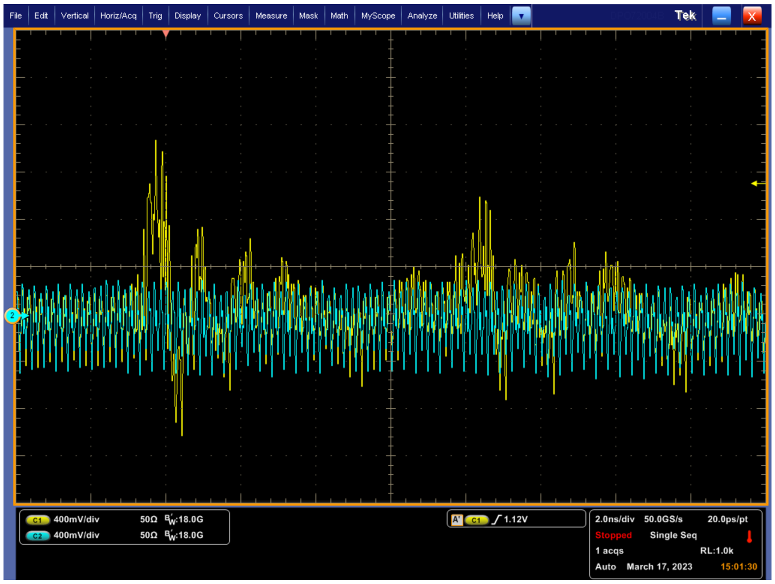

C1 400mV/div 50Ω BW:18.0G
C2 400mV/div 50Ω BW:18.0G
A' C1 1.12V
2.0ns/div 50.0GS/s 20.0ps/pt
Stopped Single Seq
1 acqs RL:1.0k
Auto March 17, 2023 15:01:30

Fig. D.49 An oscilloscope capture is taken from the experimental setup demonstrated in Fig. D.44 where the linear antenna waveguide structure is placed external to an AWG 4 on a fixed axis translated at $z = 0cm$.

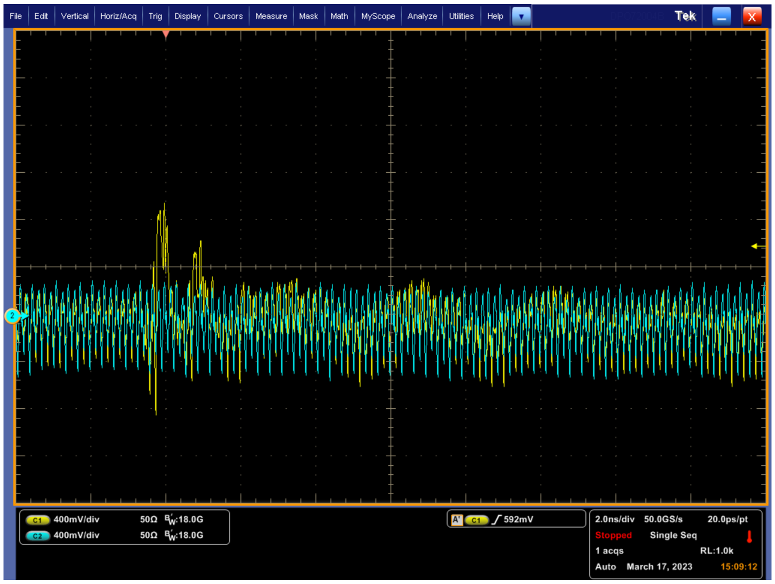

C1 400mV/div 50Ω BW:18.0G
C2 400mV/div 50Ω BW:18.0G
A' C1 ∫ 592mV
2.0ns/div 50.0GS/s 20.0ps/pt
Stopped Single Seq
1 acqs RL:1.0k
Auto March 17, 2023 15:09:12

Fig. D.50 An oscilloscope capture is taken from the experimental setup demonstrated in Fig. D.44 where the linear antenna waveguide structure is placed external to an AWG 4 on a fixed axis translated at $z = +2.5cm$.

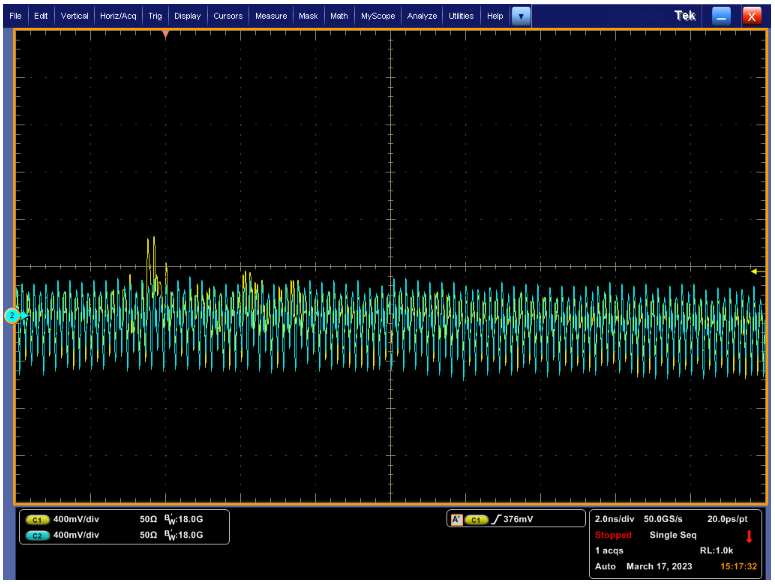

C1 400mV/div 50Ω BW:18.0G
C2 400mV/div 50Ω BW:18.0G
A' C1 ∫ 376mV
2.0ns/div 50.0GS/s 20.0ps/pt
Stopped Single Seq
1 acqs RL:1.0k
Auto March 17, 2023 15:17:32

Fig. D.51 An oscilloscope capture is taken from the experimental setup demonstrated in Fig. D.44 where the linear antenna waveguide structure is placed external to an AWG 4 on a fixed axis translated at $z = +7.6cm$.

D.5 Experiment 5: Mock DPF Time of Flight from a Linear Antenna (Pulse Generator)

In Chapter 4, Section 4.4.5, an experiment is documented in which a pulse generator is utilized to discharge a $4kV$, $20ns$ pulse into the mock DPF terminated by a matched load $R_L = 17\Omega$. A linear antenna is positioned external to the mock DPF at two different heights as shown in Fig. D.52 (a, b) located near the base of the mock DPF and Fig. D.52 (c, d) located near the termination end of the mock DPF. It should be noted that the waveguide and linear antenna do not make contact with the mock DPF.

For the oscilloscope captures provided in this section, channel 1 (yellow) is representative of the $60dB$ attenuated $4kV$, $20ns$ pulse signal from the output monitor of the pulse generator. Channel 2 (turquoise) is representative of the internal waveguide diode antenna. Channel 3 (magenta) is representative of the linear antenna protruding externally from one of the wide walls of the waveguide structure.

In Section 4.4.5, a graph is presented for oscilloscope channel 3 providing direct signal comparison when the linear antenna is positioned at the base of the mock DPF and the termination end of the mock DPF. This section is intended to provide the oscilloscope captures where the data is extrapolated from. The data from this experiment was captured on July 1st, 2021. Further information about this experiment can be referred back to in Chapter 4, Section 4.4.5.

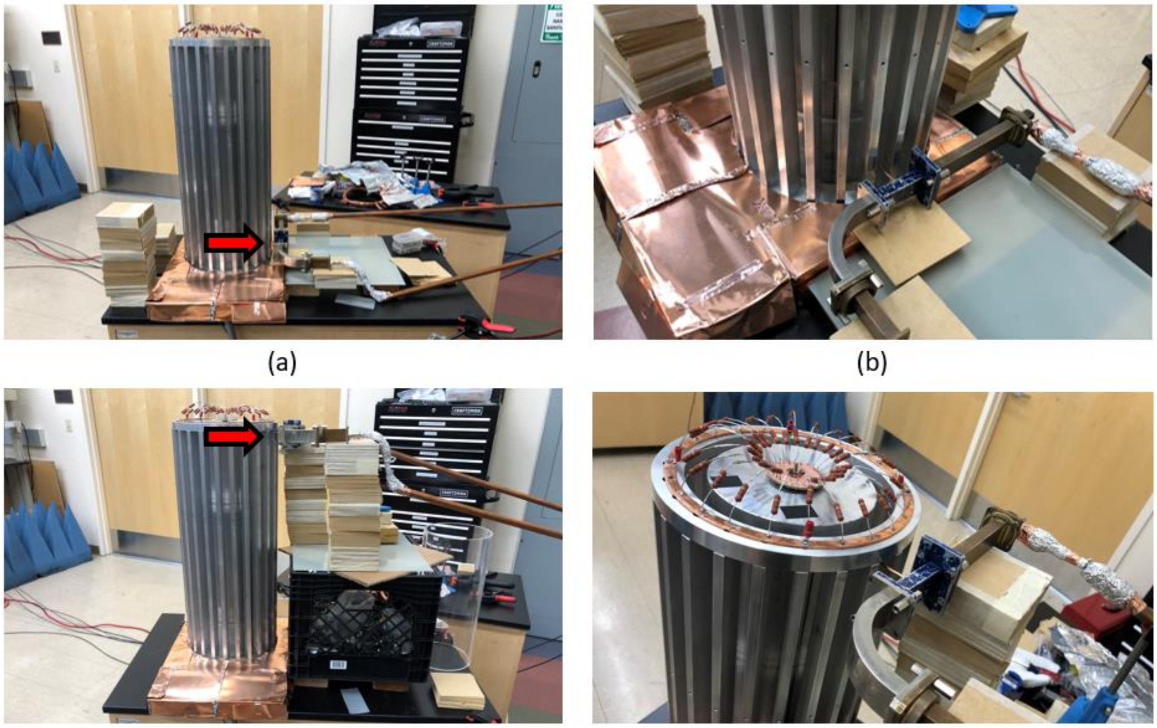

(a) (b) (c) (d)

Fig. D.52 (a, b, c, d) A pulse generator is used to fire a $4kV$ pulse signal along the mock DPF structure with a 17Ω load termination. An oscilloscope channel 1 connects to the output monitor of the pulse generator (attenuated by 80dB) and channel 3 connects to the linear antenna. Results are captured for when the linear antenna is positioned towards the base of the mock DPF in (a) and (b), and positioned towards the termination end of the mock DPF in (c) and (d).

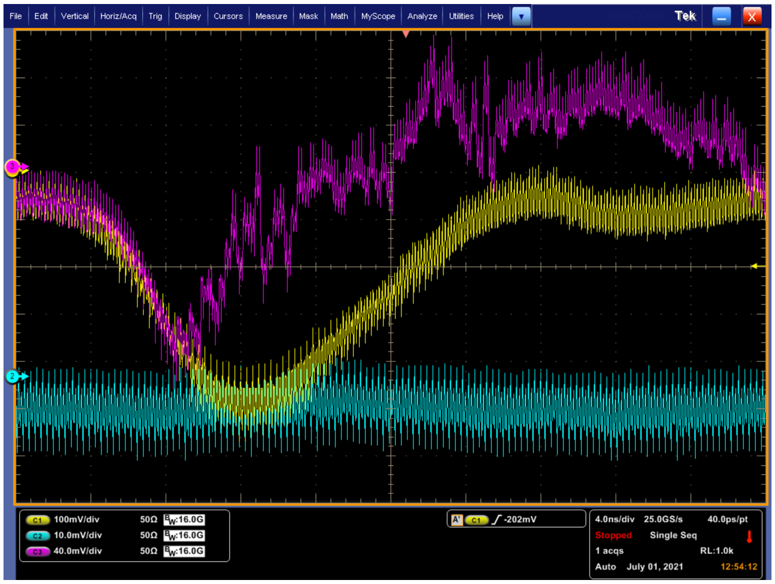

Fig. D.53 An oscilloscope capture is taken from the experimental setup demonstrated in Fig. D.52 where the linear antenna waveguide structure is placed externally at the base of the mock DPF ($z = -l_{DPF}$).

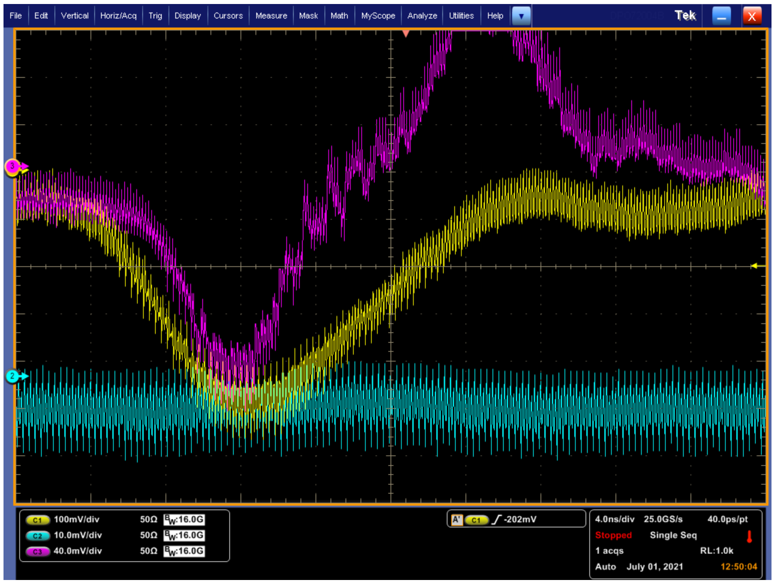

Fig. D.54 An oscilloscope capture is taken from the experimental setup demonstrated in Fig. D.52 where the linear antenna waveguide structure is placed externally at the termination end of the mock DPF ($z = 0$).

D.6 Experiment 6: Mock DPF Current Redirection (RC Source)

In Chapter 4, Section 4.4.4, an experiment is documented in which an RC configured circuit is utilized to discharge a $1kV$, $120\mu s$ pulse into the mock DPF terminated by a matched load $R_L = 17\Omega$. A linear antenna is positioned perpendicularly external to the mock DPF at a fixed height as shown in Fig. D.55 (a, b, c). Oscilloscope captures are then taken for three different scenarios provided in Fig. D.55: (a) no shorted path implemented along the mock DPF, (b) a shorted path placed at a position along the mock DPF after the linear antenna, and (c) a shorted path placed at a position along the mock DPF just before the linear antenna.

For the oscilloscope captures provided in this section, channel 1 (yellow) is representative of the linear antenna protruding externally from one of the wide walls of the waveguide structure. Channel 2 (turquoise) is representative of the internal waveguide diode antenna.

In Section 4.4.6, a graph is presented for oscilloscope channel 1 providing direct signal comparison for the linear antenna signal as recorded by the three different scenarios in this experiment. This section is intended to provide the oscilloscope captures where the data is extrapolated from. The data from this experiment was captured on March 17th, 2023. Further information about this experiment can be referred back to in Chapter 4, Section 4.4.6.

(a) (b) (c)

Fig. D.55 (a, b, c) A linear antenna is positioned external to the mock DPF at a fixed height. Three different perspectives are shown in (a), (b), and (c).

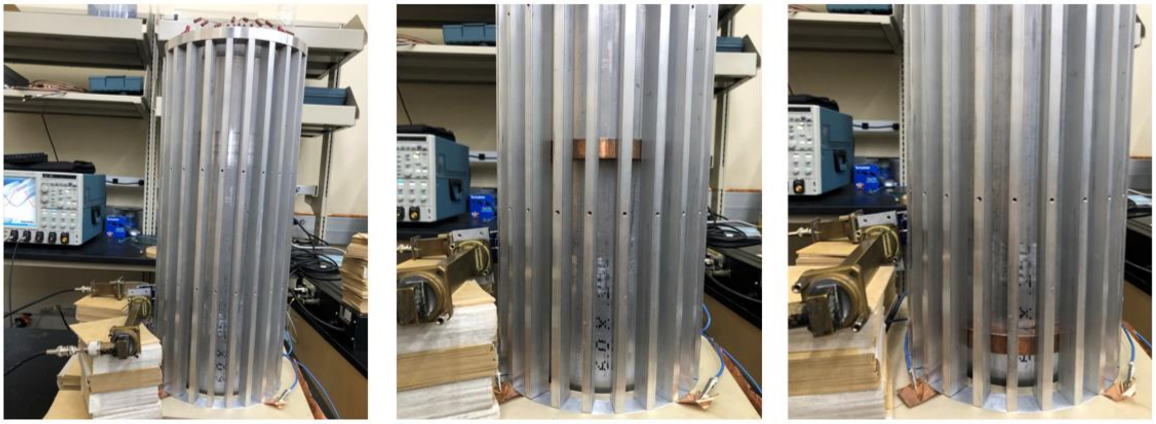

(a) (b) (c)

Fig. D.56 (a, b, c) Three different scenarios are provided for the experiment to be demonstrated: (a) no shorted path implemented along the mock DPF, (b) a shorted path placed at a position along the mock DPF after the linear antenna, and (c) a shorted path placed at a position along the mock DPF just before the linear antenna.

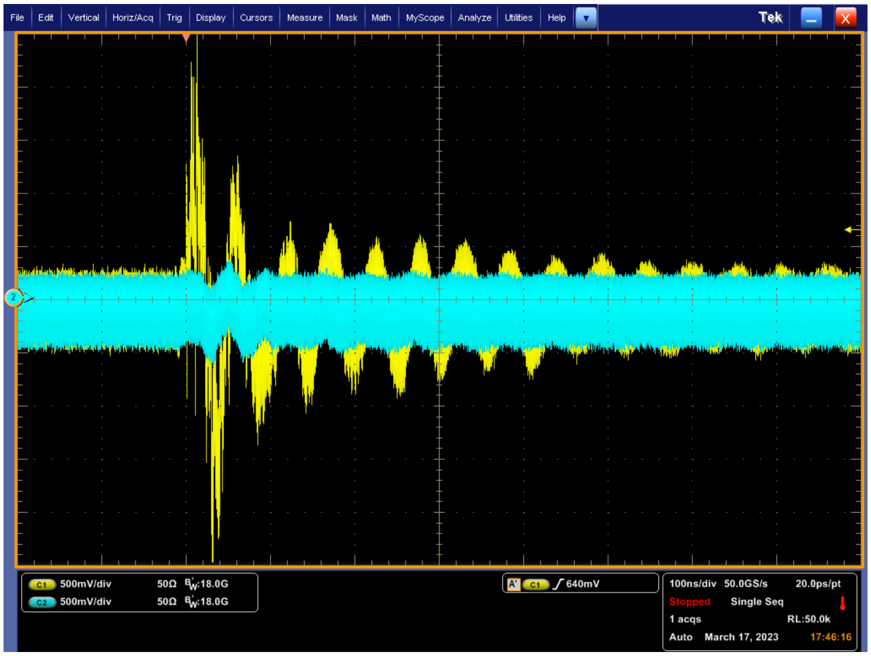

C1 500mV/div 50Ω BW:18.0G
C2 500mV/div 50Ω BW:18.0G
A' C1 ∫ 640mV
100ns/div 50.0GS/s 20.0ps/pt
Stopped Single Seq
1 acqs RL:50.0k
Auto March 17, 2023 17:46:16

Fig. D.57 An oscilloscope capture is taken from the experimental setup demonstrated in Fig. D.55 where no shorted path is implemented along the mock DPF consistent with Fig. D.55 (a).

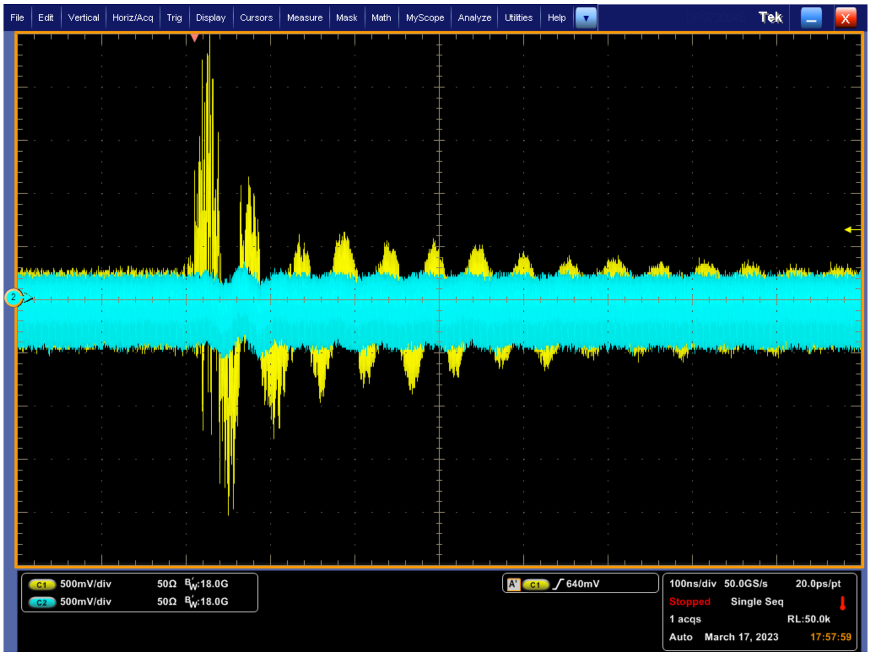

C1 500mV/div 50Ω BW:18.0G
C2 500mV/div 50Ω BW:18.0G
A' C1 ∫ 640mV
100ns/div 50.0GS/s 20.0ps/pt
Stopped Single Seq
1 acqs RL:50.0k
Auto March 17, 2023 17:57:59

Fig. D.58 An oscilloscope capture is taken from the experimental setup demonstrated in Fig. D.55 where a shorted path is placed at a position along the mock DPF after the linear antenna consistent with Fig. D.55 (b).

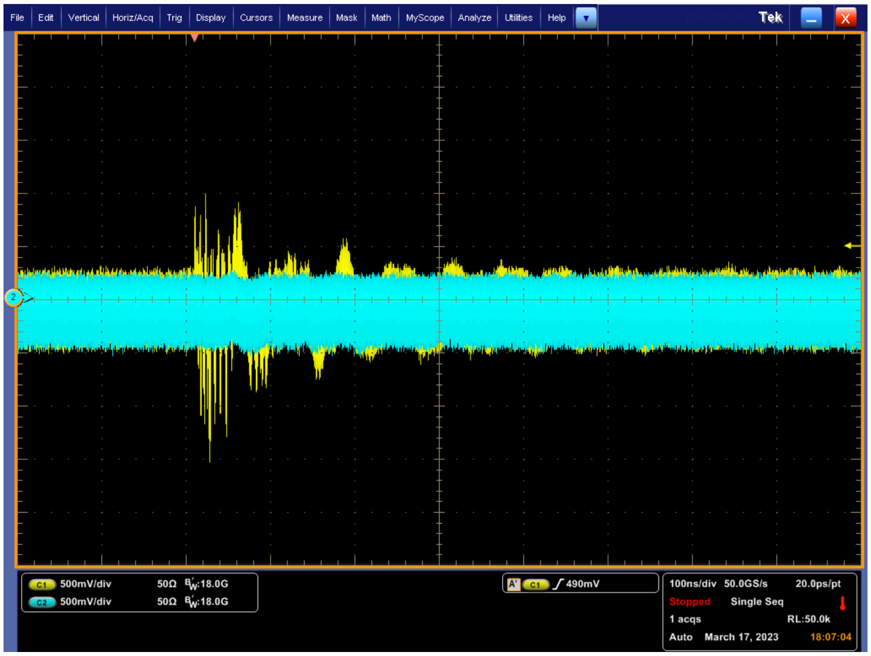

C1 500mV/div 50Ω B_W:18.0G
C2 500mV/div 50Ω B_W:18.0G
A' C1 490mV
100ns/div 50.0GS/s 20.0ps/pt
Stopped Single Seq
1 acqs RL:50.0k
Auto March 17, 2023 18:07:04

Fig. D.59 An oscilloscope capture is taken from the experimental setup demonstrated in Fig. D.55 where a shorted path is placed at a position along the mock DPF just before the linear antenna consistent with Fig. D.55 (c).

References

[1] Mather, J. (1965). Formation of a High-Density Deuterium Plasma Focus. *The Physics of Fluids, 8(2), 366-377.*

[2] Filippov, N., Filippova, T., & Vinogradov, V. (1962). DENSE HIGH-TEMPERATURE PLASMA IN A NON-CYLINDRICAL Z-PINCH COMPRESSION. *Nucl. Fusion, Suppl.*.

[3] Soto, L., Pavez, C., No, A., Moreno, J., & Veloso, F. (2010). Studies on scalability and scaling laws for the plasma focus: Similarities and differences in devices from 1MJ to 0.1 J. *Plasma Sources Sci. Technol, 1047256, 55017-9.*

[4] Zheng, L. (2019). Fusion energy: concepts and prospects. In: Magnetically Confined Fusion Plasma Physics. Morgan & Claypool Publishers. https://doi.org/10.1088/978-1-64327-138-5ch1

[5] Bittencourt, J.A. (2004). Introduction. In: Fundamentals of Plasma Physics. Springer, New York, NY. https://doi.org/10.1007/978-1-4757-4030-1_1.

[6] Jeremy P Chittenden (2000). The Z-pinch: approach to fusion. *Physics World, 13(5), 39.*

[7] A C Hayes (2017). Applications of nuclear physics. *Reports on Progress in Physics, 80(2), 026301.*

[8] J G Linhart (1988). Beam-target fusion in a dense Z-pinch. *Plasma Physics and Controlled Fusion, 30(12), 1641.*

[9] Arshad M Mirza, & Farah Deeba (2004). Thermonuclear Fusion Conditions in an Impurity-Seeded Multicascade Liner Staged Z-Pinch. *Physica Scripta, 70(4), 265.*

[10] Leopoldo Soto (2005). New trends and future perspectives on plasma focus research. *Plasma Physics and Controlled Fusion, 47(5A), A361.*

[11] S T Ong, K Chaudhary, J Ali, & S Lee (2014). Numerical experiments on neutron yield and soft x-ray study of a ~100 kJ plasma focus using the current profile fitting technique. *Plasma Physics and Controlled Fusion, 56(7), 075001.*

[12] Krishnan, M. (2012). The Dense Plasma Focus: A Versatile Dense Pinch for Diverse Applications. *IEEE Transactions on Plasma Science, 40(12), 3189-3221.*

[13] R S Rawat (2015). Dense Plasma Focus - From Alternative Fusion Source to Versatile High Energy Density Plasma Source for Plasma Nanotechnology. *Journal of Physics: Conference Series, 591(1), 012021.*

[14] V A Gribkov (2015). Physical processes taking place in dense plasma focus devices at the interaction of hot plasma and fast ion streams with materials under test. *Plasma Physics and Controlled Fusion, 57(6), 065010.*

[15] V A Gribkov, R Miklaszewski, M Paduch, E Zielinska, M Chernyshova, T Pisarczyk, V N Pimenov, E V Demina, J Niemela, M-L Crespo, A Cicuttin, K Tomaszewski, M J Sadowski, E Skladnik- Sadowska, K Pytel, A Zawadka, G Giannini, F Longo, A Talab, & S E Ul'yanenko (2015). Dense Plasma Focus: physics and applications (radiation material

science, single-shot disclosure of hidden illegal objects, radiation biology and medicine, etc. *Journal of Physics: Conference Series, 591(1), 012020.*

[16] Bennett, N., Blasco, M., Breeding, K., Constantino, D., DeYoung, A., DiPuccio, V., Friedman, J., Gall, B., Gardner, S., Gatling, J., Hagen, E., Luttman, A., Meehan, B., Misch, M., Molnar, S., Morgan, G., O'Brien, R., Robbins, L., Rundberg, R., Sipe, N., Welch, D., & Yuan, V. (2017). Development of the dense plasma focus for short-pulse applications. *Physics of Plasmas, 24(1).*

[17] Rishi VERMA, Ekansh MISHRA, Prosenjit DHANG, Basanta Kumar DAS, Manraj MEENA, Lakshman RONGALI, & Archana SHARMA (2020). Development and performance characterization of a compact plasma focus based portable fast neutron generator. *Plasma Science and Technology, 22(11), 115506.*

[18] Bennett, N., Blasco, M., Breeding, K., DiPuccio, V., Gall, B., Garcia, M., Gardner, S., Gatling, J., Hagen, E., Luttman, A., Meehan, B., Molnar, S., O'Brien, R., Ormond, E., Robbins, L., Savage, M., Sipe, N., & Welch, D. (2017). Kinetic simulations of gas breakdown in the dense plasma focus. *Physics of Plasmas, 24(6).*

[19] S Lee, S H Saw, L Soto, S V Springham, & S P Moo (2009). Numerical experiments on plasma focus neutron yield versus pressure compared with laboratory experiments. *Plasma Physics and Controlled Fusion, 51(7), 075006.*

[20] Lee, S. (2014). Plasma Focus Radiative Model: Review of the Lee Model Code. *Journal of Fusion Energy, 33.*

[21] G S Rakib, M A Malek, K A kabir, & M K Islam (2020). Numerical experiments on D-T gas filled PF1000 device with pressure variation. *Plasma Research Express, 2(4), 045004.*

[22] S H Saw, & S Lee (2015). Multi-scaling of the dense plasma focus. *Journal of Physics: Conference Series, 591(1), 012022.*

[23] S Lee, P Lee, S H Saw, & R S Rawat (2008). Numerical experiments on plasma focus pinch current limitation. *Plasma Physics and Controlled Fusion, 50(6), 065012.*

[24] M. G. Haines (1981). Dense Plasma in Z-pinches and the Plasma Focus. *Philosophical Transactions of the Royal Society of London. Series A, Mathematical and Physical Sciences, 300(1456), 649–663.*

[25] G. Decker, & R. Wienecke (1976). Plasma focus devices. *Physica B+C, 82(1), 155-164.*

[26] Kiuttu, G., Graham, J., Degnan, J., Brzosko, J., Coffey, S., Gale, D., Holmberg, C., Kreh, B., Meyers, J., Outten, C., Ruden, E., & Ware, K. (1996). New method of initiating multi-megampere, multi-megajoule plasma focus discharges using magnetized plasma flow switches. In *IEEE Conference Record - Abstracts. 1996 IEEE International Conference on Plasma Science* (pp. 238-).

[27] V A Gribkov, A Banaszak, B Bienkowska, A V Dubrovsky, I Ivanova-Stanik, L Jakubowski, L Karpinski, R A Miklaszewski, M Paduch, M J Sadowski, M Scholz, A Szydlowski, & K Tomaszewski (2007). Plasma dynamics in the PF-1000 device under full-scale energy storage: II. Fast electron and ion characteristics versus neutron emission parameters and gun optimization perspectives. *Journal of Physics D: Applied Physics, 40(12), 3592.*

[28] Daniel R. Lowe, personal communication, November 25, 2019.

[29] S. R. Seshadri, "Fundamentals of Transmission Lines and Electromagnetic Fields," Addison-Wesley Publishing Company, Copyright 1971, Chapter 1, pp. 1-33 (Book).

[30] Miner, Gayle F. (1996). Section 3-7 Transients on Transmission Lines. In: Lines and Electromagnetic fields for Engineers. Oxford Press, New York, NY (pgs. 200-220).

[31] Sadiku M. N, O. (2015). *Elements of Electromagnetics* (6th ed). Oxford University Press, New York, NY (pgs. 536-538).

[32] Pasternack, “Flexible RG58 Coax Cable Single Shielded with Black PVC (NC) Jacket,” 3-RG58C/U datasheet, 2017 [Revised Nov. 2023]

[33] Alexander C. K., Sadiku M. N, O. (2013). *Fundamentals of Electric Circuits* (5th ed). McGraw-Hill, New York, NY (pgs. 254-259).

[34] TE Connectivity, “Power Resistor – Type RR Series,” 3-1773449-2 datasheet, Oct. 2010 [Revised Nov. 2023]

[35] Colin L Defreitas, & Steve J Kane (2019). The noise handling properties of the Talbot algorithm for numerically inverting the Laplace transform. *Journal of Algorithms & Computational Technology, 13, 1748301818797069.*

[36] M. R. Spiegel, “Mathematical Handbook of Formulas and Tables,” Schaum’s Outline Series, McGraw-Hill, New York, 1969.

[37] Tucker McClure (2023). Numerical Inverse Laplace Transform (https://www.mathworks.com/matlabcentral/fileexchange/39035-numerical-inverse-laplace-transform), MATLAB Central File Exchange. Retrieved December 6, 2023.

Curriculum Vitae

Rocky Yasuaki Gonzalez

rockyg1995@outlook.com

Bachelor of Science – Electrical and Computer Engineering

University of Nevada, Las Vegas

December 2019